DISS. ETH NO. 27348

Investigation of Folate-Based Radiopharmaceuticals for Theragnostic Application and Combination Therapy

A thesis submitted to attain the degree of

DOCTOR OF SCIENCES of ETH ZURICH

(Dr. sc. ETH Zurich)

presented by

PATRYCJA SYLWIA GUZIK

MSc Eng in Biotechnology, Warsaw University of Technology

born on 17.08.1991

citizen of Poland

accepted on the recommendation of

Prof. Dr. Roger Schibli, examiner

Prof. Dr. Simon M. Ametamey, co-examiner

PD Dr. Cristina Müller, co-examiner

2021

Acknowledgment

Thank you!

Contents

Summary

The theragnostic concept in nuclear medicine makes use of radiolabeled ligands for targeting tumor-associated markers suitable for imaging and therapy of cancer diseases. The folate receptor-α (FRα) is a potential target to address numerous tumors of epithelial origin, including gynecological cancers, breast and lung cancers. Importantly, the FR presents also as isoform β that is a marker of activated macrophages involved in inflammatory diseases. Commonly, FR-specific binding of radioconjugates was achieved by employment of folic acid as a targeting agent that binds to both FR isoforms with nanomolar affinity. Although a distinct uptake of radiofolates was observed in tumors, the concomitant binding to the FRs expressed in the kidneys remained of concern due to the risk of damage to the kidneys caused by particle-emitting radiation of therapeutic radioconjugates. Modification of a folic acid conjugate with an albumin binder enhanced blood retention and resulted in tremendous increase of the tumor-to-kidney ratio. This in turn allowed for using radiofolates in preclinical therapy setting for the first time. The unselective binding of folic acid to the FRα and FRβ may be unfavorable for selection of cancer patients who could be inadequately treated based on false-positive (FRβ-based) imaging results. The focus of this thesis was, therefore, to improve radiofolates in the aspect of their diagnostic value for FRα-expressing tumors and therapeutic potential.

Wang et al. reported in 1992 that the *6S* isomer of 5-methyltetrahydrofolate (MTHF) binds with higher affinity to the FRα than to the FRβ. Thus, for the purpose of developing a tumor-selective (= FRα-selective) imaging agent, 5-MTHF was proposed as an alternative targeting molecule instead of folic acid. The design and syntheses of a series of ^{18}F-labeled 5-MTHF derivatives were performed by Boss et al. In the present thesis (chapter 2), the selectivity of the PET radiofolates, **6R**-[^{18}F]Aza-5-MTHF* and **6S**-[^{18}F]Aza-5-MTHF*, was investigated in comparison to the folic acid-based analogue, [^{18}F]AzaFol. Comparative studies with FRα- or FRβ-expressing cells performed in vitro revealed ~12-fold higher accumulation of **6R**-[^{18}F]Aza-5-MTHF in FRα-positive cells than in FRβ-expressing cells (~62% vs. ~5% of total added activity) and ~43-fold higher binding affinity to the FRα (IC_{50}=1.8 nM) than to the FRβ (IC_{50}=77 nM). Neither **6S**-[^{18}F]Aza-5-MTHF nor [^{18}F]AzaFol demonstrated differentiated binding to FR isoforms. In vivo studies with a mouse model bearing a FRα- and a FRβ-positive xenograft confirmed the in vitro findings and clearly indicated FRα selectivity of **6R**-[^{18}F]Aza-5-MTHF. As a next step, experiments with a mouse model that combines a FRα-positive tumor and FRβ-positive activated macrophages in inflammation will be necessary to confirm the

---

* The *R/S* nomenclature changes with the introduction of the heteroaromate in ^{18}F-labeled aza-5-MTHFs

6S/6R-5-MTHF = 6-[[4-[(2-Amino-5-methyl-4-oxo-1,6,7,8-tetrahydropteridin-6-yl)methylamino]**benzamido**]4-carboxy-butanoate

6R/6S-[^{18}F]Aza-5-MTHF = 6-[[4-[(2-Amino-5-methyl-4-oxo-1,6,7,8-tetrahydropteridin-6-yl)methylamino]2-[^{18}F]fluoro-**nicotinamido**]4-carboxybutanoate acid

feasibility to unambiguously image tumors in the presence of inflammatory sites.

It was previously shown in our group that pre-injection of the antifolate, pemetrexed (PMX), reduced renal accumulation of conventional radiofolates without simultaneous blockade of the uptake in the tumor. In this thesis (chapter 3) we combined this strategy with the albumin-binding folic acid radioconjugate ([^{177}Lu]Lu-cm13) to further improve the tissue distribution profile which is particularly important in view of therapeutic application. Biodistribution studies with mice that were injected with PMX prior to the [^{177}Lu]Lu-cm13, demonstrated increased tumor-to-kidney ratios by 33–53%, depending on the type of FR-positive tumor. It was found that additional injections of PMX, at 3 h or 7 h after the administration of the radioconjugate resulted in 46–72% higher ratios as compared to the values obtained with radiofolate alone. These results were confirmed by SPECT/CT scans which readily visualized the tumor xenografts, whereas accumulation of [^{177}Lu]Lu-folate in the kidneys was significantly reduced in mice injected with PMX. Although PMX had a positive impact in terms of reducing the kidney uptake of albumin-binding radiofolates, the effect was only moderate. Moreover, the repeated injections and potential toxicity of PMX make this concept challenging with regard to clinical application.

The concept of exchanging the FR-targeting molecule and replacing folic acid with **6R**- or **6S**-isomer of 5-MTHF was employed for albumin-binding folate conjugates as well (chapter 4). **6R**-RedFol-1 and **6S**-RedFol-1 were radiolabeled with ^{177}Lu and compared in vitro and in vivo to [^{177}Lu]Lu-OxFol-1, a previously developed and characterized folic acid-based FR-targeting agent. Both [^{177}Lu]Lu-**6R**-RedFol-1 and [^{177}Lu]Lu-**6S**-RedFol-1 demonstrated similar in vitro properties as [^{177}Lu]Lu-OxFol-1, however, the biodistribution studies revealed 4–5-fold enhanced blood retention in the case of the 5-MTHF radioconjugates. Notably, the tumor uptake expressed as integrated area under the time-activity curve (AUC$_{0 \to 120h}$) of [^{177}Lu]Lu-**6R**-RedFol-1 and [^{177}Lu]Lu-**6S**-RedFol-1 was 3.2-fold and 3.6-fold increased in comparison to [^{177}Lu]Lu-OxFol-1, respectively. In the case of [^{177}Lu]Lu-**6S**-RedFol-1 the kidney uptake was ~3-fold increased, whereas the renal retention of [^{177}Lu]Lu-**6R**-RedFol-1 was similar to that of [^{177}Lu]Lu-OxFol-1. This led to an almost 4-fold increased tumor-to-kidney AUC$_{0 \to 120h}$ ratio for [^{177}Lu]Lu-**6R**-RedFol-1 than for [^{177}Lu]Lu-**6S**-RedFol-1 and [^{177}Lu]Lu-OxFol-1. In a comparative therapy study, it was demonstrated that at equal activity (10 MBq), the therapeutic effect of [^{177}Lu]Lu-**6R**-RedFol-1 was better than that of [^{177}Lu]Lu-OxFol-1, reflected by a slower tumor growth and, consequently, an increased median survival time (49 d and 34 d, respectively) as compared to the control (22 d). If radioconjugates were applied at 15 MBq activity, mice injected with [^{177}Lu]Lu-OxFol-1 showed median survival of 44 d, whereas all mice treated with [^{177}Lu]Lu-**6R**-RedFol-1 survived until the end of the study (>56 d).

It was previously shown by other research groups that a radiation stimulus can improve the tumor response to therapy with immune checkpoint inhibitors in preclinical and clinical studies. This effect is caused by increased infiltration of immune cells upon tumor irradiation and is described as a switch from an immunologically "cold" tumor to a "hot" tumor. We envisioned that such sensitizing effect

could be achieved using FR-targeting radioconjugate (chapter 5). The concept was tested in a syngeneic mouse model established from NF9006 mammary gland tumor cells derived from MMTV-neu transgenic mice. The model was characterized in our group with regard to FR expression and in vitro and in vivo targeting. The ^{177}Lu-DOTA-folate conjugate (folic acid-based) applied at a low activity (5 MBq), resulting in an absorbed tumor dose of 3.5 Gy, sensitized the FR-positive NF9006 tumors to anti-CTLA-4 immunotherapy which was manifested by reduced tumor growth. This resulted in a significantly improved median survival of mice (>70 days) as compared to mice that received the ^{177}Lu-folate conjugate or the anti-CTLA-4 antibody alone. Each modality had only a minor effect on tumor growth and did not substantially increase the median survival (23 d and 19 d, respectively) as compared to untreated controls (12 d). Future studies may be directed towards the investigation of the immune-profile to characterize the changes in tumor microenvironment upon the treatment with ^{177}Lu-folate conjugate and the anti-CTLA-4 antibody.

Transgenic mice with spontaneously developed tumors present a more representative preclinical cancer model than mice bearing subcutaneous human tumors. This refers primarily to the higher complexity of spontaneous models, and the interplay between tumor microenvironment and the immune system. In chapter 6 of this thesis, we set out to investigate the uptake of ^{177}Lu-DOTA-folate conjugate in spontaneous breast tumors of MMTV-neu mouse strain, and compare it with NF9006 syngeneic model. SPECT/CT images demonstrated significant uptake of the radiofolate in the tumors and kidneys. The quantity of injected activity for imaging (25 MBq) was revealed to have a therapeutic effect as tumors started to shrink shortly after. Subsequent follow-up scans with [^{177}Lu]Lu-DOTA-folate allowed visualizing the changes in sub-tissue distribution of radiofolate over time. The MMTV-neu transgenic mice could serve as a more sophisticated model for investigation of FR-targeted therapies in combination with immune checkpoint inhibitors and other immune-modulatory agents.

The results of this thesis represent a major step towards the theragnostic application of radiofolates. The new generation of 5-MTHF-based ^{18}F-radiotracers were designed for unambiguous cancer imaging using PET. On the other hand, the 5-MTHF-based ^{177}Lu-folate conjugates will enable a safer therapeutic application by preventing damage to radiosensitive kidneys. Finally, it was demonstrated that the application of folate radioconjugates can sensitize tumors to immunotherapeutic effects, which may open new perspectives for future management of FR-positive cancer diseases.

Zusammenfassung

Das theragnostische Konzept in der Nuklearmedizin beruht auf der Verwendung von Radioliganden, welche an tumorassoziierte Zielstrukturen binden, die sich für die Bildgebung und Therapie von Krebserkrankungen eignen. Der Folatrezeptor-α (FRα) stellt eine solche Zielstruktur dar, weil er auf zahlreichen Tumoren epithelialen Ursprungs wie gynäkologische Krebsarten, Brust- und Lungenkrebs vorkommt. Darüber hinaus wird die β-Isoform des FRs von aktivierten Makrophagen, welche in Entzündungskrankheiten involviert sind, exprimiert. Eine FR-spezifische Bindung von Radiokonjugaten wurde durch den Einsatz von Folsäure als Ligand erreicht. Folsäure bindet mit einer Affinität im nanomolaren Bereich an beide FR Isoformen. Obwohl eine deutliche Aufnahme der Radiofolate in Tumoren beobachtet wurde, erwies sich deren gleichzeitige Bindung an die in den Nieren exprimierten FR als ungünstig, da die partikelemittierende Strahlung therapeutischer Radiokonjugate das Risiko einer Nierenschädigung birgt. Die Modifikation eines Folatkonjugats mit einer albuminbindenden Einheit führte zu einer Verlängerung dessen Blutzirkulation und dadurch zu einer enormen Verbesserung des Tumor-zu-Nieren-Verhältnisses der angereicherten Aktivität. Dies wiederum ermöglichte erstmals den Einsatz von Radiofolaten in präklinischen Therapiestudien. Die nicht-selektive Bindung der Folsäure an den FRα könnte sich jedoch in Bezug auf die Selektion von Krebspatienten als ungünstig erweisen, da aufgrund der potentiell falsch-positiven (FRβ-basierten) Bildgebungsresultate, Patienten einer nicht angemessenen Behandlung unterzogen werden könnten. Daher lag der Schwerpunkt dieser Arbeit auf der Untersuchung von Radiofolaten hinsichtlich deren diagnostischer Bedeutung für FRα exprimierende Tumoren und deren therapeutischen Potenzials. Wang et al. zeigte im Jahr 1992, dass die Bindungsaffinität des **6S**-Isomer des 5-Methyltetrahydrofolats (MTHF) zum FRα höher ist als zum FRβ. Aus diesem Grund wurde für die Entwicklung eines tumorselektiven (d.h. FRα-selektiven) Folatkonjugates das 5-MTHF anstelle von Folsäure als alternativer Ligand vorgeschlagen. Das Design und die Synthesen einer Reihe von ^{18}F-markierten 5-MTHF-Derivaten wurden von Boss et al. etabliert. In der vorliegenden Arbeit wurde die Selektivität der PET Radiofolate, **6R**-[^{18}F]Aza-5-MTHF* und **6S**-[^{18}F]Aza-5-MTHF*, im Vergleich zu dem auf Folsäure basierenden Analogon [^{18}F]AzaFol untersucht (Kapitel 2). In vitro durchgeführte Vergleichsstudien mit FRα- oder FRβ-exprimierenden Zellen zeigten für **6R**-[^{18}F]Aza-5-MTHF eine ~12-fach höhere Akkumulation in FRα-positiven Zellen gegenüber FRβ-exprimierenden Zellen (~62% vs. ~5% der gesamten hinzugefügten Aktivität) und eine ~43-fach höhere Bindungsaffinität zum FRα

_____

* Die *R/S*-Nomenklatur ändert sich durch die Einführung des Heteroaromaten in die Struktur des ^{18}F-markierten aza-5-MTHF
6*S*/6*R*-5-MTHF = 6-[[4-[(2-Amino-5-methyl-4-oxo-1,6,7,8-tetrahydropteridin-6-yl)methylamino]**benzamido**]4-carboxy-butansäure
6*R*/6*S*-[^{18}F]Aza-5-MTHF = 6-[[4-[(2-Amino-5-methyl-4-oxo-1,6,7,8-tetrahydropteridin-6-yl)methylamino]2-[^{18}F]fluoro-**nicotinamido**]4-carboxybutansäure

(IC$_{50}$=1.8 nM) als zum FRβ (IC$_{50}$=77 nM). Weder **6S**-[^{18}F]Aza-5-MTHF noch [^{18}F]AzaFol zeigten jedoch eine selektive Bindung an den FRα. In vivo Studien, die auf einem Mausmodell mit FRα- und FRβ-positiven Xenograften beruhten, bestätigten die in vitro Resultate und zeigten die selektive Bindung von 6R-[^{18}F]Aza-5-MTHF an den FRα. Um die Möglichkeit einer eindeutigen Darstellung von Tumoren in Gegenwart von Entzündungsherden zu verifizieren, sollen in einem nächsten Schritt Experimente mit einem Mausmodell durchgeführt werden, welches einen FRα-positiven Tumor und gleichzeitig eine Entzündung, welche FRβ-positive aktivierte Makrophagen involviert, kombiniert.

In unserer Gruppe wurde bereits gezeigt, dass die Injektion des Antifolats Pemetrexed (PMX) vor dem Radiofolat die renalen Aktivitätsakkumulation reduziert, ohne dabei die Aufnahme in den Tumor zu blockieren. In dieser Arbeit kombinierten wir diese Strategie mit dem albuminbindenden Folatkonjugat [^{177}Lu]Lu-cm13, um das Gewebeverteilungsprofil weiter zu verbessern (Kapitel 3). Dies ist im Hinblick auf eine therapeutische Anwendung besonders wichtig. Biodistributionsstudien mit Mäusen, denen PMX vor der Injektion des [^{177}Lu]Lu-cm13 appliziert wurde, zeigten je nach Xenograft ein um 33–53% erhöhtes Tumor-zu-Nieren-Verhältnis. Eine zusätzliche PMX Injektion, drei oder sieben Stunden nach Verabreichung des Radiokonjugats, führte zu einem 46–72% höheren Tumor-zu-Nieren Verhältnis verglichen mit den Werten, welche mit dem Radiofolat alleine erzielt wurden. Diese Ergebnisse entsprachen den SPECT/CT Bildern, die eine den Tumor gut visualisierten, während die Nierenakkumulation von [^{177}Lu]Lu-Folat in Mäusen, denen PMX appliziert wurde, signifikant reduziert wurde. Obwohl PMX bezüglich der Verringerung der Nierenaufnahme von albuminbindenden Radiofolaten einen positiven Einfluss hatte, war der Effekt nur mässig. Wiederholte Injektionen des potenziell toxischen PMX wäre für eine klinische Anwendung jedoch eher schwierig realisierbar.

Die Strategie, Folsäure als FR-bindendes Molekül mit den **6R**- und **6S**-Isomeren von 5-MTHF zu ersetzen, wurde auch auf die albuminbindenden Folatkonjugate übertragen (Kapitel 4). **6R**-RedFol-1 und **6S**-RedFol-1 wurden mit ^{177}Lu radioaktiv markiert und die in vitro und in vivo Eigenschaften der beiden Konjugate mit jenen von [^{177}Lu]Lu-OxFol-1 verglichen. Sowohl [^{177}Lu]Lu-**6R**-RedFol-1 also auch [^{177}Lu]Lu-**6S**-RedFol-1 wiesen ähnliche in vitro Eigenschaften wie [^{177}Lu]Lu-OxFol-1 auf, jedoch konnte in Bioverteilungsstudien gezeigt werden, dass die 5-MTHF basierenden Radiokonjugate eine 4–5-fach höhere Blutretention aufwiesen. Die Aufnahme von [^{177}Lu]Lu-**6R**-RedFol-1 und [^{177}Lu]Lu-**6S**-RedFol-1 in den Tumor, ausgedrückt als integrierte Fläche unter der Zeit-Aktivitätskurve (AUC$_{0→120h}$), war im Vergleich zu [^{177}Lu]Lu-OxFol-1 um einen Faktor 3.2, respektive 3.6 grösser. Während [^{177}Lu]Lu-**6S**-RedFol-1 eine dem [^{177}Lu]Lu-OxFol-1 vergleichbare Nierenaufnahme zeigte, war diese für [^{177}Lu]Lu-**6S**-RedFol-1 ~3-fach erhöht. Dies führte zu einem fast 4-fach höheren Tumor-zu-Nieren-Verhältnis (AUC$_{0→120h}$) für [^{177}Lu]Lu-**6R**-RedFol-1 im Vergleich zu [^{177}Lu]Lu-**6S**-RedFol-1 und [^{177}Lu]Lu-OxFol-1. In einer Therapievergleichsstudie wurde gezeigt, dass bei gleicher Aktivität (10 MBq) mit [^{177}Lu]Lu-**6R**-RedFol-1 ein langsameres Tumorwachstum und eine längere mittlere

Überlebenszeit (49 Tage) erzielt werden konnte als dies bei Mäusen, die mit [^{177}Lu]Lu-OxFol-1 behandelt wurden (mittlere Überlebenszeit 34 Tage) oder gar nicht behandelt wurden (mittlere Überlebenszeit 22 Tage) der Fall war. Bei einer Aktivität von 15 MBq überlebten die Mäuse, die mit [^{177}Lu]Lu-OxFol-1 injiziert wurden, im Schnitt 44 Tage während alle Mäuse, denen [^{177}Lu]Lu-*6R*-RedFol-1 verabreicht wurde, bis zum Ende der Studie (>56 Tage) überlebten.

Es wurde bereits von anderen Forschungsgruppen in präklinischen und klinischen Studien gezeigt, dass ein Strahlungsstimulus die Sensitivität gegenüber einer Therapie mit Immuncheckpoint Inhibitoren verbessern kann. Dieser Effekt wurde durch eine erhöhte Infiltration von Immunzellen nach der Tumorbestrahlung verursacht und demzufolge als Umwandlung eines immunologisch «kalten» in einen «heissen» Tumor bezeichnet. Ein solcher Effekt zur Sensibilisierung des Tumors könnte mit einem folatrezeptorbindenden Radiokonjugat erzielt werden (Kapitel 5). Dieses Prinzip wurde in einem syngenen Mausmodell getestet, welches mit NF9006 Milchdrüsentumorzellen von MMTV-neu transgenen Mäusen etabliert wurde. Das Modell wurde hinsichtlich der Folatrezeptorexpression und der in vitro und in vivo Bindung von unserer Gruppe charakterisiert. Das ^{177}Lu-DOTA-Folatkonjugat, welches auf Folsäure basiert, zeigte bei einer tiefen injizierten Aktivität (5 MBq) und einer absorbierten Tumordosis von 3.5 Gy einen sensibilisierenden Effekt auf die FR-positiven NF9006 Tumoren gegenüber einer anti-CTLA-4 Immuntherapie. Dies führte zu einem verringerten Tumorwachstum und einer längeren mittleren Überlebenszeit der Mäuse (>70 Tage) im Vergleich zu Mäusen, die entweder nur das ^{177}Lu-Folatkonjugat oder nur den anti-CTLA-4 Antikörper erhalten hatten. Beide Monotherapien zeigten einen minimalen Einfluss auf das Tumorwachstum und konnten die mittlere Überlebenszeit gegenüber der Kontrollgruppe nicht massgeblich verlängern (^{177}Lu-Folatkonjugat: 23 Tage; anti-CTLA-4: 19 Tage; Kontrollgruppe: 12 Tage). Weiterführende Studien könnten sich dem Erstellen von Immunprofilen widmen, um die Veränderungen der Tumormikroumgebung nach einer Therapie mit ^{177}Lu-Folatkonjugat und anti-CTLA-4 Antikörper zu charakterisieren.

Transgene Mäuse mit sich spontan entwickelnden Tumoren sind für die klinische Situation repräsentativer als Mäuse mit subkutanen humanen Tumoren. Dies bezieht sich vor allem auf die höhere Komplexität der spontan entwickelten Tumoren und das Zusammenspiel zwischen der Tumorumgebung und des Immunsystems. In Kapitel 6 dieser Arbeit untersuchten wir die Aufnahme von ^{177}Lu-DOTA-Folatkonjugat in die spontanen Brusttumore von MMTV-neu Mäusen und verglichen diese mit dem NF9006 syngenen Modell. SPECT/CT Bilder zeigten eine signifikante Aufnahme des Radiofolats in den Tumoren und Nieren. Die Menge injizierter Aktivität für die Bildgebung (25 MBq) hatte einen therapeutischen Effekt und die Tumoren begannen bereits kurze Zeit nach der Injektion zu schrumpfen. Die darauffolgende Bildgebung mit [^{177}Lu]Lu-DOTA-Folat erlaubten Veränderungen der Verteilung der Aktivität in den Geweben über die Zeit aufzuzeigen. Das MMTV-neu transgene Mausmodell könnte als ein weiterentwickeltes Modell für die Untersuchung von FR-gezielten Therapien in Kombination mit Immuncheckpoint Inhibitoren oder anderen immunregulierenden Wirkstoffen dienen.

Die Resultate dieser Arbeit stellen einen weiteren Schritt in der Entwicklung von Radiofolaten in Richtung theragnostischer Anwendung dar. Die neue Generation von 5-MTHF-basierenden ^{18}F-Radiofolaten wurden für eine eindeutige Krebsbildgebung mittels PET entworfen. Die 5-MTHF-basierenden ^{177}Lu-Folatkonjugate scheinen eine sichere therapeutische Anwendung zu ermöglichen, um Gewebsschäden in den radiosensitiven Nieren zu vermeiden. Ausserdem wurde gezeigt, dass Radiofolatkonjugate die Tumoren für eine Immuntherapie sensibilisieren können. Dies könnte neue Perspektiven für die Behandlung von Krebserkrankungen mit FR-positiven Tumoren eröffnen.

Abbreviations

ALP	Alkaline phosphatase
ALB	Albumin
AML	Acute myeloid leukemia
ANOVA	Analysis of variance
AUC	Area under the curve
Bl	Blood/ Urinary bladder
BUN	Blood urea nitrogen
B_{50}	Half maximum binding
CDX	Cell line-derived xenograft
CT	Computed tomography
CML	Chronic myeloid leukemia
CRE	Creatinine
Da	Dalton (= 1 g/mol)
DMSO	Dimethyl sulfoxide
DOTA	1,4,7,10-tetraazacyclododecane-1,4,7,10-tetraacetic acid
DTPA	Diethylenetriaminepentaacetic acid
EDTA	Ethylenediaminetetraacetic acid
FA	Folic acid
FCS	Fetal calf serum
FFRPMI	Folate-free RPMI cell culture medium
FR	Folate receptor
FWHM	Full width at half maximum
Gy	Gray (J/kg)
HCl	Hydrochloric acid
HE	Hematoxylin-eosin
HER2	Human epidermal growth factor receptor 2
HPLC	High performance liquid chromatography
HRP	Horseradish peroxidase
I	Intensity of radiation in percent
IA/g	Injected activity per gram
IC_{50}	Half-maximal inhibitory concentration
ICI	Immune checkpoint inhibitors
IgG	Immunoglobulin G
i.p.	Intraperitoneal
i.v.	Intravenous
keV	Kiloelectron volt
Ki	Kidneys
L	Length of tumor
LET	Linear energy transfer
Li	Liver
mAb	Monoclonal antibody
MBq	Megabequerel
MIP	Maximum intensity projection
MMTV	Mouse mammary tumor virus
5-MTHF	5-Methyltetrahydrofolate
NaCl	Sodium chloride

NODAGA	1,4,7-triazacyclononane,1-glutaric acid-4,7-acetic acid
PBS	Phosphate-buffered saline
PDX	Patient derived xenograft
PET	Positron Emission Tomography
p.i.	Post-injection
PMX	Pemetrexed (antifolate drug)
PSMA	Prostate Specific Membrane Antigen
RBW	Relative Body Weight
RIPA	Radioimmunoprecipitation assay buffer
RPMI	Roswell Park Memorial Institute medium
RT	Room temperature
RTV	Relative tumor volume
s.c.	Subcutaneous
SD	Standard deviation
SDS-PAGE	Sodium dodecyl sulfate polyacrylamide gel electrophoresis
SPECT	Single Photon Emission Computed Tomography
TBIL	Total bilirubin
TGD	Tumor growth delay
TGDI	Tumor growth delay index
TGI	Tumor growth inhibition
t_R	Retention time
Tu	Tumor
$T_{1/2}$	Physical half-life
W	Width of tumor

I. General Introduction

1.1. Clinical Potential of Tumor-Targeting Radiopharmaceuticals

1.1.1. General Features of Diagnostic and Therapeutic Radiopharmaceuticals

The role of nuclear medicine in oncology has grown during the last two decades. It relies on development of tumor-targeting radiopharmaceuticals that can be applied for non-invasive cancer diagnosis as well as for therapy. Such radiopharmaceutical consists of a molecule which localizes a tumor-associated target (Fig. 1.1), and consequently, allows for an accurate assessment of cancer location, possible dissemination, and later on, precise treatment with particle-emitting radiation [1]. The radiopharmaceutical is labeled with a radiometal via a chelating system or, if the radionuclide is not metal-based, it can be directly installed to the backbone of the tumor-targeting agent [1].
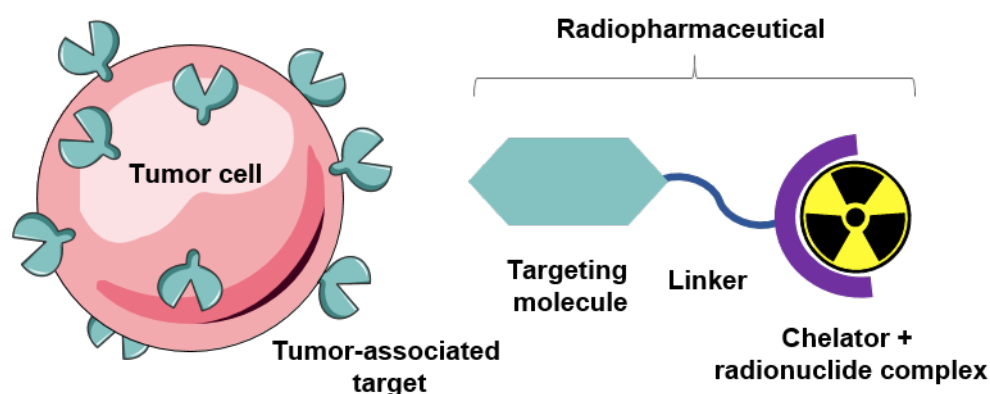
Fig. 1.1 Concept of a tumor-targeting radiopharmaceutical. Visualization of the tumor cell was prepared using Servier Medical Art licensed under a Creative Commons Attribution 3.0 Unported License.

The choice of radionuclide depends on the purpose of the radiopharmaceutical's application (Table 1.1). The type of decay plays a critical role in this regard. Radionuclides used for SPECT imaging emit γ-radiation with a tissue range up to several centimeters [2,3]. PET radioisotopes decay by emission of positrons (β^+), which annihilate with electrons in the surrounding tissue. The annihilation results in emission of two γ-rays of 511 keV energy that travel at opposite directions. Importantly, due to this defined geometry of annihilation photons, PET does not require additional collimator, and therefore has higher sensitivity as compared to SPECT in a clinical setting [2,3].

The radionuclides decaying by the emission of electrons (β^-, Auger or conversion electrons) or alpha particles are suitable for therapeutic application, since this type of particle radiation destroys tumor cells. So far β^--emitters are the most frequently used radionuclides for targeted radionuclide therapy in clinics [4]. Compared to α-particles and Auger electron, β^--particles emitted by medical radionuclides can have a tissue range of up to ten millimeter, which results in irradiation of a cluster of adjacent tumor cells. This observation is commonly referred to as "crossfire" effect [5,6]. Alpha-emitters and Auger electron-emitters are suitable for the treatment of small metastases and single tumor cells, due to the short tissue range and high linear energy transfer (LET), which is the energy deposited per unit of distance. In contrast to β^--emitters, these properties allow for minimizing the damage to the normal tissues and

delivering a high dose-burden to the tumor, since the "crossfire" effect is not existent or reduced, respectively [1,7].

In an ideal case, pre-therapeutic imaging and therapy would be performed using radionuclides of the same chemical element enabling radiotheragnostic application with chemically identical tumor-targeting radiopharmaceuticals, e.g. iodine radioisotopes. However, commonly, this is accomplished with diagnostic and therapeutic radionuclides of different elements, which provide similar but not the same chelation chemistry.

Table 1.1 Examples of clinically used radionuclides and their physical decay properties. Decay data were provided from NuDat database (version 2.8) [8]

Nuclide	Half-life	Energy [keV]; (Intensity)	Application
^{177}Lu	6.65 d	$E\beta^-_{av} = 134$ (100%) $E\gamma = 208$ (10%); 113 (6%)	Therapy (& SPECT)
^{90}Y	2.67 d	$E\beta^-_{av} = 934$ (100%)	Therapy
^{131}I	8.03 d	$E\gamma = 284$ (6.1%), 364 (81.5%) $E\beta^-_{av} = 182$ (100%)	Therapy (& SPECT)
^{223}Ra	11.43 d	$E\alpha = 5979$ (100%)	Therapy
^{111}In	2.80 d	$E\gamma = 171$ (91%), 245 (94%)	SPECT
^{99m}Tc	6.0 h	$E\gamma = 141$ (89%)	SPECT
^{67}Ga	3.26 d	$E\gamma = 93$ (39%), 184 (21%)	SPECT
^{68}Ga	68 min	$E\beta^+_{av} = 830$ keV (89%)	PET
^{18}F	110 min	$E\beta^+_{av} = 250$ (97%)	PET
^{11}C	20 min	$E\beta^+_{av} = 386$ keV (100%)	PET

1.1.2. Clinically Used Receptor-Targeted Radiopharmaceuticals for Cancer Diagnosis and Therapy

The first and best established radiopharmaceuticals in the clinics are radiolabeled somatostatin (SST) analogs targeting the somatostatin receptor (SSTR). SSTR is overexpressed on neuroendocrine tumors (NETs) originating from gastroenteropancreatic or pulmonary tract [7]. Somatostatin is a natural peptide hormone with a short blood plasma half-life due to enzymatic degradation [9]. Introduction of D-amino acids and shortening the peptide chain resulted in a number of analogs which are more resistant to degradation while preserving binding properties of the natural SSTR binding peptide. [^{111}In]In-DTPA-octreotide (OctreoScan®) was the first somatostatin analog that was approved for diagnosis and monitoring of patients with SSTR-expressing tumors. Currently, a newer analog linked to a DOTA-chelating system, [^{68}Ga]Ga-DOTATOC is being used for PET/CT [10,11]. The development of SST analogs comprising a DOTA chelator, also enabled the chelation of β^--emitting radionuclides suitable for therapeutic purposes, among those ^{90}Y and ^{177}Lu. Both [^{90}Y]Y-DOTATOC and [^{177}Lu]Lu-DOTATATE showed encouraging results in peptide receptor radionuclide therapy (PRRT) [12,13]. Owing to the lower energy and range of β^--particles emitted by ^{177}Lu as compared with ^{90}Y, [^{177}Lu]Lu-

DOTATATE showed less toxicity to normal tissues, including kidneys and bone marrow. Therefore, [¹⁷⁷Lu]Lu-DOTATATE has become the most widely used somatostatin analog for PRRT [14]. Recently, PRRT with [¹⁷⁷Lu]Lu-DOTATATE was approved in the USA and several European countries for the treatment of patients with progressive metastatic gastroenteropancreatic NETs [15].

Another successful example of radiopharmaceuticals are prostate-specific membrane antigen (PSMA)-targeting radioligands. PSMA is a transmembrane protein, which is overexpressed particularly in metastatic castration-resistant prostate cancer (mCRPC) [16]. PSMA is also present in the healthy prostate, kidneys and brain, but at significantly lower levels. Development of radiopharmaceuticals for prostate cancer resulted in small-molecule-based PSMA inhibitors [17]. Until now, [⁶⁸Ga]Ga-PSMA-11 and [¹⁷⁷Lu]Lu-PSMA-617 are most often used for diagnosis and radionuclide therapy of prostate cancers, respectively, in clinics. [¹⁷⁷Lu]Lu-PSMA-617 revealed encouraging results in the treatment of mCRPC patients in terms of efficiency, response rate as well as safety [18,19]. Moreover, it was clinically demonstrated that pre-therapeutic PSMA PET imaging can be used for therapy planning, since the uptake of [⁶⁸Ga]Ga-PSMA-11 strongly correlated with the tumor response to [¹⁷⁷Lu]Lu-PSMA-617 treatment, despite the different structure and radionuclide [20]. Another promising PSMA-targeting theragnostic is [⁶⁸Ga]Ga/[¹⁷⁷Lu]Lu-PSMA I&T, which is currently investigated in clinical trials. Similarly to [¹⁷⁷Lu]Lu-PSMA-617, [¹⁷⁷Lu]Lu-PSMA I&T was found effective and safe for the treatment of metastatic prostate cancer patients [21,22].

The diagnostic and therapeutic SSTR-targeting radiopeptides and PSMA-targeting radioligands demonstrated a great clinical potential of receptor-targeted radiopharmaceuticals, and hence, encouraged to apply this concept to other tumor types and promising targets. Recently, radiolabeled fibroblast activation protein (FAP)-targeting agents for PET/CT imaging were tested in patients of various tumor types and demonstrated improved tumor-to-background signal as compared with the current gold standard, [¹⁸F]FDG [23]. About two decades ago, the folate receptor (FR) emerged as a potential target for cancer imaging and therapy due to the frequent overexpression by numerous tumors of epithelial origin, including gynecological cancers [24]. Since FR-targeted agents could address the needs of a vast number of oncologic patients, exploiting this target through nuclear medicine is rational. It would provide new treatment options and open further the prospects for radiopharmaceuticals and personalized medicine.

1.2.   Properties of Folates and Mechanisms of Their Cellular Uptake

Folates comprise a large family of structurally related derivatives with vitamin B9 activity [25]. Folic acid (pteroyl-glutamic acid) is the oxidized, synthetic version of folate vitamins, which is not biologically active before enzymatic reduction in the cell (Fig. 1.2a). Physiologically active folates display differential oxidation states, and therefore, are conventionally referred to as "reduced folates". 5-Methyltetrahydrofolate (5-MTHF) is the most prevalent form of folate in blood plasma (Fig. 1.2b).
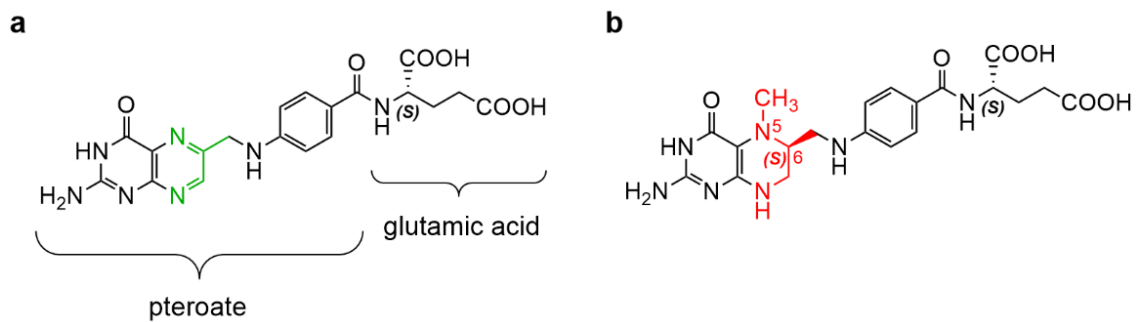
Fig. 1.2 Chemical structures of folates: (**a**) folic acid (oxidized folate; synthetic form); (**b**) 5-methyl-tetrahydrofolate (reduced folate; biologically active form).

They undergo distinct biochemical processes and, in principle, act as a methyl donors in one-carbon transfer reactions involved in essential metabolic pathways. Examples are e.g. de novo synthesis of purine nucleotides and thymidylate, synthesis of methionine from homocysteine as well as DNA methylation (Fig. 1.3) [26]. Hence, folates play a critical role in proliferation and survival of cells, which consequently, require an efficient transport mechanism to meet the folate demand [25].
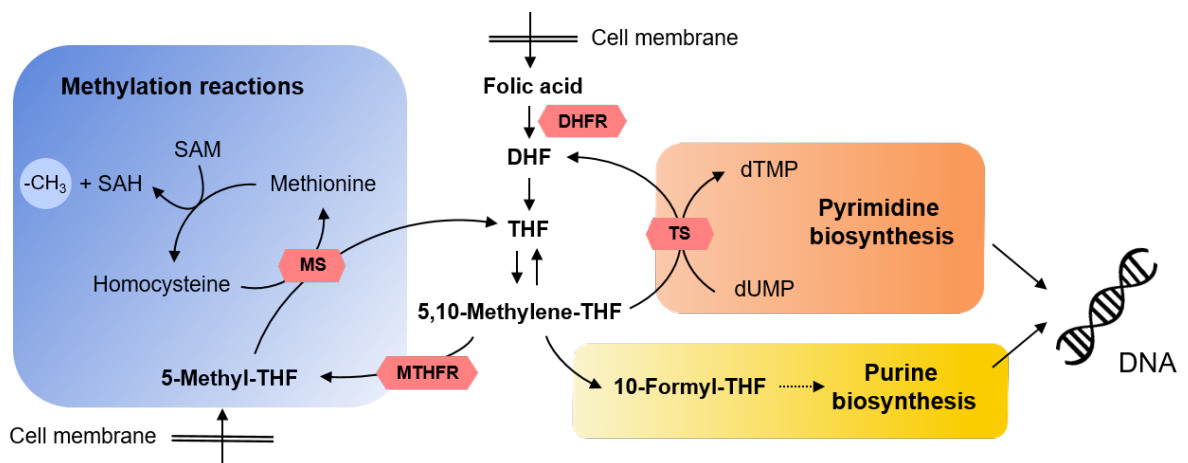
Fig. 1.3 Folate metabolism cycle depicting the main molecular species and their essential functions in the cell. Folic acid is a fully oxidized synthetic form of folate, which upon transport into the cell, needs to be reduced by dihydrofolate reductase (DHFR) to dihydrofolate (DHF) and tetrahydrofolate (THF) that are metabolized to the primary substrate of pyrimidine and purine synthesis, 5,10-methylene-THF. 5,10-Methylenetetrahydrofolate reductase (MTHFR) is a key enzyme in formation of 5-methyl-THF, which is the most abundant form of physiologically active folate, and is a substrate of methionine synthase (MS) and methylation reactions, notably, of DNA. Other abbreviations: TS, tymidylate synthase, dTMP, deoxytymidylate; dUMP, deoxyuridylate; SAM, *S*-adenosulmethionine, SAH, *S*-adenosylhomocysteine. Figure was adapted from Liu et al. *Adv Genet* 2010; 71:79-121 [26].

1.2.1. Folate Transporters and Receptors

Eukaryotic cells are not capable of producing folate vitamins, which in turn cannot passively cross the cell membrane due to their highly hydrophilic character [27]. For this reason, three distinct molecular carriers are engaged in the cellular uptake of exogenous folates, namely the reduced folate carrier (RFC), the proton-coupled folate transporter (PCFT) and several types of folate receptors (FRs)

(Fig. 1.4). Reduced folates are delivered predominantly by a bidirectional organic anion-exchange mechanism, using the RFC. The RFC is ubiquitous tissue expression in healthy cells of the body and characterized by high transport capacity and, therefore, it plays an important role in folate homeostasis [27].

The PCFT is another carrier protein enabling folate transport which requires a pH-gradient and, thus, acts as a folate-proton symporter [28]. The highest expression levels of PCFT in human and murine tissues were found in the small intestine, kidneys, liver, placenta, retina and brain [28].

Folate uptake can also occur via FR-mediated endocytosis. This uptake mechanism is initiated upon FR-ligand complex formation on the cell surface and followed by release of the folate molecule in the endosome from where it is delivered into the cell cytosol. It was demonstrated that the PCFT is co-expressed with the FR and mediates the export of folates from the acidic endosomes, being created upon FR-mediated endocytosis [29]. FRs exist in four isoforms (FRα, FRβ, FRγ, and FRδ), however, only two of them, the FRα and FRβ, play a significant role in folate uptake. The FRα and FRβ are cell-membrane anchored by a glycosylphosphatidylinositol (GPI) entity. Folic acid displays high affinity to FRs ($K_d <$ 1 nM) [30], whereas the FR-binding affinities of reduced folates are 10- to 100-fold lower [25]. In contrast to RFCs, FRs have limited expression in normal tissues. The FRα is present on the apical surface of epithelial cells of the kidneys, lungs, choroid plexus, placenta, uterus as well as in the salivary glands [31]. Importantly, the FRα is frequently overexpressed in tumors of epithelial origin such as the ovaries, breast, uterus, kidneys, lungs, as well as in cervical and endometrial cancers [32]. Expression of the FRβ is limited to the hematopoietic tissue, like spleen and thymus, as well as monocytes and placenta. Similarly to the FRα, it can be expressed in tumors, e.g. in cancers of hematological origin, primarily the myelogenous leukemias [32]. FRβ gained a lot of interest in research as a marker of activated macrophages which are significantly involved in numerous inflammatory diseases such as rheumatoid arthritis, psoriasis, Crohn's disease, atherosclerosis, ulcerative colitis and osteoarthritis [33].
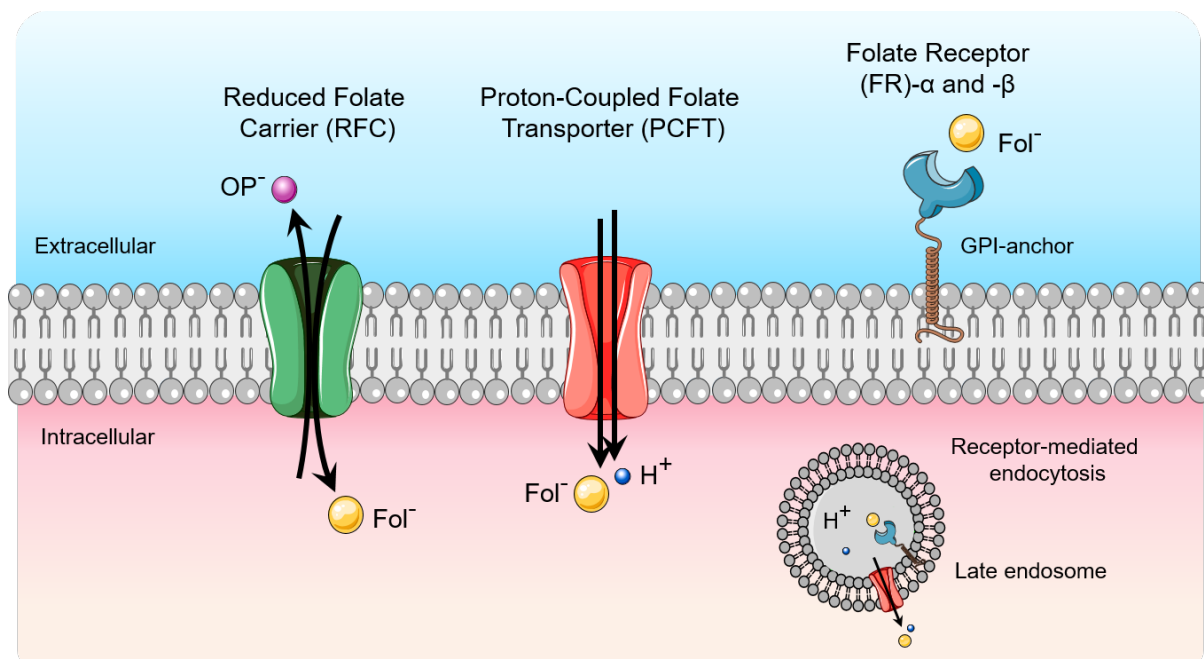
Fig. 1.4 Folate transporters: reduced folate carrier (RFC); proton-coupled folate transporter (PCFT); folate receptor (FR). Abbreviations: OP⁻ = organic phosphate; Fol⁻ = folate; H⁺ = proton; GPI = glycosyl-phosphatidylinositol. Visualization of transporters was prepared using Servier Medical Art licensed under a Creative Commons Attribution 3.0 Unported License.

Antifolates have been applied for treatment of cancer and inflammatory diseases, and are used in clinics to date, including methotrexate (MTX), raltitrexed (RTX, Tomudex™) and pemetrexed (PMX, Alimta™) [34,35]. Folate uptake mechanisms are utilized by antifolate drugs to enter the affected cells. Antifolates have commonly a similar structure as folates, however, they inhibit the activity of folate-dependent enzymes, and hence, disrupt the production of essential entities such as building blocks for RNA and DNA which in turn leads to cell death [34,36]. The uptake of most antifolates occurs via RFC and PCFT [28,35], however, since they are expressed in healthy tissues, newer antifolate drugs were tailored in the direction of FR-targeting as this may limit the toxicity to normal cells [37]. Recently, a Phase I clinical trial (NCT02360345) was initiated with FRα-targeted thymidylate synthase inhibitor, CT900 (also known as BGC 945 or ONX-0801) [38].

1.3. Concepts of FR-Targeting Pharmaceuticals

Due to the overexpression on a wide range of tumors and a concurrently limited expression at only a few sites in normal tissue, the FRα has been exploited in the diagnosis and treatment of cancer patients. In view of therapeutic application, it was targeted with FR-specific antibodies, antibody-drug conjugates (ADCs), vaccine-based approaches, anti-FRα chimeric antigen receptor (CAR) T cells, folate-drug conjugates as well as some antifolates (Fig. 1.5) [24,39]. From numerous FRα-targeting agents that have been developed over the past years, only few reached clinical studies.

Farletuzumab (MORAb-003) is a fully humanized FRα-targeting monoclonal IgG1 antibody which

induces tumor cell death through antibody-dependent cellular cytotoxicity and complement cytotoxicity. It was evaluated in combination with carboplatin and a taxane in a Phase III clinical trial in platinum-sensitive recurrent ovarian cancer patients. Due to the unmet primary endpoint in progression-free survival, the study was, however, suspended [40,41]. Another Phase III clinical study, was conducted with platinum-resistant ovarian cancer patients who received farletuzumab in combination with paclitaxel, however, also this study was discontinued owing to the unmet criteria of progression-free survival and overall survival [42]. A MOv18 IgE antibody, which was developed from the MOv18 IgG1 chimeric antibody, is currently in a Phase I clinical trial (NCT02546921) [43,44].

Mirvetuximab soravtansine is an example of ADC consisting of maytansinoid DM4 conjugated via a cleavable linker. Based on a positive overall response rate of 26% as a single-agent in patients with platinum-resistant FRα-positive ovarian cancer, the ADC was moved to a Phase III trial. The study failed, however, due to the unmet progression-free survival endpoint [45,46]. Currently, a new cohort of patients is being recruited to a similar study using a selection method based on immunohistochemical staining of patient biopsies and more careful analysis of FR expression (NCT04209855) [24].

Folic acid played a significant role in the development of FR-targeted pharmaceuticals owing to the multitude of advantages such as nanomolar binding affinity to the FR, lack of toxicity or immunogenic reaction [47]. Importantly, it has two carboxylic groups of glutamate moiety that are not involved in the binding to the FR and, hence, can be functionalized with diverse payloads such as fluorescent probes and toxins. This allows the receptor-mediated internalization of folate-drug conjugate without loss of binding affinity.

Folate-FITC conjugate (EC17, Endocyte) is a conjugate for FR-targeted immunotherapy, which aims at an increased tumor immunogenicity, provided by a decoration of tumor cells with a highly immunogenic fluorescein [48]. EC17 was tested in a Phase II trial (NCT00485563) involving patients with progressive metastatic renal cell carcinoma, however, the study was terminated due to the lower response rate than expected [24,39].

In the case of folates conjugated to a cytotoxic payload, the critical step, however, is an efficient release of the free toxin in the tumor cell, to enable release into the cytosol and nucleus where it induces cancer cell death [49]. This was addressed by conjugation via a cleavable linker, which is labile in acidic pH of a late endosome. EC145 (Vintafolide^{TM}, Endocyte) is a folic acid-drug conjugate in which folic acid is connected via a disulfide bond to the potent microtubule-destabilizing agent desacetylvinblastine monohydrazide [50]. It was tested in combination with PEGylated liposomal doxorubicin in a Phase III study in women with platinum-resistant ovarian cancer (NCT01170650), however, the trial was terminated, since no improvement in progression-free survival was observed compared to doxorubicin [51]. Another study conducted in lung cancer patients revealed benefits of EC145 in combination with

docetaxel in overall response rate and progression-free survival [52]. Recently, a Phase I trial (NCT01999738) was initiated with a folate-tubulysin conjugate, EC1456 [53].

The concept of FR-targeting has been explored also in terms of cancer imaging (Fig. 1.5). EC17, which was conjugated to a fluorescent isothiocyanate, was clinically applied for intraoperative imaging of ovarian cancer lesions [54]. The other clinically tested FR-targeting imaging agents include radiolabeled folates for single photon emission computed tomography (SPECT) and positron emission computed tomography (PET), which are discussed in the next chapter.
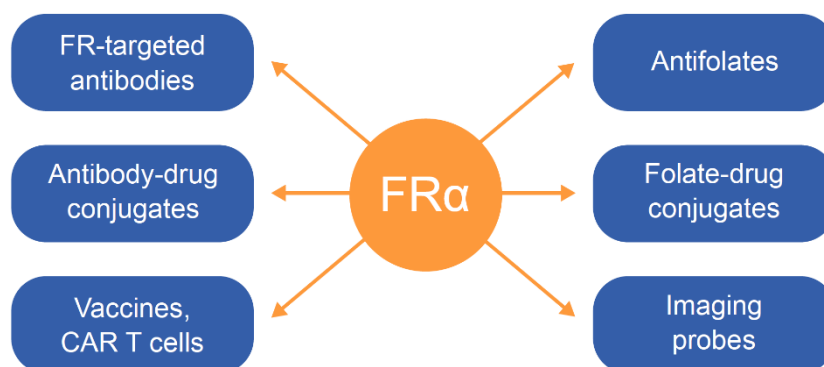
Fig. 1.5 Overview of the concepts of FR-targeting pharmaceuticals: FR-targeted antibodies (farletuzumab, MOv18 IgG1/IgE); antibody-drug conjugates (Mirvetuximab soravtansine); vaccines (EC17); CAR T cells; FRα-targeted antifolates (CT900); folate-drug conjugates (EC145, EC1456); folate conjugates for optical and nuclear imaging.

1.4. FR-Targeted Radioconjugates for Imaging of Cancer and Inflammatory Diseases

The concept of FR-targeting has been extensively studied for the purpose of nuclear imaging, therefore, dozens of folate-based radiotracers for SPECT and PET imaging have been developed [55,56]. Beyond the goal of imaging diverse types of cancer, most recently FR-targeting has been used for imaging of immune cells, namely the activated macrophages, which are involved in inflammatory diseases [57].

1.4.1. Folate-Conjugates Labeled with Radiometals

Folate radioconjugates can be obtained by derivatization of glutamate moiety with a suitable linker and chelator that forms stable complexes with radiometals dedicated for SPECT or PET imaging. For example, [111In]In-DTPA-folate was designed with a diethylenetriamine pentaacetate (DTPA) chelator suitable for radiolabeling with 111In, a clinically employed SPECT radionuclide. [111In]In-DTPA-folate demonstrated fast renal clearance and a good tumor-to-background accumulation in preclinical studies, and thus, was clinically tested in patients with suspected ovarian and endometrial cancers [58]. The studies revealed that the radiotracer was safe and allowed for a rapid accumulation in the target-tissue [58]. In the meantime, 99mTc emerged as a preferable radionuclide due to the more suitable decay

properties for SPECT, lower costs and the on-site availability in the hospitals due to the [99]Mo/^{99m}Tc-generator production system. As a result, a ^{99m}Tc-labeled folate conjugate, [^{99m}Tc]Tc-EC20 (Etarfolatide[TM], Endocyte) (Fig. 1.6a) appeared to be a promising candidate for imaging of FR-positive tumors [59]. In preclinical studies, [^{99m}Tc]Tc-EC20 exhibited a high tumor uptake (~17.7% IA/g; 4 h p.i.) and a fast wash-out from background tissues. It was successfully translated to clinics and tested is several trials in a tandem with a FR-targeted chemotherapeutic, EC145 (Vintafolide[TM], Endocyte) [50]. Moreover, clinical studies with [^{99m}Tc]Tc-EC20 revealed that it accumulates not only in the FRα-positive tumors but also in the arthritic joints [60] due to the binding to the FRβ expressed on activated macrophages [61]. These data as well as other studies demonstrated that FRβ is a promising marker for imaging of inflammatory diseases that involve activated macrophages, and that it can be achieved with folic acid-based radioconjugates that bind equally well to the FRα and FRβ [62].

Further development of folate radiotracers focused on the employment of macrocyclic chelators into their structure, such as DOTA or NODAGA, and resulted in a range of candidates suitable for both SPECT and PET imaging. Among those was DOTA-Bz-folate (EC0800, Endocyte) (Fig. 1.6b) [63] and other DOTA-folate conjugates combined via different linkers (DOTA-click-folate, P3026 and P1254) [64,65].
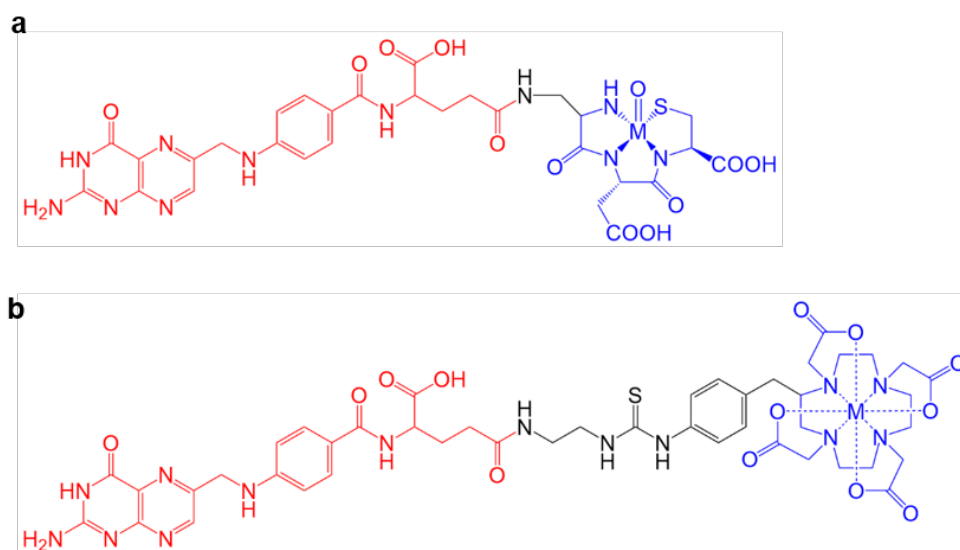
Fig. 1.6 Chemical structures of folate radioconjugates labeled with radiometals (M): (**a**) M-EC20; (**b**) M-EC0800. Both conjugates were based on the structure of folic acid (red) and comprise a chelator (blue). EC20 was outfitted with a peptide-based chelator suitable for radiolabeling with [99m]Tc. EC0800 contained DOTA chelator that can be used for complexation of diverse radiometals, e.g. [177]Lu, [67/68]Ga, [111]In.

Employment of macrocyclic chelators prompted also the development of folate-based PET radiotracers as it allowed for radiolabeling with ^{68}Ga and ^{64}Cu and other positron-emitting radiometals such as [44]Sc, [152]Tb or [55]Co [65-70], which are currently under preclinical investigation. Importantly, the attachment of a DOTA chelating system to folate-conjugates opened new perspectives for theragnostic application using diagnostic and therapeutic radioisotopes [67,68].

1.4.2. Folate-Based ^{18}F-Radiotracers

The increasing number of installed PET scanners in hospitals throughout Europe, together with the advantages of PET over SPECT that refer to higher sensitivity and better spatial image resolution, prompted researchers also to develop ^{18}F-based folate radiotracers. To date a cyclotron-produced ^{18}F is the most widely used radionuclide for PET imaging in the clinics, therefore, a number of ^{18}F-labeled folate tracers were developed over the last two decades with a significant contribution of our group [71].

The structural design ^{18}F-labeled folate radiotracers was based on two different approaches: 1) the "pendant approach" which refers to conjugation of folate at the glutamate moiety with a ^{18}F-labeled prosthetic group [72,73]; 2) the "integrated approach" which implies radiolabeling of the folate derivative by attachment of the ^{18}F-atom directly to the backbone of the folate molecule [74]. The most promising candidate was 3'-aza-2'-[^{18}F]fluorofolic acid ([^{18}F]AzaFol) (Fig. 1.7) which was obtained with a high radiochemical yield and showed favorable in vivo properties [75]. [^{18}F]AzaFol was successfully tested in a first-in-human clinical trial in patients with FR-negative and FR-positive metastatic ovarian and non-small cell lung cancers (NCT03242993) [76]. The interim analysis of PET images obtained with [^{18}F]AzaFol demonstrated inter- and intratumoral heterogeneity confirmed by histological assessment, and high specificity of the radiotracer's uptake [71,76]. Recently, Boss et al. reported on the development of a pair of ^{18}F-labeled tracers that were obtained from diastereomerically pure 6S- and 6R-5-MTHF via the integrated approach (Fig. 1.7) [77]. Based on preclinical studies, the 6S-[^{18}F]Aza-5-MTHF and 6R-[^{18}F]Aza-5-MTHF have outperformed the corresponding oxidized version, [^{18}F]AzaFol, as they revealed about ~2-fold higher uptake in FR-positive KB tumors.

[^{18}F]AzaFol

6R-[^{18}F]Aza-5-MTHF   6S-[^{18}F]Aza-5-MTHF
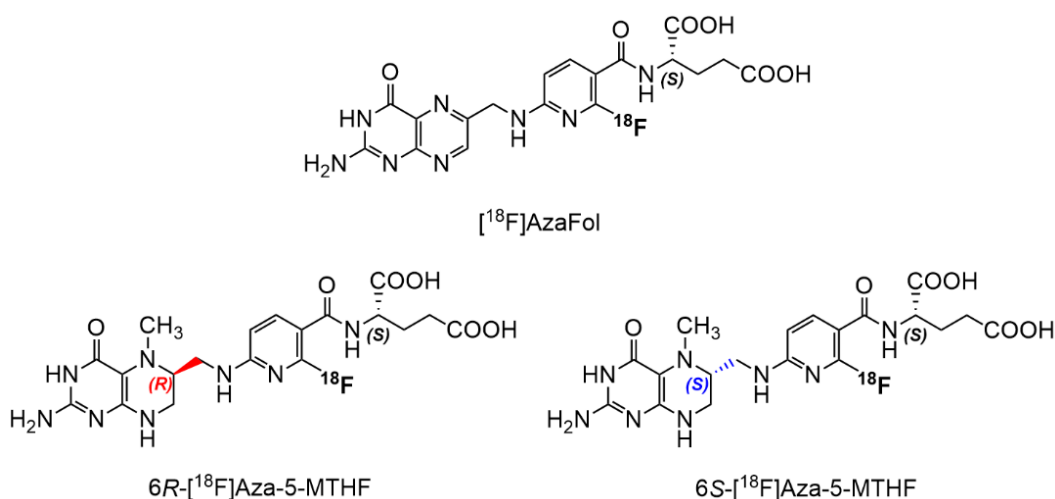
Fig. 1.7 Chemical structures of ^{18}F-radiotracers based on the structure of folic acid ([^{18}F]AzaFol) and 5-MTHF (6R-[^{18}F]Aza-5-MTHF and 6S-[^{18}F]Aza-5-MTHF).

Recently, Gent et al. reported on promising results demonstrating imaging of activated macrophages with [^{18}F]fluoro-polyethyleneglycol (PEG)-folate which was investigated in first-in-human trial with rheumatoid arthritis patients [78]. The binding of folic acid radioconjugates to the FRα and FRβ

expressing tissue enables the imaging of cancer cells and activated macrophages, respectively. This situation could, however, eventually lead to false-positive diagnosis of one or the other disease and inaccurate treatment planning.

1.5. Low Tumor-to-Kidney Ratio as a Major Challenge of FR-Targeted Radionuclide Therapy

The concept of FR-targeted radioconjugates seemed propitious for therapeutic application. Targeted radionuclide therapy, through the use of β^--particle emitting radionuclides, would enable the treatment of FR-positive tumors. A major concern of folate-based radioconjugates was, however, the undesired uptake in the kidneys, where the FR is abundantly expressed. This situation may have a detrimental effect on the kidney function when they would be exposed to particle-radiation accumulated from therapeutic radioconjugates [79]. At the time of this thesis the primary goal was the development of folate radioconjugate for radionuclide therapy with increased tumor-to-kidney ratios of accumulated activity, either by reducing the kidney uptake or increasing accumulation in the tumor.

1.5.1. Pharmacological Approach to Reduce Kidney Uptake of Radiofolates

It was assumed that an increased tumor-to-kidney ratio can be achieved by application of agents, which would accelerate the renal clearance or interfere with the accumulation of radiopharmaceuticals in the kidneys. None of the tested substances, including charged aminoacids and diuretics had an impact on the kidney uptake of radiofolates [63]. The antifolate pemetrexed revealed, however, a beneficial effect on the distribution profile of radiofolates [80]. It was found that administration of pemetrexed at 1 h prior to the radiofolate results in a selective blockade of the kidney uptake without concomitant reduction of the uptake in the tumor. This intervention led to almost 10-fold increased tumor-to-kidney ratio of accumulated radiofolates. The effect was later reproduced in several tumor mouse models using different folate radioconjugates, such as [^{99m}Tc]Tc-EC20 [81], [^{111}In]In/[^{177}Lu]Lu-DOTA-click-folate [82], [^{67}Ga]Ga-EC0800 [63] and [^{68}Ga]Ga-NODAGA-folate [66]. This approach was successful with regard to the imaging of intraperitoneal lesions of an ovarian cancer mouse model using [^{111}In]In-DTPA-folate, whereby selective blockade of the kidneys resulted in appreciable uptake in abdominal lesions [80]. In the scope of a therapeutic application of folate radioconjugates, it was found that co-application of pemetrexed facilitated antitumor therapy using ^{177}Lu-labeled DOTA-folate ([^{177}Lu]Lu-EC0800) owing to the radionephroprotective and radiosensitizing feature of this antifolate [83]. Based on these findings, it was concluded that the combination of pemetrexed with [^{177}Lu]Lu-folate may be of interest for the treatment of non-small cell lung cancer patients, who commonly receive pemetrexed as an approved indication.

The impact of pemetrexed on the pharmacokinetic profile of folate radioconjugates was genuinely exceptional, since blockade of radiofolate uptake in the kidneys was previously impossible without simultaneously compromised tumor uptake [84,85]. Moreover, it was shown that the effect was not

universal and only valid for FR-targeting radiotracers [85]. The underlying mechanism was not further investigated. However, it was assumed that due to the high affinity to the FR, pemetrexed competed with radiofolate for FR in the proximal tubules of the kidneys, while its uptake in the tumor might have been mediated via RFC or PCFT. [86]. Presumably, this was the reason why the tumor uptake remained largely unaffected.

1.5.2. Chemical Modification of Radiofolates to Improve the Pharmacokinetic Profile

Previous studies showed that pharmacokinetics of radiofolates may distinctly change depending on the hydrophobic/hydrophilic character of the compound [36]. Introduction of macrocyclic chelators, eg. DOTA or NODAGA, reduced off-target accumulation of radiofolates in the liver and intestinal tract, but increased in turn the uptake in the kidneys, as a result of enhanced renal excretion [63,66,82]. The idea of modifying folate radioconjugates with an albumin-binding entity (Fig. 1.8a) resulted in a new conjugate referred to as cm09. It was equipped with a small-molecular weight albumin-binding entity [87], which was previously established by Dumelin et al. [88]. The idea was prompted by the results reported for anti-HER2 antibody fragment (Fab) endowed with an albumin-binding peptide [89], which showed that non-covalent association with albumin not only reduced renal clearance, but also led to excellent tumor deposition of the bifunctional Fab. Preclinical evaluation of [^{177}Lu]Lu-cm09 confirmed the favorable impact of an albumin binder [87]. Compared to the conventional folate, the tumor uptake of [^{177}Lu]Lu-cm09 was ~2.5-fold increased, whereas the accumulation in the kidneys was significantly lowered, resulting in even 7-fold higher tumor-to-kidney ratio.

Further efforts in optimizing the tumor-to-kidney ratio of folate radioconjugates concerned employment of variable linker entities, in order to investigate whether the extension of the distance between folic acid and the albumin binder had an impact on pharmacokinetics [90]. In this preclinical study, the in vitro and in vivo characteristics of [^{177}Lu]Lu-cm10 (Fig. 1.8b), a new version of an albumin-binding DOTA-folate conjugate similar to [^{177}Lu]Lu-cm09, were compared to two novel folic acid radioconjugates: cm12 with a long hydrophilic spacer consisting of PEG-11, and cm13 with a short hydrophobic alkane chain. The study showed that a linker in the proximity to the albumin binder had a significant impact on tissue distribution profile. While [^{177}Lu]Lu-cm13 showed generally similar properties as [^{177}Lu]Lu-cm10, [^{177}Lu]Lu-cm12 revealed a reduced tumor-to-kidney ratio. It was concluded that a short lipophilic spacer was well-tolerated and increased the albumin-binding properties, whereas a long hydrophilic linker compromised the favorable distribution profile of the folate radioconjugate.
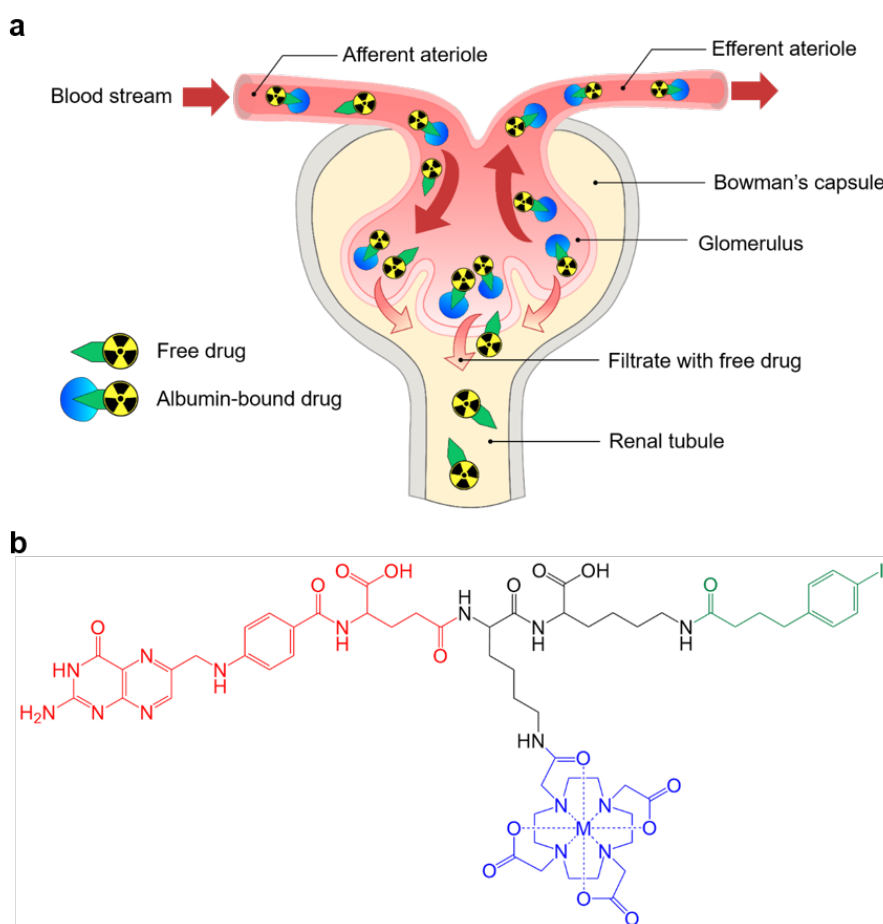
Fig. 1.8 (**a**) Concept of the albumin-binding radiopharmaceutical: An albumin-binding radioconjugate circulates in the blood as a protein-bound fraction and a free drug. During glomerular filtration in the kidneys, the free drug is excreted, whereas the albumin-bound fraction is retained due to the protein size (66 kDa) being above the molecular weight cut-off (<45 kDa). The albumin-bound drug returns to blood circulation; (**b**) Chemical structure of the albumin-binding folic acid-based radioconjugate, M-cm10. The conjugate was endowed with 4-(*p*-iodophenyl)butyric acid entity (green) that provides non-covalent reversible binding to serum albumin.

1.6.   Cancer Therapy with Immune Checkpoint Inhibitors (ICIs)

Within the last decade, immune checkpoint inhibitors (ICIs) have been clinically validated as an effective treatment modality for diverse solid tumors and haematological malignancies [91]. Owing to the proven durable responses in patients, ICIs emerged as a new pillar of cancer therapy, next to the conventional interventions [92]. The concept of this treatment is based on stimulating the immune system against cancer, namely, by sustaining activation of CD8+ T cells [92]. A critical step in T cell activation was found to lie in tumor recognition by antigen-presenting cells (APCs) which then display tumor-derived peptides (antigens) in the context of major histocompatibility complex (MHC) I on the cell-surface. T cell activation is provided by the binding of the tumor antigen with the T cell receptor (TCR) and the co-stimulation signal occurring between B7 molecules of APC and CD28 T cell antigen. Immune

checkpoint molecules, such as cytotoxic T cell antigen 4 (CTLA-4) or programed cell death protein 1 (PD-1), are naturally upregulated upon T cell activation and provide inhibitory signals that will downregulate the T cell, and consequently, prevent their antitumor effector function. Abrogation of these inhibitory pathways by immune checkpoint targeting antibodies revealed to be efficacious in enhancing T cell responses against cancer, and therefore, provided strong rationale to be used in treatment of various tumor types. ICIs were employed as monotherapy, but also in combination with other therapy modalities, since clinical responses were observed only in a fraction of patients when used as a single therapy arm [93-95]. One of the reasons of low response rate to ICIs was found to be a poor tumor immunogenicity, which limits tumor recognition by immune cells and recruitment of CD8+ T cells. Various approaches of combination therapies with ICIs were extensively reviewed by Melero et al. [96]. Among these, agents inducing immunogenic cell death, such as chemo- and radiotherapy, revealed to efficiently increase tumor immunogenicity, and hence, improve the responses to immune checkpoint therapy (Fig. 1.9) [97,98]. These findings prompted recently investigation of targeted radionuclide therapy in combination with immune checkpoint blockade [99-103], however, the impact of this treatment on tumor immunogenicity and response to ICIs was scarcely described so far.
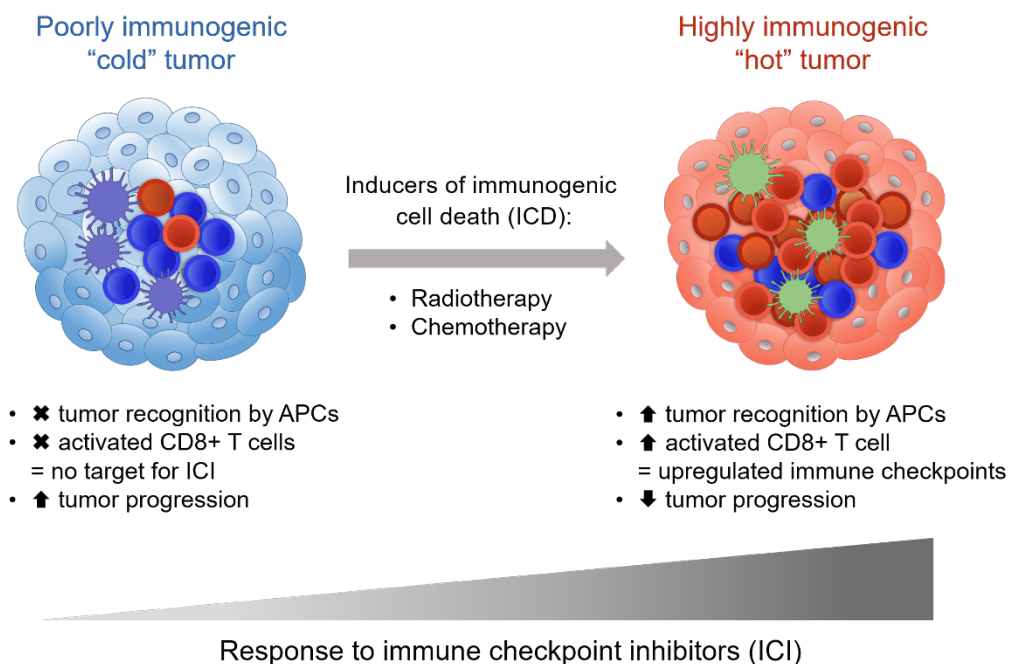
Fig. 1.9 Sensitization of poorly immunogenic tumors to immune checkpoint therapy. Cancer treatments that induce immunogenic cell death, e.g. radiotherapy, chemotherapy, promote recruitment of immune cells, including CD8+ T cells, which results in higher immunogenicity and improved tumor response to immune checkpoint antibodies. Figure was adapted from Demaria et al. *Trends Cancer* 2016; 2 (6), 286-294 [98].

1.7. Characteristics and Applications of Tumor Mouse Models for Investigation of FR-Targeting Agents

The preclinical cancer models that are used in drug discovery should enable efficient and reliable screening of pharmaceuticals and, in an ideal case, accurately predict clinical efficacy of a drug [104]. Hence, the choice of the model is a critical step in the development process, which is based on the properties of a drug and the stage of preclinical evaluation (Fig. 1.10) [105].

In radiopharmaceutical research, new developments are commonly tested in standard mouse models based on in vitro established cell lines, which were derived from human or murine cancer tissues and engrafted into an immunodeficient or immunocompetent mouse strain, respectively [105]. Human xenograft models, also referred to as cell line-derived xenograft (CDX) models, are widely used and generally accepted in radiopharmaceutical research as they allow for validation of drug targeting as well as its specificity, and hence, are useful in quantitative assessment of the tumor uptake and specificity of a radiolabeled drug [105]. CDX models enable also comparative studies with regard to therapeutic efficacy of radiopharmaceuticals. However, the shortcomings of these models include: i) limited pathophysiological relevance; ii) possibly altered target expression caused by in vitro cell culture; iii) loss of heterogeneity of primary tumor; and iv) lack of native tumor microenvironment. These factors might be a reason for a poor predictiveness of CDX models in terms of clinical outcome [104]. Furthermore, since CDX models have to be established in immunodeficient mice to avoid tumor rejection, the influence and response of certain subsets of immune cells is neglected, and therefore, these models are not suitable for assessment of immunomodulatory agents, neither as single treatment nor in combination with other modalities, e.g. with radiopharmaceuticals. This limitation can be overcome by syngeneic tumor mouse models established from murine cancer cell lines which are inoculated back into the mouse of the same genetic background with fully functional immunity [106]. It has to be mentioned, however, that syngeneic models are restricted to a number of tumor types and represent only murine biology, including immune response, drug metabolism and molecular structure of a target [104,106].

Models which resemble metastatic lesions are of high value, especially when it comes to the evaluation of different types of radionuclides such as short-range particle-emitters for therapy [107,108]. In order to mimic tumor development and invasiveness, tumor cells can be injected orthotopically, namely into the site of origin tissue [104]. Orthotopic models can develop lesions in the common metastasis sites, such as bones or lungs [109]. Another possibility to mimic formation of metastases in a mouse is an intravenous, intracardiac, intratibial or intraperitoneal injection of tumor cells [110]. Yet these models are technically challenging and the tumor development is problematic to monitor [104].

Recently, patient-derived xenografts (PDX) models are increasingly used in the radiopharmaceutical research. They are generated by implantation of an intact human cancer tissue into immunodeficient mice, and hence, the histologic and molecular heterogeneity of the tumor is well preserved [105]. Owing

to the increasing interest in immunomodulatory drugs, further advancements of PDX models include the use of mice with a humanized immune system [111]. PDX models are promising in predicting clinical efficacy of a drug, however, their application is still limited given the expensive, time consuming, technically demanding and highly variable establishment [105].

Genetically engineered mice (GEM) provide the most complete representation of cancer development, including structural heterogeneity and immune responses. Nevertheless, transgenic mice are costly and require longer time until the tumors are developed. Moreover, the tumor growth of individual mice is not synchronous and challenging to monitor. For these reasons, transgenic mice are not suitable for a fast screening phase aiming at an efficient selection of the most promising candidates [105].
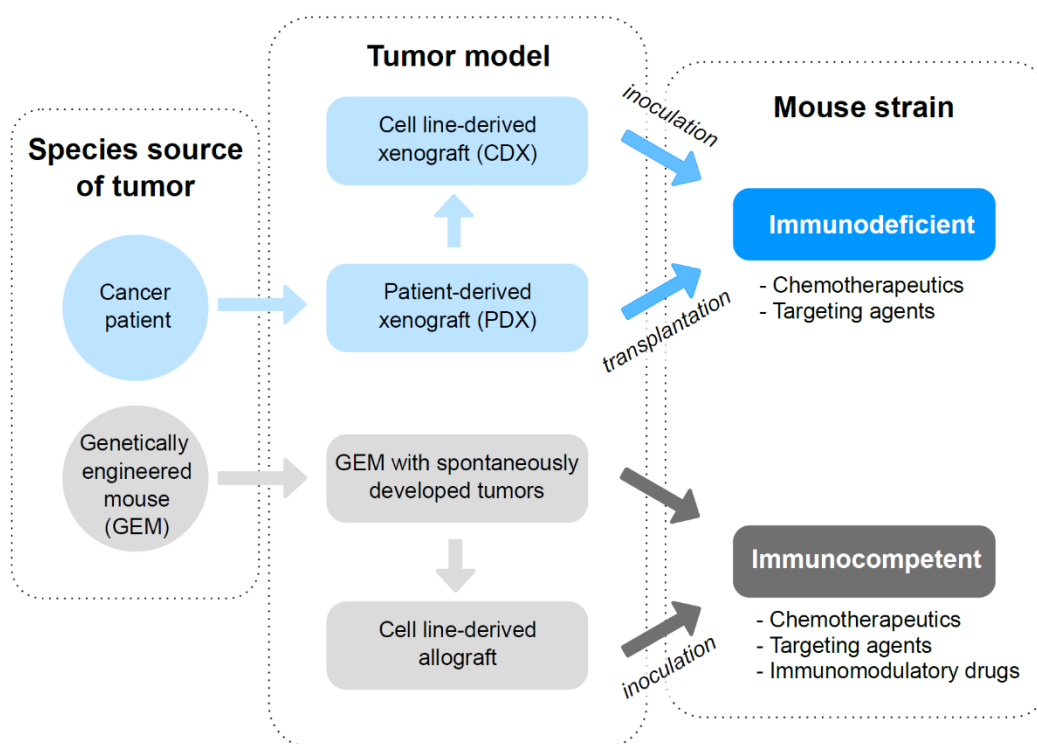
Fig. 1.10 Types of preclinical in vivo models used for evaluation of pharmaceuticals. Figure was adapted from Day et al. *Cell* 2015; 163(1):39-53 [105].

With regard to the FR-targeting research, the CDX models are the most commonly used and are based on well-established cell lines employed for in vitro preclinical evaluations (Table 1.2). A FR-positive human cervical cancer cell line, KB, is considered as a "gold standard" for FR-targeting research, due to the high FR expression, rapid growth and simple culturing [112]. IGROV-1 cells and SKOV-3 tumor cells, both human ovarian adenocarcinoma and SKOV-3 [112] have also been used in the past. While these cell lines are inoculated subcutaneously, the SKOV-3.ip model was established by intraperitoneal injection to mimic ovarian cancer metastasis in mouse abdomen [113]. There are also several syngeneic models established from FR-positive murine cancer cell lines (Table 1.2), such as MKP-L ovarian cancer [114], M109 lung cancer cell line [59,115] or a FR-transfected 24JK-FBP sarcoma cells [116]. These models were used for FR imaging studies as well as for evaluation of therapeutic potential. Transfected

tumor cell lines are, however, not suitable for therapy studies due to a different cell metabolism, which can influence the response to the treatment. Due to the higher clinical relevance, PDX models of FR-expressing cancers, e.g. ovarian, endometrium or triple negative breast cancers, were successfully employed for preclinical evaluation of FR-targeting chemotherapeutic [117] and FRα-targeted antibody-drug conjugate (ADC) [118].

Table 1.2 Preclinical tumor mouse models commonly used in FR-targeting research

Model	FR-positive cell line	Origin	FR expression	Study example
Xenograft (CDX)	KB	Human cervical cancer	High	Müller et al. [87]
	IGROV-1		Medium	Müller et al. [80], Siwowska et al. [112]
	SKOV-3	Human ovarian cancer	Medium	
	SKOV-3.ip		Medium	
Syngeneic	MKP-L	Murine ovarian cancer	Medium	Ocak et al. [114]
	M109	Murine lung cancer	Low	Reddy et al. [115], Paulos et al. [119]
	24JK-FBP	FR-transfected sarcoma cells	Medium	Guo et al. [116], Müller et al. [120]

1.8.　Aim of the Thesis

The aim of the thesis was to further optimize the properties of FR-targeting radiofolates with regard to their utility for tumor diagnosis and therapy. Moreover, therapeutic folate radioconjugates were investigated for the purpose of enhancing the anti-tumor efficacy of immune checkpoint inhibitors (Fig. 1.10). The specific aims of the herein described projects were the following:

1. **Development of a radiotracer for specific diagnosis of FRα-positive tumors using PET:**

   The development of a FRα-specific PET radiotracer would have a high potential for clinical translation as it would allow selection of cancer patients that could profit from FRα-targeted therapies. Accurate patient selection may increase the success of these novel therapies due to the elimination of false-positive results due to radiotracer accumulation in inflamed tissues. The goal of this project was to evaluate the previously developed 5-methyltetrahydrofolate (MTHF)-based ^{18}F-tracers and to investigate whether they display selective binding to the FRα.

2. **Optimization of the pharmacokinetic profile of albumin-binding radiofolates in view of therapeutic application:**

   The aim was to increase the tumor-to-kidney ratio of albumin-binding folate radioconjugates in order to reduce the risk of radionephrotoxicity and, hence, enable a safer application for therapeutic purposes. This need was addressed using a pharmacological and a chemical approach, respectively.

   a. The pharmacological approach was based on the administration of the antifolate pemetrexed (PMX), which was previously shown to reduce the uptake of conventional radioconjugates in the kidneys. The question to address was whether PMX application would result in a further optimization of the tumor-to-kidney ratio of albumin-binding radiofolates.

   b. The specific aim of the chemical approach was to increase the accumulation of the albumin-binding radioconjugates by introducing 6*S*- or 6*R*-5-MTHF as a FR-targeting molecule. This strategy was based on the observations made with ^{18}F-labeled aza-5-MTHF radiotracers which demonstrated higher tumor uptake, and in addition, the 6*R*-isomer showed a reduced retention in the kidneys than the folic acid-based analogue. Assuming that the same properties would apply for the 5-MTHF-based albumin-binding radioconjugates, a significant increase of the tumor-to-kidney ratio was expected for one of them.

3. **Sensitization of FR-positive tumors to therapy with immune checkpoint inhibitors:**

   In recent experiments of other groups, external beam radiation was shown to increase tumor immunogenicity, and hence, improve the tumor response to immune checkpoint inhibitors as compared to the single modality treatment. Based on this promising concept, it was

hypothesized that a radiation stimulus delivered to the tumor by folate radioconjugates can potentiate the efficacy of anti-CTLA-4 immunotherapy.

a. In order to test this hypothesis, an immunocompetent mouse model using NF9006 murine mammary gland cancer cells was established and used in a therapy experiment that combined [^{177}Lu]Lu-DOTA-folate and an immune checkpoint inhibitor.

b. The second aim was to test whether folate radioconjugates do also accumulate in the spontaneously developed mammary gland tumors of transgenic mice demonstrated by SPECT/CT imaging and biodistribution studies.
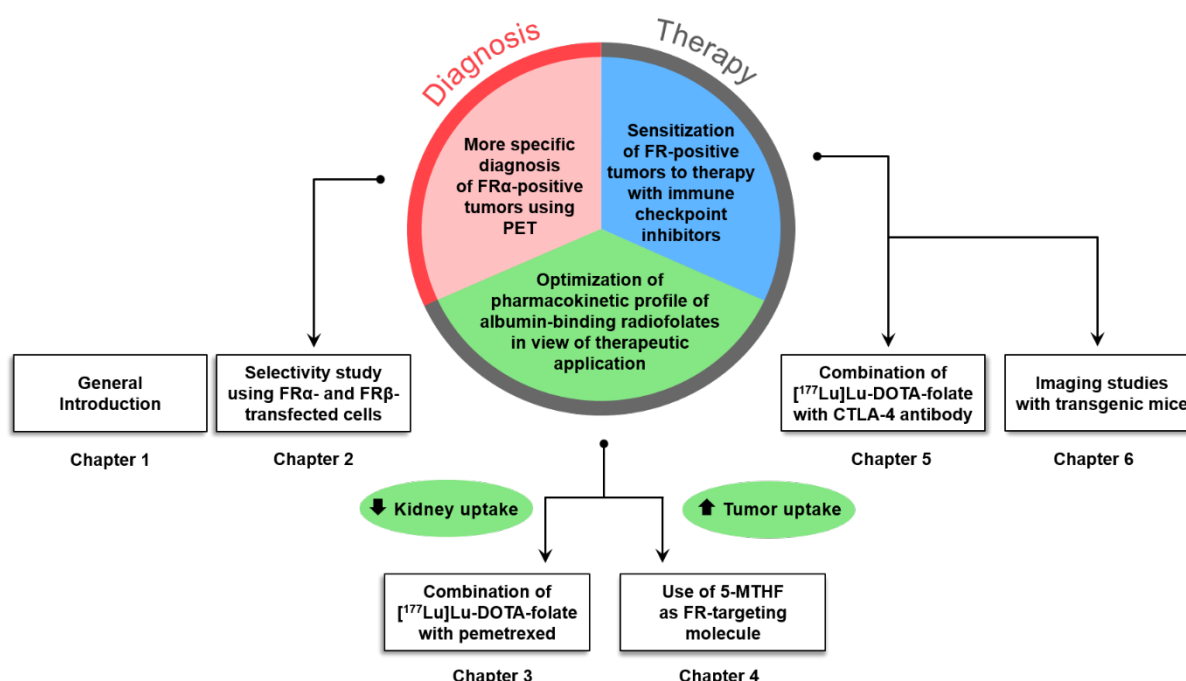
Fig. 1.10 Overview of the thesis objectives related to the diagnosis and therapy of FR-positive tumors using folate-based radioconjugates alone and in combination with other modalities.

II. Identification of a PET Radiotracer for Imaging of the Folate Receptor-α – a Potential Tool to Select Patients for Targeted Tumor Therapy

Patrycja Guzik[1], Hsin-Yu Fang[1], Luisa M. Deberle[1], Martina Benešová[1,2], Susan Cohrs[1], Silvan D. Boss[2], Simon M. Ametamey[2], Roger Schibli[1,2], Cristina Müller*[,1,2]

[1] *Center for Radiopharmaceutical Sciences ETH-PSI-USZ, Paul Scherrer Institute, 5232 Villigen-PSI, Switzerland*

[2] *Department of Chemistry and Applied Biosciences, ETH Zurich, 8093 Zurich, Switzerland*

Author Contributions:

Patrycja Guzik performed the experiments, analyzed and interpreted the data, and wrote the manuscript. Hsin-Yu Fang established the immunohistochemical staining of the FRα and FRβ. Luisa M. Deberle, and Martina Benešová contributed to the synthesis of the ^{18}F-radiotracers and reviewed the manuscript. Susan Cohrs supported the animal experiments. Silvan D. Boss synthesized the ^{18}F-radiotracers. Simon M. Ametamey originally initiated the ^{18}F-labeled folate project at CRS and revised the manuscript. Roger Schibli reviewed the final manuscript. Cristina Müller supervised the study, contributed to the writing of the manuscript and reviewed the final version.

2.1. Introduction

The folate receptor-α (FRα) is a cell membrane-associated protein which has been used for targeted therapies in oncology [24]. Among FRα-expressing malignancies are gynecologic cancers, such as ovarian, endometrial and cervical tumors, but also non-small cell lung cancer [121-123]. Triple-negative breast cancer as well as kidney and colon cancer were also reported to be frequently positive for the FRα [122-125].

The use of folic acid-based radiotracers for nuclear imaging was proposed for diagnosis of FR-positive cancer and for the selection of patients who would profit from FR-targeted tumor therapies [126-129]. [^{111}In]In-DTPA-folate and [^{99m}Tc]Tc-EC20 suitable for single photon emission computed tomography (SPECT) were the first two folate radioconjugates tested in patients [58,127,130]. A drawback of folic acid-based radiotracers is, however, that they bind to both the FRα and the FRβ, which have distinct tissue expression profiles [2,39]. The FRα is present in malignant tissue [131], whereas the FRβ is expressed on activated macrophages involved in inflammatory diseases [57]. As a result, folic acid-based radiotracers accumulate not only in tumors but also at sites of inflammation, which may result in false-positive findings due to co-existing inflammatory conditions in cancer patients.

6*S*/6*R*-5-Methyltetrahydrofolates (MTHF) are reduced forms of folates, in contrast to the fully oxidized folic acid, which is a synthetic version of folate vitamins. It was previously reported that the physiological 6*S*-5-MTHF, but not the 6*R*-5-MTHF, binds with ~50-fold higher affinity to the FRα than to the FRβ [132,133]. In a proof-of-concept study published by Low and co-workers, a dimethylated reduced version of [^{99m}Tc]Tc-EC20 was, thus, prepared to achieve FRα selectivity [134]. Indeed, it was experimentally demonstrated that [^{99m}Tc]Tc-DMTHF accumulated much more in tumors of mice than at sites of inflammation [134].

In view of a clinical application, folate radiotracers for positron emission tomography (PET) imaging would be clearly favored compared to tracers dedicated for single photon emission computed tomography (SPECT) [55,71]. Of major interest are ^{18}F-based radiotracers which profit from the favorable decay characteristics of ^{18}F ($T_{1/2}$ = 110 min, $E\beta^{+}_{av}$ = 250 keV) and the option of quantifying the accumulated activity using standard protocols that are also employed for interventions with [^{18}F]fluoro-deoxy-glucose [135].

Among a large number of developed ^{18}F-labeled folate tracers [71], only two were employed in clinics. Verweij et al. reported on the use of [^{18}F]fluoro-PEG-folate for macrophage imaging in patients with rheumatoid arthritis [136], whereas [^{18}F]AzaFol has recently been tested in a clinical Phase I trial in ovarian and lung cancer patients in Switzerland (NCT0342993) [75,76]. In spite of the promising results obtained with [^{18}F]AzaFol, it is without any doubts that a tumor-selective folate radiotracer, that targets solely the FRα but not the FRβ, would be essential to unambiguously identify patients that could profit from FRα-targeted therapies.

We have previously developed radiotracers based on 6*S*- and 6*R*-5-MTHF as a targeting agent [77], in

which the ^{18}F-label was integrated in the folate backbone as it was the case for [18F]AzaFol (Fig. 2.1) [77]. These 5-MTHF-based ^{18}F-tracers accumulated to a much higher extent in tumor xenografts of mice than [18F]AzaFol and the 6R-isomer showed even a favorable excretion profile. The goal of the present study was now to investigate 6R-[18F]Aza-5-MTHF and 6S-[18F]Aza-5-MTHF with regard to their binding affinity to the FRα and FRβ, respectively, in order to assess the option of using them for tumor-selective PET imaging.
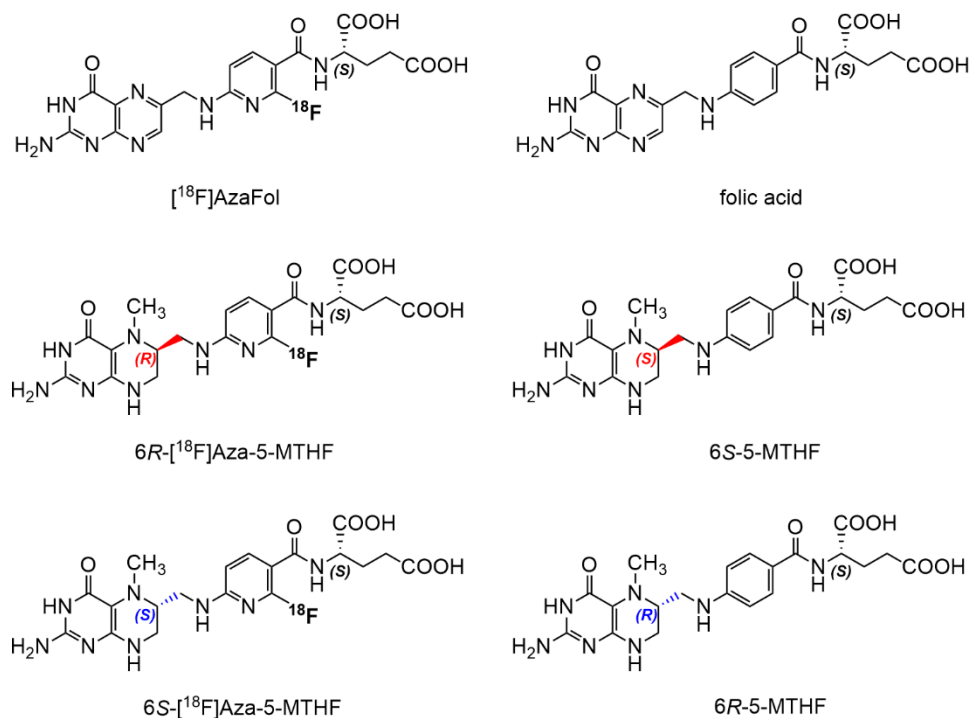
Fig. 2.1 Chemical structures of [18F]AzaFol, 6R-[18F]Aza-5-MTHF and 6S-[18F]Aza-5-MTHF as well as folic acid, 6S-5-MTHF and 6R-5-MTHF [77]. Stereochemical nomenclature of the corresponding isomers of non-fluorinated and fluorinated 5-MTHFs are inversed due to the change in the substituents' priority at the stereogenic center.

2.2. Materials & Methods

2.2.1. Folate Derivatives

The precursors (6*R*- or 6*S*-N^2-acetyl-3′-aza-2′-chloro-5-MTHF di-*tert*-butylester and N^2-acetyl-3′-aza-2′-chlorofolic acid di-*tert*-butylester) for the radiofluorination and the non-radioactive 6*S*-5-MTHF (physiological form) and 6*R*-5-MTHF (non-physiological form) were provided by Merck & Cie, Switzerland. Folic acid was obtained from Sigma-Aldrich, Switzerland. The non-radioactive fluoro-folates as well as 6*R*-3′-aza-2′-[18F]fluoro-5-methyltetrahydrofolate (6*R*-[18F]Aza-5-MTHF), 6*S*-3′-aza-2′-[18F]fluoro-5-methyltetrahydrofolate (6*S*-[18F]Aza-5-MTHF) and 3′-aza-2′-[18F]fluorofolic acid ([18F]AzaFol) were prepared at ETH Zurich according to a previously reported method [75,77]. [3H]folic acid was obtained from Moravek Biochemicals, Inc. California, U.S.A.

2.2.2. Cell Culture

CHO cells transfected with the FRα (designated as RT16 cells) or FRβ (designated as D4 cells) were kindly provided by Prof. Larry Matherly, Wayne State University, Detroit, U.S.A. [137]. The cells were cultured in folate-free minimal essential medium-alpha (FF-MEM-α; Cell Culture Technologies GmbH, Switzerland). KB cells (FR-positive, human cervical carcinoma cell line, ACC-136) were obtained from DSMZ (German Collection of Microorganisms and Cell Cultures GmbH, Germany) and cultured in folate-deficient RPMI medium (FFRPMI, Cell Culture Technologies GmbH, Gravesano, Switzerland). PC-3 cells (FR-negative, human prostate cancer cell line, ACC-465) were also obtained from DSMZ but cultured in normal RPMI 1640 medium. Cell culture media were supplemented with 10% fetal calf serum, L-glutamine and antibiotics.

2.2.3. Western Blot

Expression of the FRα and FRβ in RT16 and D4 cells, respectively, was confirmed by western blot analysis whereas FRα-expressing KB and FR-negative PC-3 tumor cells were used as positive and negative controls, respectively. The cell lysates were prepared using RIPA lysis and extraction buffer (89900, Thermo Scientific) and a protease inhibitor cocktail (cOmplete™, Roche). The protein content (6–12 mg/mL) was determined by addition of Coomassie brilliant blue reagent (Thermo Scientific) using a UV/Vis-photometer (Eppendorf, Biophotometer). Cell protein extracts were separated by sodium dodecyl sulfate polyacrylamide gel electrophoresis (SDS-PAGE) (30 µg protein/well) and transferred to a polyvinylidene difluoride membrane followed by blockade with a 5% bovine serum albumin (BSA) solution in Tris-buffered saline containing 0.05% Tween™. The membrane was incubated with a primary anti-FRα antibody (1:625, FRα-specific rabbit monoclonal antibody (mAb), PA5-42004, Invitrogen) or anti-FRβ antibody (1:1000, FRβ-specific rabbit mAb, GTX105822, GeneTex) overnight at 4 °C. For signal detection, a secondary anti-rabbit IgG antibody (1:5000, goat antibody, 7074S, Cell Signaling Technology) functionalized with horseradish peroxidase (HRP) was used together with Super Signal West Pico Plus chemiluminescent substrate (Thermo Scientific, 34579).

Detection of β-actin served as a protein loading control (anti-β-actin antibody; 1:2000, mouse mAb, 3700, Cell Signaling Technology and HRP-conjugated anti-mouse IgG, 1:5000, 7076S, Cell Signaling Technology). Quantification of the western blot signals was based on the peaks in the profile plot obtained in ImageJ software (version 1.52d). The intensity of the bands of FRα and FRβ were standardized to the respective signal of the β-actin band and put into relation to the signal obtained with KB cells (set as 100%). The results are presented as average ± SD (n=3). The graph was prepared using GraphPad Prism software (version 7.0).

2.2.4. Cell Internalization of 6R/6S-[^{18}F]Aza-5-MTHF and [^{18}F]AzaFol

Cell uptake studies of 6R-[^{18}F]Aza-5-MTHF, 6S-[^{18}F]Aza-5-MTHF and [^{18}F]AzaFol were performed as previously reported [77,82]. In brief, RT16 and D4 cells were seeded in poly-L-lysine coated 12-well plates (1×10^6 cells/well) to form confluent monolayers overnight. After washing the cells, they were incubated with the respective folate radiotracers (~200 kBq; 25 µL) for 1 h at 37 °C. Non-specific binding was determined by blocking the FR with excess folic acid (~100 µM). The results were expressed as percentage of total added activity. The statistical significance was assessed using a two-way ANOVA with Tukey's multiple comparisons post-test using GraphPad Prism software (version 7.0). A p-value of <0.05 was considered as statistically significant.

2.2.5. FRα- and FRβ-Binding Affinity (IC$_{50}$ Values)

The binding affinities (IC$_{50}$ values) to the FRα and the FRβ were determined in displacement experiments using non-radioactive fluoro-folates (6R-Aza-5-MTHF, 6S-Aza-5-MTHF and AzaFol) and [^{3}H]folic acid. The binding affinities to the FRα and FRβ were compared to the affinities of the corresponding non-fluorinated analogues (6S-5-MTHF, 6R-5-MTHF and folic acid). The experiments were performed with RT16 and D4 cells according to a previously published procedure [75]. The folate derivatives of interest were applied in the concentration range of 5 pM–50 µM (Table 2.1). The FR-bound [^{3}H]folic acid fraction in a specific cell line was measured using a liquid-scintillation counter (Packard Bioscience Cobra II). The IC$_{50}$ values were determined by non-linear regression analysis of displacement curves from at least three independent experiments using GraphPad Prism software (version 7.0). In order to enable relative comparison, the affinities of 6S-Aza-5-MTHF and 6R-Aza-5-MTHF were indicated as percentage of the AzaFol affinity (set as 100%). The calculation for the receptor binding affinity of 6S-5-MTHF and 6R-5-MTHF was performed in analogy and expressed relative to the binding affinity of folic acid (set as 100%).

Table 2.1 Concentration range of folate derivatives (6*R*-Aza-5-MTHF, 6*S*-Aza-5-MTHF, AzaFol) and their non-fluorinated analogs (6*S*-5-MTHF, 6*R*-5-MTHF, folic acid) used for determination of the binding affinity (IC$_{50}$ values) to the FRα (RT16 cells) and the FRβ (D4 cells).

Cell line (FR isoform)	Folate concentration (final)*		
	6*R*-Aza-5-MTHF/ 6*S*-5-MTHF	6*S*-Aza-5-MTHF/ 6*R*-5-MTHF	AzaFol/ Folic acid
RT16 (FRα)	5 pM–5 µM	5 pM–5 µM	5 pM–5 µM
D4 (FRβ)	50 pM–50 µM	5 pM–5 µM	5 pM–5 µM

* The concentration range was applied using an aliquot of cell suspension (7000 cells in 240 µL PBS), the respective dilution of the folate derivative (PBS; 250 µL) and [^{3}H]folic acid (41 nM; 10 µL).

2.2.6.   Autoradiography Studies

Autoradiography studies were performed using tissue sections of RT16, D4 and KB xenografts as previously reported [138]. The sections were incubated in 167 mM Tris-HCl buffer containing 5 mM MgCl$_2$ and 0.25% BSA for 10 min. After removal of the buffer, the sections were incubated with the ^{18}F-labeled folate radiotracers (150 kBq/100 µL) in Tris-buffer containing 1% BSA for 1 h at RT. Blockade was performed using excess folic acid (100 µM). Autoradiographic images were obtained using a storage phosphor system (Cyclone Plus, Perkin Elmer) and quantified using OptiQuant software (version 5.0, Perkin Elmer^{TM}). The signals obtained from RT16 and D4 xenograft sections were normalized to the signal obtained from KB xenograft section (set as 100%). The resulting values of 6*R*-[^{18}F]Aza-5-MTHF and 6*S*-[^{18}F]Aza-5-MTHF were expressed relative to the signal of [^{18}F]AzaFol which was set as 100%. Representative images were prepared using ImageJ (version 1.52d).

2.2.7.   Immunohistochemistry

After deparaffinization and rehydration of the paraffin tissue sections, the slides were subjected to heat-mediated antigen retrieval, followed by treatment with 3.5% hydrogen peroxide to block endogenous peroxidase activity, followed by endogenous biotin blockade using avidin solution (Avidin/Biotin Blocking kit SP-2001, Vector Laboratories, U.S.A.) in a mixture of 3% BSA and 5% normal goat serum. The sections were incubated with an anti-FRα antibody (PA5-42004, Invitrogen) and an anti-FRβ antibody (GTX105822, GeneTex), diluted 1:800 and 1:400 in biotin solution mixed with 3% BSA, respectively, at 4 °C overnight. Afterwards, the sections were incubated with a biotinylated secondary antibody (goat anti-rabbit IgG, BA-1000, Vector Laboratories, U.S.A.) diluted 1:1000 and 1:500 in PBS containing 3% BSA. Signal visualization was performed using reagents of commercial kits (Vectostain^{TM} Elite ABC-HRP kit, peroxidase PK-6100 and DAB substrate kit peroxidase (HRP), SK-4100, Vector Laboratories, U.S.A.), followed by counterstaining using hematoxylin (109249, Sigma-Aldrich). After tissue dehydration, the sections were fixed with xylene and images were taken using a light microscope (Axio Lab.A1, Zeiss).

2.2.8. In Vivo Studies

All applicable international, national and institutional guidelines for the care and use of laboratory animals were followed and the studies were carried out according to the guidelines of the Swiss Regulations for Animal Welfare after ethical approval by the Cantonal Committee of Animal Experimentation and permission by the responsible cantonal authorities. Five- to six-week-old female, SCID CB17 mice were purchased from Charles River Laboratories (Sulzfeld, Germany). All animals were fed with a folate-deficient rodent diet (ssniff Spezialdiäten GmbH, Germany). The mice were inoculated with RT16 cells (6×10^6 cells in 100 µL PBS) on the right shoulder and D4 cells (6×10^6 cells in 100 µL PBS) on the left shoulder. Biodistribution and PET/CT imaging studies were performed after 8–10 days when tumors reached an approximate volume of 300 mm³.

2.2.9. Biodistribution Studies

Mice were intravenously injected with the respective ^{18}F-labeled folate radiotracer (~5 MBq, 100 µL, ~0.2 nmol) and sacrificed at 1 h and 3 h p.i. Selected tissues and organs were collected, weighed, and the activity was measured using a γ-counter (Perkin Elmer, Wallac Wizard 1480). The results of n=3–4 mice per time point were listed as a percentage of the injected activity per gram of tissue mass (% IA/g), using counts of a standard solution (5% IA) measured at the same time. The data sets were analyzed for significance using a one-way ANOVA with Tukey's multiple comparisons post-test using GraphPad Prism software (version 7.0). A p-value of <0.05 was considered statistically significant.

2.2.10. PET/CT Imaging Studies

PET/CT scans were performed using a small-animal PET/CT scanner (G8, Perkin Elmer, U.S.A. [139]) as previously reported [77]. During the scans, mice were anesthetized with a mixture of isoflurane (1.5–2.0%) and oxygen. Static whole-body PET scans of 10 min duration were performed at 1 h and 3 h after injection of ^{18}F-labeled folate radiotracers (5 MBq, ~0.2 nmol, 100 µL), followed by a CT scan of 1.5 min. The acquisition of the data and their reconstruction was performed using the G8 PET/CT scanner software (version 2.0.0.10). All images were prepared using VivoQuant post-processing software (version 3.5, inviCRO Imaging Services and Software, U.S.A.).

2.3. Results

2.3.1. Western Blot Analysis of FRα and FRβ Expression

Western blot analysis unambiguously confirmed FRα expression on RT16 cells and the presence of FRβ on D4 cells by detection of the bands at 38 kDa and 29 kDa, respectively (Fig. 2.2a). Quantification of the signal for RT16 showed $66 \pm 45\%$ of FRα expression level in KB cells (set as 100%), while staining of the FRβ-isoform was negligible (~6%) and corresponded to the signal of FR-negative PC-3 xenograft (~6%) (Fig. 2.2b). In D4 cell lysates, the signal for FRβ was in the range of $42 \pm 39\%$ of the FRα expression level of KB cells (set as 100%), however, only background signal was observed for the FRα (~7%) which was on the same level as FR-negative control (~6%).
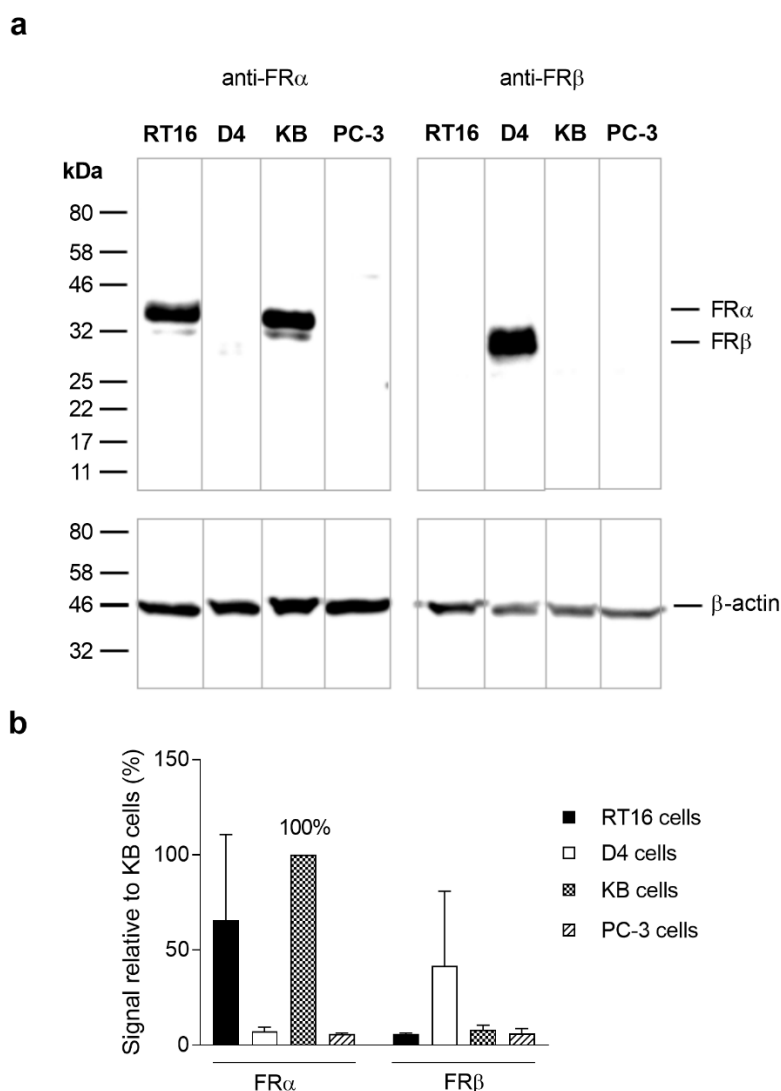
Fig. 2.2 (**a**) Western blot analysis of FRα expression in RT16 cell lysates (~38 kDa) and FRβ expression in D4 cell lysates (~29 kDa) (top panel) in comparison to FRα-positive KB and FR-negative PC-3 tumor cell samples. Beta-actin-staining (~45 kDa) was used as a protein loading control (bottom panel). (**b**) Quantification of the western blot signals (n=3) for RT16 and D4 cells in comparison to KB (set as 100%) and PC-3 tumor cells.

2.3.2. Uptake of ^{18}F-Radiotracers in RT16 and D4 Cells

Uptake of 6R-[^{18}F]Aza-5-MTHF (62 ± 10% of total added activity) and 6S-[^{18}F]Aza-5-MTHF (64 ± 15%) into RT16 cells was slightly higher than for [^{18}F]AzaFol (52 ± 4%) after a 3 h-incubation period (Fig. 2.3a). The internalized fractions were in the range of 11–13% of total added activity. FRα-specific uptake was confirmed by complete blockade of radiotracer uptake in cell samples pre-incubated with excess folic acid (Fig. 2.3a). Uptake studies performed with FRβ-expressing D4 cells showed only a negligible uptake of 6R-[^{18}F]Aza-5-MTHF (5 ± 2%) (Fig. 2.3b). This was significantly lower than the uptake of 6S-[^{18}F]Aza-5-MTHF (70 ± 7%) which was similar to the uptake (61 ± 14%) of [^{18}F]AzaFol. Co-incubation of D4 cells with excess folic acid reduced the uptake of all radiotracers to background levels (<0.1%) (Fig. 2.3b).
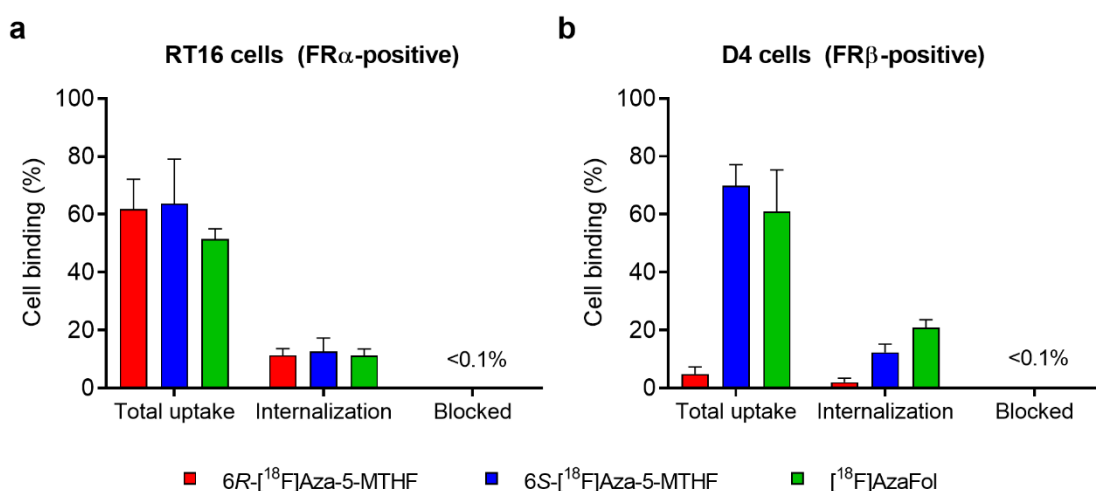
Fig. 2.3 Cell uptake and internalization of 6R-[^{18}F]Aza-5-MTHF, 6S-[^{18}F]Aza-5-MTHF and [^{18}F]AzaFol in (**a**) RT16 and (**b**) D4 cells after 3 h-incubation at 37 ºC. Unspecific binding of radiotracers (blocked) was determined by co-incubation of cells with folic acid (100 μM). The results are presented as percentage of total added activity expressed as average ± SD (n=3).

2.3.3. Receptor-Binding Affinity of Fluorinated Folates (IC$_{50}$ Values)

The binding affinity of 6R-Aza-5-MTHF to the FRα was ~40-fold higher (IC$_{50}$ values: 1.8 ± 0.1 nM) than to the FRβ (77 ± 27 nM) (Fig. 2.4, Table 2.2). In contrast, the binding affinity of 6S-Aza-5-MTHF was similar to both FR-isoforms (2.1 ± 0.4 nM and 0.8 ± 0.2 nM, respectively) and the same held true also for AzaFol (0.6 ± 0.3 nM and 0.3 ± 0.1 nM, respectively). These findings corresponded well with the determined values of the respective non-fluorinated analogues demonstrating a ~70-fold increased binding of 6S-5-MTHF to the FRα but equal binding affinity to both FR isoforms in the case of 6R-5-MTHF and folic acid (Fig. 2.4, Table 2.2).
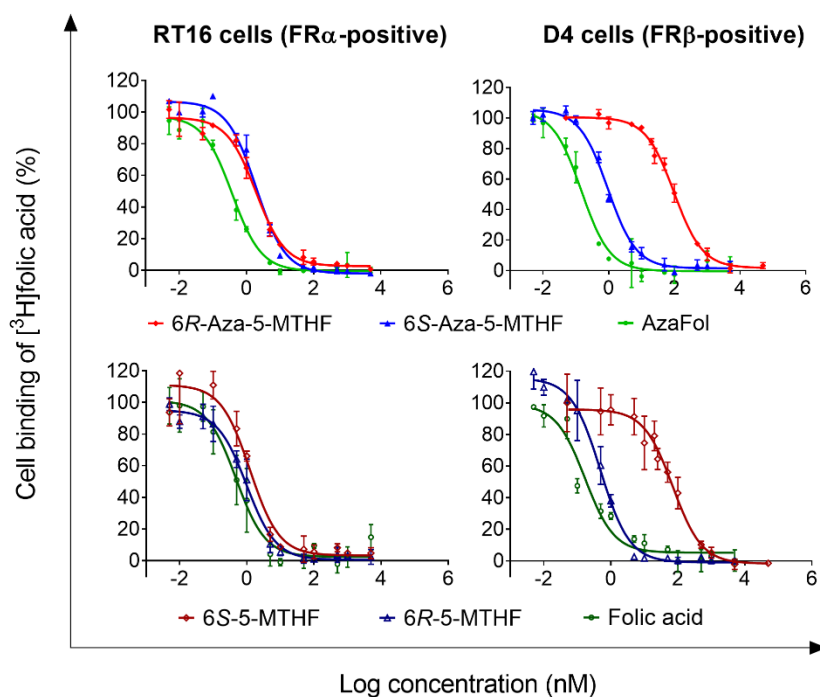
Fig. 2.4 Receptor-binding curves for 6*R*-Aza-5-MTHF, 6*S*-Aza-5-MTHF and AzaFol (upper panel) as well as for the non-fluorinated analogues, 6*S*-5-MTHF, 6*R*-5-MTHF and folic acid (lower panel) using [³H]folic acid as the radioactive tracer (0.82–0.98 nM). The data were generated using FRα-positive RT16 cells (left panel) and FRβ-positive D4 cells (right panel).

Determination of the FRα-binding affinity of 6*R*-Aza-5-MTHF and 6*S*-Aza-5-MTHF relative to AzaFol (set as 100%) revealed a lower binding affinity of the reduced folates (29–34%) which was in line with the results obtained for non-fluorinated 6*S*-5-MTHF and 6*R*-5-MTHF relative to folic acid (28–44%). The relative binding affinity to the FRβ indicated a 300-fold lower value of the 6*R*-Aza-5-MTHF as compared to AzaFol, whereas the FRβ-binding affinity of 6*S*-Aza-5-MTHF was only slightly reduced, which corresponded well with the binding affinities of the non-fluorinated folates to the FRβ relative to folic acid (Table 2.2).

Table 2.2 FR-binding affinities of fluorinated and non-fluorinated (aza)-5-MTHF derivatives relative to AzaFol or folic acid, respectively (set as 100%), determined with FRα-expressing RT16 and FRβ-expressing D4 cells

Compound	Relative affinity to FRα (absolute binding affinity)	Relative affinity to FRβ (absolute binding affinity)
AzaFol	100% (0.6 ± 0.3 nM)	100% (0.3 ± 0.1 nM)
6*R*-Aza-5-MTHF	34% (1.8 ± 0.1 nM)	0.3% (77 ± 27 nM)
6*S*-Aza-5-MTHF	29% (2.1 ± 0.4 nM)	32% (0.8 ± 0.2 nM)
Folic acid	100% (0.4 ± 0. 2 nM)	100% (0.3 ± 0.1 nM)
6*S*-5-MTHF[*]	44% (0.9 ± 0.3 nM)	0.4% (64 ± 10 nM)
6*R*-5-MTHF[*]	28% (1.4 ± 0.5 nM)	34% (0.8 ± 0.4 nM)

[*]Stereochemical nomenclature of the corresponding isomers of non-fluorinated 5-MTHFs are inversed due to the different priority of substituents at the stereogenic center.

2.3.4. Autoradiography Studies Using ^{18}F-labeled Folate Radiotracers

In vitro autoradiography studies revealed a similar signal intensity on RT16 xenograft sections for 6R-[18F]Aza-5-MTHF (74 ± 28%) and 6S-[18F]Aza-5-MTHF (89 ± 33%) which was comparable to the signal of [18F]AzaFol (set as 100%) (Fig. 2.5a). These results were confirmed by experiments performed with FRα-positive KB xenograft sections which revealed a similar binding pattern for all three radiotracers (data not shown). The autoradiography images obtained with D4 xenograft sections demonstrated, however, an over 10-fold lower signal for 6R-[18F]Aza-5-MTHF (7 ± 4%; $p<0.05$) as compared to the signal intensity of 6S-[18F]Aza-5-MTHF (81 ± 36%) relative to [18F]AzaFol (set as 100%). The co-incubation of ^{18}F-labeled folates with excess folic acid to block the FR-specific binding resulted in only background signals.

The expression of the FRα and FRβ on RT16 and D4 xenograft sections, respectively, was verified by a positive immunohistochemical staining using an anti-FRα antibody and an anti-FRβ antibody (Fig. 2.5b). The absence of unspecific binding of the secondary antibody was confirmed as well on additional tissue slides (data not shown).
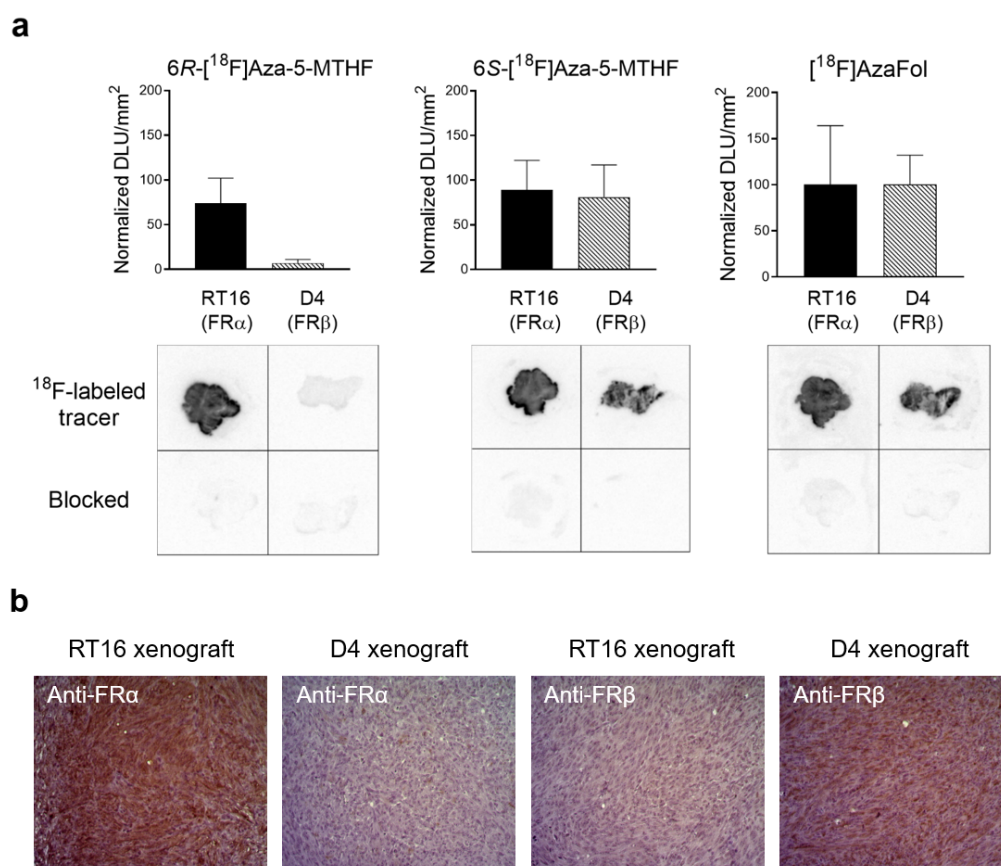
Fig. 2.5 (**a**) Signal intensities of 6R-[18F]Aza-5-MTHF, 6S-[18F]Aza-5-MTHF and [18F]AzaFol (set as 100%) quantified based on RT16 (left) or D4 (right) autoradiography images. The lower panel demonstrates FR-blockade performed in excess folic acid. (**b**) Immunohistochemical staining of FRα and FRβ on RT16 and D4 tissues.

2.3.5.   Biodistribution of ^{18}F-labeled Folate Radiotracers

Biodistribution studies were performed in RT16/D4 xenograft-bearing mice. At 1 h and 3 h p.i., the uptake of 6R-[18F]Aza-5-MTHF into FRα-positive RT16 xenografts ranged from 81 to 94% IA/g and was significantly higher than the uptake into D4 xenografts (7.3–7.6% IA/g) that express the FRβ (Fig. 2.6; Table 2.3). Accumulation of 6S-[18F]Aza-5-MTHF was, however, high in both types of xenografts, RT16 (53–122% IA/g) and D4 (77–149% IA/g) (Fig. 2.6; Table 2.4). [18F]AzaFol showed lower uptake in RT16 (26–45% IA/g) and D4 xenografts (28–52% IA/g), however, the accumulation was in the same range irrespectively of the expressed FR isoform (Fig. 2.6; Table 2.5).

As previously reported by Boss et al. [77], the renal retention of 6R-[18F]Aza-5-MTHF was also about 3-fold lower (11–25% IA/g) than for 6S-[18F]Aza-5-MTHF (31–41% IA/g) and [18F]AzaFol (35–58% IA/g) in SCID mice. Retention of activity in all other tissues and organs was low and comparable to the previous findings obtained in KB tumor-bearing nude mice (Tables 2.3–2.5) [77].
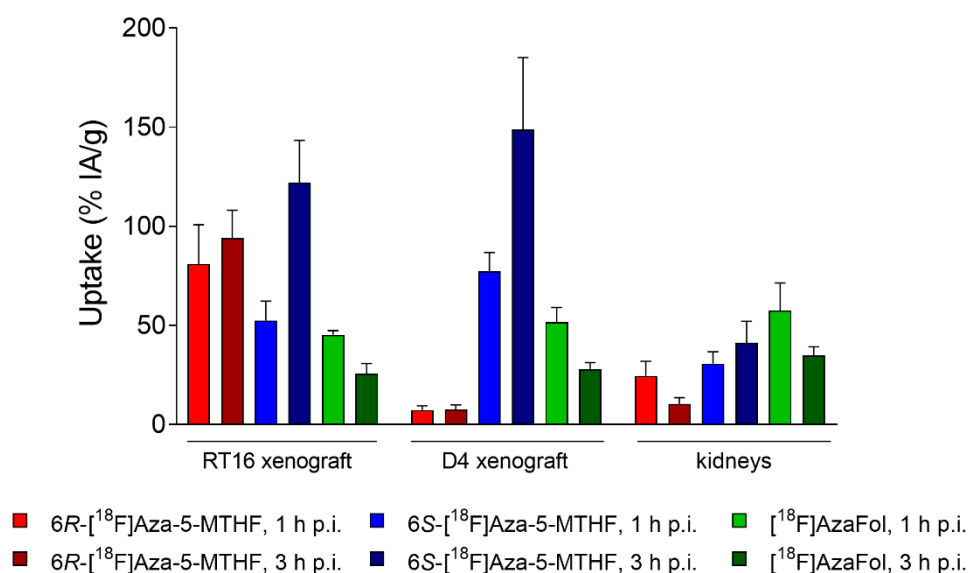
Fig. 2.6 Graph representing the uptake of 6R-[18F]Aza-5-MTHF (red), 6S-[18F]Aza-5-MTHF (blue) and [18F]AzaFol (green) in RT16 and D4 xenografts and in the kidneys at 1 h and 3 h after injection of the ^{18}F-labeled radiofolates (5 MBq/mouse).

Table 2.3 Biodistribution data and xenograft-to-background ratios obtained in RT16 and D4 xenograft-bearing mice at 1 h and 3 h after injection of 6R-[^{18}F]Aza-5-MTHF. Decay-corrected data of accumulated activity are shown as percentage of the injected activity per gram of tissue (% IA/g), representing the average ± SD of data obtained from n=4 mice per cohort. Xenograft-to-background ratios were calculated for blood, liver and kidneys.

Organs	6R-[^{18}F]Aza-5-MTHF	
	1 h p.i.	**3 h p.i.**
Blood	2.4 ± 0.5	0.68 ± 0.20
Lung	3.3 ± 0.7	2.2 ± 0.6
Spleen	17 ± 6	26 ± 7
Kidneys	25 ± 7	11 ± 3
Stomach	3.0 ± 1.0	2.1 ± 0.7
Intestines	8.3 ± 1.4	8.1 ± 3.5
Liver	16 ± 3	13 ± 4
Salivary glands	7.4 ± 1.7	6.6 ± 2.5
Muscle	1.8 ± 0.4	0.97 ± 0.24
Bone	2.3 ± 0.5	2.5 ± 0.5
Brain	1.7 ± 0.6	2.3 ± 0.5
RT16 xenograft	81 ± 20	94 ± 14
D4 xenograft	7.3 ± 2.1	7.6 ± 2.3
Organ Ratios	**Xenograft-to-Background Ratios**	
	1 h p.i.	**3 h p.i.**
RT16-to-blood	35 ± 10	145 ± 37
D4-to-blood	2.7 ± 0.8	11 ± 1
RT16-to-liver	5.1 ± 1.5	7.5 ± 1.2
D4-to-liver	0.40 ± 0.10	0.59 ± 0.11
RT16-to-kidney	3.5 ± 1.3	9.3 ± 1.5
D4-to-kidney	0.28 ± 0.10	0.73 ± 0.11

Table 2.4 Biodistribution data and xenograft-to-background ratios obtained in RT16 and D4 xenograft-bearing mice at 1 h and 3 h after injection of 6S-[^{18}F]Aza-5-MTHF. Decay-corrected data of accumulated activity are shown as percentage of the injected activity per gram of tissue (% IA/g), representing the average ± SD of data obtained from n=4 mice per cohort. Xenograft-to-background ratios were calculated for blood, liver and kidneys.

Organs	6S-[^{18}F]Aza-5-MTHF	
	1 h p.i.	3 h p.i.
Blood	1.5 ± 0.4	1.2 ± 0.1
Lung	2.4 ± 0.5	2.3 ± 0.2
Spleen	3.0 ± 0.5	2.9 ± 0.4
Kidneys	31 ± 6	41 ± 11
Stomach	2.1 ± 0.6	2.0 ± 0.2
Intestines	2.6 ± 0.4	2.1 ± 0.4
Liver	5.5 ± 0.6	4.0 ± 0.5
Salivary glands	15 ± 2	23 ± 4
Muscle	1.4 ± 0.2	1.4 ± 0.4
Bone	1.4 ± 0.1	1.4 ± 0.2
Brain	1.6 ± 0.4	3.1 ± 0.1
RT16 xenograft	53 ± 10	122 ± 21
D4 xenograft	77 ± 10	149 ± 36
Organ Ratios	Xenograft-to-Background Ratios	
	1 h p.i.	3 h p.i.
RT16-to-blood	37 ± 10	105 ± 13
D4-to-blood	50 ± 5	127 ± 24
RT16-to-liver	9.5 ± 1.0	30 ± 3
D4-to-liver	15 ± 2	37 ± 5
RT16-to-kidney	1.7 ± 0.2	3.0 ± 0.5
D4-to-kidney	2.8 ± 0.9	3.6 ± 0.3

Table 2.5 Biodistribution data and xenograft-to-background ratios obtained in RT16 and D4 xenograft-bearing mice at 1 h and 3 h after injection of [^{18}F]AzaFol. Decay-corrected data of accumulated activity are shown as percentage of the injected activity per gram of tissue (% IA/g), representing the average ± SD of data obtained from n=3–4 mice per cohort. Xenograft-to-background ratios were calculated for blood, liver and kidneys.

Organs	[^{18}F]AzaFol	
	1 h p.i.	3 h p.i.
Blood	0.69 ± 0.06	0.57 ± 0.04
Lung	2.1 ± 0.2	1.9 ± 0.3
Spleen	2.0 ± 0.2	6.2 ± 0.6
Kidneys	58 ± 14	35 ± 4
Stomach	2.2 ± 0.2	2.1 ± 0.3
Intestines	2.0 ± 0.5	2.8 ± 0.5
Liver	7.4 ± 0.3	11 ± 1
Salivary glands	11 ± 1	13 ± 1
Muscle	1.8 ± 0.2	1.2 ± 0.2
Bone	1.6 ± 0.2	1.4 ± 0.2
Brain	0.92 ± 0.09	1.2 ± 0.1
RT16 xenograft	45 ± 2	26 ± 5
D4 xenograft	52 ± 7	28 ± 3
Organ Ratios	**Xenograft-to-Background Ratios**	
	1 h p.i.	3 h p.i.
RT16-to-blood	66 ± 8	45 ± 7
D4-to-blood	74 ± 4	49 ± 6
RT16-to-liver	6.1 ± 0.5	2.3 ± 0.3
D4-to-liver	6.9 ± 0.7	2.5 ± 0.3
RT16-to-kidney	0.81 ± 0.14	0.74 ± 0.10
D4-to-kidney	0.94 ± 0.30	0.81 ± 0.07

2.3.6. PET/CT Imaging Studies Using ^{18}F-lableled Folate Radiotracers

Mice bearing a RT16 xenograft on the right shoulder and a D4 xenograft on the left shoulder were imaged at 1 h and 3 h after injection of the ^{18}F-labeled folate radiotracers using preclinical PET/CT (Fig. 2.7). In agreement with the biodistribution data, the selective accumulation of 6R-[^{18}F]Aza-5-MTHF in the RT16 xenograft was readily visualized on PET/CT images. This was in clear contrast to the PET/CT images obtained after injection of 6S-[^{18}F]Aza-5-MTHF and [^{18}F]AzaFol, which accumulated equally in both RT16 and D4 xenografts. It was further confirmed that the 6R-[^{18}F]Aza-5-MTHF exhibited the most favorable tumor-to-background profile, in particular due to the significantly lower renal retention of activity as compared to 6S-[^{18}F]Aza-5-MTHF and [^{18}F]AzaFol.
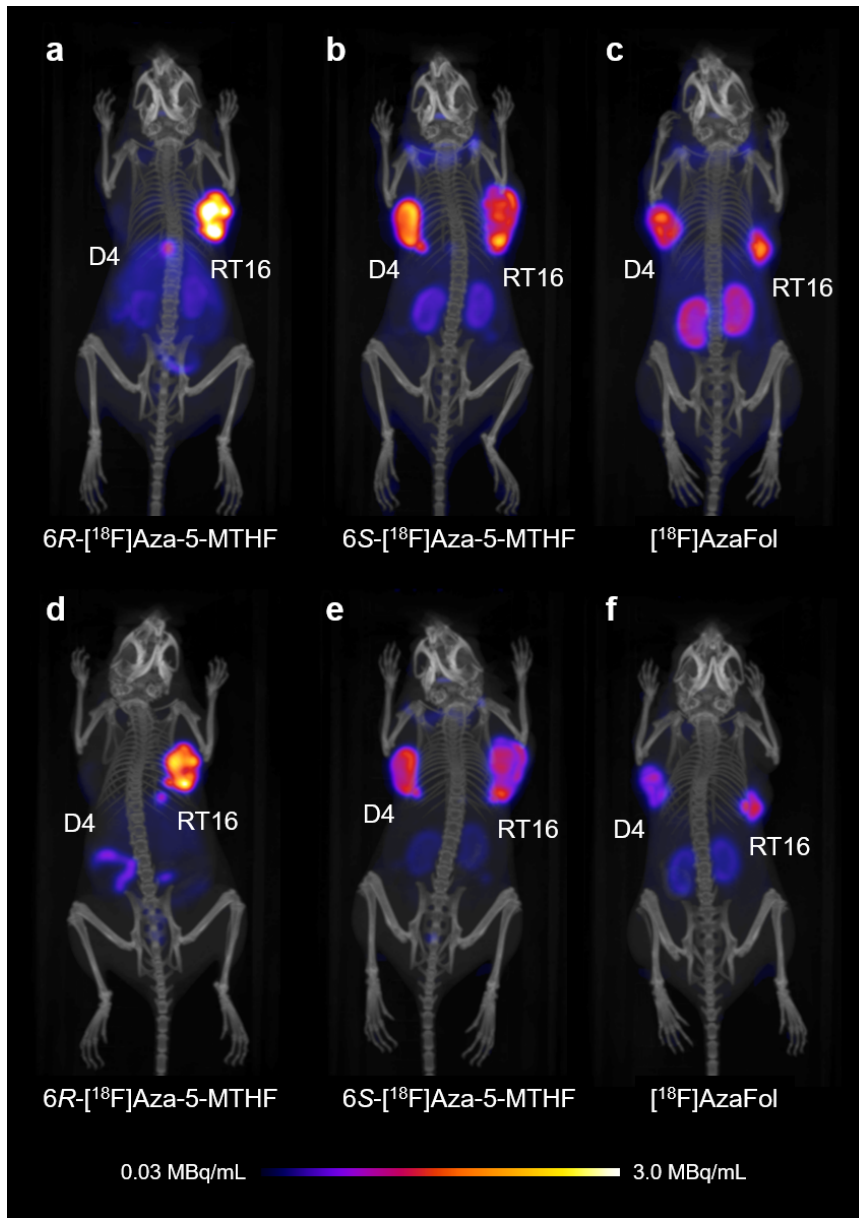
Fig. 2.7 PET/CT images of mice bearing RT16 and D4 xenografts 1 h (**a–c**) and 3 h (**d–f**) after injection of ^{18}F-labeled radiofolates (5 MBq/mouse) shown as maximum intensity projections (MIPs). (**a/d**) 6*R*-[^{18}F]Aza-5-MTHF; (**b/e**) 6*S*-[^{18}F]Aza-5-MTHF and (**c/f**) [^{18}F]AzaFol.

2.4.   Discussion

FR-targeted cancer therapy outcomes reported in the recent past were not always convincing which may be ascribed to uncertainties of patient inclusion criteria [51,127,140]. This situation is unsatisfactory as only patients with FRα-positive lesions would ideally profit from such treatments. In contrast, patients with a FR-negative disease would only experience undesired side effects without any benefit from these costly treatment options. While the application of [^{18}F]AzaFol does visualize FR-positive tissue using PET [76], false-positive results may occur due to concomitant accumulation of the radiotracer in FRβ-expressing macrophages involved at sites of inflammation. Having a means in hands to provide a full picture of FRα-positive lesions in an individual patient would present an essential step for the success of any FRα-targeted tumor therapy concept. This includes novel FRα-targeted immunotherapies as well as folic acid conjugates of highly toxic chemotherapeutics and folate radioconjugates for targeted radionuclide therapy [24,127].

In this study, we have demonstrated that 6*R*-Aza-5-MTHF displayed significantly higher affinity to the FRα than to the FRβ indicating the anticipated FRα selectivity. These findings were in agreement with those obtained with the corresponding non-fluorinated versions of 5-MTHF that confirmed the original observation of Wang et al. who reported on the ~50-fold higher affinity of 6*S*-5-MTHF to the FRα than to the FRβ [132,133]. Folic acid and the non-physiological 6*R*-5-MTHF as well as their fluorinated analogues showed, however, equal binding to both FR isoforms.

The fact that only the 6*R*-isomer of the novel aza-5-MTHF-based ^{18}F-labeled radiotracers bound with a higher affinity to the FRα than to the FRβ, but not the 6*S*-isomer, is an essential finding. It indicates the need for diastereomerically pure folate radiotracers other than previously proposed by the development of a racemic mixture of [^{99m}Tc]Tc-DMTHF, a dimethylated version of the reduced form of [^{99m}Tc]Tc-EC20 [134].

The in vivo evaluation of tumor-specific folate radiotracers in the presence of inflammation is challenging in mice, since the number of activated macrophages is commonly low and, hence, the expected signal from inflammatory sites is lower than the signal from the tumor tissue. This situation may complicate the interpretation of the results with regard to FRα selectivity. In order to unambiguously determine whether the ^{18}F-labeled folate radiotracers accumulated specifically in FRα-expressing tissue, we have established a mouse model using D4 and RT16 cells to grow xenografts of comparable volumes. Using these mice enabled the determination of FRα-selective uptake of 6*R*-[^{18}F]Aza-5-MTHF in RT16 xenografts, while the accumulation in D4 xenografts was significantly lower. In contrast, both 6*S*-[^{18}F]Aza-5-MTHF as well as [^{18}F]AzaFol showed comparable accumulation in both xenografts.

It is important to recognize that in addition to the FRα-selective tissue accumulation of 6*R*-[^{18}F]Aza-5-MTHF, this radiotracer also showed the most favorable clearance from background tissues, including the kidneys as previously demonstrated by Boss et al., who used KB tumor-bearing nude mice [77]. The

~33% lower FRα-binding affinity of the 5-MTHF-based ^{18}F-radiotracers as compared to the receptor-binding of [^{18}F]AzaFol is in line with the common knowledge that reduced folates display lower affinity to the FR than folic acid [131-133]. While the high FR-affinity of folic acid was postulated as a particular advantage of FR-targeting agents, we believe that 5-MTHF-based ^{18}F-radiotracers may be favorably used for this purpose as they may be more efficiently released from the FR upon internalization [141]. This could explain the higher uptake of 6R-[^{18}F]Aza-5-MTHF and 6S-[^{18}F]Aza-5-MTHF in RT16 and KB xenografts as compared to [^{18}F]AzaFol [77].

2.5. Conclusion

In this study, we have identified 6R-[^{18}F]Aza-5-MTHF as a promising novel PET agent, which accumulated in FRα-positive RT16 xenografts, but not in FRβ-positive D4 xenografts grown in the same mouse. The favorable tissue distribution profile of 6R-[^{18}F]Aza-5-MTHF together with the herein determined FRα selectivity means a breakthrough in the field. This novel radiotracer may serve for the unambiguous identification of patients that could profit from FRα-targeted therapies. It is, thus, without any doubts that 6R-[^{18}F]Aza-5-MTHF deserves highest attention in view of a clinical translation.

III. Combining Albumin-Binding Properties and Interaction with Pemetrexed to Improve the Tissue Distribution of Radiofolates

Cristina Müller[1], **Patrycja Guzik**[1], Klaudia Siwowska[1], Susan Cohrs[1], Raffaella M. Schmid[1] and Roger Schibli[1,2]

[1] *Center for Radiopharmaceutical Sciences ETH-PSI-USZ, Paul Scherrer Institute, 5232 Villigen-PSI; Switzerland*

[2] *Department of Chemistry and Applied Biosciences, ETH Zurich, 8093 Zurich; Switzerland*

3.1. Introduction

Folic acid-based radioconjugates have been developed and pre-clinically investigated over the past years for the purpose of nuclear imaging of folate receptor (FR)-positive tumors using Single Photon Emission Computed Tomography (SPECT) or Positron Emission Tomography (PET). Only a very limited number of candidates have been translated to clinical studies, among those [^{111}In]In-DTPA-folate and [^{99m}Tc]Tc-EC20 (Etarfolatide[TM]) [58,130]. [^{99m}Tc]Tc-EC20 has been used for imaging of FR-positive malignancies enabling the selection of patients who could potentially profit from FR-targeted chemotherapy [123,127,142]. PET imaging agents using ^{18}F-labeled folate tracers are currently under investigation for the same purposes [75,143]. The application of folate radioconjugates for targeted radionuclide therapy would be extremely attractive, given the fact that a large variety of tumor types express the FR, among those several gynecological cancer types, but also other frequently occurring cancer types such as non-small cell (NSC) lung cancer [121,123]. The high accumulation of folic acid radioconjugates in the kidneys has, however, presented a drawback in this regard [63]. A tumor-to-kidney ratio of accumulated activity in the range of 0.1–0.2, as was the case for conventional folate radioconjugates (without albumin binder), prevented the realization of the therapeutic concept completely. Our group has made major efforts to develop concepts that can enable the application of therapeutic folic acid radioconjugates [47].

We were the first to demonstrate the fact that the antifolate pemetrexed (PMX, Alimta[TM], Fig. 3.1a [144]) increases the tumor-to-background ratio of accumulated activity when injected one hour prior to the radiofolate [85]. This concept was further investigated in different preclinical settings with a variety of radioligands including [^{111}In]In-DTPA-folate and [^{99m}Tc]Tc-EC20 that had previously been tested in patients [80,81,84,145]. The "antifolate effect" was reproducible in different animal models including xenograft and syngeneic tumor mouse models [80,81,84]. Hence, it could be shown repeatedly by our group and others that this concept improved the tissue distribution of any radiofolate by reducing retention in the kidneys [66]. We were also able to demonstrate, that the combination of PMX and [^{177}Lu]Lu-folate can enhance the therapeutic outcome and, in addition, reduce undesired side effects of radiofolates [83]. These findings were based on the radiosensitizing potential of PMX [146-148], and the reduction of accumulated activity in the kidneys [85]. Even though this approach revealed to be highly promising, the tumor-to-kidney ratio of accumulated activity was still <1 when using the most promising folate radioconjugates (e.g. DOTA-conjugates [82]). This fact presented a hurdle for therapeutic application of radiofolates as the risk of damage to the kidneys would be high.

More recently, we have pursued another strategy in which we modified the folate conjugate chemically by introducing an albumin-binding entity [87]. This modification was thought to enhance the blood circulation time of the radiofolate ([^{177}Lu]Lu-cm09) and, hence, improve the tissue distribution profile [87]. Indeed, this concept led to unprecedentedly high tumor-to-kidney ratios of accumulated activity (0.5–0.7 over 5 days p.i.) and had the advantage of avoiding the use of additional medication to reach

the desired effect.

By changing the linker entity of the radiofolate, we aimed at further improving the tissue distribution profile [90]. Integration of a short alkane spacer between folic acid and the albumin-binding entity was realized in compound cm13 [90] (Fig. 3.1b). This modification appeared favorable based on a slightly improved tumor-to-kidney ratio of accumulated activity after application of [^{177}Lu]Lu-cm13 [90].

Based on the observation that PMX improves the tissue distribution of folate radioconjugates the question arose whether the combined application of PMX and [^{177}Lu]Lu-cm13 would enable a further increase in the tumor-to-kidney ratio of accumulated activity. The aim of this study was, therefore, to combine [^{177}Lu]Lu-cm13 and PMX in vivo by investigating a potentially positive effect on the tissue distribution of activity. Mice with KB tumor xenografts (cervical cancer type), the most often used mouse model to test folate (radio)conjugates, were employed at first place for this study. In addition, we investigated mice bearing IGROV-1 tumor xenografts, an ovarian cancer model, which has been used previously for the investigation of folate radioconjugates [80,112]. Biodistribution studies were performed in order to investigate [^{177}Lu]Lu-cm13 applied alone and combined with PMX injected before (and after) the radiofolate. SPECT/CT imaging was carried out to visualize the anticipated effects.
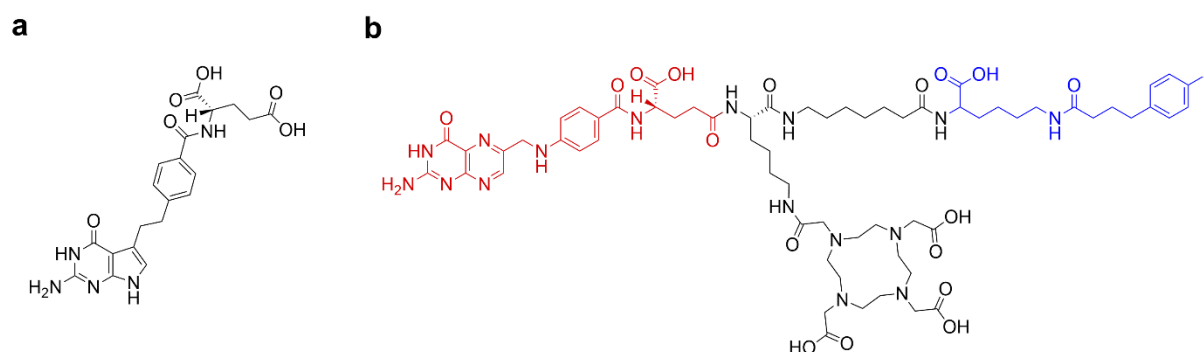
Fig. 3.1 (**a**) Chemical structure of the antifolate pemetrexed (PMX, Alimta^{TM}). (**b**) Chemical structure of the most promising albumin-binding DOTA-folate conjugate referred to as cm13 [90]; folic acid (red) serves as the targeting agent; the albumin binding entity (blue) enables binding to serum albumin and, hence, enhanced residence time in the blood; the DOTA chelator allows stable coordination of ^{177}Lu.

3.2. Materials & Methods

3.2.1. Preparation of [^{177}Lu]Lu-Folate

The DOTA-folate conjugate (cm13 [90], herein referred to as "folate") previously developed by our group was kindly provided by Merck & Cie (Schaffhausen, Switzerland). No-carrier added ^{177}Lu was obtained from ITM Medical Isotopes (ITM GmbH, Germany). Radiolabeling of the folate conjugate was performed in a mixture of HCl (0.05 M) and Na-acetate (0.5 M) at pH 4.5 at 95 °C and an incubation time of 10 min, as previously reported [90]. Quality control of [^{177}Lu]Lu-folate was carried out using high-performance liquid chromatography (HPLC) as previously reported [90].

3.2.2. Cell Culture

Human KB tumor cells (cervical carcinoma cell line, subclone of HeLa cells, ACC-136) were purchased from the German Collection of Microorganisms and Cell Cultures (DSMZ, Braunschweig, Germany). The human ovarian tumor cell line, IGROV-1, was a kind gift of Dr. Gerrit Jansen, Free University Medical Center Amsterdam, The Netherlands. Both cell lines were cultured under standard conditions (37 °C, humidified atmosphere, 5% CO_2) in folate-deficient RPMI 1640 medium (FFRPMI, Cell Culture Technologies, Gravesano, Switzerland), supplemented with 10% fetal calf serum, L-glutamine, and antibiotics.

3.2.3. In Vivo Studies

In vivo experiments were approved by the local veterinarian department and conducted in accordance with the Swiss law of animal protection. Athymic female nude mice (CD-1 Foxn-1/nu) were obtained from Charles River Laboratories (Sulzfeld, Germany) at the age of 5–6 weeks. All animals were fed with a folate-deficient rodent diet (ssniff Spezialdiäten GmbH, Soest, Germany). Mice were inoculated with 5×10^6 KB cells or 5×10^6 IGROV-1 cells in 100 μL phosphate-buffered saline (PBS) into the subcutis of each shoulder for biodistribution studies. Additional mice were inoculated with the same number of tumor cells into the subcutis of the right shoulder for SPECT/CT imaging studies. For the in vivo scans, mice were anesthetized with a mixture of isoflurane (1.5–2%) and oxygen.

3.2.4. Biodistribution Studies

Biodistribution studies were performed with 4–5 mice per group, 12–14 days after KB cell inoculation and 14–16 days after IGROV-1 tumor cell inoculation. [^{177}Lu]Lu-folate (5 MBq, 1 nmol/mouse) was diluted in 100 μL PBS and injected into a lateral tail vein (0.05% bovine serum albumin was added to prevent adhesion to the syringe). Pemetrexed (PMX, Alimta^{TM}) was diluted in saline (4 mg/mL) and administered at defined time points (0.4 mg per injection) before and after the injection of [^{177}Lu]Lu-folate. The animals were sacrificed at 4 h and 24 h after administration of the [^{177}Lu]Lu-folate. Selected tissues and organs were collected, weighed, and activity was measured using a γ-counter (PerkinElmer Wallac Wizard 1480). The results were decay corrected and presented as a percentage of the injected activity per gram of tissue mass (% IA/g).

3.2.5. Statistics

Biodistribution data were compared using a two-way ANOVA Sidak's multiple comparisons test (4 h p.i. time point) and a two-way ANOVA Tukey's multiple comparisons test (24 h p.i. time point; Graph Pad Prism version 7.0). Tumor-to-background ratios were compared using an unpaired t-test with Welch's correction (4 h p.i. time point) and ordinary one-way ANOVA Tukey's multiple comparisons test (24 h p.i. time point), respectively. Statistically significant differences were calculated using data based on the average (% IA/g)-values for the activity accumulation in the blood, kidneys, liver, muscle, salivary glands and tumors. Values for tissue uptake that differed significantly from the control group are indicated with asterisks in Tables 3.1–3.3. Statistically significant differences in tissue uptake among the PMX-pre/post-treated mice were indicated as a footnote of Table 3.3. All statistically significant differences of tumor-to-background ratios between the groups were indicated with asterisks in Figure 3.2. Statistically significant values were indicated as follows: ns: $p > 0.05$: * $p \leq 0.05$; ** $p \leq 0.01$; *** $p \leq 0.001$; **** $p \leq 0.0001$.

3.2.6. SPECT/CT Studies

Imaging studies were performed using a small-animal SPECT/CT camera (NanoSPECT/CT^{TM}, Mediso Medical Imaging Systems, Budapest, Hungary). [^{177}Lu]Lu-folate was injected into the lateral tail vein of tumor-bearing mice (25 MBq, ~1 nmol per mouse). SPECT scans of 38 min duration were performed 4 h and 24 h after injection of the [^{177}Lu]Lu-folate after CT scans of 7.30 min duration. The images were acquired using Nucline Software (version 1.02, Mediso Ltd., Budapest, Hungary). The reconstruction was performed using HiSPECT software (Scivis GmbH, Göttingen, Germany). Images were analyzed using VivoQuant software (version 3.0, inviCRO Imaging Services and Software, Boston, US). Gauss post-reconstruction filter (FWHM = 1 mm) was applied twice to the SPECT images, and the scale of activity was set as indicated on the images (minimum value = 3 Bq/voxel to maximum value = 30 Bq/voxel).

3.3. Results

3.3.1. Biodistribution Studies

Biodistribution in KB and IGROV-1 Tumor-Bearing Mice. Biodistribution studies were performed at 4 h and 24 h after injection of the [^{177}Lu]Lu-folate (5 MBq, 1 nmol per mouse) using nude mice bearing KB or IGROV-1 tumor xenografts. The uptake of [^{177}Lu]Lu-cm13 in KB tumors was high (22.4 ± 4.50% IA/g) at 4 h p.i. and largely retained over the time of investigation (18.6 ± 6.80% IA/g, 24 h p.i.) (Tables 3.1/3.2). Pre-injection of PMX reduced the uptake in KB tumor (17.6 ± 0.90% IA/g, $p<0.001$) at 4 h p.i., but had no impact on the tumor uptake at later time points (22.1 ± 3.60% IA/g; 24 h p.i.). At 4 h p.i. retention of activity in the kidneys was significantly reduced when PMX was pre-injected (15.8 ± 2.60% IA/g vs. control mice: 26.5 ± 1.20% IA/g; $p<0.0001$). The same effect was observed at 24 h p.i. (24.7 ± 5.70% IA/g vs. control mice: 30.9 ± 3.90% IA/g; $p<0.01$) (Table 3.2). If PMX was injected for a second time, 3 h or 7 h after administration of the radiofolate, kidney uptake was even more effectively reduced at 24 h p.i. (21.8 ± 0.70% IA/g; $p<0.0001$ and 21.0 ± 4.70% IA/g; $p<0.0001$, respectively) (Table 3.2). In the liver, muscles and salivary glands, PMX did not affect uptake of radiofolate significantly, even though a slight increase in blood activity was seen at 4 h p.i. (~9.13% IA/g vs. control ~7.32% IA/g; $p>0.05$), but not at later time points (Tables 3.1/3.2). The uptake of the radiofolate in IGROV-1 tumor xenografts was consistently higher (31.5 ± 5.60% IA/g; 4 h p.i. and 37.7 ± 5.10% IA/g, 24 h p.i.) than in KB tumor xenografts (Tables 3.1/3.3). Pre-injection of PMX did not reduce the tumor uptake significantly ($p>0.05$). A significant difference in tumor accumulated activity was determined, however, between groups of mice that received PMX according to different application schemes. It is not entirely understood why the mice which received PMX only 1 h before the application of [^{177}Lu]Lu-folate showed the highest tumor uptake (40.7 ± 9.00% IA/g), whereas mice that were injected with PMX 1 h before and 7 h after the radiofolate showed significantly reduced tumor accumulation (32.9 ± 5.30; 24 h p.i.; $p<0.001$) (Table 3.3). As compared to control values, PMX reduced the uptake in the kidneys ($p<0.001$) 4 h after injection of [^{177}Lu]Lu-folate and in all cases 24 h after injection of the radiofolate ($p<0.001$). Activity levels in the blood were slightly but not significantly ($p>0.05$) increased in IGROV-1 tumor-bearing mice that received PMX before the radiofolate (~10.8% IA/g, 4 h p.i.) when compared to control mice (~7.88% IA/g, 4 h p.i.). This effect was still observable at later time points (~1.97% IA/g, 24 h p.i. vs. control mice: ~1.46% IA/g, 24 h p.i.; $p>0.05$) (Tables 3.1/3.3). In the liver, muscles and salivary glands, PMX did not have a significant effect on the retention of the radiofolate.

Table 3.1 Biodistribution data obtained in KB and IGROV-1 tumor-bearing mice, 4 h after injection of [^{177}Lu]Lu-folate with and without pre-injected pemetrexed (PMX). Data are shown as % IA/g tissue, representing the average ± SD.

Tissues	[^{177}Lu]Lu-cm13			
	-	PMX [1]	-	PMX [1]
	4 h p.i.	4 h p.i.	4 h p.i.	4 h p.i.
	KB	KB	IGROV-1	IGROV-1
	n = 5	*n* = 5	*n* = 4	*n* = 4
Blood	7.32 ± 0.85	9.13 ± 0.89	7.88 ± 1.70	10.8 ± 1.43
Lung	4.33 ± 0.44	4.92 ± 0.39	4.47 ± 0.97	6.14 ± 0.97
Spleen	1.51 ± 0.15	1.45 ± 0.06	1.74 ± 0.15	2.16 ± 0.45
Kidneys	26.5 ± 1.20	15.8 ± 2.60 ****	26.9 ± 2.90	16.9 ± 3.10 ***
Stomach	1.37 ± 0.35	1.41 ± 0.19	1.58 ± 0.47	1.83 ± 0.39
Intestines	1.29 ± 0.42	1.38 ± 0.32	1.10 ± 0.18	1.12 ± 0.20
Liver	3.88 ± 0.49	3.31 ± 0.43	3.27 ± 0.49	3.38 ± 0.56
Muscle	1.92 ± 0.25	1.55 ± 0.28	1.17 ± 0.43	1.28 ± 0.38
Bone	1.55 ± 0.10	1.67 ± 0.24	1.38 ± 0.30	1.57 ± 0.25
Tumor	22.4 ± 4.50	17.6 ± 0.90 ***	31.5 ± 5.60	29.2 ± 8.80
Salivary glands	6.78 ± 0.57	5.84 ± 1.25	6.17 ± 0.49	6.18 ± 0.88

[1] PMX (400 µg/mouse) was injected 1 h prior to the [^{177}Lu]Lu-folate; Statistical significance is indicated by asterisks (statistically significant difference between uptake in the tissue of control mice and PMX injected mice) *** $p \leq 0.001$; **** $p \leq 0.0001$.

Table 3.2 Biodistribution data obtained in KB tumor-bearing mice, 24 h after injection of [^{177}Lu]Lu-folate with and without pre- and post-injected pemetrexed (PMX). Data are shown as % IA/g tissue, representing the average ± SD.

Tissues	[^{177}Lu]Lu-cm13			
	-	PMX [1]	PMX [2]	PMX [3]
	24 h p.i.	24 h p.i.	24 h p.i.	24 h p.i.
	KB	KB	KB	KB
	n = 4	*n* = 5	*n* = 4	*n* = 4
Blood	1.28 ± 0.23	1.39 ± 0.14	1.37 ± 0.17	1.31 ± 0.14
Lung	1.74 ± 0.45	1.69 ± 0.22	1.66 ± 0.15	1.60 ± 0.35
Spleen	0.69 ± 0.14	0.79 ± 0.13	0.80 ± 0.13	0.72 ± 0.15
Kidneys	30.9 ± 3.90	24.7 ± 5.70 **	21.8 ± 0.70 ****	21.0 ± 4.70 ****
Stomach	0.77 ± 0.19	0.70 ± 0.20	0.80 ± 0.14	0.63 ± 0.21
Intestines	0.27 ± 0.07	0.47 ± 0.14	0.30 ± 0.07	0.34 ± 0.06
Liver	2.46 ± 0.16	1.91 ± 0.44	2.04 ± 0.57	2.05 ± 0.05
Muscle	1.56 ± 0.10	1.31 ± 0.25	1.17 ± 0.20	1.50 ± 0.49
Bone	1.09 ± 0.31	0.97 ± 0.15	0.85 ± 0.06	0.95 ± 0.16
Tumor	18.6 ± 6.80	22.1 ± 3.60	22.4 ± 3.20	20.9 ± 5.10
Salivary glands	4.18 ± 0.62	3.71 ± 0.33	3.39 ± 0.30	3.86 ± 0.44

[1] PMX (400 µg/mouse) was injected 1 h prior to the [^{177}Lu]Lu-folate; [2] PMX (twice 400 µg/mouse) was injected 1 h prior to the [^{177}Lu]Lu-folate and 3 h after [^{177}Lu]Lu-folate; [3] PMX (twice 400 µg/mouse) was injected 1 h prior to the [^{177}Lu]Lu-folate and 7 h after [^{177}Lu]Lu-folate. Statistical significance is indicated with asterisks (statistically significant difference between uptake in the tissue of control mice and PMX injected mice) ** $p \leq 0.01$; **** $p \leq 0.0001$.

Table 3.3 Biodistribution data obtained in IGROV-1 tumor-bearing mice, 24 h after injection of [^{177}Lu]Lu-folate with and without pre- and post-injected pemetrexed (PMX). Data are shown as % IA/g tissue, representing the average ± SD.

Tissues	[^{177}Lu]Lu-cm13			
	-	PMX [1]	PMX [2]	PMX [3]
	24 h p.i.	24 h p.i.	24 h p.i.	24 h p.i.
	IGROV-1	IGROV-1	IGROV-1	IGROV-1
	$n = 4$	$n = 5$	$n = 5$	$n = 5$
Blood	1.46 ± 0.19	1.97 ± 0.15	2.21 ± 0.29	2.08 ± 0.31
Lung	1.88 ± 0.24	2.16 ± 0.23	2.23 ± 0.25	2.21 ± 0.33
Spleen	0.92 ± 0.17	1.19 ± 0.26	1.26 ± 0.33	1.20 ± 0.30
Kidneys	34.0 ± 2.00	26.2 ± 3.50 ***	21.8 ± 2.00 ****	20.8 ± 3.40 **** [4]
Stomach	0.69 ± 0.19	0.69 ± 0.31	0.78 ± 0.13	0.65 ± 0.17
Intestines	0.49 ± 0.12	0.44 ± 0.08	0.48 ± 0.07	0.43 ± 0.14
Liver	2.75 ± 0.57	2.47 ± 0.51	2.73 ± 0.65	2.41 ± 0.49
Muscle	1.52 ± 0.19	1.36 ± 0.37	1.28 ± 0.52	1.28 ± 0.32
Bone	0.95 ± 0.11	0.96 ± 0.12	1.02 ± 0.17	0.95 ± 0.10
Tumor	37.7 ± 5.10	40.7 ± 9.00	38.6 ± 3.50	32.9 ± 5.30 [5]
Salivary glands	4.43 ± 0.63	4.28 ± 0.43	3.95 ± 1.03	3.77 ± 0.45

[1] PMX (400 µg/mouse) was injected 1 h prior to the [^{177}Lu]Lu-folate; [2] PMX (twice 400 µg/mouse) was injected 1 h prior to the [^{177}Lu]Lu-folate and 3 h after [^{177}Lu]Lu-folate; [3] PMX (twice 400 µg/mouse) was injected 1 h prior to the [^{177}Lu]Lu-folate and 7 h after [^{177}Lu]Lu-folate. [4] This value was significantly different from the value obtained in mice that received PMX 1 h before the radiofolate; [5] This value was significantly different from the values obtained in mice that received PMX 1 h before (and 3 h after) the radiofolate. Statistical significance is indicated with asterisks (statistically significant difference between uptake in the tissue of control mice and PMX injected mice) *** $p \leq 0.001$; **** $p \leq 0.0001$.

Tumor-to-Background Ratios. The tumor-to-background ratios were determined at 4 h and 24 h after injection of [^{177}Lu]Lu-folate in order to better assess the effects of PMX. This appeared important since the absolute tumor uptake may have varied from mouse to mouse based on the size of the tumor xenograft. In line with the increased activity in the blood 4 h after injection of the [^{177}Lu]Lu-folate in mice that received PMX, the tumor-to-blood ratios were significantly reduced in KB tumor-bearing mice (1.93 ± 0.18 vs. control mice: 3.05 ± 0.49; $p<0.01$) as well as in IGROV-1 tumor-bearing mice (2.67 ± 0.58 vs. control mice: 4.05 ± 0.72; $p<0.05$). At 24 h after injection of the radiofolate, tumor-to-blood ratios of KB tumor-bearing mice were in the same range among the different groups ($p>0.05$). In IGROV-1 tumor-bearing mice, tumor-to-blood ratios were significantly decreased at 4 h p.i. ($p<0.05$) in mice that received PMX as well as at 24 h when PMX was applied twice ($p<0.05$).

The most important parameter to assess the effect of PMX was undoubtedly the tumor-to-kidney ratio of mice that received PMX compared to the ratio in control mice (Fig. 3.2). In both mouse models, an increased value was observed when PMX was applied. At 4 h after injection of [^{177}Lu]Lu-folate, the tumor-to-kidney ratio was significantly increased in KB tumor-bearing mice that received PMX (1.13 ± 0.17; $p<0.05$). An increased tumor-to-kidney ratio was also visible in the IGROV-1 tumor mouse model, however, in this case the effect was not significant due to the large standard deviation in the PMX-

injected group.

Investigation of the 24 h-time point revealed also consistently increased tumor-to-kidney ratios when PMX was applied. The highest ratios in KB tumor-bearing mice were observed in mice that received PMX 1 h before and 3 h or 7 h after injection of the [^{177}Lu]Lu-folate (1.03 ± 0.16 and 0.99 ± 0.06, respectively). In IGROV-1 tumor-bearing mice the ratios obtained under these conditions were even higher (1.78 ± 0.18 and 1.62 ± 0.39, respectively) but only significant when PMX was injected 1 h before and 3 h after the radiofolate.
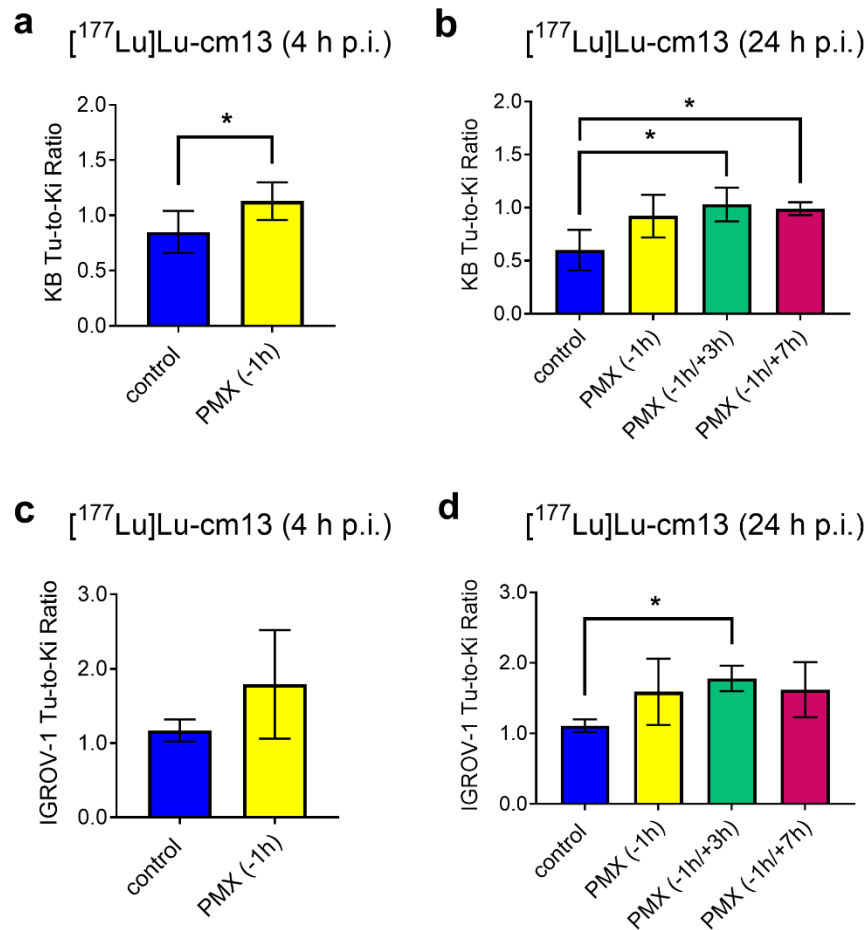
Fig. 3.2 Tumor-to-kidney ratios of mice after injection of [^{177}Lu]Lu-folate (5 MBq, 1 nmol). (**a**) Tumor-to-kidney ratios of KB tumor-bearing mice 4 h after injection of [^{177}Lu]Lu-cm13 without pre-injected PMX (blue) or with pre-injected PMX (yellow). (**b**) Tumor-to-kidney ratios of KB tumor-bearing mice 24 h after injection of [^{177}Lu]Lu-cm13 without pre-injection of PMX (blue) or with pre-injection of PMX 1 h before the radiofolate (yellow) or 1 h before and 3 h (green) or 7 h (red) after injection of the radiofolate. (**c**) Tumor-to-kidney ratios of IGROV-1 tumor-bearing mice 4 h after injection of [^{177}Lu]Lu-cm13 without pre-injected PMX (blue) or with pre-injected PMX (yellow). (**d**) Tumor-to-kidney ratios of IGROV-1 tumor-bearing mice 24 h after injection of [^{177}Lu]Lu-cm13 without pre-injection of PMX (blue) or with pre-injection of PMX 1 h before the radiofolate (yellow) or 1 h before and 3 h (green) or 7 h (red) after injection of the radiofolate. Statistically significant values are indicated with asterisks (* $p \leq 0.05$).

Tumor-to-liver ratios were in the same range for mice injected with [^{177}Lu]Lu-folate only and mice that received [^{177}Lu]Lu-folate combined with PMX, independent of which tumor xenograft (KB or IGROV-1) and time point (4 h p.i. or 24 h p.i.) was investigated and whether PMX was injected only once or twice.

3.3.2. In Vivo SPECT/CT Experiments

KB and IGROV-1 tumor-bearing mice were used for SPECT/CT imaging studies 4 h and 24 h after injection of the [^{177}Lu]Lu-folate only or [^{177}Lu]Lu-folate in combination with PMX which was injected before and after the radiofolate. Measurement of the whole mice immediately before the 4 h p.i.-scan revealed that 91–95% of the injected activity (non-decay corrected) was retained in the body independent on whether the mice received PMX. After 24 h, mice that received PMX showed lower activity retention in the body (~62% IA retained in the body, non-decay corrected) as compared to the mice which were injected only with the [^{177}Lu]Lu-folate (~70% IA retained in the body, non-decay corrected). These data were in line with increased excretion through the kidneys in mice injected with PMX.

SPECT/CT Imaging of KB Tumor-Bearing Mice. SPECT/CT scans of KB tumor-bearing mice 4 h and 24 h after injection of the [^{177}Lu]Lu-folate showed high uptake of activity in the tumor xenografts and accumulation of activity was also observed in the kidneys (Fig. 3.3). Based on a visual analysis, the tumor-to-kidney ratio was ~1 and did not change significantly over the time of investigation up to 24 h p.i.. In mice injected with PMX 1 h before the administration of the [^{177}Lu]Lu-folate, the tumor uptake was slightly increased, while retention of activity in the kidneys was reduced in comparison to the renal uptake observed in control mice. Background activity in blood circulation was reduced over time due to efficient blood clearance of the radiofolate. Other than that, the distribution profile of the radiofolate remained almost identical at 24 h p.i. in the mouse that received PMX a second time 7 h after radiofolate injection.

SPECT/CT Imaging of IGROV-1 Tumor-Bearing Mice. SPECT/CT studies were also performed with IGROV-1 tumor-bearing mice (Fig. 3.4). Activity in the blood pool and heart (background activity) was visible at 4 h p.i. but not anymore at later time points. In line with the biodistribution data, the uptake of the radiofolate was higher in IGROV-1 tumor xenografts than in KB tumor xenografts. Based on visual analysis of the images, the tumor-to-kidney ratios were > 1 at 4 h and 24 h after injection of the [^{177}Lu]Lu-folate. The favorable tissue distribution profile of the [^{177}Lu]Lu-folate observed in this model was further improved when mice received PMX before (and after) the radiofolate injection. Accumulation of activity in lymph nodes (in the armpit region and next to salivary glands) was more pronounced in IGROV-1 tumor-bearing mice than in mice with KB tumor xenografts.
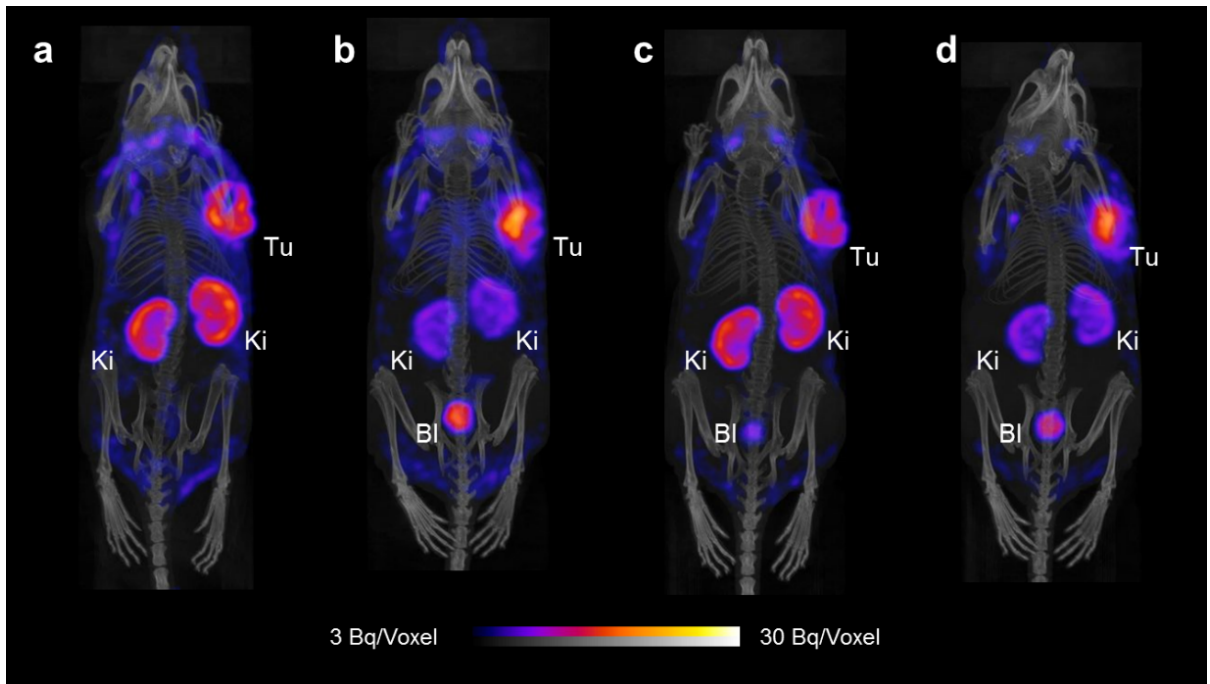
Fig. 3.3 SPECT/CT scans of tumor-bearing mice injected with [^{177}Lu]Lu-cm13 (25 MBq; 1 nmol) shown as maximum intensity projections (MIPs). (**a**) KB tumor-bearing mouse 4 h after injection of [^{177}Lu]Lu-cm13. (**b**) KB tumor-bearing mouse 4 h after injection of [^{177}Lu]Lu-cm13 with PMX injected 1 h before the radiofolate. (**c**) KB tumor-bearing mouse 24 h after injection of [^{177}Lu]Lu-cm13. (**d**) KB tumor-bearing mouse 24 h after injection of [^{177}Lu]Lu-cm13 with PMX injected 1 h before and 7 h after the radiofolate. (Tu = KB tumor; Ki = kidney; Bl = urinary bladder).
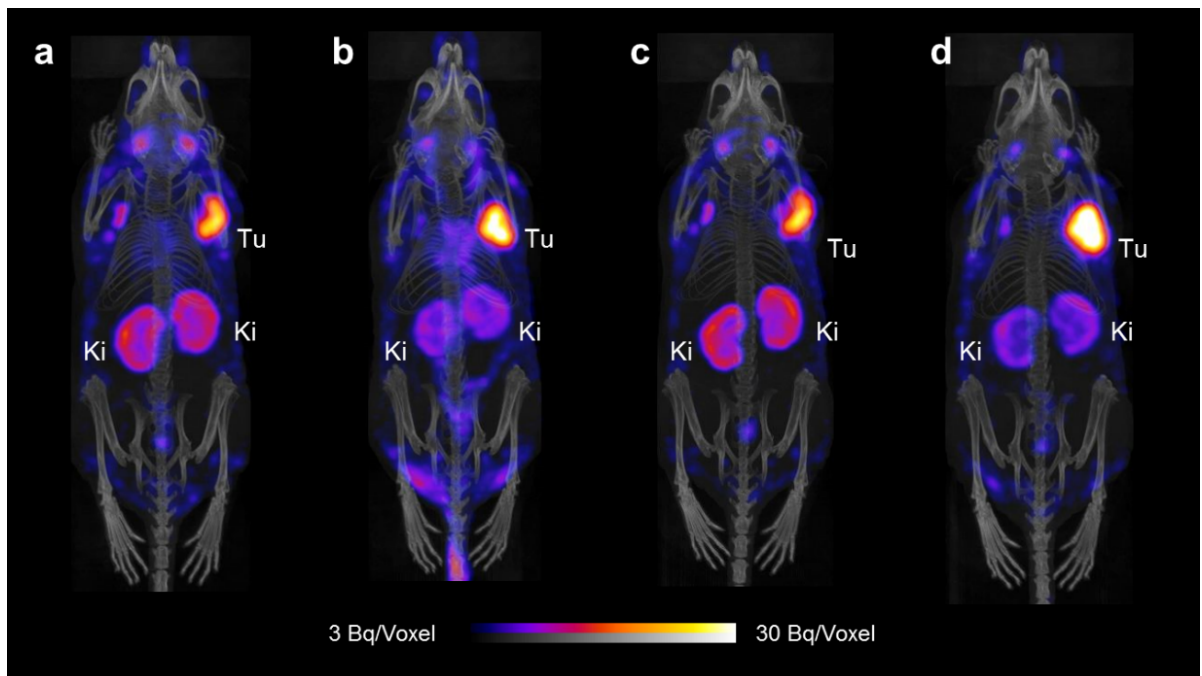
Fig. 3.4 SPECT/CT scans of tumor-bearing mice injected with [^{177}Lu]Lu-cm13 (25 MBq; 1 nmol) shown as maximum intensity projections (MIPs). (**a**) IGROV-1 tumor-bearing mouse 4 h after injection of [^{177}Lu]Lu-cm13. (**b**) IGROV-1 tumor-bearing mouse 4 h after injection of [^{177}Lu]Lu-cm13 with PMX injected 1 h before the radiofolate. (**c**) IGROV-1 tumor-bearing mouse 24 h after injection of [^{177}Lu]Lu-cm13. (**d**) IGROV-1 tumor-bearing mouse 24 h after injection of [^{177}Lu]Lu-cm13 with PMX injected 1 h before and 7 h after the radiofolate. (Tu = IGROV-1 tumor; Ki = kidney).

3.4. Discussion

In this study, we aimed at combining PMX with the currently most promising albumin-binding radiofolate ($[^{177}Lu]$Lu-cm13) in order to optimize the tumor-to-kidney ratios further. Our current results were in agreement with those of a preliminary experiment performed with KB tumor-bearing mice and $[^{177}Lu]$Lu-cm09, the first DOTA-folate conjugate developed in our group, which was outfitted with an albumin-binding entity (Supporting Information of [87]). Although PMX increased the tumor-to-kidney ratio of conventional folate conjugates 5- to 6-fold when injected 1 h prior to the radiofolate [80,85], it was revealed that the effect was much less pronounced when PMX was combined with $[^{177}Lu]$Lu-cm09 [87].

In this study, it was shown that PMX was able to increase the tumor-to-kidney ratio of the albumin-binding radiofolate by a factor of ~1.3 at 4 h p.i. and by a factor of 1.5–1.7 at 24 h p.i. in the KB tumor mouse model. The situation was similar in the IGROV-1 tumor model, in which PMX increased the ratio by a factor ~1.5 at 4 h p.i. and by a factor of 1.4–1.6 at 24 h p.i.. It was revealed that the distribution of the albumin-binding $[^{177}Lu]$Lu-folate benefited from an additional injection of PMX, 3 h or 7 h after the administration of the radiofolate, in order to further reduce the renal uptake and, therewith, increase the tumor-to-kidney ratios.

Even though the accumulation of $[^{177}Lu]$Lu-cm13 was clearly higher in IGROV-1 tumor xenografts than in KB tumors, the reported effect was consistent in both types of tumor mouse models. In the case of KB tumor mice the tumor-to-kidney ratios were in the range of ~1.0 when PMX was used whereas these ratios reached values of up to ~1.8 in the case of IGROV-1 tumor-bearing mice.

When performing this study, it was observed that there were inter-individual differences with regard to the tissue distribution of $[^{177}Lu]$Lu-folate. The absolute uptake values determined in this study were also different from previously published values, however, the tumor-to-background ratios were in the same range [90]. The effect of PMX was not exactly the same in each mouse, hence, the interaction between the two drugs appeared to be very sensitive and possibly dependent on other factors.

As already observed in previous studies, the effect of PMX is critically dependent on the time of pre-injection and injected quantity as well as on the amount of injected folate conjugate [84,87]. It is, thus, not surprising that the effect of PMX was less pronounced when combined with long-circulating radiofolates. The albumin-bound fraction of folate radioconjugates is not excreted since albumin is a large protein (>60 kDa) that cannot readily be filtered in the kidneys. Hence, only the free fraction of radiofolates (not bound to albumin) may be affected by pre-injected PMX. Most probably, PMX was excreted already when a major fraction of the radiofolate was still circulating in the blood due to albumin-binding. The fact that repeated injection of PMX was favorable to reduce renal uptake supported the hypothesis that the fast pharmacokinetics of PMX is responsible for the only moderate effect on the distribution profile of the radiofolate. A more sophisticated scheme of PMX application using repeated injections or a slow infusion over the first hours may be successful to reduce renal uptake

of albumin-binding radiofolates more effectively. This would, however, be difficult to realize in a clinical setting given the fact that PMX is a chemotherapeutic agent, hence, potentially toxic to the patient and not easily up-scalable.

3.5.   Conclusion

In this study, the combination of a "chemical approach", which refers to the radioligand modification with an albumin binder, and a "pharmacological approach" referring to the pre-injection of PMX, was investigated with the aim to further improve the tumor-to-kidney ratio of accumulated activity in tumor-bearing mice. This combination led to the best tissue distribution profiles ever obtained with radiometal-based folate conjugates so far. A clinical translation of this approach would be challenging, however, particularly when PMX had to be applied at a dose that induces pharmacological/chemotherapeutic effects.

IV. Preclinical Evaluation of 5-Methyltetrahydrofolate-Based Radioconjugates – New Perspectives for Folate Receptor-Targeted Radionuclide Therapy

Patrycja Guzik[1], Martina Benešová[1,2], Magdalena Ratz[1], Josep M. Monné Rodríguez[3], Luisa M. Deberle[2], Roger Schibli[1,2], Cristina Müller*[,1,2]

[1] *Center for Radiopharmaceutical Sciences ETH-PSI-USZ, Paul Scherrer Institute, Villigen-PSI, Switzerland*

[2] *Department of Chemistry and Applied Biosciences, ETH Zurich, Zurich, Switzerland*

[3] *Laboratory for Animal Model Pathology (LAMP), Institute of Veterinary Pathology, Vetsuisse Faculty, University of Zurich, Zurich, Switzerland*

Author Contributions:

Patrycja Guzik performed the experiments, analyzed and interpreted the data, and wrote the manuscript. Martina Benešová synthesized the conjugates and reviewed the manuscript. Magdalena Ratz synthesized the conjugates and contributed to the in vitro experiments. Josep M. Monné Rodríguez performed histological analysis and interpreted the histology data. Luisa M. Deberle contributed to the synthesis of the conjugates and writing of the manuscript. Roger Schibli reviewed the final manuscript. Cristina Müller supervised the study, contributed to the writing of the manuscript and reviewed the final version.

4.1. Introduction

Targeted radionuclide therapy emerged as a promising concept for the palliative treatment of metastasized cancer using β^--particle-emitting radionuclides in combination with a specific tumor-targeting agent [149,150]. The experience made with somatostatin receptor-targeted radiopeptides (e.g. [177Lu]Lu-DOTATATE [151,152]) and prostate-specific membrane antigen (PSMA)-targeted radioligands (e.g. [177Lu]Lu-PSMA-617 [153,154]) is encouraging to further explore suitable targets and develop radiopharmaceuticals to enable the treatment of additional tumor types.

The folate receptor (FR) is a membrane-anchored glycoprotein, which is overexpressed in gynecological and other tumor types, including lung, breast and colon cancer [39,122,155]. Folic acid radioconjugates have been translated to clinics for nuclear imaging of FR-positive tumors [58,130], however, their therapeutic exploitation remains challenging. The relatively low tumor-to-kidney ratio of accumulated folate radioconjugates would limit the applicable quantity of activity in order to prevent the risk of damage to the kidneys [63].

The high renal uptake of folate-based radiopharmaceuticals has been addressed with various strategies [36], including pharmacological interactions [80,81,83]. A major step forward was achieved by introducing an albumin-binding entity into the structure of radiofolates to prolong their blood circulation [87,90]. The resulting radioconjugates revealed significantly increased tumor uptake and improved tumor-to-kidney ratios, which enabled their use in preclinical therapy studies in mice [79,87]. The therapeutic effects of this approach were promising, however, the kidneys remained the dose-limiting organ.

Recently, Boss et al. reported on results obtained with a novel class of [18F]-based radiotracers, in which folic acid (oxidized version of folate) was exchanged with the two stereoisomers (6R and 6S, respectively) of 5-methyltetrahydrofolate (5-MTHF) [77,156]. It was found that 6R-[18F]Aza-5-MTHF as well as 6S-[18F]Aza-5-MTHF accumulated to a significantly higher extent in the tumor tissue than [18F]-labeled aza-folic acid ([18F]AzaFol), in which folic acid was employed as a targeting agent [77]. Importantly, the 6R-[18F]Aza-5-MTHF isomer was cleared much more effectively through the kidneys as compared to [18F]AzaFol.

Thus, the aim of this study was to translate the concept of using 5-MTHF as a targeting agent to albumin-binding DOTA-conjugates in order to increase the tumor uptake and possibly reduce renal retention of activity. 6R-RedFol-1 and 6S-RedFol-1, based on 6R-5-MTHF and 6S-5-MTHF, respectively, were designed as structural equivalents to the previously developed albumin-binding DOTA-folate conjugate (cm10, herein referred to as OxFol-1 [90]) (Fig. 4.1). 6R-RedFol-1 and 6S-RedFol-1 were labeled with 177Lu and evaluated in vitro and in vivo for comparison of their characteristics with those of [177Lu]Lu-OxFol-1 [90]. Therapy studies with KB tumor-bearing mice were performed in order to compare the therapeutic effect of the more promising [177Lu]Lu-RedFol-1 isomer, with [177Lu]Lu-OxFol-1.
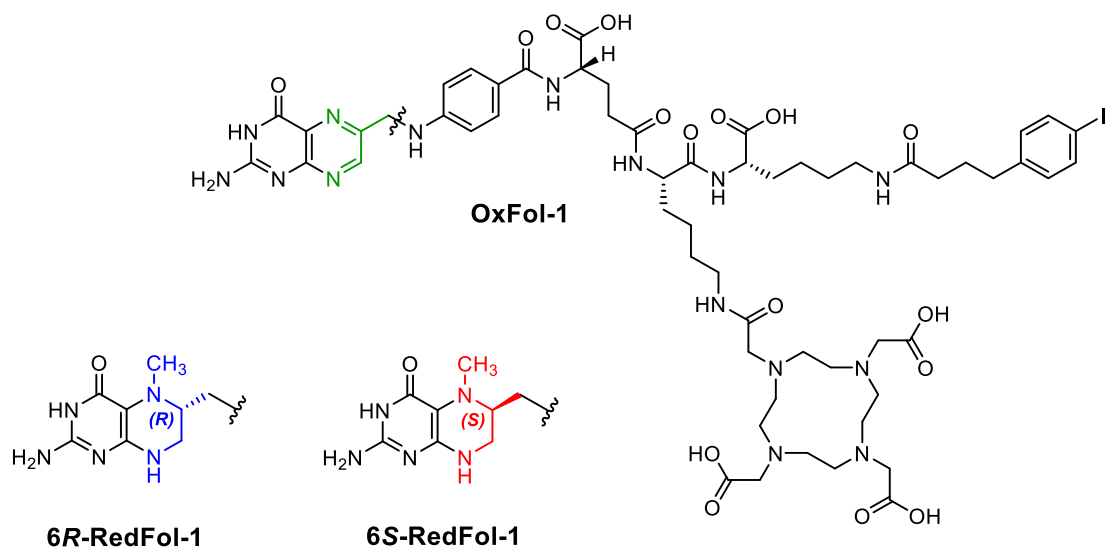
Fig. 4.1 Chemical structure of OxFol-1 (green), 6*R*-RedFol-1 (blue) and 6*S*-RedFol-1 (red)

4.2. Materials & Methods

4.2.1. Radiolabeling and Quality Control of the Folate Radioconjugates

The synthesis of 6*R*-RedFol-1 and 6*S*-RedFol-1 will be published elsewhere. OxFol-1 (previously referred to as cm10) was employed in previous preclinical studies [36,157]. The radiolabeling of the folate conjugates with ^{177}Lu ($T_{1/2}$ = 6.65 days, $E\beta^{-}_{av}$ = 134 keV, $E\gamma$ = 113 keV, 208 keV) was performed at pH ~4.5 using no-carrier-added ^{177}Lu ([^{177}Lu]LuCl$_3$ in HCl 0.04 M; ITM Medical Isotopes GmbH, Germany). In brief, ^{177}Lu was added to a mixture of HCl (0.05 M) and Na-acetate (0.5 M, pH 8) containing the respective folate conjugate to obtain molar activities of 10–50 MBq/nmol. L-Ascorbic acid (6 mg) was added to the labeling mixture of 6*R*-RedFol-1 and 6*S*-RedFol-1 to prevent oxidation. The reaction mixture was incubated at 95 °C for 15 min. The radiolabeling of OxFol-1 was performed as previously reported without addition of L-ascorbic acid [90]. Quality control of the radiolabeled folate conjugates, diluted in MilliQ water containing sodium diethylenetriamine pentaacetic acid (Na-DTPA; 50 µM), was performed with a Merck Hitachi LaChrom HPLC system, equipped with a D-7000 interface, a L-7200 autosampler, a radiation detector (LB 506 B from Berthold) and a L-7100 pump connected with a reversed-phase C18 column (5 µm, 150×4.6 mm, Xterra^{TM}, MS, Waters, U.S.A). The mobile phase consisted of 0.1% trifluoroacetic acid in MilliQ water (A) and acetonitrile (B) using a linear gradient of solvent A (95–20% over 15 min) in solvent B at a flow rate of 1 mL/min.

4.2.2. In Vitro Stability of Folate Radioconjugates in PBS

The stability of the folate radioconjugates was determined to assess the period in which they could be used for experiments. After the quality control was performed using HPLC (t = 0), the labeling solutions of [^{177}Lu]Lu-6*R*-RedFol-1 and [^{177}Lu]Lu-6*S*-RedFol-1 (50 MBq/nmol) were diluted with phosphate-buffered saline (PBS) pH 7.4 to obtain an activity concentration of 100 MBq/500 µL. Sodium acetate (130 µL, 0.5 M, pH 8) was added to the sample to maintain a neutral pH value. The integrity of the folate radioconjugates was determined by HPLC over a period of 24 h. The HPLC chromatograms were analyzed by determination of the peak area of the radiolabeled product, the released ^{177}Lu as well as degradation products of unknown structure. The quantity of the intact product was expressed as percentage of the sum of integrated peak areas of the entire chromatogram and set into relation to the original value determined at t = 0, which was set as 100%.

4.2.3. In Vitro Stability of Folate Radioconjugates in Human Plasma

Investigation of plasma stability was performed for quantitative analysis of intact folate radioconjugates and potential radiometabolites formed in the plasma. Radiolabeling of folate conjugates was performed according to the same procedure as described for the stability experiments in PBS. Quality control of the radiolabeled folate conjugates was performed as described above, however, the HPLC program was adapted. The mobile phase consisted of 0.1% trifluoroacetic acid in MilliQ water (A) and acetonitrile (B) using a linear gradient of solvent A (95–50%) and solvent B (5–50%) over 35 min at a flow rate of

0.8 mL/min. After dilution of radioconjugates to 30 MBq/500 µL in PBS 7.4, a sample of 50 µL was mixed with 250 µL human plasma (Stiftung Blutspende SRK Aargau-Solothurn, Switzerland) and incubated at 37 °C. After 4 h and 24 h of incubation, a sample of 50 µL was mixed with 150 µL cold methanol containing ammonium hydroxide (0.025%) and 2-mercaptoethanol (10 mg/mL) for precipitation of the proteins. After centrifugation (4 °C, 3 min, 8000 rpm), the supernatant was collected and centrifuged for a second time. After filtration of the supernatant through a polytetrafluoroethylene membrane filter (0.2 µm), the samples were injected into HPLC. The chromatograms were analyzed by determination of the peak area of the radiolabeled product, the released ^{177}Lu as well as degradation products of unknown structure. The quantity of the intact product was expressed as percentage of the sum of integrated peak areas of the entire chromatogram and set into relation to the original value determined for the quality control, which was set as 100%.

4.2.4.   Determination of LogD Values

Distribution coefficients (logD values) of the folate radioconjugates were determined by a shake-flask method using n-octanol and PBS pH 7.4 followed by phase separation, as previously reported [90]. In brief, the folate conjugates were labeled at a molar activity of 50 MBq/nmol. A sample of each folate radioconjugate (~0.5 MBq, 25 µL) was mixed with 1475 µL PBS pH 7.4 and 1500 µL n-octanol. The vials were vortexed vigorously for 1 min and then centrifuged (2500 rpm) for 6 min for phase separation. The activity concentration in a defined volume of each layer was measured in a γ-counter (Perkin Elmer, Wallac Wizard 1480). The distribution coefficients were calculated as the logarithm of the ratio of counts per minute (cpm) measured in the n-octanol phase relative to the cpm measured in the PBS pH 7.4 phase. The results were reported as mean ± standard deviation (SD) of the data obtained from three to five independent experiments, each performed with five replicates.

4.2.5.   Binding Affinity to Mouse and Human Plasma Proteins

To compare the plasma protein-binding properties of the folate radioconjugates, the percentage of the fraction bound to mouse and human plasma proteins was determined at variable plasma dilutions calculated as [albumin]-to-[radioconjugate] molar ratios. Determination of the binding affinity was performed by measuring the free fraction of the radioconjugate separated from the albumin-bound fraction using an ultrafiltration method as previously reported [158]. The amount of albumin in mouse plasma (Rockland, USA) and human plasma (Stiftung Blutspende SRK Aargau-Solothurn, Switzerland) was determined using a dry chemistry analyzer (DRI-CHEM 4000i, FUJIFILM, Japan) and was found to be 550 µM and 850 µM, respectively. An aliquot of the diluted radioconjugate (~500 kBq, 25 µL, 0.01 nmol) was mixed with diluted plasma in molar ratios of mouse serum albumin (MSA)-to-folate conjugate or human serum album (HSA)-to-folate conjugate in the range of 0.01–21250. The highest molar ratio represented the situation of the radioligand in undiluted plasma. Afterwards, samples were incubated for 30 min at 37 °C. Aliquots of the samples were loaded to the ultrafiltration device

(Centrifree ultrafiltration devices; 30000 Da nominal molecular weight limit, methyl-cellulose micropartition membranes, Millipore) and centrifuged at 800 rcf for 40 min at 20 °C. The activity in the filtrate as well as aliquots of the incubation solutions were measured in a γ-counter (Perkin Elmer, Wallac Wizard 1480). The albumin-bound fraction was calculated based on the measurement of the filtrates, which corresponded to the free fractions, and was expressed as the percentage of total added activity, which was set to 100%. In a control experiment, the $[^{177}Lu]$Lu-folate conjugates were filtered after incubation in PBS instead of plasma. In this case, the majority of activity (>90%) was found in the filtered fraction indicating that the unbound folate radioconjugates were readily filtered through the membrane. The results were presented as average ± SD of three independent experiments. The data were fitted to a semi-logarithmic plot using non-linear regression (one-site, specific binding) to obtain the half maximum binding (B_{50}) using GraphPad Prism software (version 7.0). The B_{50} value of $[^{177}Lu]$Lu-OxFol-1 was set to 1.0. The inverse ratio of the B_{50} of $[^{177}Lu]$Lu-6R-RedFol-1 and $[^{177}Lu]$Lu-6S-RedFol-1 was calculated to allow the comparison of the relative binding affinity of each radioconjugate.

4.2.6. Tumor Cell Culture and Cell Uptake Studies

KB tumor cells (cervical carcinoma cell line, subclone of HeLa cells, ACC-136) were purchased from the German Collection of Microorganisms and Cell Cultures (DSMZ, Germany). Cells were cultured in folate-deficient RPMI medium (FFRPMI, Cell Culture Technologies GmbH, Gravesano, Switzerland) supplemented with 10% fetal calf serum, L-glutamine and antibiotics.

Cellular uptake and internalization studies were performed with all folate radioconjugates according to a previously published procedure [90]. In brief, KB tumor cells were seeded in 12-well plates (0.7×10^6 cells in 2 mL folate-free RPMI (FFRPMI) medium/well) allowing cell adhesion and growth overnight at 37 °C and 5% CO_2. After removal of the supernatant, cells were washed with PBS prior to the addition of FFRPMI medium without supplements (975 µL/well). The $[^{177}Lu]$Lu-folate conjugates (50 MBq/nmol) were added to each well in a volume of 25 µL (0.75 pmol, 38 kBq). In some wells, tumor cells were co-incubated with excess folic acid (100 µM) to block FRs on the cell surface. After incubation of the well plates for 2 h or 4 h at 37 °C and 5% CO_2, cells were washed three times with ice-cold PBS to determine total uptake of the folate radioconjugates. In order to assess the internalized fraction, a stripping buffer (aqueous solution of 0.1 M acetic acid and 0.15 M NaCl, pH 3) was applied to release FR-bound folate radioconjugates from the cell surface. Cell samples were lysed by addition of NaOH (1 M, 1 mL) to each well. The radioactive cell lysates were measured in a γ-counter (Perkin Elmer, Wallac Wizard 1480). After homogenization of the cell suspensions by vortexing, the concentration of proteins was determined for each sample by a Micro BCA Protein Assay kit (Pierce, Thermo Scientific) in order to standardize measured activity to the average content of protein (~0.2 mg) in a single well. The results were expressed as percentage of total added activity and presented as average ± SD of 3–6 independent experiments performed in triplicate.

4.2.7. In Vivo Studies

All applicable international, national, and/or institutional guidelines for the care and use of animals were followed. In particular, all animal experiments were carried out according to the guidelines of Swiss Regulations for Animal Welfare. The preclinical studies have been ethically approved by the Cantonal Committee of Animal Experimentation and permitted by the responsible cantonal authorities. Five- to six-week-old female, athymic nude mice (CD-1 Foxn-1/nu) were purchased from Charles River Laboratories (Sulzfeld, Germany) and fed with a folate-deficient rodent diet (ssniff Spezialdiäten GmbH; Soest, Germany). Mice were subcutaneously inoculated with KB tumor cells (5×10^6 cells in 100 µL PBS) on both shoulders for biodistribution and imaging studies or with KB tumor cells (4.5×10^6 cells in 100 µL PBS) on the right shoulder for the therapy study.

4.2.8. In Vivo Stability of Folate Radioconjugates in Blood Plasma

Investigation of plasma stability was performed for determination of intact folate radioconjugates and potential radiometabolites formed in the blood plasma of mice. Radiolabeling of folate conjugates and quality control were performed according to the same procedure as for the in vitro stability experiments. [^{177}Lu]Lu-6*R*-RedFol-1, [^{177}Lu]Lu-6*S*-RedFol-1 and [^{177}Lu]Lu-OxFol-1 were diluted in PBS pH 7.4 containing 0.05% BSA (25 MBq, 0.5 nmol, 100 µL) and injected into CD-1 Foxn-1/nu mice (Charles River) without tumors (n=2). Blood was drawn from the retrobulbar vein under anesthesia 4 h after injection of the respective folate radioconjugate followed by immediate euthanasia of the mouse. Blood samples were centrifuged (4 °C, 20 min, 1600 rpm) to allow collecting blood plasma. A volume of 450 µL cold methanol containing ammonium hydroxide (0.025%) and 2-mercaptoethanol (10 mg/mL) was added to 150 µL plasma for precipitation of the proteins. After centrifugation (4 °C, 3 min, 8000 rpm), the supernatant was collected and centrifuged for a second time. After filtration of the supernatant through a polytetrafluoroethylene membrane filter (0.2 µm) the samples were injected into HPLC and the chromatograms analyzed in the same way as described for in vitro stability experiments.

4.2.9. Biodistribution Studies

Biodistribution studies were performed 10–14 days after tumor cell inoculation when the tumor size reached a volume of ~300 mm^3. Mice (n=4) were injected into a lateral tail vein with the respective folate radioconjugate (3 MBq, 0.5 nmol, 100 µL) diluted in PBS containing 0.05% bovine serum albumin (BSA). The animals were sacrificed at various time points up to 120 h after administration of the radioconjugates. Additional mice (n = 3) were injected with excess folic acid (100 µg/100 µL PBS pH 7.4) ~5 min prior to the folate radioconjugates and sacrificed 1 h later. Selected tissues and organs were collected, weighed, and counted using a γ-counter (Perkin Elmer, Wallac Wizard 1480). The results were listed as a percentage of the injected activity per gram of tissue mass (% IA/g), using counts of a defined volume of the original injection solution measured at the same time resulting in decay corrected values.

4.2.10. Determination of Areas Under the Curve

Biodistribution data were converted to non-decay-corrected values to obtain the time-dependent curves of accumulated activity in the tumor xenografts, blood, kidneys and liver. The data points were used to calculate the areas under the curves (AUC) using GraphPad Prism (version 7.0) as previously reported [90]. The $AUC_{0\rightarrow120h}$ values of the [^{177}Lu]Lu-OxFol-1 were set to 1.0 to determine the relative values of [^{177}Lu]Lu-6R-RedFol-1 and [^{177}Lu]Lu-6S-RedFol-1, respectively.

4.2.11. SPECT/CT Imaging Studies

Imaging studies were performed using a four-head, multiplexing, multipinhole small-animal SPECT camera (NanoSPECT/CT™, Mediso Medical Imaging Systems, Budapest, Hungary) as previously reported [90]. Each head was outfitted with a tungsten-based aperture of nine 1.4 mm-diameter pinholes and a thickness of 10 mm. The SPECT/CT images were acquired at 4 h and 24 h after injection of respective radioconjugate. CT scans of 7.5 min duration were followed by SPECT scans of ~40 min acquisition time. The images were acquired using Nucline Software (version 1.02, Mediso Ltd., Budapest, Hungary). The real-time CT reconstruction used a cone-beam filtered backprojection. The reconstruction of SPECT data was performed with HiSPECT software (version 1.4.3049, Scivis GmbH, Göttingen, Germany) using γ-energies of 56.1 keV (± 10%), 112.9 keV (± 10%) and 208.4 keV (± 10%) for ^{177}Lu. Images were prepared using VivoQuant post-processing software (version 3.5, inviCRO Imaging Services and Software, Boston, U.S.). A Gauss post-reconstruction filter (FWHM = 1 mm) was applied and the scale of activity was set as indicated on the images (minimum value = 2.5 Bq/voxel to maximum value = 50 Bq/voxel).

To visualize and compare the distribution of [^{177}Lu]Lu-6R-RedFol-1, [^{177}Lu]Lu-6S-RedFol-1 and [^{177}Lu]Lu-OxFol-1, KB tumor-bearing CD1 nude mice were injected in tail vein with 25 MBq/0.5 nmol/100 μL of respective radioconjugate diluted in PBS containing 0.05% BSA. SPECT/CT imaging studies to demonstrate the ability to block uptake of the folate radioconjugates in FR-positive tissues were performed with KB tumor-bearing mice (n=2). These mice were pre-injected with excess folic acid (100 μg) or excess non-labeled albumin-binding folate, cm13 [90], and scanned at 4 h and 24 h after injection of the radioconjugate. An additional KB tumor-bearing mouse was injected with equal amounts of [^{177}Lu]Lu-DOTA-PPB-01, a radioligand consisting of the p-iodophenyl-based albumin binder and a DOTA-chelator [159], in order to demonstrate the FR-unrelated accumulation of activity in tumors.

4.2.12. Therapy Study

Mice were randomly assigned to five groups consisting of 6–9 animals 4 days after tumor cell inoculation when tumors reached an average size of 60–100 mm³. The mice were injected with vehicle only (Group A: PBS with 0.05% BSA; control), 10 MBq [^{177}Lu]Lu-6R-RedFol-1 (Group B) or 10 MBq [^{177}Lu]Lu-OxFol-1 (Group C) at an amount of 0.5 nmol folate conjugate. Additional groups of mice

were injected with 15 MBq [^{177}Lu]Lu-6R-RedFol-1 (Group D) or 15 MBq [^{177}Lu]Lu-OxFol-1 (Group E) at an amount of 0.5 nmol folate conjugate (Table 4.1). The relative body weight (RBW) was defined as [BW$_x$/ BW$_0$], where BW$_x$ is the body weight in gram at a given Day x and BW$_0$ the body weight in gram at Day 0. The tumor dimensions were determined by measuring the longest tumor axis (L) and its perpendicular axis (W) with a digital caliper. The tumor volume (TV) was calculated according to the equation [TV = 0.5 × (L × W^2)]. The relative tumor volume (RTV) was defined as [TV$_x$/TV$_0$], where TV$_x$ is the tumor volume in mm^3 at a given Day x and TV$_0$ the tumor volume in mm^3 at Day 0. Endpoint criteria were defined as (i) a tumor volume of ≥1000 mm^3, (ii) loss of ≥15% of initial body weight, (iii) a combination of a tumor size of ≥800 mm^3 and body weight loss of ≥10% and/or (iv) ulceration of the tumor and/or (v) abnormal behavior, indicating pain or unease. Mice were removed from the study and euthanized when an endpoint was reached.

Table 4.1 Design of the therapy study including the average tumor volumes and body weights of mice at therapy start

Group	Treatment	Number of mice	Injected activity and molar amount	Tumor volume[2] (mm^3) (average ± SD) Day 0	Body weight (g) (average ± SD) Day 0
A	Vehicle[1]	9	–	84 ± 24	23.7 ± 2.7
B	[^{177}Lu]Lu-6R-RedFol-1	6	10 MBq, 0.5 nmol	66 ± 8	24.6 ± 1.2
C	[^{177}Lu]Lu-OxFol-1	6	10 MBq, 0.5 nmol	69 ± 22	24.9 ± 1.2
D	[^{177}Lu]Lu-6R-RedFol-1	6	15 MBq, 0.5 nmol	99 ± 33	20.0 ± 0.8[3]
E	[^{177}Lu]Lu-OxFol-1	6	15 MBq, 0.5 nmol	95 ± 20	20.9 ± 1.2[3]

[1] Vehicle: 0.05% BSA in PBS
[2] No significant differences determined between the tumor volumes measured for each group ($p > 0.05$);
[3] Significantly lower body weights compared to mice of groups A, B and C.

4.2.13. Assessment of the Therapy Study

The efficacy of the radionuclide therapy was assessed by determination of the tumor growth delay (TGD$_x$), which was calculated as the time required for the tumor volume to increase x-fold over the initial volume at Day 0. The tumor growth delay indices [TGDI$_x$ = TGD$_x$(T)/TGD$_x$(C)] were calculated as the TGD$_x$ ratio of treated mice (T) over control mice (C) for a 2-fold (x = 2, TGD$_2$), 5-fold (x = 5, TGD$_5$) and 8-fold (x = 8, TGD$_8$) increase of the initial tumor volume. The percentage of tumor growth inhibition (TGI) was calculated as [100 – (RTV$_T$/RTV$_C$ × 100)] where RTV$_T$ is a relative tumor volume of treated mice at Day 14, when the first mouse of the control group (Group A) reached the endpoint and the average relative tumor volume of control mice was RTV$_C$.

The average of relative body weights of mice from each group were compared to that of control mice at Day 14 and at the endpoint. Blood plasma parameters were determined once an endpoint was reached or at the end of the study. Immediately before euthanasia of the mice, blood was sampled from the retrobulbar vein. The values of creatinine (CRE), blood urea nitrogen (BUN), alkaline phosphatase

(ALP), total bilirubin (TBIL) and albumin (ALB) were determined in the plasma after centrifugation of the blood using a dry chemistry analyzer (DRI-CHEM 4000i, FUJIFILM, Japan). After euthanasia, kidneys, liver, spleen and brain were collected and weighed. The organ mass-to-brain ratios were calculated using the organ masses collected at the day of euthanasia.

A full macroscopic examination was performed in each animal and kidneys, bone marrow (sternum and femur) and spleen were sampled for histological assessment as previously reported [160,161]. In brief, the collected organs and tissues were fixed in 4% neutral-buffered formalin and routinely embedded in paraffin wax. Formalin fixed sternum and femur were decalcified at room temperature in an ethylenediaminetetraacetic acid (EDTA)-citrate solution for 48 h before embedding in paraffin wax. Sections of 3–5 μm thickness were prepared on glass slides and routinely stained with hematoxylin eosin (HE). Histological lesions were semi-quantitatively scored by a veterinary pathologist in a blind manner using a severity grading scheme that ranged from 0 to 5.

4.2.14. Statistical Analysis

Binding affinity to plasma proteins was statistically analyzed using one-way ANOVA with Dunnett's multiple comparisons post-test. Analyses of biodistribution data and the absolute $AUC_{0 \to 120h}$ values were performed with two-way or one-way ANOVA with Tukey's multiple comparisons post-test. The therapy study was analyzed for significance using a one-way ANOVA with Tukey's or Dunnett's test. Survival of mice was assessed using Kaplan-Meier curves to determine median survival of mice of each group. All analyses were performed using GraphPad Prism program (version 7.0). A p-value of <0.05 was considered statistically significant.

4.3. Results

4.3.1. Radiolabeling and Quality Control of Folate Radioconjugates

Radiolabeling with ^{177}Lu was readily achieved to obtain the folate radioconjugates at a radiochemical purity of >99% (Fig. 4.2). The HPLC retention times were equal for all three folate radioconjugates (Fig. 4.2). The radiofolates were used for in vitro and in vivo experiments without further purification.
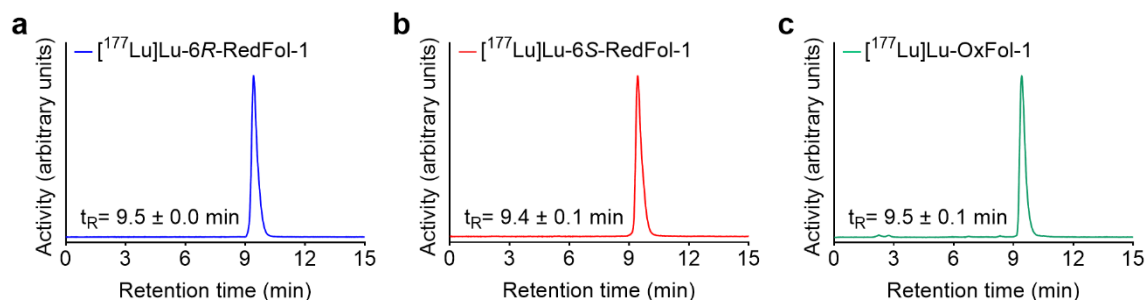
Fig. 4.2 Representative chromatograms obtained after radiolabeling of 6*R*-RedFol-1, 6*S*-RedFol-1 and OxFol-1 with ^{177}Lu. (**a**) [^{177}Lu]Lu-6*R*-RedFol-1; (**b**) [^{177}Lu]Lu-6*S*-RedFol-1; (**c**) [^{177}Lu]Lu-OxFol-1. (Retention times (t_R) are indicated as the average ± standard deviation (SD), n = 6). The presence of uncoordinated ^{177}Lu detected as [^{177}Lu]Lu-DTPA would appear with $t_R = 2.4 ± 0.2$ min.

4.3.2. In Vitro Stability and LogD Values of [^{177}Lu]Lu-Folate Conjugates

All folate radioconjugates were stable in PBS at room temperature (>97% intact radioconjugates) over 24 h (Supplementary Material of [162]). High stability was also determined after incubation of the folate radioconjugates in human plasma (≥98% intact radioconjugates) over 24 h at 37 °C. The logD values of [^{177}Lu]Lu-6*R*-RedFol-1 (–3.92 ± 0.11) and [^{177}Lu]Lu-6*S*-RedFol-1 (–3.70 ± 0.10) were slightly higher than the logD value of [^{177}Lu]Lu-OxFol-1 (–4.21 ± 0.14).

4.3.3. Binding Affinity to Mouse and Human Plasma Proteins

At a physiological albumin concentration, represented by the highest [mouse serum albumin (MSA)]-to-[radioconjugate] molar ratio used in this study, ~93% of [^{177}Lu]Lu-6*R*-RedFol-1 and [^{177}Lu]Lu-6*S*-RedFol-1, were bound to plasma proteins (Fig. 4.3a). Under the same experimental conditions, the plasma-bound fraction of [^{177}Lu]Lu-OxFol-1 was slightly lower (~90%). The binding at the corresponding molar ratio of human serum albumin (HSA) was higher for all three radioconjugates, but in analogy to the results obtained with MSA, [^{177}Lu]Lu-6*R*-RedFol-1 and [^{177}Lu]Lu-6*S*-RedFol-1 showed slightly stronger binding (97– 99%) than [^{177}Lu]Lu-OxFol-1 (~94%) (Fig. 4.3b). The values of a 50% binding in mouse plasma (B_{50}; determined by a semi-log plots) were in the same range for [^{177}Lu]Lu-6*R*-RedFol-1 (614 ± 129) and [^{177}Lu]Lu-6*S*-RedFol-1 (627 ± 172), but slightly higher for [^{177}Lu]Lu-OxFol-1 (747 ± 252) (Fig. 4.3a) resulting in a relative affinity of 1.2 for both [^{177}Lu]Lu-6*R*-RedFol-1 and [^{177}Lu]Lu-6*S*-RedFol-1, as compared to [^{177}Lu]Lu-OxFol-1 which was set as 1.0. The B_{50} values obtained in human plasma were considerably lower resulting in a [HSA]-to-[radioconjugate] molar ratios of 149 ± 26 for [^{177}Lu]Lu-6*R*-RedFol-1, 184 ± 51 for [^{177}Lu]Lu-6*S*-RedFol-1 and 211 ± 39

for [^{177}Lu]Lu-OxFol-1 (Fig. 4.3b). This meant relative affinities of 1.4 and 1.2 for [^{177}Lu]Lu-6*R*-RedFol-1 and [^{177}Lu]Lu-6*S*-RedFol-1, respectively.
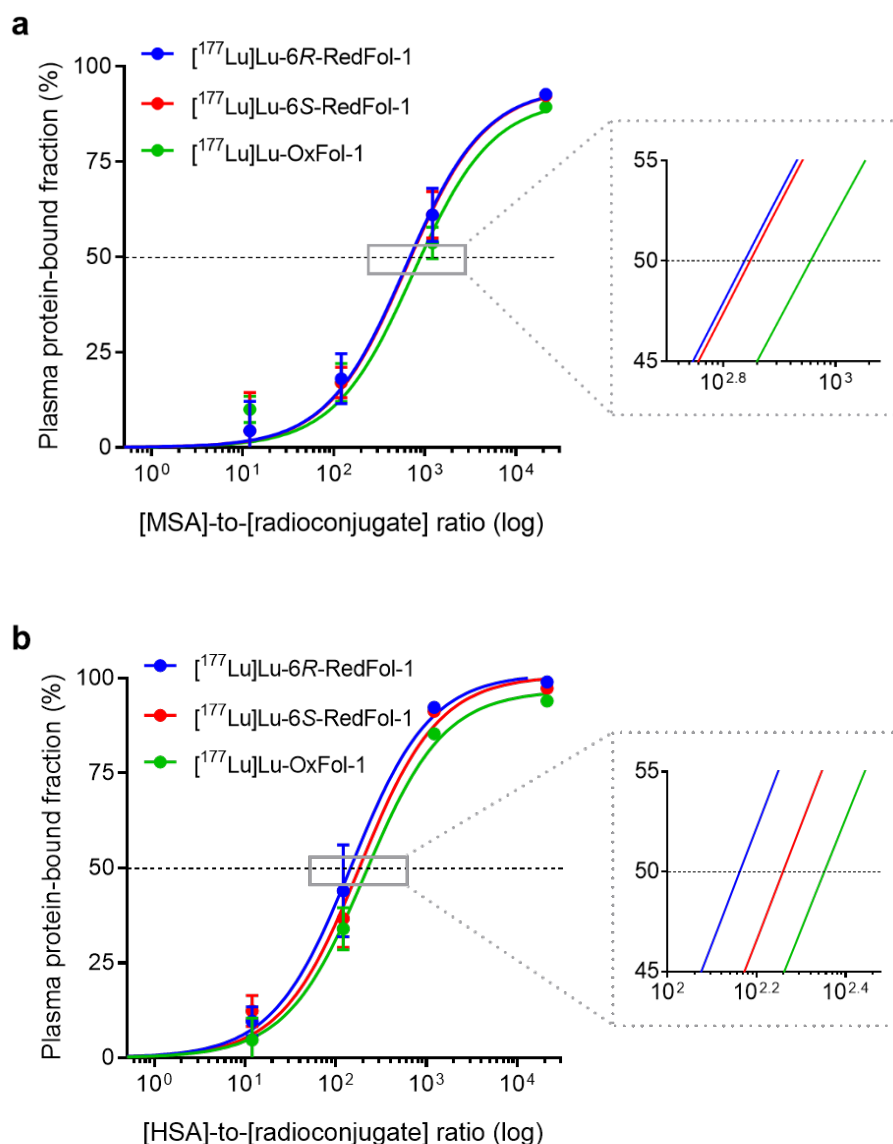
Fig. 4.3 Plasma protein-binding curves of the folate radioconjugates. (**a**) Affinity curves obtained in mouse plasma; (**b**) Affinity curves obtained in human plasma. The plasma was diluted to defined molar ratios of mouse or human albumin-to-folate radioconjugate. (MSA = mouse serum albumin; HSA = human serum albumin).

4.3.4. Cell Uptake and Internalization Studies

In vitro studies with KB tumor cells that express the FR revealed a trend of higher uptake of [^{177}Lu]Lu-6*R*-RedFol-1 (28–30%) and [^{177}Lu]Lu-6*S*-RedFol-1 (42–53%) than for [^{177}Lu]Lu-OxFol-1 (20–26%) (Fig. 4.4a). The internalized fraction of [^{177}Lu]Lu-6*R*-RedFol-1 (14–15%) and [^{177}Lu]Lu-6*S*-RedFol-1 (14–19%) were also increased as compared to the internalized fraction of [^{177}Lu]Lu-OxFol-1 (10–11%) (Fig. 4.4b). Co-incubation of KB tumor cells with excess of folic acid to block FRs reduced the uptake to <0.1%, indicating FR-specific uptake of all investigated folate radioconjugates (Fig. 4.4c).
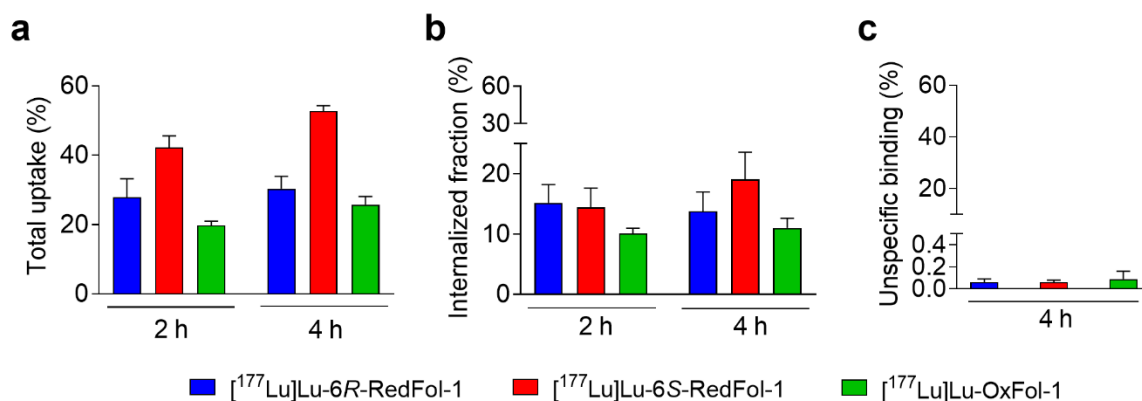
Fig. 4.4 Results of the in vitro tumor cell uptake of $[^{177}Lu]Lu$-6*R*-RedFol-1, $[^{177}Lu]Lu$-6*S*-RedFol-1 and $[^{177}Lu]Lu$-OxFol-1 in KB tumor cells after 2 h and 4 h of incubation at 37 ºC. (**a**) Tumor cell uptake; (**b**) Internalized fraction; (**c**) Unspecific binding.

4.3.5. In Vivo Stability of Folate Radioconjugates

In vivo stability studies performed in mice without tumors revealed ≥99% of intact folate radioconjugates in blood plasma at 4 h after injection of $[^{177}Lu]Lu$-6*R*-RedFol-1, $[^{177}Lu]Lu$-6*S*-RedFol-1 and $[^{177}Lu]Lu$-OxFol-1.

4.3.6. Biodistribution Studies

Biodistribution studies of the folate radioconjugates were performed in KB tumor-bearing mice over a period of 5 days (Fig. 4.5, Tables 4.2/4.3). Retention of activity in the blood at 1 h post injection (p.i.) was higher ($p<0.05$) for $[^{177}Lu]Lu$-6*R*-RedFol-1 (23 ± 3% IA/g) and $[^{177}Lu]Lu$-6*S*-RedFol-1 (19 ± 2% IA/g) than for $[^{177}Lu]Lu$-OxFol-1 (7.9 ± 1.4% IA/g). At 24 h p.i. blood activity levels were, however, below 3% IA/g in all cases. The uptake of $[^{177}Lu]Lu$-6*R*-RedFol-1 and $[^{177}Lu]Lu$-6*S*-RedFol-1 in KB tumors was significantly increased from 24 h onwards when compared with the uptake of $[^{177}Lu]Lu$-OxFol-1 ($p<0.05$). The maximum accumulation of $[^{177}Lu]Lu$-6*R*-RedFol-1 in KB tumor xenografts (47 ± 4% IA/g) was reached at 24 h p.i. while in the case of $[^{177}Lu]Lu$-6*S*-RedFol-1 the highest uptake (51 ± 7% IA/g) was observed at 48 h p.i.. Both values were much higher than the maximum tumor uptake of $[^{177}Lu]Lu$-OxFol-1 (18 ± 3% IA/g at 24 h p.i.).

$[^{177}Lu]Lu$-6*R*-RedFol-1 and $[^{177}Lu]Lu$-OxFol-1 showed a similar wash-out after they reached maximum kidney uptake (24 ± 4% IA/g and 28 ± 3% IA/g, respectively) at 24 h. The renal uptake of $[^{177}Lu]Lu$-6*S*-RedFol-1 was much higher (69 ± 7% IA/g; 24 h p.i.). In other tissues such as liver, lungs, spleen and heart, the uptake of $[^{177}Lu]Lu$-6*R*-RedFol-1 and $[^{177}Lu]Lu$-6*S*-RedFol-1 was elevated at early time points, but cleared within 24 h. As a consequence of the distribution profile, the tumor-to-kidney and tumor-to-liver ratios of $[^{177}Lu]Lu$-6*R*-RedFol-1 were significantly increased in comparison to $[^{177}Lu]Lu$-OxFol-1, whereas in the case of $[^{177}Lu]Lu$-6*S*-RedFol-1 only tumor-to-liver ratios were improved (Fig. 4.6). The uptake of activity in KB tumors and kidneys at 1 h p.i. of all folate radioconjugates was reduced

to ~5–7% IA/g and ~5–9% IA/g, respectively, when folic acid was pre-injected to block FRs in these tissues (Table 4.4).
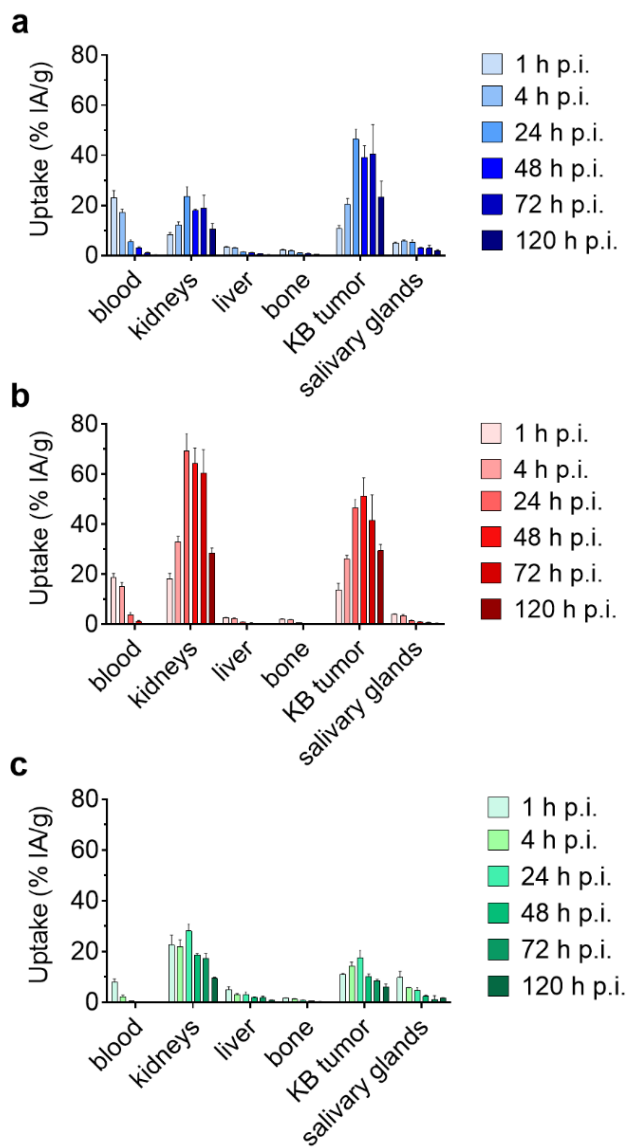
Fig. 4.5 Graphs representing the decay-corrected tissue distribution profile of the folate radioconjugates over 120 h. (**a**) [^{177}Lu]Lu-6*R*-RedFol-1; (**b**) [^{177}Lu]Lu-6*S*-RedFol-1 and (**c**) [^{177}Lu]Lu-OxFol-1. The data of [^{177}Lu]Lu-OxFol-1 were reproduced from Siwowska et al., 2017 Mol Pharm 14:523 [90]. Copyright 2020 American Chemical Society.
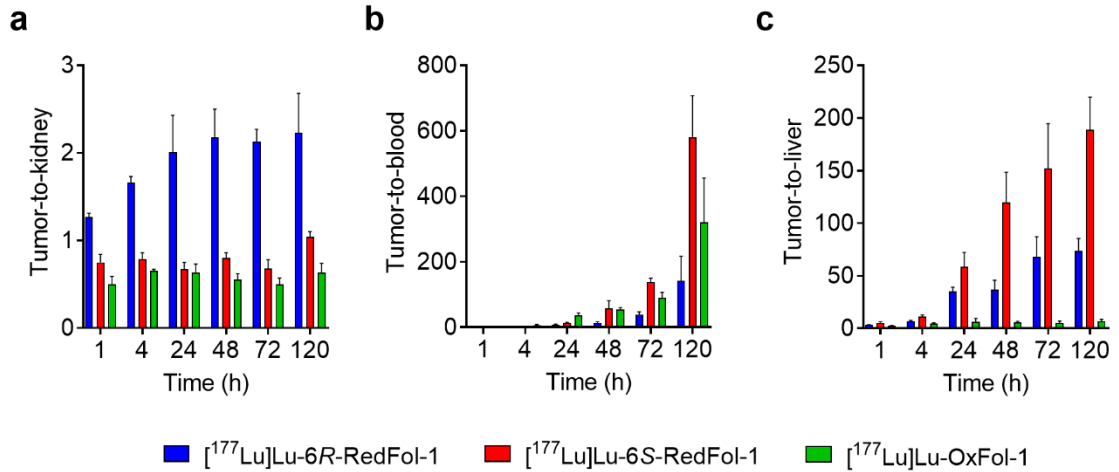
Fig. 4.6 Comparison of tumor-to-background ratios determined based on biodistribution data obtained at various time points after administration of [^{177}Lu]Lu-6*R*-RedFol-1, [^{177}Lu]Lu-6*S*-RedFol-1 and [^{177}Lu]Lu-OxFol-1. (**a**) Tumor-to-kidney ratios; (**b**) Tumor-to-blood ratios; (**c**) Tumor-to-liver ratios.

Table 4.2 Biodistribution data and tumor-to-background ratios obtained in KB tumor-bearing mice at various time points after injection of [^{177}Lu]Lu-6*R*-RedFol-1. Decay-corrected data of accumulated activity are shown as percentage of the injected activity per gram of tissue (% IA/g), representing the average ± SD.

Organs	[^{177}Lu]Lu-6*R*-RedFol-1					
	1 h p.i.	4 h p.i.	24 h p.i.	48 h p.i.	72 h p.i.	120 h p.i.
Blood	23 ± 3	17 ± 1	5.4 ± 0.9	3.0 ± 0.4	1.0 ± 0.3	0.20 ± 0.13
Lung	10 ± 1	7.9 ± 1.4	3.2 ± 0.6	2.4 ± 0.2	0.99 ± 0.24	0.37 ± 0.08
Spleen	2.6 ± 0.2	2.2 ± 0.2	1.7 ± 0.1	1.5 ± 0.1	1.3 ± 0.4	0.95 ± 0.14
Kidneys	8.4 ± 0.8	12 ± 1	24 ± 4	18 ± 1	19 ± 5	11 ± 2
Stomach	1.9 ± 0.4	1.9 ± 0.3	0.80 ± 0.11	0.46 ± 0.07	0.29 ± 0.10	0.13 ± 0.02
Intestines	2.9 ± 0.3	2.6 ± 0.7	0.80 ± 0.09	0.53 ± 0.07	0.30 ± 0.09	0.32 ± 0.23
Liver	3.3 ± 0.3	3.0 ± 0.2	1.3 ± 0.2	1.1 ± 0.2	0.61 ± 0.14	0.32 ± 0.05
Salivary gl.	5.0 ± 0.3	5.7 ± 0.5	5.2 ± 1.0	3.0 ± 0.3	3.0 ± 1.1	2.0 ± 0.3
Muscle	1.6 ± 0.2	1.4 ± 0.1	0.82 ± 0.22	0.82 ± 0.06	0.28 ± 0.08	0.28 ± 0.15
Bone	2.1 ± 0.3	1.9 ± 0.2	0.91 ± 0.22	0.75 ± 0.17	0.37 ± 0.09	0.19 ± 0.01
KB Tumor	11 ± 1	20 ± 2	47 ± 4	39 ± 5	41 ± 12	23 ± 7

Organ Ratios	Tumor-to-Background Ratios					
	1 h p.i.	4 h p.i.	24 h p.i.	48 h p.i.	72 h p.i.	120 h p.i.
Tu-to-blood	0.46 ± 0.01	1.2 ± 0.1	8.8 ± 0.8	13 ± 4	39 ± 8	142 ± 75*
Tu-to-liver	3.3 ± 0.2	6.9 ± 0.7	35 ± 4	37 ± 9*	68 ± 19*	74 ± 12*
Tu-to-kidney	1.3 ± 0.1*	1.7 ± 0.1*	2.0 ± 0.4*	2.2 ± 0.3*	2.1 ± 0.1*	2.2 ± 0.5*

* Significantly different (*p*<0.05) from the value of [^{177}Lu]Lu-OxFol-1 [90]

Table 4.3 Biodistribution data and tumor-to-background ratios obtained in KB tumor-bearing mice at various time points after injection of [^{177}Lu]Lu-6S-RedFol-1. Decay-corrected data of accumulated activity are shown as percentage of the injected activity per gram of tissue (% IA/g), representing the average ± SD.

Organs	[^{177}Lu]Lu-6S-RedFol-1					
	1 h p.i.	4 h p.i.	24 h p.i.	48 h p.i.	72 h p.i.	120 h p.i.
Blood	19 ± 2	15 ± 2	3.8 ± 0.9	1.0 ± 0.5	0.27 ± 0.11	0.05 ± 0.01
Lung	8.5 ± 0.6	6.7 ± 0.6	2.2 ± 0.4	0.85 ± 0.31	0.36 ± 0.10	0.15 ± 0.03
Spleen	2.0 ± 0.2	1.9 ± 0.3	1.1 ± 0.2	1.1 ± 0.3	0.89 ± 0.14	0.67 ± 0.11
Kidneys	18 ± 2	33 ± 2	69 ± 7	64 ± 6	60 ± 10	28 ± 2
Stomach	1.5 ± 0.3	1.2 ± 0.2	0.51 ± 0.14	0.23 ± 0.06	0.11 ± 0.03	0.06 ± 0.02
Intestines	1.8 ± 0.4	1.9 ± 0.1	0.49 ± 0.04	0.21 ± 0.09	0.11 ± 0.04	0.06 ± 0.02
Liver	2.6 ± 0.1	2.3 ± 0.2	0.81 ± 0.22	0.46 ± 0.16	0.28 ± 0.07	0.16 ± 0.03
Salivary gl.	4.0 ± 0.2	3.5 ± 0.4	1.4 ± 0.2	0.84 ± 0.23	0.62 ± 0.18	0.45 ± 0.05
Muscle	1.6 ± 0.2	1.3 ± 0.1	0.47 ± 0.15	0.21 ± 0.05	0.13 ± 0.06	0.10 ± 0.01
Bone	2.0 ± 0.2	1.7 ± 0.2	0.53 ± 0.08	0.28 ± 0.08	0.16 ± 0.05	0.11 ± 0.01
KB Tumor	14 ± 3	26 ± 1	46 ± 3	51 ± 7	42 ± 10	29 ± 3
Organ Ratios	**Tumor-to-Background Ratios**					
	1 h p.i.	4 h p.i.	24 h p.i.	48 h p.i.	72 h p.i.	120 h p.i.
Tu-to-blood	0.73 ± 0.12	1.7 ± 0.2	13 ± 3	58 ± 23	138 ± 12	580 ± 127*
Tu-to-liver	5.3 ± 1.0	11 ± 1	59 ± 13*	120 ± 29*	152 ± 43*	189 ± 31*
Tu-to-kidney	0.75 ± 0.09	0.79 ± 0.07	0.67 ± 0.08	0.80 ± 0.06	0.68 ± 0.10	1.0 ± 0.1*

* Significantly different ($p<0.05$) from the value of [^{177}Lu]Lu-OxFol-1 [90]

Table 4.4 Accumulation of [^{177}Lu]Lu-6R-RedFol-1, [^{177}Lu]Lu-6S-RedFol-1 and [^{177}Lu]Lu-OxFol-1 in selected organs of KB tumor-bearing mice at 1 h after injection in comparison to the uptake upon FR-blockade with pre-injected folic acid (FA). Decay-corrected data of accumulated activity are shown as percentage of the injected activity per gram of tissue (% IA/g), representing the average ± SD (n=3–4).

Organs	[^{177}Lu]Lu-6R-RedFol-1		[^{177}Lu]Lu-6S-RedFol-1		[^{177}Lu]Lu-OxFol-1	
	1 h p.i.	1 h p.i. + FA	1 h p.i.	1 h p.i. + FA	1 h p.i.[1]	1 h p.i. + FA
Blood	23 ± 3	25 ± 2	19 ± 2	23 ± 2	7.9 ± 1.4	20 ± 1
Kidneys	8.4 ± 0.8	4.9 ± 0.6	18 ± 2	7.0 ± 0.5	23 ± 4	9.2 ± 4.0
Liver	3.3 ± 0.3	4.1 ± 0.4	2.6 ± 0.1	3.7 ± 0.5	5.0 ± 1.3	3.3 ± 0.2
Salivary gl.	5.0 ± 0.3	5.3 ± 0.4	4.0 ± 0.2	4.6 ± 0.4	9.8 ± 2.4	3.9 ± 0.8
KB Tumor	11 ± 1	5.2 ± 0.5	14 ± 3	6.0 ± 0.9	11 ± 1	6.6 ± 0.7

[1] The data were reproduced from Siwowska et al., 2017 Mol Pharm 14:523 [90]. Copyright 2020 American Chemical Society.

4.3.7. Determination of Areas Under the Curve (AUC)

The $AUC_{0\rightarrow120h}$ of the tumor uptake after injection of [^{177}Lu]Lu-6R-RedFol-1 and [^{177}Lu]Lu-6S-RedFol-1 revealed similar values, which were at least 3-fold higher than the respective value of [^{177}Lu]Lu-OxFol-1 (Fig. 4.7, Tables 4.5/4.6) [90]. The $AUC_{0\rightarrow120h}$ of kidney uptake was ~3-fold higher for [^{177}Lu]Lu-6S-RedFol-1 than for [^{177}Lu]Lu-6R-RedFol-1 and [^{177}Lu]Lu-OxFol-1. Consequently, [^{177}Lu]Lu-6R-RedFol-1 revealed a 3.6-fold increased tumor-to-kidney $AUC_{0\rightarrow120h}$ ratio as compared to [^{177}Lu]Lu-OxFol-1, while tumor-to-kidney $AUC_{0\rightarrow120h}$ ratios of [^{177}Lu]Lu-6S-RedFol-1 and [^{177}Lu]Lu-OxFol-1 were similar (Table 4.6). The tumor-to-blood $AUC_{0\rightarrow120h}$ ratio of [^{177}Lu]Lu-6R-RedFol-1 was lower than for [^{177}Lu]Lu-OxFol-1 while no change in this regard was observed for [^{177}Lu]Lu-6S-RedFol-1. The tumor-to-liver $AUC_{0\rightarrow120h}$ ratios of [^{177}Lu]Lu-6R-RedFol-1 and [^{177}Lu]Lu-6S-RedFol-1 were 6-fold and 11-fold higher as compared to the tumor-to-liver $AUC_{0\rightarrow120h}$ ratio of [^{177}Lu]Lu-OxFol-1.

Table 4.5 Area under the curve ($AUC_{0\rightarrow120h}$) values (indicated as [(% IA/g)·h]) based on non-decay-corrected biodistribution data and tumor-to-background AUC ratios

	$AUC_{0\rightarrow120h}$ **Values**		
	[^{177}Lu]Lu-6R-RedFol-1	**[^{177}Lu]Lu-6S-RedFol-1**	**[^{177}Lu]Lu-OxFol-1[1]**
KB tumor	3332 ± 263*	3750 ± 232*	1041 ± 59
Blood	485 ± 20*	361 ± 21*	108 ± 6
Kidneys	1621 ± 118	5028 ± 230*	1799 ± 75
Liver	108 ± 5*	66 ± 5*	205 ± 24
	$AUC_{0\rightarrow120h}$ **Ratios**		
	[^{177}Lu]Lu-6R-RedFol-1	**[^{177}Lu]Lu-6S-RedFol-1**	**[^{177}Lu]Lu-OxFol-1[1]**
AUC_{Tu}-to-AUC_{Bl}	6.9 ± 0.8	10 ± 2	9.6 ± 1.1
AUC_{Tu}-to-AUC_{Ki}	2.1 ± 0.4*	0.7 ± 0.1	0.6 ± 0.1
AUC_{Tu}-to-AUC_{Li}	31 ± 4*	57 ± 8*	5.1 ± 0.9

* Significantly different (p<0.05) from the value of [^{177}Lu]Lu-OxFol-1
[1] Data were reproduced from Siwowska et al. 2017 Mol Pharm 14:523 [90]. Copyright 2020 American Chemical Society.

Table 4.6 Areas under the curve up to 120 h p.i. ($AUC_{0\rightarrow120h}$) calculated as [(% IA/g)·h] and tumor-to-background $AUC_{0\rightarrow120h}$ ratios presented as a value relative to [^{177}Lu]Lu-OxFol-1 which was set as 1.0

	Relative $AUC_{0\rightarrow120h}$		
	[^{177}Lu]Lu-6R-RedFol-1	**[^{177}Lu]Lu-6S-RedFol-1**	**[^{177}Lu]Lu-OxFol-1**
KB tumor	3.2 ± 0.3	3.6 ± 0.3	1.0 ± 0.1
Blood	4.5 ± 0.2	3.3 ± 0.2	1.0 ± 0.1
Kidneys	0.90 ± 0.07	2.8 ± 0.2	1.0 ± 0.1
Liver	0.53 ± 0.02	0.32 ± 0.02	1.0 ± 0.2
	Relative $AUC_{0\rightarrow120h}$ **Ratios**		
	[^{177}Lu]Lu-6R-RedFol-1	**[^{177}Lu]Lu-6S-RedFol-1**	**[^{177}Lu]Lu-OxFol-1**
AUC_{Tu}-to-AUC_{Bl}	0.71 ± 0.09	1.1 ± 0.2	1.0 ± 0.2
AUC_{Tu}-to-AUC_{Ki}	3.6 ± 0.6	1.3 ± 0.2	1.0 ± 0.1
AUC_{Tu}-to-AUC_{Li}	6.1 ± 0.8	11 ± 2	1.0 ± 0.2
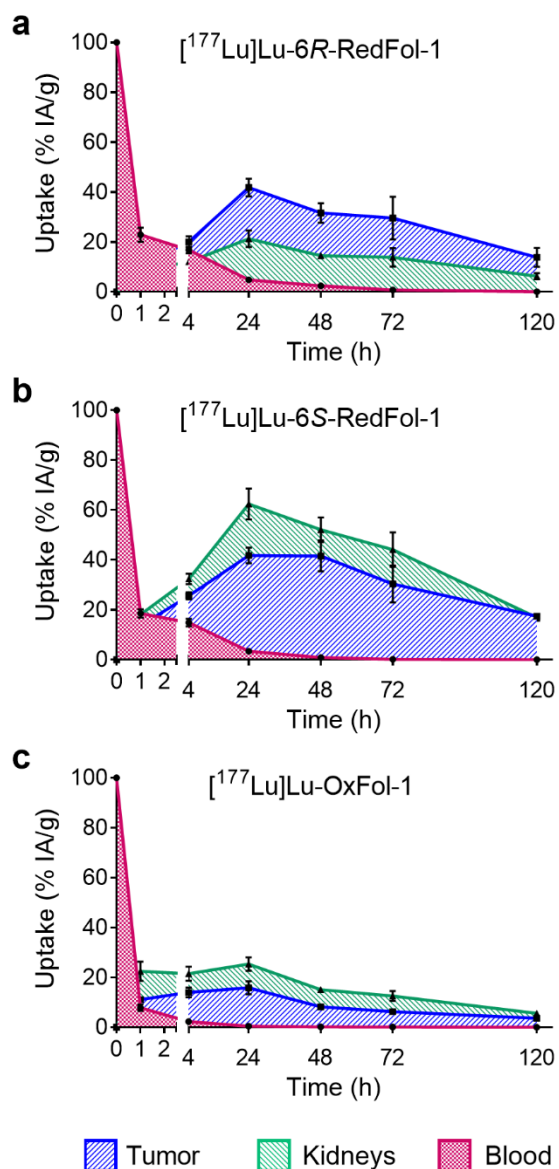
Fig. 4.7 Graphs representing the $AUC_{0\rightarrow120h}$ of non-decay-corrected biodistribution data up to 120 h p.i. of the folate radioconjugates. (**a**) [^{177}Lu]Lu-6R-RedFol-1; (**b**) [^{177}Lu]Lu-6S-RedFol-1; (**c**) [^{177}Lu]Lu-OxFol-1 (adapted with permission from Siwowska et al. 2017 Mol Pharm 14:523 [90]. Copyright 2020 American Chemical Society). Each data point represents the average of a group of mice $\pm$ SD (n=4).

4.3.8.   SPECT/CT Imaging Studies

The SPECT/CT images of mice injected with [^{177}Lu]Lu-6*R*-RedFol-1 showed high accumulation of activity in the tumors and less in the kidneys (Fig. 4.8a/e). The same high tumor uptake was observed after injection of [^{177}Lu]Lu-6*S*-RedFol-1, however, in this case also the kidney uptake was increased (Fig. 4.9a/e). [^{177}Lu]Lu-OxFol-1 demonstrated lower activity in the tumor tissue and a similar kidney retention as observed for [^{177}Lu]Lu-6*R*-RedFol-1 (Fig. 4.10a/e). The images visualized clearly higher tumor-to-kidney ratios of [^{177}Lu]Lu-6*R*-RedFol-1 as compared to [^{177}Lu]Lu-6*S*-RedFol-1 and [^{177}Lu]Lu-OxFol-1.

The SPECT/CT images of KB tumor-bearing mice injected with folate radioconjugates only (Fig. 4.8a/e, 4.9a/e, 4.10a/e) or with excess folic acid (Fig. 4.8b/f, 4.9b/f, 4.10b/f) or excess cm13 (Fig. 4.8c/g, 4.9c/g, 4.10c/g), respectively, demonstrated that the uptake of the folate radioconjugates in tumors and kidneys was mostly FR-dependent. Due to the fast excretion of folic acid, the uptake of the radioconjugates in FR-positive tumors and kidneys became manifest again at later time points (24 h p.i.), in particular in the case of [^{177}Lu]Lu-6*S*-RedFol-1 (Fig. 4.9f) which accumulated to a high extent in tumors and kidneys (Fig. 4.9e). Pre-injection of cm13, an albumin-binding folate conjugate with similar kinetics as the herein described folate radioconjugates, resulted in almost entire blockade of [^{177}Lu]Lu-6*S*-RedFol-1 accumulation in tumors and kidneys, respectively (Fig. 4.9g). The images of a mouse that was injected with [^{177}Lu]Lu-DOTA-PPB-01 (Fig. 4.8d/h, 4.9d/h, 4.10d/h) demonstrated only low accumulation of activity in the tumors, which can be ascribed to an unspecific uptake mechanism. The extent of uptake in the tumors corresponded relatively well with residual activity in tumors of mice pre-injected with folic acid or cm13, indicating that it was caused by a FR-unrelated mechanism.
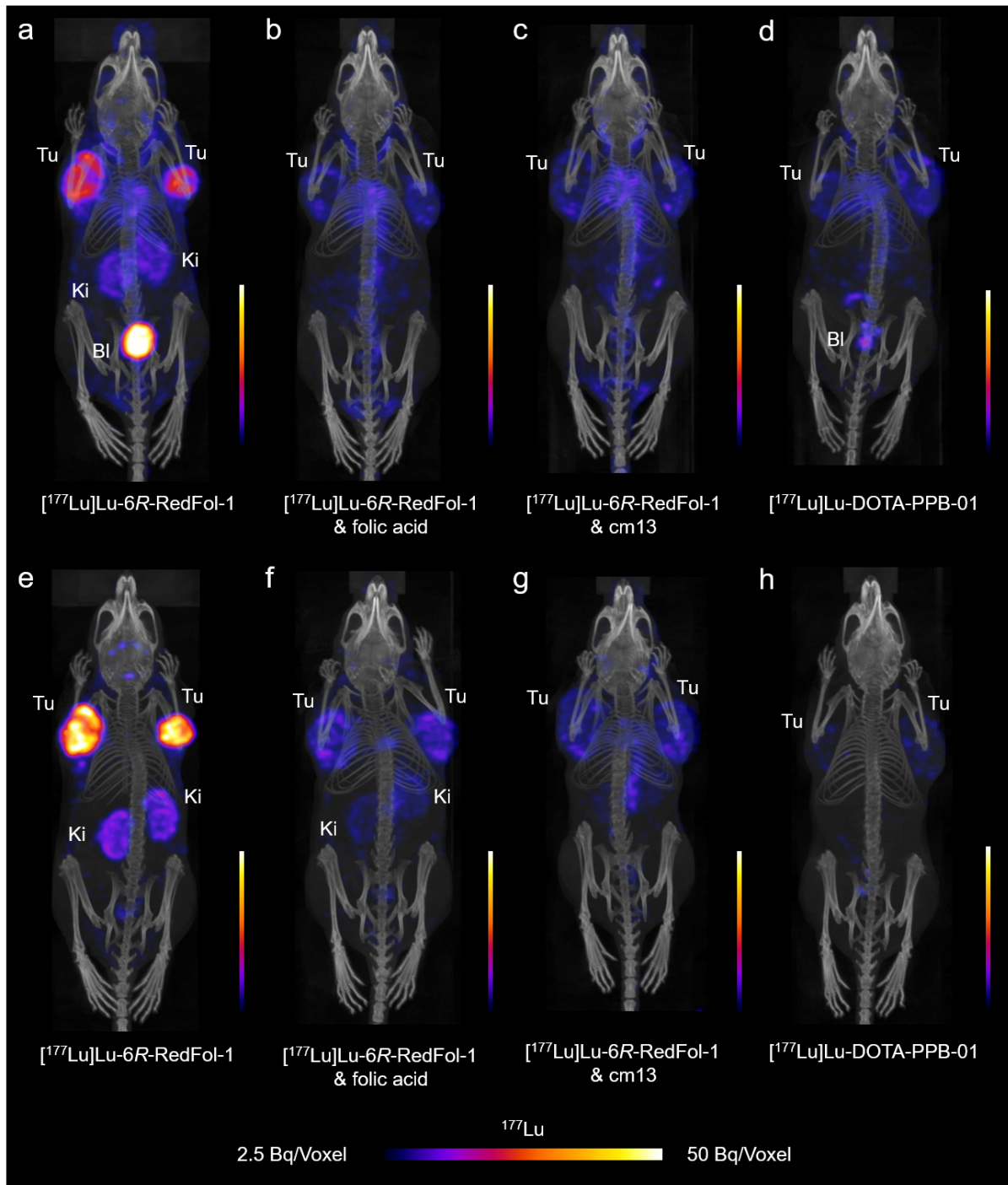
Fig. 4.8 SPECT/CT images shown as maximum intensity projections (MIPs) of KB tumor-bearing mice at 4 h p.i. (**a–d**) and 24 h p.i. (**e–h**). (**a/e**) Mouse injected with [^{177}Lu]Lu-6R-RedFol-1 (25 MBq; 0.5 nmol per mouse) only; (**b/f**) Mouse pre-injected with folic acid (100 μg); (**c/g**) Mouse pre-injected with cm13 (100 μg); (**d/h**) Mouse injected with [^{177}Lu]Lu-DOTA-PPB-01. Tu = KB tumor; Ki = kidney; Bl = urinary bladder.
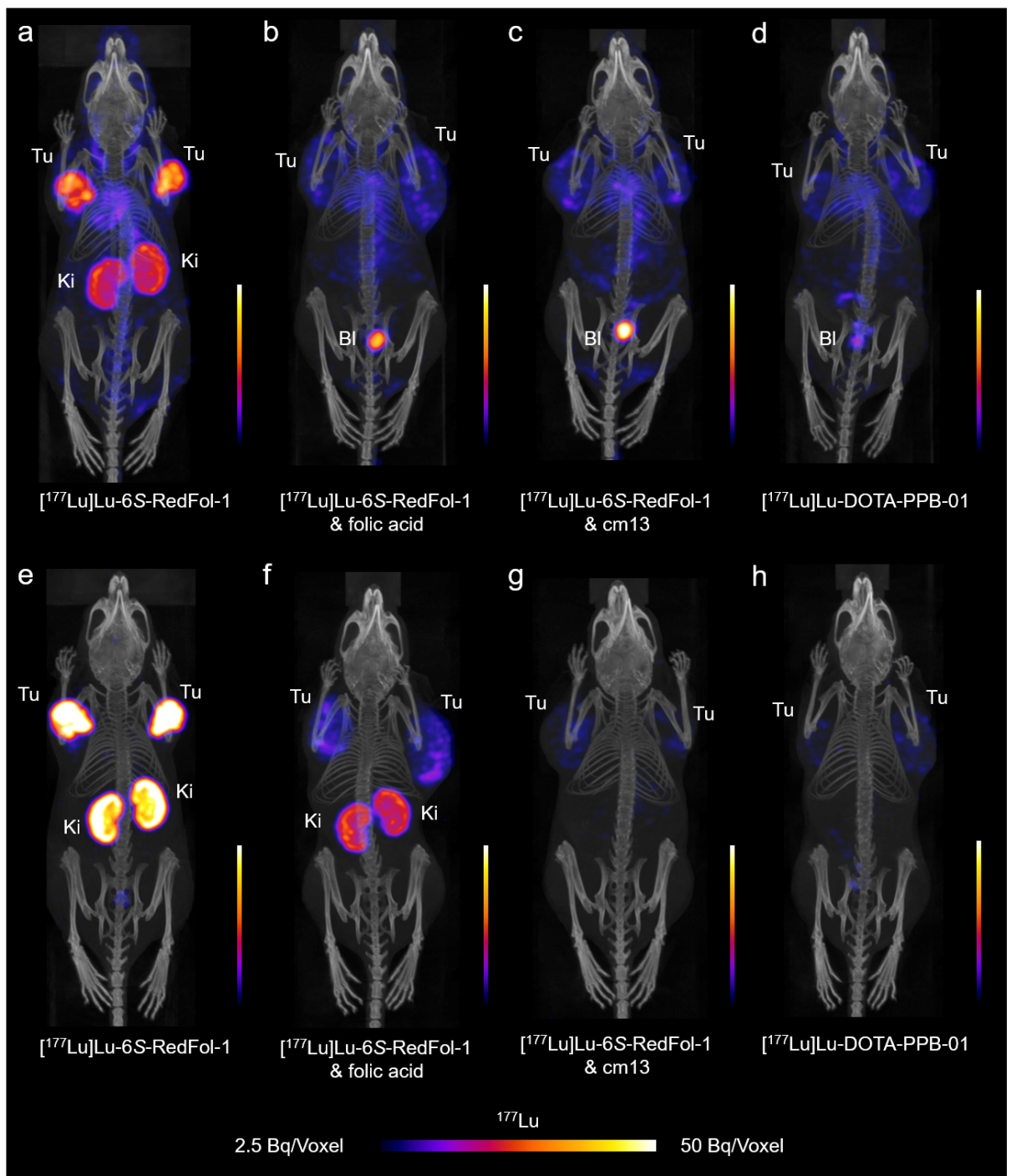
Fig. 4.9 SPECT/CT images shown as maximum intensity projections (MIPs) of KB tumor-bearing mice at 4 h p.i. (**a–d**) and 24 h p.i. (**e–h**). (**a/e**) Mouse injected with [^{177}Lu]Lu-6S-RedFol-1 (25 MBq; 0.5 nmol per mouse) only; (**b/f**) Mouse pre-injected with folic acid (100 μg); (**c/g**) Mouse pre-injected with cm13 (100 μg); (**d/h**) Mouse injected with [^{177}Lu]Lu-DOTA-PPB-01. Tu = KB tumor; Ki = kidney; Bl = urinary bladder.
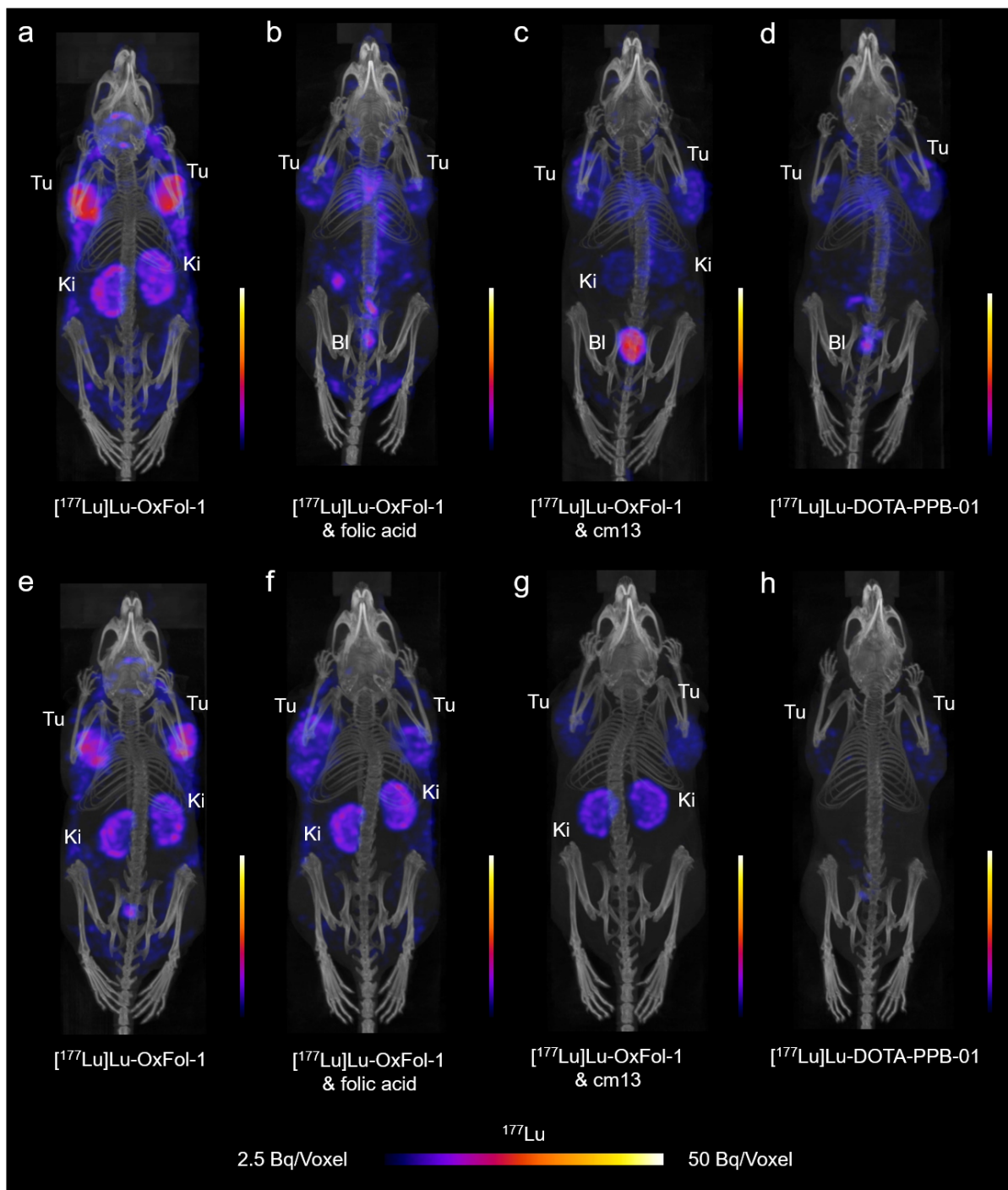
Fig. 4.10 SPECT/CT images shown as maximum intensity projections (MIPs) of KB tumor-bearing mice at 4 h p.i. (**a–d**) and 24 h p.i. (**e–h**). (**a/e**) Mouse injected with [^{177}Lu]Lu-OxFol-1 (25 MBq; 0.5 nmol per mouse) only; (**b/f**) Mouse pre-injected with folic acid (100 μg); (**c/g**) Mouse pre-injected with cm13 (100 μg); (**d/h**) Mouse injected with [^{177}Lu]Lu-DOTA-PPB-01. Tu = KB tumor; Ki = kidney; Bl = urinary bladder.

4.3.9. Therapy Study

The tumor size of untreated control mice (Group A) was constantly increasing over time, whereas a considerable tumor growth delay was observed in treated mice of Groups B–E. This was reflected by significantly increased tumor growth delay indices (TGDI) in treated groups as compared to control mice where the TGDIs were defined as 1.0 (Fig. 4.11, Table 4.7).

A significantly more pronounced tumor growth delay was observed in mice treated with 10 MBq [^{177}Lu]Lu-6R-RedFol-1 (Group B) than in the mice treated with 10 MBq [^{177}Lu]Lu-OxFol-1 (Group C) resulting in increased TGDI$_2$ (Group B: 4.2 ± 0.6 vs. Group C: 2.4 ± 0.3; $p<0.05$) (Fig. 4.11a/b, Table 4.7). Mice that received 15 MBq [^{177}Lu]Lu-6R-RedFol-1 (Group D) showed complete remission of the tumors. Consequently, it was not possible to calculate TGDIs. Interestingly, the mice that received 15 MBq [^{177}Lu]Lu-OxFol-1 (Group E) had a TGDI$_2$ of 4.5 ± 0.3 which was similar to the results observed with 10 MBq [^{177}Lu]Lu-6R-RedFol-1 ($p>0.05$). These findings were also reflected by the tumor growth inhibition (TGI) determined at Day 14 when the first mouse of control group had to be euthanized (Table 4.8).

The median survival of treated mice was increased compared to the median survival of control mice (Group A) (Table 4.8). The median survival of 49 days for mice treated with 10 MBq [^{177}Lu]Lu-6R-RedFol-1 (Group B) was much longer than for mice that received 10 MBq [^{177}Lu]Lu-OxFol-1 (Group C: 34 days). All mice injected with 15 MBq [^{177}Lu]Lu-6R-RedFol-1 (Group D) survived until the end of the study at Day 56 whereas mice that received 15 MBq [^{177}Lu]Lu-OxFol-1 (Group E) had a median survival of only 44 days.

4.3.10. Assessment of the Therapy Study

The average relative body weight (1.00–1.08) was comparable in all groups of mice at Day 14, when the first mouse of the control group reached an endpoint. Organ-to-body weight as well as organ-to-brain mass ratios may serve as indicators of the health status, since it is known that the brain of the mice does not increase in size after the age of 3 weeks (Table 4.9) [163,164]. The calculated organ-to-brain mass ratios were in the same range for untreated mice and mice treated with 10 MBq of the folate radioconjugates (Groups B/C). The organ-to-brain mass ratios of mice treated with 15 MBq of the folate radioconjugates (Groups D/E) were decreased ($p<0.05$).

No significant differences between the untreated mice and mice treated with [^{177}Lu]Lu-6R-RedFol-1 or [^{177}Lu]Lu-OxFol-1 were found in the blood plasma levels of CRE, TBIL, BUN and ALP measured at the endpoint of the therapy ($p>0.05$) (Supplementary Material of [162]). The determined levels of CRE and TBIL were <18 µmol/L and <3 µmol/L, respectively. The average plasma level of BUN and ALP was in the range of 5.8–7.4 mmol/L, and 77–95 U/L, respectively. The albumin plasma concentrations were comparable for Groups A–C and Group E (21–22 g/L), apart from Group D which was significantly different (23 ± 1 g/L; $p<0.05$).

Histological investigations of the kidneys, spleen and bone marrow did, however, not reveal any

significant lesion attributed to the treatment. In particular, bone marrow of mice that received [^{177}Lu]Lu-6R-RedFol-1 showed an overall haematopoietic cellularity comparable to the control animals and mice treated with [^{177}Lu]Lu-OxFol-1 (Table 4.10).
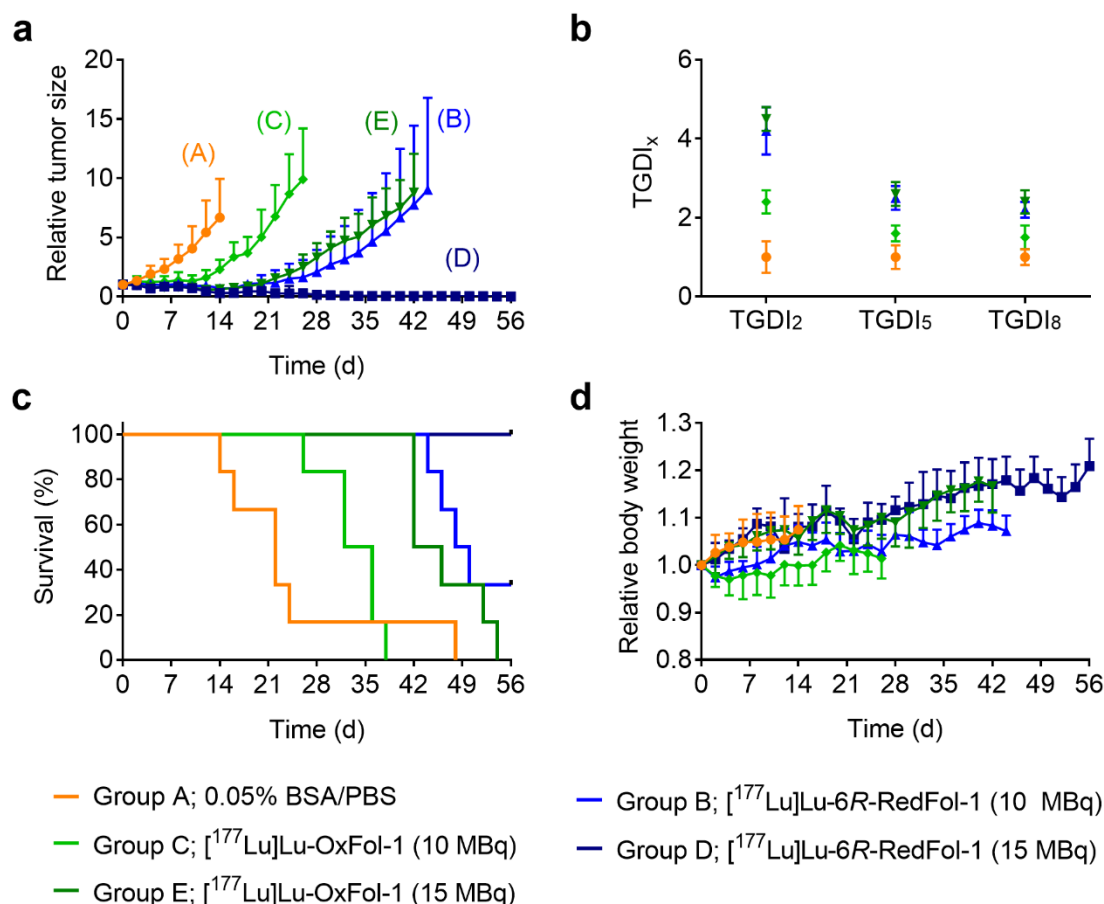
Fig. 4.11 (**a**) Tumor growth curves relative to the tumor volume at Day 0 (set to 1.0) for mice that received PBS (Group A), mice treated with [^{177}Lu]Lu-6R-RedFol-1 (Group B/D) or [^{177}Lu]Lu-OxFol-1 (Group C/E); (**b**) TGDI$_2$, TGDI$_5$ and TGDI$_8$ determined for respective groups (TGDIs of Group D were not determined due to RTV below the threshold value); (**c**) Kaplan-Meier plot of Groups A–E; (**d**) Relative body weight of Groups A–E. Tumor growth and body weights are shown until the first mouse of the respective group reached the endpoint.

Table 4.7 Tumor growth delay index with x-fold increase of tumor size (TGDI$_x$) of [^{177}Lu]Lu-6R-RedFol-1 and [^{177}Lu]Lu-OxFol-1

Group (n=6–9)	Treatment	TGDI$_2$	TGDI$_5$	TGDI$_8$
A	0.05% BSA/PBS	1.0 ± 0.4	1.0 ± 0.3	1.0 ± 0.2
B	[^{177}Lu]Lu-6R-RedFol-1 (10 MBq)	4.2 ± 0.6	2.5 ± 0.3	2.2 ± 0.2
C	[^{177}Lu]Lu-OxFol-1 (10 MBq)	2.4 ± 0.3	1.5 ± 0.2	1.5 ± 0.3
D	[^{177}Lu]Lu-6R-RedFol-1 (15 MBq)[1]	n.d.	n.d.	n.d.
E	[^{177}Lu]Lu-OxFol-1 (15 MBq)	4.5 ± 0.3	2.6 ± 0.3	2.4 ± 0.3

[1] TGDI$_x$ of Group D was not determined (n.d.) due to RTV < 2

Table 4.8 Data regarding euthanasia period and median survival of mice

Group	Treatment	Time frame of euthanasia (d)	Median survival (d)	TGI (%)
A	0.05% BSA/PBS	14–48	22	0
B	[^{177}Lu]Lu-6*R*-RedFol-1 (10 MBq)	44–56*	49	89 ± 3
C	[^{177}Lu]Lu-OxFol-1 (10 MBq)	26–38	34	66 ± 12
D	[^{177}Lu]Lu-6*R*-RedFol-1 (15 MBq)	56*	n.d.	96 ± 2
E	[^{177}Lu]Lu-OxFol-1 (15 MBq)	42–54	44	91 ± 4

* Day 56 = End of the study

n.d. = not determined since all mice survived until the end of the study

Table 4.9 Organ mass-to-brain mass and organ mass-to-body weight ratios

Group (n=6–9)	Organ mass-to-brain mass ratios (average ± SD)		
	Kidney-to-brain	Liver-to-brain	Spleen-to-brain
A	0.83 ± 0.07	2.8 ± 0.2	0.31 ± 0.05
B	0.79 ± 0.05	2.7 ± 0.1	0.25 ± 0.06*
C	0.81 ± 0.10	2.9 ± 0.4	0.30 ± 0.04
D	0.64 ± 0.05*	2.7 ± 0.2	0.13 ± 0.01*
E	0.69 ± 0.05*	2.5 ± 0.2	0.20 ± 0.02*
Group (n=6–9)	**Organ mass-to-body weight ratios (average ± SD)**		
	Kidney-to-body	Liver-to-body	Spleen-to-body
A	0.014 ± 0.001	0.047 ± 0.003	0.005 ± 0.001
B	0.014 ± 0.001	0.048 ± 0.003	0.004 ± 0.001*
C	0.014 ± 0.001	0.052 ± 0.004*	0.005 ± 0.001
D	0.012 ± 0.001*	0.051 ± 0.002	0.002 ± 0.000*
E	0.012 ± 0.001*	0.045 ± 0.003	0.003 ± 0.000*

* Significantly different ($p<0.05$) from the value of Group A

Table 4.10 Histopathological scoring of kidneys, bone marrow and spleen collected from KB tumor-bearing mice which received [^{177}Lu]Lu-6*R*-RedFol-1 or [^{177}Lu]Lu-OxFol-1 at 10 MBq or 15 MBq activity level.

Folate Radioconjugate	Activity	Kidneys	Spleen		Bone Marrow
		Radiation nephropathy	White pulp depletion	Extramedullary haematopoiesis	Hypocellularity
– (0.05% BSA/PBS)	0	0 (9/9)	0 (9/9)	1 (1/9) 2 (1/9) 3 (7/9)	0 (9/9)
Average		0.0	0.0	2.7	0.0
[^{177}Lu]Lu-6*R*-RedFol-1	10 MBq	0 (6/6)	0 (5/6) 1 (1/6)	1 (1/6) 2 (4/6) 3 (1/6)	0 (4/6) 1 (2/6)
Average		0.0	0.2	2.0	0.3
[^{177}Lu]Lu-OxFol-1	10 MBq	0 (6/6)	0 (4/6) 1 (2/6)	3 (6/6)	0 (6/6)
Average		0.0	0.3	3.0	0.0
[^{177}Lu]Lu-6*R*-RedFol-1	15 MBq	0 (5/6) 1 (1/6)	0 (6/6)	1 (3/6) 2 (3/6)	0 (3/6) 1 (3/6)
Average		0.2	0.0	1.5	0.5
[^{177}Lu]Lu-OxFol-1	15 MBq	0 (6/6)	0 (3/6) 1 (3/6)	2 (2/6) 3 (4/6)	0 (6/6)
Average		0.0	0.5	2.7	0.0

4.4.   Discussion

In this study, albumin-binding radioconjugates of a new class, based on 5-MTHF as a FR-binding entity, were evaluated and compared with the previously developed [^{177}Lu]Lu-OxFol-1 [90]. [^{177}Lu]Lu-6*R*-RedFol-1 and [^{177}Lu]Lu-6*S*-RedFol-1 showed high stability in PBS and human plasma in vitro. In all three cases the binding to human plasma proteins was stronger than to mouse plasma proteins, which is in line with the reported affinity of the *p*-iodophenyl entity [88] and recently reported results obtained with albumin-binding PSMA-targeted radioligands [158]. In vitro studies revealed that the exchange of folic acid with 5-MTHF slightly increased the affinity of the respective radioconjugates to both mouse and human plasma proteins when compared to the affinity determined for [^{177}Lu]Lu-OxFol-1. It remains, however, unclear whether this was the reason for the increased blood retention of 5-MTHF-based folate radioconjugates or if it was due to another, yet unknown, mechanism. The hypothesis that the observed phenomenon was due to radiometabolite formation was refuted by stability experiments that showed only intact folate radioconjugates in the blood plasma of mice four hours after injection. The FR-specific in vitro uptake of the radioconjugates into KB tumor cells was demonstrated in vitro and pre-injection of excess folic acid reduced the accumulation of the radioconjugates in tumors and kidneys of mice. The application of excess non-labeled albumin-binding folic acid conjugate (cm13) was, however, much more effective in this regard due to its enhanced blood circulation similar to the folate radioconjugates in question.

[^{177}Lu]Lu-6*R*-RedFol-1 and [^{177}Lu]Lu-6*S*-RedFol-1 showed a somewhat higher in vitro uptake and internalization in FR-positive KB tumor cells as compared to [^{177}Lu]Lu-OxFol-1 and the in vivo results revealed even a 3–4-fold increased tumor uptake of [^{177}Lu]Lu-6*R*-RedFol-1 and [^{177}Lu]Lu-6*S*-RedFol-1. The in vivo results were likely due to the enhanced blood retention of the 5-MTHF-based radioconjugates, however, it may also be due to the easier release of 5-MTHF from the FR upon internalization and, thus, more efficient accumulation as compared to folic acid [141]. The latter hypothesis is further supported by the results of Boss et al. who observed an increased tumor uptake of ^{18}F-labeled 5-MTHF radiotracers as compared to the folic acid analogue even though these radiotracers did not comprise an albumin-binding entity [77]. In parallel to the increased tumor uptake, [^{177}Lu]Lu-6*S*-RedFol-1 showed also higher retention in the kidneys resulting in similar tumor-to-kidney ratios as observed with [^{177}Lu]Lu-OxFol-1. In the case of [^{177}Lu]Lu-6*R*-RedFol-1, the retention in the kidneys remained relatively low resulting in substantially improved tumor-to-kidneys AUC$_{0 \to 120h}$ ratios to a value that has never been achieved before. This radioconjugate was, thus, selected for further investigations in a preclinical therapy study.

As expected, the treatment of KB tumor-bearing mice with 10 MBq or 15 MBq [^{177}Lu]Lu-6*R*-RedFol-1, showed an activity-dependent tumor growth inhibition and survival of mice. In line with the higher tumor uptake, the outcome of the [^{177}Lu]Lu-6*R*-RedFol-1 therapy was superior over that of [^{177}Lu]Lu-OxFol-1. Comparison of the TGDI and TGI results suggested that application of 10 MBq [^{177}Lu]Lu-6*R*-

RedFol-1 was equipotent to the application of 15 MBq [^{177}Lu]Lu-OxFol-1 which confirmed the enhanced therapeutic potential of this novel radioconjugate.

As the tumor-to-kidney AUC$_{0\rightarrow120h}$ ratio of [^{177}Lu]Lu-6R-RedFol-1 was almost 4-fold increased compared to [^{177}Lu]Lu-OxFol-1, the use of [^{177}Lu]Lu-6R-RedFol-1 would most probably allow delivering an effective tumor dose without the risk of long-term damage to the kidneys. In our study, no obvious early side effects were observed. Neither the body weights nor the blood plasma parameters of treated mice were significantly different from the control values. Moreover, no significant histopathological changes in kidneys and spleen were observed that would indicate radiation-induced damage of these tissues. Most importantly, the evaluation of the bone marrow of mice treated with [^{177}Lu]Lu-6R-RedFol-1 confirmed the absence of hematological side effects, in spite of the enhanced blood retention of this novel radioconjugate.

4.5.   Conclusion

It was demonstrated in this study, that 5-MTHF-based radioconjugates have the potential to be used for targeted radionuclide therapy. Due to the unprecedentedly high tumor-to-kidney ratios of [^{177}Lu]Lu-6R-RedFol-1, this radioconjugate outperformed any other folate radioconjugate. It was, thus, shown to have enhanced therapeutic efficacy as compared to [^{177}Lu]Lu-OxFol-1, which makes [^{177}Lu]Lu-6R-RedFol-1 attractive for clinical translation.

V. Promising Potential of [177Lu]Lu-DOTA-Folate to Enhance Tumor Response to Immunotherapy – a Preclinical Study Using a Syngeneic Breast Cancer Model

Patrycja Guzik[1], Klaudia Siwowska[1], Hsin-Yu Fang[1], Susan Cohrs[1], Peter Bernhardt[2,3], Roger Schibli[1,4], Cristina Müller[1,4*]

[1] *Center for Radiopharmaceutical Sciences ETH-PSI-USZ, Paul Scherrer Institute, 5232 Villigen-PSI, Switzerland*

[2] *Department of Radiation Physics, The Sahlgrenska Academy, University of Gothenburg, SE-413 45 Gothenburg, Sweden*

[3] *Department of Medical Physics and Medical Bioengineering, Sahlgrenska University Hospital, SE-413 45 Gothenburg, Sweden*

[4] *Department of Chemistry and Applied Biosciences, ETH Zurich, 8093 Zurich, Switzerland*

Author Contributions:

Patrycja Guzik performed the experiments, analyzed and interpreted the data, and wrote the manuscript. Klaudia Siwowska contributed to some of the experiments and analysis. Susan Cohrs contributed to the animal experiments. Peter Bernhardt performed the dosimetry calculations. Hsin-Yu Fang and Roger Schibli reviewed the final manuscript. Cristina Müller supervised the entire study, contributed to the writing of the manuscript and reviewed the final version.

5.1. Introduction

Immune checkpoint inhibitors (ICIs) have revolutionized cancer therapy and, thus, attracted increasing interest of clinicians over the last years [94,165]. Immune checkpoints, including the cytotoxic T lymphocyte antigen 4 (CTLA-4), provide inhibitory signals, which inactivate cytotoxic CD8+ T cells that are a key player in the anti-cancer immune response. ICI such as anti-CTLA-4 antibodies are used to block these signals and, hence, stimulate the elimination of cancer cells [92,166]. It was, however, observed that only a subset of patients responded to ICI monotherapy [94,167]. As demonstrated in (pre)clinical studies [168,169], the lack of response may have been ascribed to specific characteristics of the tumor, which defines it as poorly immunogenic ("cold"). In current clinical therapy settings, ICIs are, therefore, often combined with immune sensitizers, including chemotherapeutics [97,167].

Radiation therapy has long been regarded as an exclusively genotoxic therapy modality that induces various types of cell damage and death while radiation effects involving the immune system have been neglected for decades [170]. The discovery of the "abscopal" effect, referring to systemic anti-tumor radiation effects outside irradiated lesions, has, however, proven the impact of radiation on the tumor microenvironment [171]. Based on these observations, the rationale arose for using radiation stimuli to convert immunologically "cold" tumors into highly immunogenic ("hot") tumors which is of vital interest to enhance the response rate to immunotherapies [170].

Breast cancer is the most frequently diagnosed cancer in women of the Western world and associated with a high mortality rate [172]. It presents mostly as systemic malignancy requiring – in addition to surgery and local treatments – chemotherapy and hormonal therapy which are, however, not always sufficiently effective [173,174]. ICI therapy emerged as a valid alternative for the treatment of breast cancer even though the results of early clinical trials performed with ICI monotherapy in metastatic disease were modest [175]. The concept of using external radiation to sensitize poorly immunogenic tumors and enable immune response to CTLA-4 blockade has been demonstrated previously in a 4T1 breast tumor model and in several other preclinical and clinical studies [169,176,177]. The combination of ICI with external radiation in metastatic disease is, however, dependent on the abscopal effect to enable also the response of non-irradiated distant lesions [178].

Systemic radiation, through use of tumor-targeted radiopharmaceuticals, seemed even more intriguing to be combined with ICI [101,179], as it would allow reaching even smallest lesions in disseminated disease [180]. The clinical application of radiopharmaceuticals for this purpose has been scarcely described in the literature, yet, several clinical studies designed to realize this promising concept are currently on-going. They are aimed at investigating the beneficial effect of combining [177Lu]Lu-PSMA-617 or [177Lu]Lu-DOTATATE with ICIs for the treatment of metastasized castration-resistant prostate cancer (NCT03658447; NCT03805594) and neuroendocrine tumors (NCT03457948) as well as Merkel cell carcinomas (NCT04261855), respectively.

Tumor targeting with folate-based radioconjugates has been extensively investigated over the last two decades in (pre)clinical studies [39,56]. More recently, folate-based radiopharmaceuticals have gained renewed interest for imaging purposes but also for therapeutic application [79,87,90]. The utilization of folate radioconjugates to trigger the immune response would be an additional, highly promising approach applicable for many cancer diseases due to the frequent expression of the FR on various tumor types [121-123]. In breast cancer, the FR is expressed in ~50% of the cases and was shown to be associated with ~70% of triple-negative breast cancer, which is particularly aggressive [124,125,181-183].

In this study, we evaluated and applied a murine breast cancer cell line, NF9006, originally derived from a transgenic mouse model [184,185]. In vitro and in vivo studies were performed to investigate the possibility of targeting NF9006 tumor cells with [^{177}Lu]Lu-DOTA-folate. In a proof-of-concept study, [^{177}Lu]Lu-DOTA-folate was applied to NF9006 tumor-bearing mice to investigate whether this radiation stimulus would have an impact on the efficacy of anti-CTLA-4 immunotherapy.

5.2. Materials & Methods

5.2.1. Radiosynthesis of the [^{177}Lu]Lu-DOTA-Folate

In this study, an albumin-binding DOTA-folate conjugate was used for labeling with ^{177}Lu. The DOTA-folate was labeled with ^{177}Lu (no-carrier-added, in 0.05 M HCl; Medical Isotopes ITM GmbH, Germany) in a 1:5 (*v/v*) mixture of sodium acetate (0.5 M) and HCl (0.05 M) at pH ~4.5 as previously reported [87,90]. The molar activity was commonly 50 MBq/nmol if not otherwise stated in this chapter. The reaction mixture was incubated for 10 min at 95 °C, followed by a quality control using HPLC. A Merck Hitachi LaChrom HPLC system, equipped with a D-7000 interface, a L-7200 autosampler, a radiation detector (LB 506 B; Berthold) and a L-7100 pump was connected with a reversed-phase C18 column (Xterra^{TM} MS, C18, 5 μm, 150×4.6 mm; Waters). The mobile phase consisted of Milli-Q water containing 0.1% TFA (A) and acetonitrile (B). A linear gradient of solution A (95–20%) and solvent B (5–80%) over 15 min was used at a flow rate of 1 mL/min followed by 5 min equilibration of the system. A sample of the reaction mixture was diluted in Milli-Q water containing sodium diethylenetriamine pentaacetic acid (Na-DTPA, 50 μM) for quality control using HPLC.

5.2.2. Tumor Cell Culture

NF9006 tumor cells [185-189], a breast cancer cell line derived from MMTV-neu transgenic mice with the FVB/N genetic background (FVB/N-Tg(MMTVneu)202Mul/J [190,191]), were kindly provided by Prof. Martin Pruschy, University Hospital Zurich, Switzerland. KB cells (human cervical carcinoma cell line, German Collection of Microorganisms and Cell Cultures GmbH, ACC-136) and 4T1 tumor cells (kindly provided by Dr. Dyvia Vats, ETH Zurich, Switzerland) were used as FR-positive and FR-negative controls, respectively [112,192]. NF9006 and KB cells were cultured using folate-deficient RPMI (FFRPMI) medium supplemented with 10% fetal calf serum, L-glutamine and antibiotics and 4T1 cells were cultured in supplemented RPMI medium.

5.2.3. Determination of FR Expression in NF9006 Cells Relative to KB Cells

Western Blot. Western blot analysis was performed as previously reported [112]. In brief, cells were seeded into 6-well plates (3×10^6 cells/well) in FFRPMI with supplements and incubated overnight at 37 °C and 5% CO_2 to form a monolayer. Cell lysates were prepared using 50–70 μL cell lysis buffer (RIPA lysis and extraction buffer, 89900, Thermo Scientific), with a protease inhibitor cocktail (cOmplete^{TM}, Roche). Lysates containing 60 μg protein of NF9006 and 4T1 cells or 10 μg protein of KB cells were mixed with loading buffer containing dithiothreitol (DTT), and separated by sodium dodecyl sulfate polyacrylamide gel electrophoresis (SDS-PAGE). Proteins were transferred to a polyvinylidene fluoride membrane. Skim milk (5%) in Tris-buffered saline containing 0.05% Tween^{TM} (TBST, pH 7.5) was used to prevent unspecific binding of the antibody. Incubation with the primary anti-FR antibody (Abcam, rabbit antibody, ab67422, 1:1800) was performed overnight at 4 °C. A secondary anti-rabbit

IgG antibody (Cell Signaling, goat antibody, 7074S, 1:3000) functionalized with horseradish peroxidase was used together with Amersham ECL (enhanced chemiluminescence) Prime Western Blotting Detection Reagent (GE Healthcare) for signal detection. Detection of GAPDH served as a protein loading control (Cell Signaling, 5174S, rabbit mAb, 1:2000 and (HRP)-conjugated anti-rabbit IgG, 7074S, 1:5000). The results were quantified based on the peaks in the profile plot obtained in ImageJ software (version 1.52d). The intensity of the bands of the FR were standardized to the respective signal of GAPDH band, and put into relation to the signal obtained with KB cells (set as 100%). The results were obtained from several western blots.

FR Saturation Experiments. NF9006 and KB tumor cells, respectively, were seeded in 48-well plates ($\sim$0.25$\times$10^6 cells in 0.5 mL FFRPMI with supplements), and incubated at 37 °C and 5% CO_2 to allow cell attachment overnight. [^{177}Lu]Lu-DOTA-folate (20 MBq/nmol) was diluted in PBS to obtain folate concentrations up to 5 µM and 20 µM for NF9006 and KB tumor cells, respectively. The experiment was performed on ice in order to prevent FR internalization. The tumor cells were washed with ice-cold PBS pH 7.4 before adding fresh FFRPMI without additives (450 µL per well) and [^{177}Lu]Lu-DOTA-folate (50 µL) to obtain final folate concentrations in the range of up to 500 nM and up to 2 µM per well for NF9006 and KB cells, respectively. Unspecific binding of [^{177}Lu]Lu-DOTA-folate was determined in separate cell samples which were co-incubated with excess folic acid (100 µM) to block surface-exposed FRs. After incubation of the cells by shaking the well plates for 1 h at 4 °C, cells were washed twice with PBS to remove unbound [^{177}Lu]Lu-DOTA-folate followed by cell lysis using a sodium hydroxide solution (1 M, 0.5 mL). The cell suspensions were transferred into Ria tubes for measurement in a γ-counter (Perkin Elmer Wallac Wizard 1480). The data were fitted with a one-site binding saturation curve using GraphPad Prism software (version 7.0) in order to determine the plateau and reading the counts of the B_{max} value.

5.2.4. Cell Uptake and Internalization

Uptake and internalization of [^{177}Lu]Lu-DOTA-folate (25 MBq/nmol) was determined as previously reported [90]. NF9006 tumor cells were seeded in 12-well plates ($\sim$7$\times$10^5 cells in 2 mL FFRPMI culture medium/well) and incubated at 37 °C and 5% CO_2 to allow adhesion and growth overnight. The cells were washed with PBS prior to the addition of FFRPMI cell culture medium (975 µL/well) and [^{177}Lu]Lu-DOTA-folate (37.5 kBq, 25 µL, 1.5 pmol per well). The well-plates were incubated for 4 h at 37 °C and 5% CO_2. To determine the uptake of [^{177}Lu]Lu-DOTA-folate, tumor cells were washed with ice-cold PBS. The internalized fraction was determined in cells washed with stripping buffer (aqueous solution of 0.1 M acetic acid and 0.15 M NaCl, pH 3). All cell samples were lysed by addition of NaOH (1 M, 1 mL) to each well and measured in a γ-counter (Perkin Elmer, Wallac Wizard 1480). The protein concentration was determined for each sample using a Micro BCA Protein Assay kit (Pierce, Thermo Scientific) in order to standardize the measured activity (percentage of total added activity) to the

amount of proteins in each well. The experiments were performed at least three times in triplicate. Cell internalization experiments with KB and 4T1 tumor cells were performed in analogy, however, normal RPMI medium was used for 4T1 tumor cell experiments.

5.2.5. NF9006 and KB Cell Uptake of Variable Molar Amounts of [^{177}Lu]Lu-DOTA-Folate

NF9006 tumor cell uptake and internalization of [^{177}Lu]Lu-DOTA-folate at variable molar amounts of DOTA-folate was determined to better understand potential saturation effect of the FRs by non-radioactive folate due to the lower FR-expression level on these cells. For comparison, the same experiments were also performed with KB tumor cells. Uptake and internalization of [^{177}Lu]Lu-DOTA-folate was determined as previously reported [90], using variable amounts of DOTA-folate (0.75, 1.5, 7.5, 15, 37.5 and 75 pmol per well) while keeping the activity constant. The plates were incubated at 37 °C, 5% CO_2 for 4 h and afterwards washed according to the procedure described in the section 5.2.4.

5.2.6. In Vitro Autoradiography

Autoradiography studies were performed on frozen tissue sections of NF9006, KB and 4T1 tumors as previously reported [138]. NF9006 tumors were grown in FVB mice, KB tumors were grown in CD-1 athymic nude mice and 4T1 tumors were grown in normal BALB/c mice. The collected tumors were embedded in TissueTek (Cryo-M-Bed, Bright) and frozen at –80 °C. Tumor tissue sections of 5–10 μm thickness were prepared using a cryotome (Bright OTF Cryostat, OTF/AS-001/MR/V/304/X, Huntingdon, England). Slides were thawed and incubated in Tris-buffer (167 mM Tris-HCl, 5 mM $MgCl_2$) containing 0.25% BSA for 10 min at room temperature (RT). [^{177}Lu]Lu-DOTA-folate (50 MBq/nmol) was diluted in Tris-buffer containing 1% BSA (0.5 MBq/mL; corresponding to 0.01 μM folate) and added on the tissue sections (100 μL). Excess folic acid (100 μM) was used to block FRs. After incubation of the sections for 1 h at RT, the slides were washed several times and air-dried. Autoradiographic images were obtained using a storage phosphor system (Cyclone Plus, Perkin Elmer) and the signal intensity was quantified using OptiQuant software (version 5.0, Bright Instrument Co Ltd, Perkin Elmer). The signals obtained from NF9006 and 4T1 tumor sections were expressed relative to the signal obtained for KB tumor sections (set as 100%). Representative images were prepared using Adobe Photoshop CC (version 2017).

5.2.7. In Vivo Experiments

All applicable international, national and institutional guidelines for the care and use of animals were followed and the experiments were carried out according to the guidelines of Swiss Regulations for Animal Welfare. The preclinical studies were ethically approved by the Cantonal Committee of Animal Experimentation and permitted by the responsible cantonal authorities (license N° 75679, N° 75721 and N° 79692).

Female FVB/NCrl mice were obtained from Charles River Laboratories (Sulzfeld, Germany) at the age of 6–7 weeks and fed with a folate-deficient rodent diet (ssniff Spezialdiäten GmbH; Soest, Germany). After acclimatization for 5–7 days, the mice were subcutaneously inoculated with $2.5{\times}10^6$ NF9006 tumor cells in 100 μL PBS.

5.2.8. Biodistribution and Dosimetry of [^{177}Lu]Lu-DOTA-Folate

Biodistribution studies were performed in quadruplicate, 12–14 days after NF9006 tumor cell inoculation (tumor volume: ~100–300 mm^3). Mice were intravenously injected with [^{177}Lu]Lu-DOTA-folate (3 MBq, 0.5 nmol, 100 μL) and sacrificed at defined time points. FR-specific uptake of [^{177}Lu]Lu-DOTA-folate at 4 h p.i. was confirmed by preinjection of excess folic acid (100 μg, 100 μL per mouse) to block FRs. Selected tissues and organs were collected, weighed, and counted using a γ-counter (Perkin Elmer, Wallac Wizard 1480). The results were listed as a percentage of the injected activity per gram of tissue mass (% IA/g).

Dosimetric calculations were performed based on non-decay-corrected biodistribution data. The cumulated activity was estimated by calculating the time-integrated activity concentration coefficients (TIACCs) and used for calculation of the mean specific absorbed dose (Gy/MBq) to the NF9006 tumors and kidneys. The absorbed fractions for the tumor and the kidneys were assessed by Monte Carlo simulations using PENELOPE 2014 [193] (Supplementary Material of [194]).

5.2.9. SPECT/CT Imaging Studies

The acquisition of SPECT/CT images was performed with a dedicated small-animal SPECT/CT scanner (NanoSPECT/CT™, Mediso Medical Imaging Systems, Budapest, Hungary) as previously reported [87,90]. CT scans of 7.5 min duration time were followed by a SPECT scan of ~40 min of NF9006 tumor-bearing mice at 4 h and 24 h after injection of [^{177}Lu]Lu-DOTA-folate (25 MBq, 0.5 nmol, 100 μL PBS pH 7.4 with 0.05% BSA). During the scans, mice were anesthetized with a mixture of isoflurane and oxygen. The images were acquired using Nucline Software (version 1.02, Mediso Ltd., Budapest, Hungary). The reconstruction of SPECT data was performed using HiSPECT software (version 1.4.3049, Scivis GmbH, Göttingen, Germany). Images were prepared using VivoQuant post-processed software (version 3.5, inviCRO Imaging Services and Software, Boston USA). A Gauss post-reconstruction filter (FWHM = 1 mm) was applied twice and the scale of activity was indicated on the images (minimum value = 3 Bq/voxel to maximum value = 20 Bq/voxel). The activity in the mice was measured immediately after injection of [^{177}Lu]Lu-DOTA-folate (set as 100%) and before scanning to allow determination of the percentage activity retained in the mice based on these non-decay corrected activity measurements.

5.2.10.   NF9006 Tumor Response to [^{177}Lu]Lu-DOTA-Folate Administration

[^{177}Lu]Lu-DOTA-folate was applied to NF9006 tumor-bearing mice to determine the maximum absorbed tumor dose of [^{177}Lu]Lu-DOTA-folate, which did not have a substantial effect on the tumor growth. In brief, mice with NF9006 tumors were divided in three groups (n=5) and injected with vehicle (PBS containing 0.05% BSA) or 5 MBq and 10 MBq [^{177}Lu]Lu-DOTA-folate to deliver a mean absorbed tumor dose of 3.5 Gy and 7 Gy, respectively. The tumor sizes and body weights were measured every other day over a period of 70 days. The mice were monitored by general observation and measuring the tumor size and body weight. The tumor dimension was determined by measuring the longest tumor axis (L) and its perpendicular axis (W) using a digital caliper to determine the tumor volume (TV) according to the equation [$TV = 0.5 \times (L \times W^2)$]. The relative tumor volume (RTV) was defined as [TV_x/TV_0], where TV_x is the tumor volume in mm^3 at a given Day x and TV_0 the tumor volume in mm^3 at Day 0. The relative body weight (RBW) was defined as [BW_x/BW_0], where BW_x is the body weight in gram at a given Day x and BW_0 the body weight in gram at Day 0. Endpoint criteria, which required euthanasia of the mice, were defined as (i) a tumor volume of ≥ 1000 mm^3, (ii) body weight loss of $\geq 15\%$, (iii) a combination of a tumor size of ≥ 800 mm^3 and body weight loss of $\geq 10\%$ and/or (iv) ulceration of the tumor and/or (v) abnormal behavior, indicating pain or unease.

5.2.11.   Therapy Study

The subtherapeutic quantity of [^{177}Lu]Lu-DOTA-folate, which was believed to sensitize tumors to ICIs, was assessed as described in the section 5.2.10. The design of the therapy study was adapted from Demaria et al. [176]. The experiment was performed with four groups of NF9006 tumor-bearing mice (n=11) with an average initial tumor volume of 70–110 mm^3 and initial body weight of ~21 g (Table 5.1). [^{177}Lu]Lu-DOTA-folate (5 MBq; 0.5 nmol) was diluted in PBS (100 μL) containing 0.05% BSA (vehicle) and injected into a lateral tail vein. The immunoglobulin G (polyclonal Syrian hamster IgG, InVivoMab, BioXCell; 200 μg) or anti-mouse CTLA-4 monoclonal antibody (anti-CTLA-4 antibody, InVivoMab, clone 9H10, BioXCell; 200 μg) were applied intraperitoneally in 200 μL dilution buffer. Control mice (Group A) were sham-treated with vehicle on Day 0 and a control antibody (IgG) at Day 1, 4 and 7. Mice of Group B received [^{177}Lu]Lu-DOTA-folate and IgG and mice of Group C received the vehicle and anti-CTLA-4 antibody in an analogous sequence. Mice of Group D received [^{177}Lu]Lu-DOTA-folate and anti-CTLA-4 antibody (Table 5.1). The methods employed for this study were identical to those applied for the therapy study where NF9006 tumor response to 5 MBq and 10 MBq [^{177}Lu]Lu-DOTA-folate was investigated. For data analysis, one mouse of Group B was excluded because it did not develop a tumor, and one mouse of Group C was excluded due to the premature death after i.p. administration of the antibody.

Table 5.1 Design of the therapy study and tumor volumes and body weights at therapy start

Group (n=11)	Treatment		Tumor volume[1] (mm³) (average ± SD) Day 0	Body weight[1] (g) (average ± SD) Day 0
	[¹⁷⁷Lu]Lu-DOTA-folate (applied at Day 0)	Antibody (applied at Days 1, 4 and 7)		
A	vehicle	Control IgG antibody (200 µg/day)	110 ± 51	22.3 ± 1.8
B	[¹⁷⁷Lu]Lu-DOTA-folate (5 MBq)	Control IgG antibody (200 µg/day)	71 ± 44^{2}	21.3 ± 1.6^{2}
C	vehicle	anti-CTLA-4 antibody (200 µg/day)	98 ± 75^{2}	21.2 ± 1.6^{2}
D	[¹⁷⁷Lu]Lu-DOTA-folate (5 MBq)	anti-CTLA-4 antibody (200 µg/day)	88 ± 67	21.4 ± 1.6

* vehicle: 0.05% BSA in PBS
[1] No significant differences determined between the values measured for each group ($p>0.05$)
[2] These values refer to the n=10 mice after exclusion of one mouse in Group B and C, respectively.

5.2.12. Assessment of the Therapy

The tumor growth inhibition (TGI) was defined as $[100 - (RTV_T/RTV_C \times 100)]$ where RTV_T is the relative tumor volume of treated mice at Day 8, when the first mouse of the control group (Group A) reached the endpoint, and RTV_C is the average relative tumor volume of control mice. The TGD_2, TGD_5 and TGD_8 were calculated as the time required for the tumor volume to increase 2-, 5-fold and 8-fold, respectively, over the initial volume at the Day 0. The tumor growth delay index (TGDI) was calculated as the TGD_2, TGD_5 and TGD_8 ratio of treated mice (T) over control mice (C) $[TGDI_x = TGD_x(T)/TGD_x(C); x = 2, 5$ or $8]$.

In order to determine whether the efficacy of the therapy was dependent on initial tumor size, the therapeutic effect, quantified by TGDIs and survival of each individual mouse, was correlated with the initial tumor size of the respective mouse.

Potential early side effects were assessed by comparison of average body weights, blood plasma chemistry and organ mass-to-brain mass ratios.

The body weight of each individual mouse was measured every other day until an endpoint was reached. Comparison of the average relative body weights (RBW) and absolute body weights (ABW) of control mice and mice of Groups B–D was performed at Day 8 and at the endpoint.

Immediately before euthanasia of the mice that reached the endpoint, the blood was sampled from the retrobulbar vein. The values of creatinine (CRE), blood urea nitrogen (BUN), alkaline phosphatase (ALP), total bilirubin (TBIL) and albumin (ALB) were determined in blood plasma after centrifugation of the blood using a dry chemistry analyzer (DRI-CHEM 4000i, FUJIFILM, Japan).

After euthanasia, selected organs were collected and weighed. The organ mass-to-brain mass ratios were calculated as previously reported [158].

5.2.13. Assessment of PET Radiotracers for Monitoring NF9006 Tumors

Radiotracers. [18F]AzaFol was synthesized at ETH Zurich according to a previously reported method [75]. [18F]Fluoro-deoxy-glucose ([18F]FDG) was purchased from the radiopharmacy of the University Hospital Zurich.

Biodistribution Studies. FVB/NCrl mice were subcutaneously inoculated with NF9006 tumor cells $(2.5 \times 10^6$ cells) on the right and left shoulder about two weeks before starting the experiment. Biodistribution studies were performed in quadruplicates, when the tumor size reached a volume of ~100–300 mm³. Mice were intravenously injected with [18F]AzaFol (5 MBq/100 µL) or [18F]FDG (5 MBq/100 µL). Receptor-specific uptake of [18F]AzaFol was confirmed by injection of excess folic acid (100 µg, 100 µL per mouse in PBS) to block FRs. The animals were sacrificed at 1 h and 2 h after administration of the respective PET agent. Selected tissues and organs were collected and weighed followed by the measurement of activity in a γ-counter (Perkin Elmer, Wallac Wizard 1480). The results are listed as percentage of the injected activity per gram of tissue mass (% IA/g), using counts of a defined volume of the original injection solution measured at the same time resulting in decay-corrected values.

PET/CT Imaging. For PET imaging, FVB/NCrl mice were subcutaneously inoculated with NF9006 tumor cells $(2.5 \times 10^6$ cells) on the right shoulder, about two weeks before the experiment. PET/CT scans were performed using a small-animal bench-top PET/CT scanner (G8, Perkin Elmer, Massachusetts, U.S. [139]), as previously reported, with a set energy window ranging from 150 keV to 650 keV [70]. Mice were intravenously injected with [18F]AzaFol (5 MBq/100 μL) or [18F]FDG (5 MBq/100 μL). Static whole-body PET scans of 10 min duration were performed at 1 h and 2 h after injection of the respective PET agent, followed by a CT scan of 1.5 min. During the scan, mice were anesthetized with a mixture of isoflurane and oxygen. The acquisition of the data and their reconstruction was performed using the G8 PET/CT scanner software (version 2.0.0.10). All images were prepared using VivoQuant post-processing software (version 3.5, inviCRO Imaging Services and Software, Boston U.S.). The scale of activity for 18F was set as indicated on the images.

5.2.14. Statistical Analysis

Statistical analysis of FR-specific binding of [177Lu]Lu-DOTA-folate determined in cell uptake and autoradiography studies was performed using one-way ANOVA with Bonferroni's multiple comparisons post-test. Biodistribution data were analyzed using two-way ANOVA with Sidak's multiple comparisons post-test. The initial body weight and tumor volume of therapy mice were tested for statistical significance using one-way ANOVA with Dunnett's multiple comparisons post-test. The average blood plasma parameters and the organ data of each group were analyzed for significance using a one-way ANOVA test with a Dunnett's multiple comparisons post-test. Survival of mice was analyzed

with Kaplan-Meier curves and a log-rank test (Mantel-Cox). All analyses were performed using GraphPad Prism (version 7.0). A *p*-value of <0.05 was considered statistically significant.

5.3. Results

5.3.1. Radiolabeling of the Folate Radioconjugate

The quality control demonstrated in high radiochemical purity (≥98%) of the [^{177}Lu]Lu-DOTA-folate labeled at a molar activity of 50 MBq/nmol (Fig. 5.1). [^{177}Lu]Lu-DOTA-folate was used for in vitro and in vivo experiments without further purification.
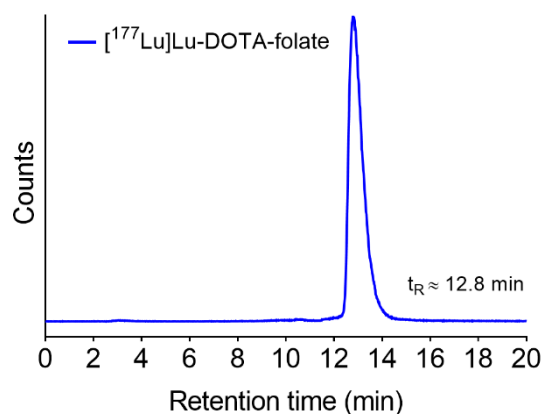
Fig. 5.1 HPLC chromatogram of the DOTA-folate labeled with ^{177}Lu. The [^{177}Lu]Lu-DOTA-folate was eluted with a retention time of $t_R \approx 12.8$ min. The presence of unreacted ^{177}Lu detected as [^{177}Lu]Lu-DTPA would appear with a retention time of $t_R \approx 3$ min.

5.3.2. Determination of FR-Expression in NF9006 Cells Relative to KB Cells

Western blot analysis demonstrated FR expression in NF9006 tumor cells at ~30-fold lower levels than in KB tumor cells, which are known to express the FR at non-physiologically high levels (Fig. 5.2a) [42]. The B_{max} value determined in saturation experiments for NF9006 tumor cells was ~35-fold lower than in KB tumor cells (Fig. 5.2b).
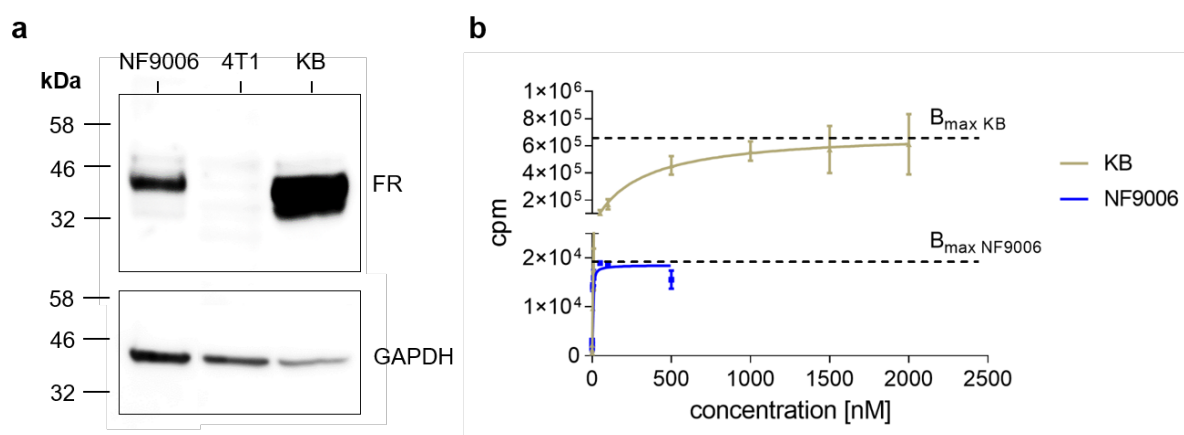
Fig. 5.2 (**a**) Image of a representative western blot. The signal of NF9006 tumor cells (60 µg) is shown in comparison to the signals of 4T1 tumor cells (60 µg) as a negative control and KB tumor cells (10 µg) as a FR-positive control. GAPDH staining was performed as a loading control. (**b**) Determination of B_{max} level of NF9006 cells in comparison to KB cells.

5.3.3. Cell Uptake and Internalization

Cell uptake and internalization studies revealed similar uptake of [^{177}Lu]Lu-DOTA-folate into NF9006 cells (102 ± 13%) as found for KB cells (set as 100%) after a 4 h-incubation period with about 50% of the activity internalized. Co-incubation with excess folic acid reduced the uptake of [^{177}Lu]Lu-DOTA-folate to <1% ($p<0.05$), which corresponded to the uptake in FR-negative 4T1 cells (~0.3%) (Fig. 5.3).
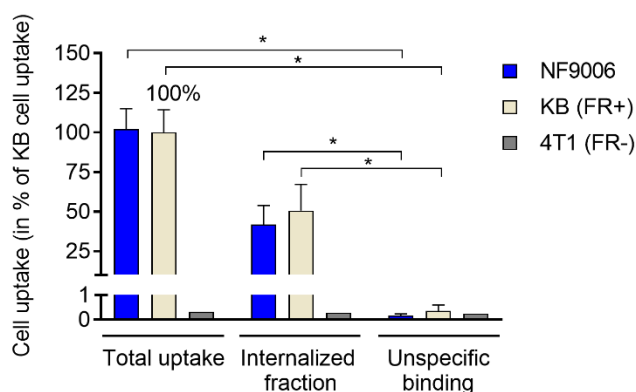
Fig. 5.3 Cell uptake and internalization of [^{177}Lu]Lu-DOTA-folate into NF9006, KB (FR-positive) and 4T1 (FR-negative) tumor cells including blocking experiments performed with excess folic acid (average ± SD, n=3–4).

5.3.4. NF9006 and KB Cell Uptake of Variable Molar Amounts of [^{177}Lu]Lu-DOTA-Folate

For NF9006 cells, application of increasing amounts of DOTA-folate (0.75, 1.5, 7.5 pmol) resulted in decreasing uptake of 50 ± 3%, 27 ± 7% and 6.5 ± 1.1%, respectively (Fig. 5.4a). Using an even higher molar amount of DOTA-folate (15, 37.5, 75 pmol) resulted in almost entire blockade of the FRs and <4% uptake of [^{177}Lu]Lu-DOTA-folate in NF9006 cells. The internalized fraction was approximately 50% of the total bound [^{177}Lu]Lu-DOTA-folate in each case. In KB cells, the use of DOTA-folate up to 37.5 pmol did not affect the uptake which ranged between 30–39%, whereof the internalized fraction
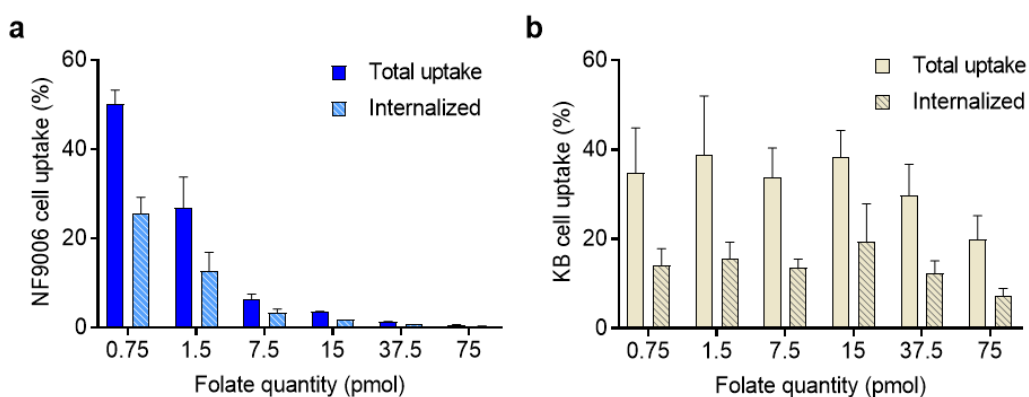
Fig. 5.4 Cell uptake of [^{177}Lu]Lu-DOTA-folate into NF9006 and KB tumor cells using variable molar quantities of the DOTA-folate. (**a**) Total uptake and internalization of [^{177}Lu]Lu-DOTA-folate into NF9006 cells; (**b**) Total uptake and internalization of [^{177}Lu]Lu-DOTA-folate into KB cells. The results are expressed as average ± SD (n=2–4).

was 12–19% (Fig. 5.4b). Cells incubated with the highest molar amount of DOTA-folate showed somewhat lower uptake of ~20% and ~7% accounted for the internalized fraction.

5.3.5.   In Vitro Autoradiography

In vitro autoradiographic images confirmed FR expression on NF9006 tumor sections, which – according to the signal intensity – was about 5-fold lower ($21 \pm 1\%$) than the signal in KB tumors (set as 100%). The binding dropped to only ~2% ($p<0.05$) on sections co-incubated with excess folic acid to block FRs, similarly to the signal for FR-negative 4T1 tumors (~4%) (Fig. 5.5a/b).
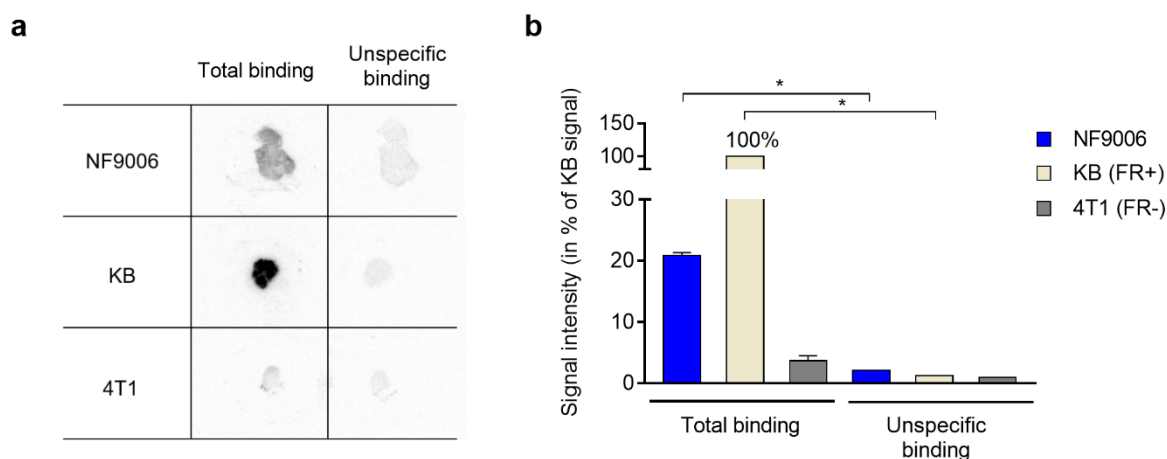
Fig. 5.5 (**a**) Autoradiographic image obtained upon binding of [^{177}Lu]Lu-DOTA-folate to NF9006, KB and 4T1 tumors sections in the absence (total binding) and presence of folic acid (unspecific binding); (**b**) Quantification of the autoradiographic signals (average $\pm$ SD, n=2). The results are presented relative to the signal intensity of KB sections (set as 100%).

5.3.6.   Assessment of the NF9006 Tumor Mouse Model for FR-Targeting

The NF9006 tumor mouse model was assessed regarding the ability to accumulate [^{177}Lu]Lu-DOTA-folate in tumors (Fig. 5.6a, Table 5.2). Significant uptake and retention was found in the tumor tissue with a maximum value of ~12% IA/g between 4 h and 24 h after injection of [^{177}Lu]Lu-DOTA-folate. Uptake of [^{177}Lu]Lu-DOTA-folate in the kidneys ($18 \pm 1\%$ IA/g; 4 h p.i.) was relatively high due to renal expression of the FR [44]. Off-target organs and tissues that do not express the FR did not substantially accumulate the [^{177}Lu]Lu-DOTA-folate. Blocking studies using excess folic acid reduced the tumor and kidney uptake of [^{177}Lu]Lu-DOTA-folate to ~50% and ~35%, respectively, of unblocked accumulation at 4 h after injection (Fig. 5.6b, Table 5.2).

Dose estimations based on non-decay corrected biodistribution data for NF9006 tumors and kidneys revealed a mean absorbed tumor dose of 0.7 Gy/MBq and a mean absorbed kidneys dose of 1.21 Gy/MBq. The resulting tumor-to-kidney dose ratio was ~0.6.
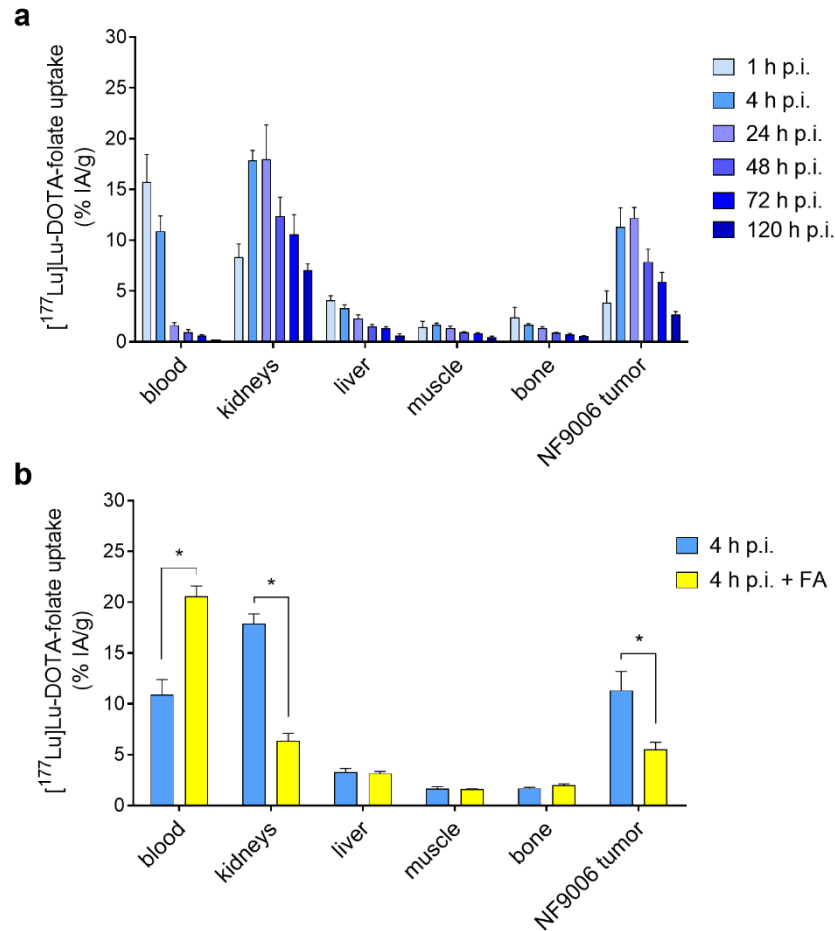
Fig. 5.6 (**a**) Graph representing the uptake of [^{177}Lu]Lu-DOTA-folate over a period of 5 days; (**b**) Graph representing the uptake of activity at 4 h p.i. of [^{177}Lu]Lu-DOTA-folate with and without pre-injected folic acid (FA). The data are decay-corrected and expressed as percentage of injected activity per gram tissue (% IA/g), reported as average ± SD obtained from each group of mice (n=3–4).

Table 5.2 Biodistribution data of [^{177}Lu]Lu-DOTA-folate in NF9006 tumor-bearing mice obtained at variable time points post injection (p.i.). The data are decay-corrected and listed as percentage of injected activity per gram tissue (% IA/g), reported as average ± SD obtained from each group of mice (n=3–4)

Organs	[^{177}Lu]Lu-DOTA-folate						
	1 h p.i.	4 h p.i.	24 h p.i.	2 days p.i.	3 days p.i.	5 days p.i.	4 h p.i. + folic acid[1]
Blood	16 ± 3	11 ± 2	1.7 ± 0.3	1.0 ± 0.2	0.60 ± 0.10	0.21 ± 0.00	21 ± 1
Heart	6.0 ± 1.3	5.6 ± 0.8	4.1 ± 0.2	2.8 ± 0.2	2.6 ± 0.2	1.3 ± 0.1	7.4 ± 0.6
Lung	6.7 ± 1.1	6.4 ± 0.6	2.6 ± 0.4	1.7 ± 0.1	1.5 ± 0.2	0.76 ± 0.18	9.0 ± 0.8
Spleen	2.0 ± 0.1	1.6 ± 0.1	0.80 ± 0.14	0.63 ± 0.09	0.55 ± 0.05	0.36 ± 0.02	2.4 ± 0.1
Kidneys	8.3 ± 1.3	18 ± 1	18 ± 3	12 ± 2	11 ± 2	7.1 ± 0.7	6.4 ± 0.7
Stomach	2.7 ± 1.2	1.7 ± 0.3	0.78 ± 0.31	0.72 ± 0.07	0.57 ± 0.15	0.38 ± 0.05	1.9 ± 0.3
Intestines	1.4 ± 0.2	1.3 ± 0.3	0.39 ± 0.03	0.32 ± 0.12	0.25 ± 0.04	0.13 ± 0.02	2.0 ± 0.5
Liver	4.1 ± 0.5	3.3 ± 0.3	2.3 ± 0.4	1.5 ± 0.2	1.3 ± 0.1	0.63 ± 0.19	3.2 ± 0.2
Salivary gl.	6.2 ± 0.4	6.4 ± 0.5	5.1 ± 0.6	3.8 ± 0.3	3.4 ± 0.5	2.7 ± 0.3	3.3 ± 0.3
Muscle	1.4 ± 0.6	1.7 ± 0.2	1.3 ± 0.2	0.93 ± 0.08	0.82 ± 0.11	0.46 ± 0.12	1.6 ± 0.1
Bone	2.4 ± 1.0	1.7 ± 0.1	1.3 ± 0.2	0.90 ± 0.03	0.74 ± 0.10	0.54 ± 0.09	2.0 ± 0.2
NF9006 Tumor	3.9 ± 1.2	11 ± 2	12 ± 1	7.9 ± 1.3	5.9 ± 0.9	2.7 ± 0.3	5.5 ± 0.7
Tu-to-blood	0.25 ± 0.09	1.1 ± 0.3	7.6 ± 1.9	8.7 ± 3.7	10 ± 4	13 ± 1	4.7 ± 5.3
Tu-to-liver	0.97 ± 0.37	3.4 ± 0.5	5.4 ± 1.1	5.3 ± 1.3	4.5 ± 1.0	4.5 ± 1.0	2.3 ± 2.4
Tu-to-kidney	0.46 ± 0.07	0.63 ± 0.10	0.69 ± 0.11	0.64 ± 0.07	0.56 ± 0.04	0.38 ± 0.06	0.31 ± 0.37

[1] excess folic acid (100 µg) was injected immediately before [^{177}Lu]Lu-DOTA-folate to block FRs

5.3.7. SPECT/CT Imaging Studies

SPECT/CT imaging studies confirmed the high uptake of [^{177}Lu]Lu-DOTA-folate in NF9006 tumors and activity in the kidneys (Fig. 5.7). The amount of [^{177}Lu]Lu-DOTA-folate injected into the mouse bearing a NF9006 tumor was 27 MBq [^{177}Lu]Lu-DOTA-folate (Fig. 5.7). In this case, ~93% of the injected activity (25 MBq) was measured in the mouse body after 4 h and ~67% (18 MBq) after 24 h p.i.
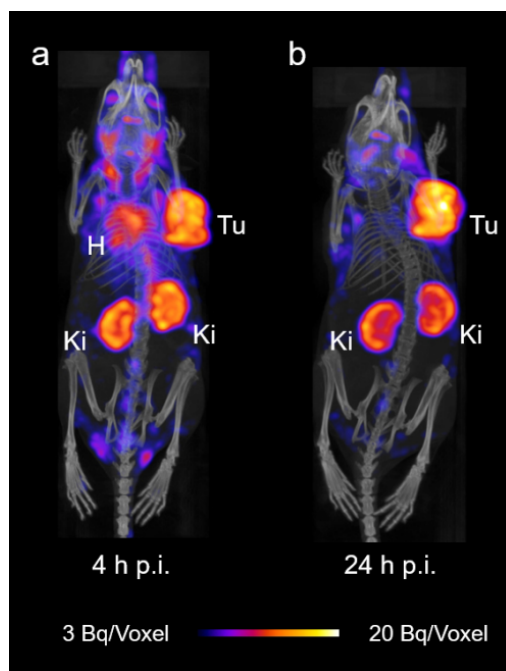
Fig. 5.7 SPECT/CT images of a NF9006 tumor-bearing mouse after injection of [^{177}Lu]Lu-DOTA-folate (25 MBq; 0.5 nmol per mouse) shown as maximum intensity projections (MIPs). Mouse images obtained (**a**) at 4 h p.i. and (**b**) at 24 h p.i. Accumulation of activity is visible in NF9006 tumors (Tu) and kidneys (Ki) and in the heart (H). Activity uptake was also observed in lymph nodes of the neck and armpit regions as well as in the choroid plexus.

5.3.8. NF9006 Tumor Response to Variable Quantities of [^{177}Lu]Lu-DOTA-Folate

The tumor size of untreated control mice (Group A) was constantly increasing over time (Fig. 5.8a). Application of 5 MBq [^{177}Lu]Lu-DOTA-folate (Group B) to obtain a tumor dose of 3.5 Gy had only a minor effect on the tumor growth visible by TGDI$_2$ and TGDI$_5$ values that were 10–20% higher than for untreated control mice (Table 5.3). Moreover, the tumor growth curve and survival curve of mice of Group B were not significantly different from those of the control group. Administration of 10 MBq [^{177}Lu]Lu-DOTA-folate (Group C) to reach a mean absorbed tumor dose of 7 Gy delayed the tumor growth significantly. The TGDIs were increased by 40–100% and the median survival was not reached within the 70 days lasting study, which was in clear contrast to the median survival time of mice of Group B (36 days) and control mice of Group A (26 days), respectively (Table 5.3, Fig. 5.8b).
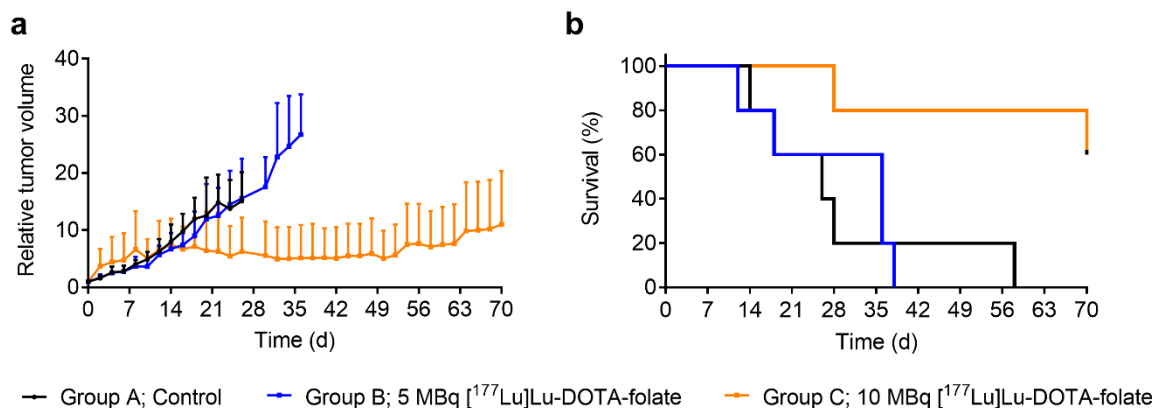
Fig. 5.8 NF9006 tumor response to variable quantities of [^{177}Lu]Lu-DOTA-folate. (**a**) Tumor growth curves relative to the tumor volume at Day 0 (set as 1) for mice that received PBS (Group A), mice treated with 5 MBq [^{177}Lu]Lu-DOTA-folate (3.5 Gy tumor dose; Group B) and 10 MBq [^{177}Lu]Lu-DOTA-folate (7.0 Gy tumor dose; Group C). (**b**) Kaplan-Meier plot indicating survival curves of mice of Groups A–C.

Table 5.3 Comparison of the time periods during which mice reached an endpoint, median survival and survival curves as well as tumor growth delay indices (TGDI$_x$)

Group	Treatment	Time frame of euthanasia (days)	Median survival (days)	Survival curve sign. different from groups[1]	TGDI$_2$	TGDI$_5$
A	Sham	14–58	26	C	1.0 ± 0.6	1.0 ± 0.3
B	[^{177}Lu]Lu-DOTA-folate, 5 MBq	12–38	36	C	1.2 ± 0.8	1.1 ± 0.4
C	[^{177}Lu]Lu-DOTA-folate, 10 MBq	28–70*	>70[2]	A, B	1.4 ± 1.3	2.0 ± 2.4

* Day 70 = End of the study

[1] Comparison of survival curves by log-rank (Mantel-Cox) test

[2] more than 50% of mice were alive at the end of the study at Day 70

5.3.9.   Therapy Study Using [^{177}Lu]Lu-DOTA-Folate and an Anti-CTLA-4 Antibody

Based on the in vitro data and biodistribution studies, the NF9006 tumor mouse model appeared useful to investigate the potential of [^{177}Lu]Lu-DOTA-folate to enhance anti-CTLA-4 immunotherapy. A subtherapeutic quantity of [^{177}Lu]Lu-DOTA-folate (3.5 Gy tumor dose; 5 MBq/mouse) was chosen to obtain a low-dose radiation stimulus of the tumor prior to immunotherapy with an anti-CTLA-4 antibody (Fig. 5.8, Table 5.3). In control mice (Group A), the tumors increased in size over the whole time of investigation (Fig. 5.9a). Mice of Groups B and C, which received either [^{177}Lu]Lu-DOTA-folate or the anti-CTLA-4 antibody, respectively (Fig. 5.9b/c), showed only ~10–40% delayed tumor growth compared to the controls (Fig. 5.9e, Table 5.4). Mice that received [^{177}Lu]Lu-DOTA-folate and anti-CTLA-4 immunotherapy (Group D), responded in 8 out of 11 cases, demonstrated by decreasing tumor volumes over time and in 7 cases the NF9006 tumors disappeared entirely (Fig. 5.9d). This led to increased tumor growth delay indices (TGDI) and tumor growth inhibition (TGI) of mice in Group D as compared to mice of the other groups (Fig. 5.9e; Table 5.4; Table 5.5). Mice of Group D also showed

the highest survival rate (~70% at Day 70) when compared to Groups A, B and C ($\leq 20\%$) (Fig. 5.9f). The median survival time of mice of Group D remained undetermined since more than 50% of the mice were still alive at the end of the study. The median survival time of mice of Group B and C was 23 days and 19 days, respectively, compared to control mice that had a median survival time of 12 days (Table 5.5).

Table 5.4 Tumor growth delay indices with x-fold increase of tumor size ($TGDI_x$) of mice that received only [^{177}Lu]Lu-DOTA-folate, anti-CTLA-4 mAb and combination of both agents

Group	Treatment	$TGDI_2$	$TGDI_5$	$TGDI_8$
A	Sham	1.0 ± 0.3 (n=11)	1.0 ± 0.3 (n=11)	1.0 ± 0.3 (n=8)
B	[^{177}Lu]Lu-DOTA-folate (5 MBq)	1.1 ± 0.7 (n=10)	1.2 ± 0.5 (n=10)	1.2 ± 0.4 (n=9)
C	Anti-CTLA-4 antibody	0.9 ± 0.4 (n=10)	1.4 ± 0.5 (n=8) n.d. (n=1)[1]	1.4 ± 0.6 (n=7) n.d. (n=1)[1]
D	Combination	1.8 ± 1.9 (n=8) n.d. (n=3)[1]	1.8 ± 1.3 (n=4) n.d. (n=6)[1]	1.9 ± 1.1 (n=4) n.d. (n=6)[1]

[1] $TGDI_2$, $TGDI_5$ and $TGDI_8$ were not determined for these mice due the small RTV which was below 2, 5 or 8, respectively.

Table 5.5 Comparison of euthanasia period and median survival of mice of the therapy study

Group	Treatment	Time frame of euthanasia* (Day)	Median survival (days)	Survival curve sig. different from groups [1]	TGI (%)
A	Sham treated	8–70	12	D	0
B	[^{177}Lu]Lu-DOTA-folate	14–70	23	D	7 ± 50
C	Anti-CTLA-4 antibody	10–70	19	D	17 ± 37
D	Combination	12–70	>70[2]	A, B, C	48 ± 28

* Day 70 = End of the study
[1] Comparison of survival curves by log-rank (Mantel-Cox) test
[2] more than 50% of mice were alive at the end of the study at Day 70
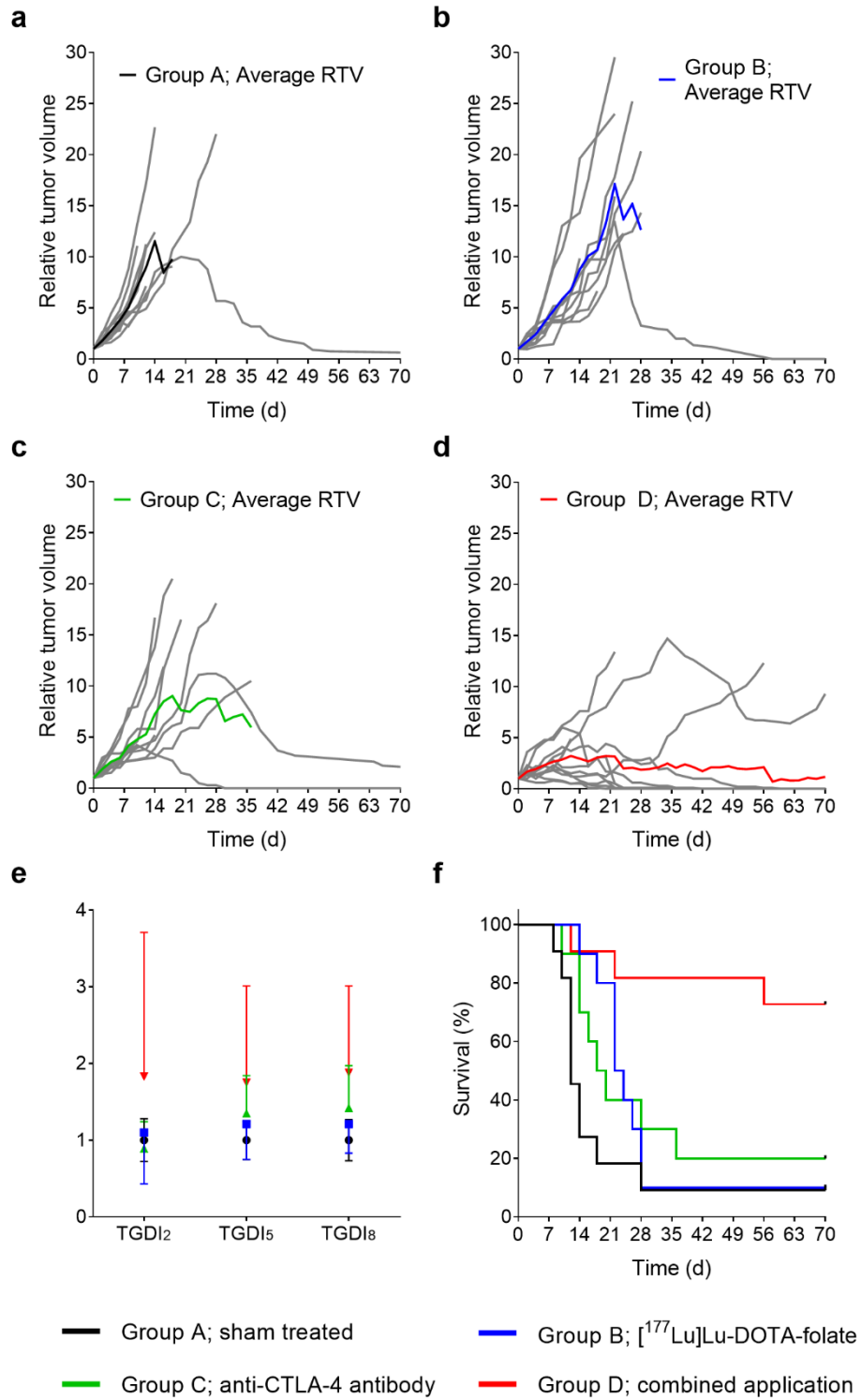
Fig. 5.9 (**a–d**) Graphs representing the relative tumor volumes (RTV) of mice in each group. (**a**) RTV of mice that received PBS (Group A), (**b**) [^{177}Lu]Lu-DOTA-folate (Group B), (**c**) anti-CTLA-4 antibody (Group C) and (**d**) a combination of both (Group D). (**e**) TGDI$_2$, TGDI$_5$ and TGDI$_8$ determined for respective groups. (**f**) Kaplan-Meier plot of Groups A–D.

Furthermore, no correlation was found between the therapeutic efficacy (TGDIs and survival) and the initial tumor size of individual mice. As demonstrated by mice of Group D (red dots), individuals with large tumors (>100 mm^3) showed comparable results as responders with small tumors (<100 mm^3) (Fig. 5.10).
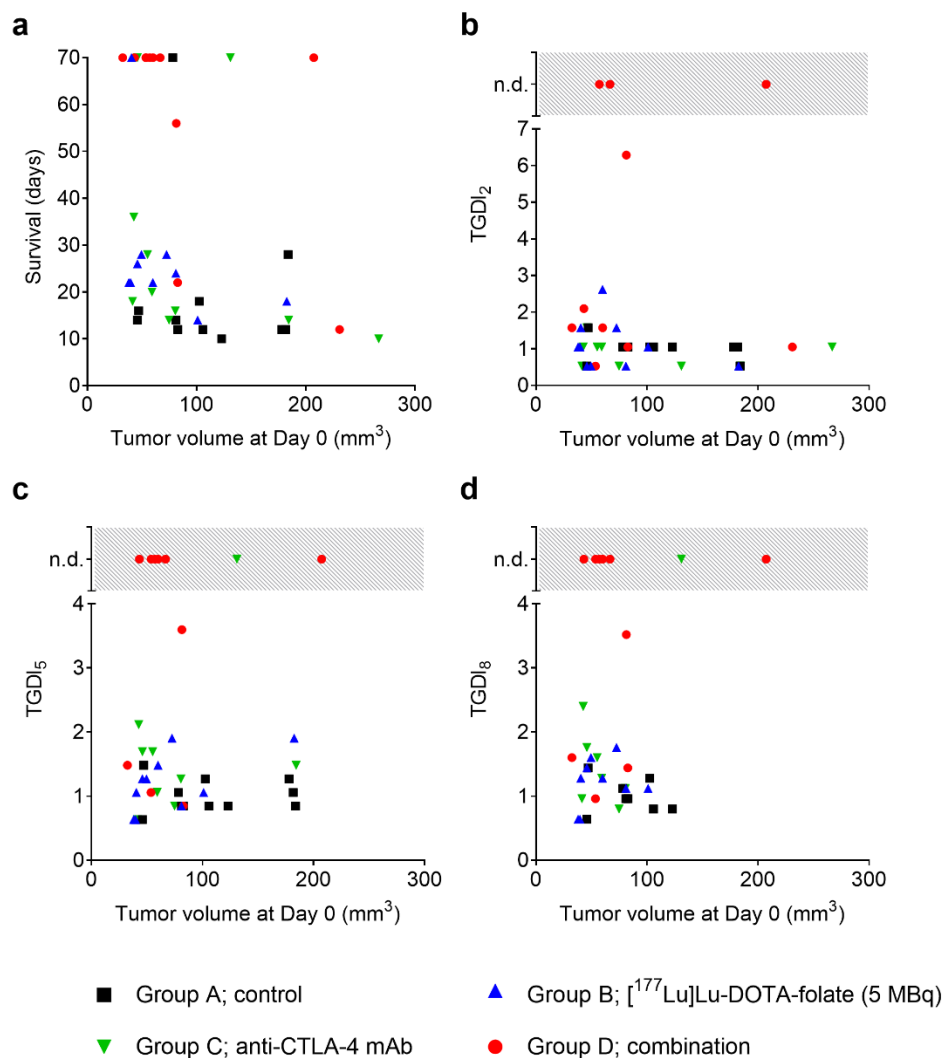
Fig. 5.10 Additional data of the therapy study performed with [^{177}Lu]Lu-DOTA-folate and anti-CTLA-4 mAb in NF9006 tumor-bearing mice. (**a–d**) Graphs that correlated the initial tumor volume of individual mice and the effect of applied treatment, expressed by (**a**) survival, (**b**) TGDI$_2$, (**c**) TGDI$_5$, (**d**) TGDI$_8$. The TGDI$_x$ points marked in the grey filled areas were not determined due to significantly delayed tumor growth, hence, the TGDI$_x$ values would be above the shown range.

5.3.10. Assessment of Potential Early Side Effects After Therapy

All mice that were euthanized before the end of the study reached the endpoint due to the tumor volume and ulceration, but not due to body weight loss. No obvious differences in body weights of mice of each group were determined among the single groups throughout the therapy study (Fig. 5.11). At Day 8, when the first mouse of the control group reached an endpoint, the body weights of mice of each group were statistically not different from each other (Supplementary Material of [194]). Comparison of the relative body weights at the endpoint of the therapy revealed significantly higher values for mice of Group D than for mice of Group A. This may be related to the fact that endpoints of mice of Group D were reached later than for mice of group A.

No significant differences between the untreated (Group A) and treated mice (Group B, C and D) were determined in blood plasma levels of CRE, BUN, ALP and TBIL at the endpoint of the therapy (Supplementary Material of [194]). Only the ALB plasma levels of Group D were elevated compared to the control mice, which might be related to the age difference of both groups at the time when they were euthanized.

No statistically significant differences were observed among treated animals (Group B–D) and untreated controls (Group A) regarding organ masses and organ-to-brain mass ratios at the time of euthanasia (Table 5.6).
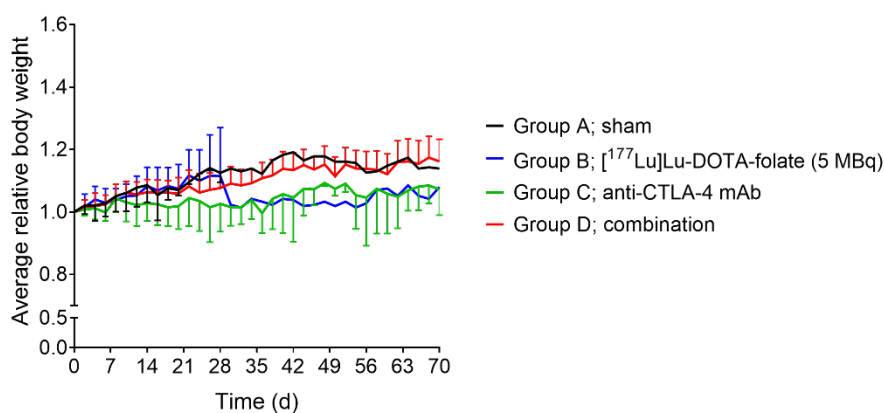
Fig. 5.11 Relative body weights of mice of the therapy study. Graph showing relative body weights of mice expressed as an average ± SD (for n ≥ 2) of each group in the time course of the study.

Table 5.6 Organ mass and corresponding organ-to-brain mass ratios obtained for the untreated and treated mice of the therapy study

Group (n=10–11)	Organ mass[1] (mg) (average ± SD)				Organ-to-brain mass ratios (average ± SD)		
	Kidneys	Liver	Spleen	Brain	Kidney-to-brain	Liver-to-brain	Spleen-to-brain
A	274 ± 27	1050 ± 80	145 ± 39	448 ± 20	0.61 ± 0.04	2.34 ± 0.16	0.32 ± 0.09
B	270 ± 21	1125 ± 109	118 ± 19	443 ± 17	0.61 ± 0.04	2.54 ± 0.24	0.27 ± 0.05
C	272 ± 22	998 ± 73	142 ± 56	436 ± 17	0.63 ± 0.05	2.29 ± 0.13	0.33 ± 0.14
D	270 ± 22	1074 ± 94	112 ± 36	448 ± 14	0.60 ± 0.04	2.40 ± 0.22	0.25 ± 0.08

[1] Data obtained at the day of euthanasia when an endpoint criterion was reached or at the end of the study (Day 70).

5.3.11. Assessment of PET Radiotracers for Monitoring NF9006 Tumors

Biodistribution Studies. [18F]AzaFol showed high accumulation in NF9006 tumors (~14% IA/g, 1 h and 2 h p.i.), but also considerable accumulation in the kidneys (42 ± 4% IA/g at 1 h p.i.; 40 ± 3% IA/g at 2 h p.i.). These findings were in line with previous experiments performed with [18F]AzaFol in KB tumor-bearing nude mice [75]. Blockade of the FRs with folic acid reduced the uptake in the tumors and kidneys to <1% IA/g and ~5% IA/g, respectively, indicating FR-specific accumulation in these tissues (Table 5.7, Fig. 5.12). Uptake of [18F]FDG in NF9006 tumors was low, in the range of ~4% IA/g (Table 5.7, Fig. 5.12). As expected, [18F]FDG accumulated in the heart, where it was ~8- to 10-fold higher than in the NF9006 tumor.

Due to the high tumor uptake, [18F]AzaFol showed higher tumor-to-blood ratios (32 ± 2; 1 h p.i.) than [18F]FDG, which reached a value of ~9 at the same time point. The tumor-to-liver and tumor-to-kidney ratios of [18F]AzaFol were, however, lower than the respective ratios of [18F]FDG, due to the lower accumulation of [18F]FDG in the liver and kidneys (Table 5.7).

Table 5.7 Biodistribution data of [18F]AzaFol and [18F]FDG, in NF9006 tumor-bearing mice at 1 h and 2 h after injection of the PET agents. The data are decay-corrected and listed as percentage of injected activity per gram tissue (% IA/g), reported as average ± SD obtained from each group of mice (n=4).

Organs & Organ Ratios	[18F]AzaFol			[18F]FDG	
	1 h p.i.	2 h p.i.	1 h p.i. + blockade	1 h p.i.	2 h p.i.
Blood	0.45 ± 0.02	0.31 ± 0.02	0.84 ± 0.19	0.44 ± 0.04	0.28 ± 0.03
Liver	8.0 ± 0.2	9.3 ± 1.1	14 ± 5	0.80 ± 0.21	0.56 ± 0.11
Kidney	42 ± 4	40 ± 3	5.2 ± 1.7	1.1 ± 0.1	0.80 ± 0.10
Tumor	14 ± 1	14 ± 1	0.64 ± 0.18	4.1 ± 1.5	3.8 ± 0.6
Tu-to-blood	32 ± 2	46 ± 3	0.76 ± 0.13	9.2 ± 2.8	14 ± 3
Tu-to-liver	1.8 ± 0.1	1.5 ± 0.1	0.05 ± 0.01	5.1 ± 1.3	7.1 ± 1.7
Tu-to-kidney	0.34 ± 0.02	0.36 ± 0.03	0.13 ± 0.03	3.9 ± 1.4	5.0 ± 1.1
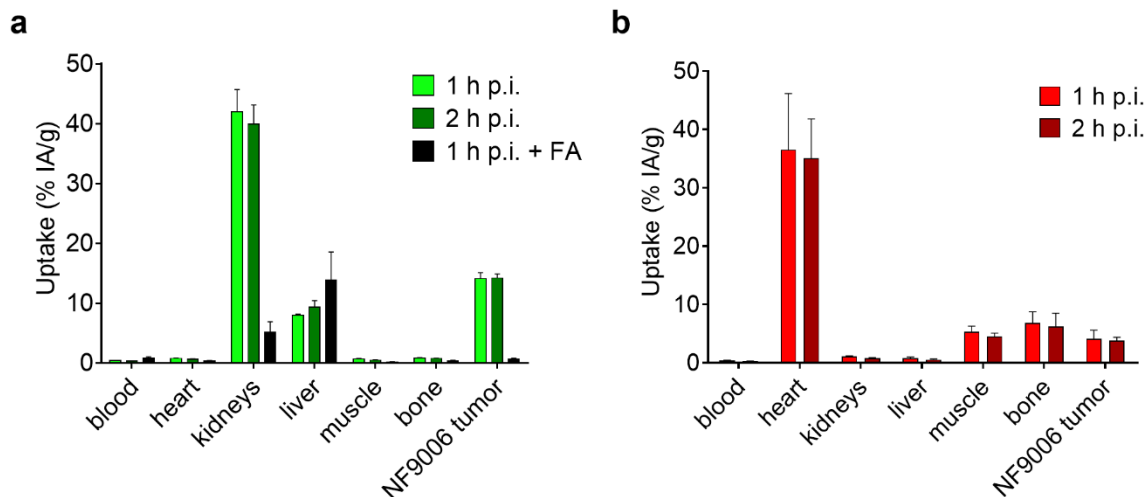
Fig. 5.12 Biodistribution data obtained in NF9006 tumor-bearing mice 1 h and 2 h after injection of [18F]AzaFol and [18F]FDG. (**a**) Tissue distribution profile of [18F]AzaFol; (**b**) Tissue distribution profile of [18F]FDG. The bars represent the average uptake of injected activity per gram of tissue (% IA/g) ± SD obtained from each group of mice (n=4).

PET/CT Imaging Studies. PET/CT images confirmed the findings of the biodistribution studies showing distinct accumulation of [18F]AzaFol in NF9006 tumors, while uptake of [18F]FDG was low and almost not visible on the images (Fig. 5.13).
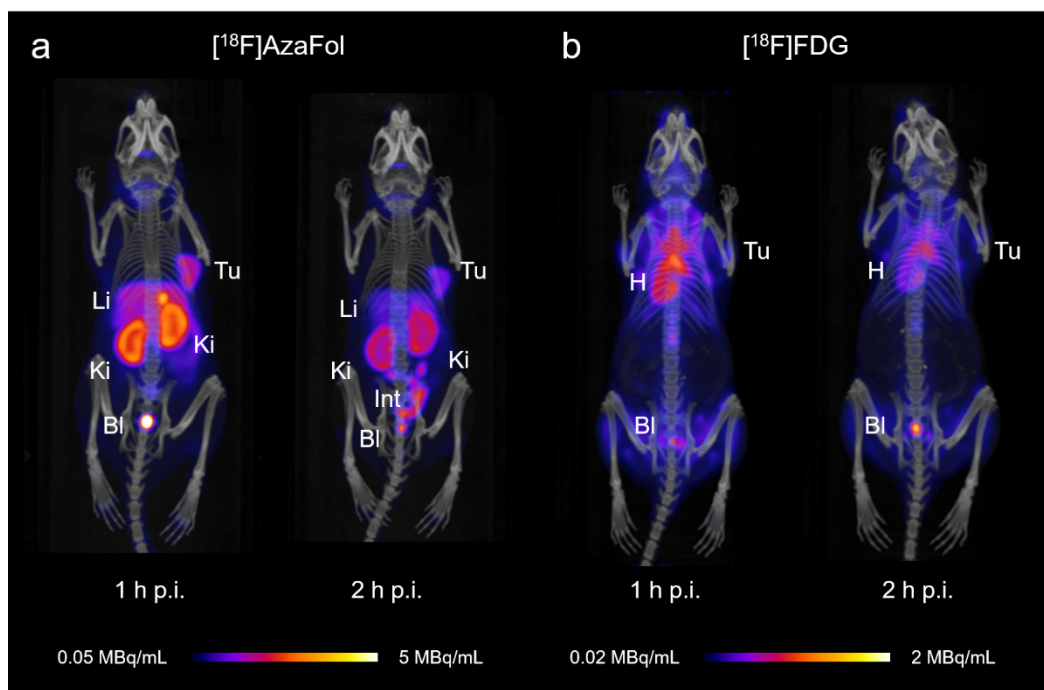
Fig. 5.13 PET/CT images of NF9006 tumor-bearing mice at 1 h and 2 after injection of or [18F]AzaFol or [18F]FDG shown as maximum intensity projections (MIPs). (**a**) PET scan obtained with [18F]AzaFol; (**b**) PET scan obtained with [18F]FDG.

5.4. Discussion

In this study, we set out to evaluate the syngeneic NF9006 breast cancer mouse model with the aim to use it for the investigation of anti-CTLA-4-based immunotherapy after low-dose irradiation delivered by application of [177Lu]Lu-DOTA-folate.

The feasibility of targeting NF9006 breast cancer with [177Lu]Lu-DOTA-folate was successfully demonstrated in vitro and in vivo. The uptake of [177Lu]Lu-DOTA-folate in NF9006 tumor cells was comparable to the results obtained with KB tumor cells in spite of the lower FR-expression level determined in NF9006 tumor cells. Obviously, the applied concentration of [177Lu]Lu-DOTA-folate was far below the quantity that would result in saturation effects of the receptor. SPECT/CT imaging and biodistribution studies with mice revealed reasonable accumulation of [177Lu]Lu-DOTA-folate in NF9006 tumors which was about half of the uptake in KB tumor xenografts (unpublished results). The uptake in lymph nodes of the neck and armpits appeared specific to the FVB mouse strain rather than related to the tumor, since the control experiments, which were performed with FVB mice without tumors, demonstrated the same distribution pattern (Supplementary Material of [194]).

The dose calculations revealed, however, that 5 MBq injected [177Lu]Lu-DOTA-folate per mouse was sufficient to obtain 3.5 Gy absorbed tumor dose. This quantity of injected [177Lu]Lu-DOTA-folate resulted in an absorbed kidney dose (~6 Gy) far below the safe limit of 23 Gy [79]. The tumor growth delay of mice that received [177Lu]Lu-DOTA-folate prior to anti-CTLA-4 antibody therapy was at least doubled, since three mice of this group did not reach the RTV of 2, and six mice did not reach the RTV of 5 and 8 during the time of investigation. As a consequence, the survival time of this group of mice substantially increased.

These data clearly indicate the promising potential of [177Lu]Lu-DOTA-folate to be used as a radiation stimulus to enhance breast tumor response to anti-CTLA-4 immunotherapy. It is hypothesized but not confirmed yet, that the observed effect was based on radiation-induced changes in the tumor microenvironment. This may include CD8+ T cell infiltration and recruitment of innate immune cells as it was previously reported in preclinical studies that used radioconjugates to enhance the response to ICIs in mouse models of melanoma [101,103], non-Hodgkin lymphoma [99] and colon cancer [179].

It is worth mentioning that the therapy data of our study resulted from mouse groups with tumors in a relatively large volume range, which is a relevant finding in view of the clinical situation, in which large inter- and intra-individual differences among the stages of tumor metastases are expected. It indicated that even larger tumors responded well, although it is known that the size of tumors may critically influence the infiltration of immune cells [195-198].

The set-up of future preclinical studies has to be carefully evaluated in order to provide robust data that are meaningful in view of clinical translation of the proposed concept. It is, thus, essential to investigate the underlying mechanism of the immune cell response upon application of [177Lu]Lu-DOTA-folate as

previously reported for [^{177}Lu]Lu-DOTATATE [102]. This may provide relevant information to allow a further optimization of the treatment scheme.

Spontaneous tumor mouse models would reflect the patient situation better, however, using transgenic MMTV-neu mice, from which NF9006 cells are derived, would require effective means to determine the tumor burden before and during therapy. In this context, we investigated the option of positron emission tomography (PET) imaging using [^{18}F]AzaFol, a clinically investigated PET folate radiotracer [75,76] which unambiguously visualized NF9006 tumors in mice, while this was not the case when using [^{18}F]FDG, the most frequently employed clinical PET radiotracer.

Certainly, the approach reported in this study is not limited to the use of [^{177}Lu]Lu-DOTA-folate but may open new application fields for other tumor-targeting radioconjugates that may induce immunogenic cell death and, thus, enhance ICI therapy as previously reported by Rouanet et al. [103]. Similarly, other systemic therapies, such as radiosensitizing chemotherapeutics and mTOR inhibitors may also profit from combination with tumor-targeting radioconjugates [14].

5.5.　Conclusion

In this study, we demonstrated the promising potential of [^{177}Lu]Lu-DOTA-folate to enhance the tumor response to ICIs. In view of a future clinical translation, further preclinical studies are warranted for an in-depth understanding of the underlying immune response to radiation in this model. The approach of turning "cold" tumors "hot" by application of low-dosed radiopharmaceuticals may provide nuclear oncology with a new dimension in the context of future perspectives in cancer therapy.

VI. Imaging Studies of FR-positive Tumors Using Transgenic Mouse Model of Mammary Gland Carcinoma

Patrycja Guzik[1], Susan Cohrs[1], Cristina Müller[1,2]

[1] *Center for Radiopharmaceutical Sciences ETH-PSI-USZ, Paul Scherrer Institute, 5232 Villigen-PSI, Switzerland*

[2] *Department of Chemistry and Applied Biosciences, ETH Zurich, 8093 Zurich, Switzerland*

6.1. Introduction

Cell line-derived subcutaneous tumor models are most often used in preclinical research as they are easy to prepare, fast, reproducible and, therefore, efficient tools for drug screening and development. Such models have, however, certain drawbacks with regard to their use for testing therapeutics whose success is dependent on the interplay with endogenous factors [199]. Human xenograft models in athymic nude mice do not reflect the patient situation properly, primarily due to tumor homogeneity and lack of a natural tumor microenvironment including the crosstalk between the tumor and immune cells [106]. Subcutaneous syngeneic models are better in this regard as they are established in immunocompetent mouse strains, however, they are also characterized by poor heterogeneity, since they are commonly generated from in vitro artificially selected tumor cell lines [104,197]. These factors may be the reason for poor predictability of clinical results based on preclinical data obtained in subcutaneous tumor mouse models. Certainly, it must be the aim to increase the probability of a successful translation of a drug to clinical practice, hence, choosing an adequate mouse model that would deliver more meaningful results, is of paramount interest.

Genetically engineered tumor mouse models (GEMMs) are generated by introducing mutations in genes associated with human cancers. They have been developed for many common tumor types including breast, lung, colon, prostate or pancreatic cancers [200]. Transgenic models are valuable for the identification of molecular targets, the investigation of tumorigenesis, and the role of tumor microenvironment or mechanisms underlying tumor responsiveness and resistance to a treatment [201]. In contrast to human xenograft and syngeneic tumor models, spontaneous models represent the entire development of a tumor that is characterized by higher heterogeneity. They are established in immunocompetent mice which allows investigation of the immune response, and hence, immune-stimulating therapies [201].

Numerous FR-targeting anticancer agents have been preclinically evaluated in terms of their pharmacokinetic properties and therapeutic efficacy in human xenograft models mostly based on KB or IGROV-1, as well as in the syngeneic M109 lung cancer mouse model. Some of these drugs were advanced to clinical trials [24], however, most of them dropped out in Phase II or Phase III clinical trials because their therapeutic efficacy in patients did not meet the predefined endpoint criteria of the study [105]. Thus, poor predictability of clinical outcomes based on preclinical data was also encountered in the context of folate receptor (FR)-targeting agents. To date, the application of FR-targeting drugs in transgenic models has been scarcely described in the literature. To the best of our knowledge, none of the existing studies reported on the application of transgenic mice for nuclear imaging of the FR. One of few publications reported on the evaluation of theragnostic nanoemulsions in transgenic model of epithelial ovarian cancer [202]. In the late 90ies, Todd et al. demonstrated that SV40 large T antigen transgenic mice (SV11) with spontaneously developing tumors in the choroid plexus could be a valuable model to investigate the FR as a potential target for the therapy of human brain tumors [203]. A few

years later, the same group performed a combination therapy study with SV11 transgenic mice that were treated with IL-12 and an anti-CD28/folate bispecific conjugate [204].

Recently, we have demonstrated that the FR is expressed in NF9006 murine mammary carcinoma cells derived from FVB/N-Tg(MMTVneu)202Mul/J transgenic mice [194]. The female MMTV-neu mice develop mammary fat-pad tumors which are known to overexpress the murine HER2 protein driven by a mouse mammary tumor virus (MMTV) promoter [205]. The aim of this study was to investigate on whether the spontaneous tumors of MMTV-neu mice can be imaged using [^{177}Lu]Lu-DOTA-folate. We also wanted to investigate whether the uptake of [^{177}Lu]Lu-DOTA-folate in these tumors would be comparable to the uptake in NF9006 tumors of a syngeneic model that was established by subcutaneous cell inoculation into mice with a FVB background.

6.2. Materials & Methods

6.2.1. Radiosynthesis of [^{177}Lu]Lu-DOTA-Folate

In this study, the same albumin-binding DOTA-folate conjugate was used as in experiments performed with NF9006 tumor-bearing mice described in Chapter 5. The DOTA-folate was labeled with ^{177}Lu (no-carrier-added, in 0.05 M HCl; Medical Isotopes ITM GmbH, Germany) in a 1:5 (v/v) mixture of sodium acetate (0.5 M) and HCl (0.05 M) at pH ~4.5 as previously reported [87,90]. The molar activity was commonly 6–25 MBq/nmol. The reaction mixture was incubated for 10 min at 95 °C, followed by a quality control using HPLC. For this purpose, a sample of the reaction mixture was diluted in Milli-Q water containing sodium diethylenetriamine pentaacetic acid (Na-DTPA, 50 μM) to inject into HPLC. A Merck Hitachi LaChrom HPLC system, equipped with a D-7000 interface, a L-7200 autosampler, a radiation detector (LB 506 B; Berthold) and a L-7100 pump was connected with a reversed-phase C18 column (Xterra^{TM} MS, C18, 5 μm, 150 × 4.6 mm; Waters). The mobile phase consisted of Milli-Q water containing 0.1% TFA (A) and acetonitrile (B). A linear gradient of solution A (95–20%) and solvent B (5–80%) over 15 min was used at a flow rate of 1 mL/min followed by 5 min equilibration of the system. The [^{177}Lu]Lu-DOTA-folate was obtained with high radiochemical purity (≥97%) and used for in vivo experiments without further purification steps.

6.2.2. In Vivo Studies

All applicable international, national and institutional guidelines for the care and use of animals were followed and the experiments were carried out according to the guidelines of Swiss Regulations for Animal Welfare. The preclinical studies were ethically approved by the Cantonal Committee of Animal Experimentation and permitted by the responsible cantonal authorities (license N° 75679). Six- or 10-week old female transgenic FVB/N-Tg(MMTVneu)202Mul/J mice (The Jackson Laboratory, Bar Harbor, ME 04609, USA) were purchased from Charles River Laboratories (Sulzfeld, Germany). Animals were fed with a normal rodent chow or folate-deficient rodent diet (ssniff Spezialdiäten GmbH; Soest, Germany). Mice were monitored by measuring the body weight twice a week, from the age of ~5 months on when the first palpable tumors were expected to appear according to literature [205]. The tumor size and body weight of the mice with already palpable tumors were monitored three times a week. The tumor dimension was determined by measuring the longest tumor axis (L) and its perpendicular axis (W) using a digital caliper to determine the tumor volume (TV) according to the equation [$TV = 0.5 \times (L \times W^2)$]. Endpoint criteria, which required euthanasia of the mice, were defined as (i) a tumor volume of ≥1500 mm^3 (cumulative volume in the case of multiple tumors), (ii) body weight loss of ≥15%, (iii) a combination of a cumulative tumor volume of ≥1000 mm^3 and body weight loss of ≥10% and/or (iv) abnormal behavior, indicating pain or unease.

6.2.3. SPECT/CT Imaging Studies

SPECT/CT imaging of mice was performed when the spontaneously developed tumor reached an absolute volume of ~200–600 mm^3 (Table 6.1). The SPECT/CT acquisitions were obtained using a dedicated small-animal SPECT/CT scanner (NanoSPECT/CT^{TM}, Mediso Medical Imaging Systems, Budapest, Hungary) [87,90]. CT scans of 7.5 min duration time were followed by a SPECT scan of ~40 min at 20 h after injection of [^{177}Lu]Lu-DOTA-folate (25 MBq; 1 nmol or 5 MBq; 0.5 nmol in 100 µL PBS pH 7.4 with 0.05% BSA). During the scans, mice were anesthetized with a mixture of isoflurane and oxygen. The images were acquired using Nucline Software (version 1.02, Mediso Ltd., Budapest, Hungary) and reconstructed using HiSPECT software (version 1.4.3049, Scivis GmbH, Göttingen, Germany). Images were prepared using VivoQuant post-processed software (version 3.5, inviCRO Imaging Services and Software, Boston USA). A Gauss post-reconstruction filter (FWHM = 1 mm) was applied twice and the scale of activity was indicated on the images. After injection of [^{177}Lu]Lu-DOTA-folate for imaging, the tumor growth was monitored at least over two weeks.

Table 6.1 Summary of MMTV-neu mice used for SPECT/CT imaging studies

	Diet type	Number of injections	Time of injection (day from tumor discovery)	Absolute tumor volume at the time of injection (mm^3)	Injected quantity of [^{177}Lu]Lu-DOTA-folate
Mouse 1	Folate-free	1	22	436; 190*	5 MBq; 0.5 nmol
Mouse 2	Folate-free	1	26	246	5 MBq; 0.5 nmol
Mouse 3	Folate-free	2	24, 45	374; 409[1]	5 MBq; 0.5 nmol
Mouse 4	Standard	3	8, 30, 58	502; 482[1]; 570[1]	25 MBq; 1.0 nmol

* absolute volume of the second tumor
[1] absolute volume at the time of the second or third SPECT scan

6.2.4. Biodistribution Study

Biodistribution studies were performed with three 9.5-month-old transgenic mice whereof two had developed tumors. Mice were injected with [^{177}Lu]Lu-DOTA-folate (3 MBq; 0.5 nmol; 100 µL) into a lateral tail vein and sacrificed after 20 h. Selected tissues and organs were collected, weighed, and counted using a γ-counter (Perkin Elmer, Wallac Wizard 1480). The results were listed as a percentage of the injected activity per gram of tissue mass (% IA/g), using counts of a defined volume of the original injection solution measured at the same time resulting in decay-corrected values. Biodistribution data were tested for significance using two-way ANOVA with Sidak's multiple comparisons post-test. The analysis was performed using GraphPad Prism (version 8.0). A p-value of <0.05 was considered statistically significant.

6.2.5.   In Vitro Autoradiography

Autoradiography studies were performed on frozen tissue sections of spontaneous tumors, NF9006, KB and 4T1 tumor according to the same procedure as previously reported [138,194]. NF9006 and KB tumor sections were used as FR-positive controls, whereas 4T1 tumors served as a FR-negative control. Spontaneous tumors of MMTV-neu mice were collected from mice that were not injected with activity. The autoradiographic signals obtained from spontaneous tumors, NF9006 and 4T1 tumor sections were quantified relative to the signal obtained for KB tumor sections (set as 100%). Representative images were prepared using ImageJ (version 1.52d). Statistical analysis of FR-specific binding of [^{177}Lu]Lu-DOTA-folate was performed using one-way ANOVA with Bonferroni's multiple comparisons post-test. The analysis was performed using GraphPad Prism (version 8.0). A p-value of <0.05 was considered statistically significant.

6.3.   Results & Discussion

6.3.1.   [^{177}Lu]Lu-DOTA-Folate Binding to Spontaneous Tumors Is FR-Specific

In vitro autoradiography studies were performed in order to demonstrate whether [^{177}Lu]Lu-DOTA-folate binds to spontaneous tumors and whether the binding is FR-specific. Autoradiographic images of frozen tumor sections exposed to [^{177}Lu]Lu-DOTA-folate showed a clear signal which confirmed the FR expression in spontaneous tumors. NF9006 tumor sections obtained from the respective syngeneic tumor mouse model and KB tumor sections, grown as xenografts in nude mice, served as FR-positive control tissue. According to the signal intensities after incubation sections of spontaneous tumors with [^{177}Lu]Lu-DOTA-folate the signal intensity level was ~36 ± 18% relative to the signal of KB tumor sections which was set as 100%. The FR expression level appeared of spontaneous tumors, therefore, comparable to that in NF9006 tumors (21 ± 1%; $p > 0.05$). Co-incubation of spontaneous tumor sections with excess folic acid resulted in <1% of [^{177}Lu]Lu-DOTA-folate binding, which was similar to the signal obtained for NF9006 and KB tumors upon FR-blockade (~2%), as well as for FR-negative 4T1 tumors (~4%) (Fig. 6.1).
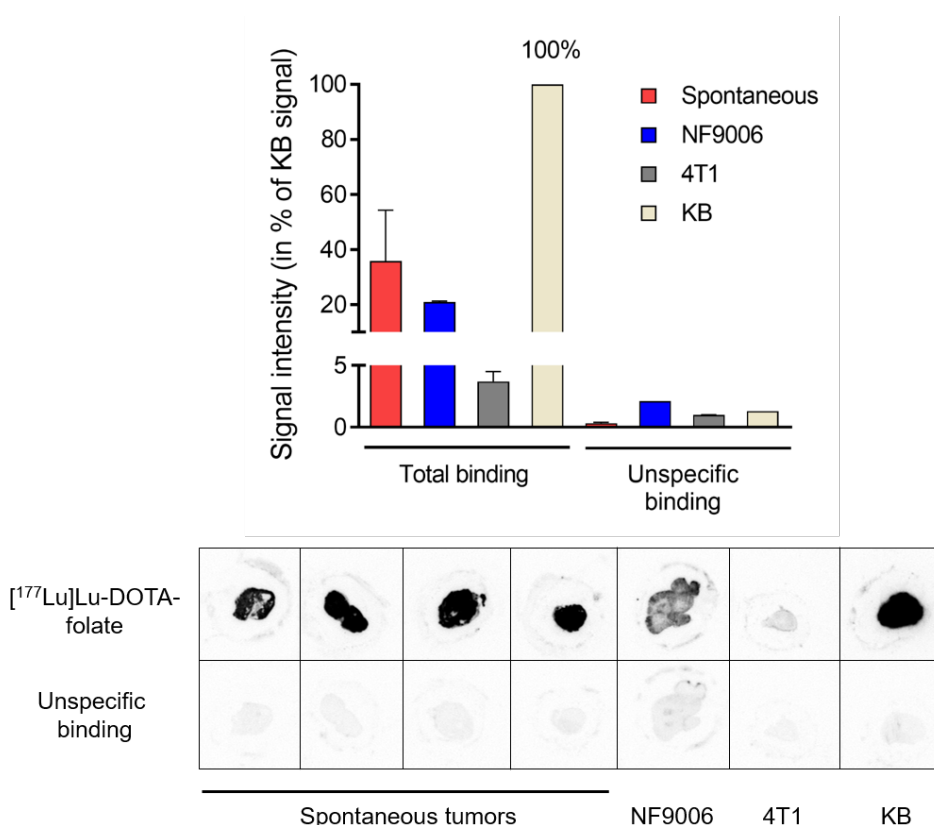
Fig. 6.1 Intensities of [^{177}Lu]Lu-DOTA-folate signal quantified based on the autoradiographic images obtained with KB tumor sections set as 100%. The intensities are shown for spontaneous tumors, NF9006 and 4T1 tumor sections in the absence (total binding) and presence of excess folic acid (unspecific binding) (average ± SD, n=2–8).

6.3.2. Spontaneous Tumors of MMTV-neu Mice Can Be Imaged with [^{177}Lu]Lu-DOTA-Folate

SPECT/CT imaging demonstrated significant accumulation of [^{177}Lu]Lu-DOTA-folate in spontaneous tumors as expected based on autoradiography studies (Fig. 6.2a/b; Fig. 6.3a/b; Fig. 6.4a/d/g). This result was in line with SPECT images obtained with NF9006 tumor-bearing mice upon injection of the same radioconjugate [194]. The images visualized the mammary gland tumors in the area of neck and armpits (Fig. 6.2a), right and left flank (Fig. 6.2b; Fig. 6.3a/b; Fig. 6.4 a/d/g) as well as inner side of hind limbs and even small lesions (data not shown). It needs to be clarified that the tumors developed on the flank
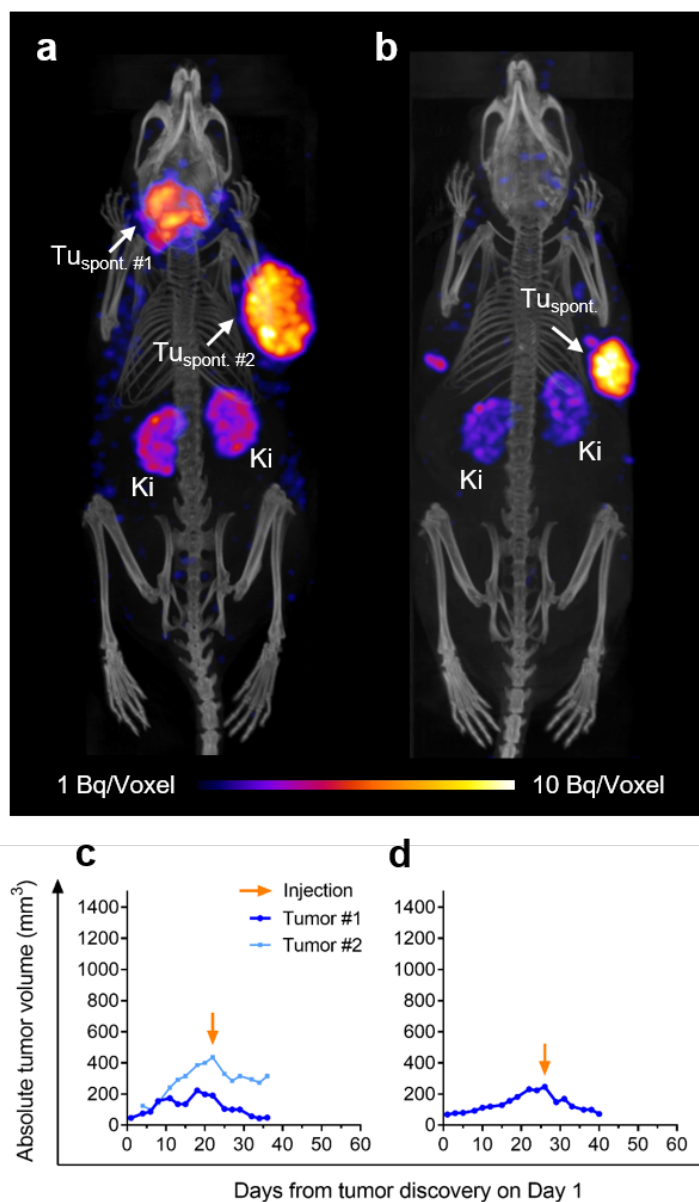
Fig. 6.2 SPECT/CT images of mice with spontaneously developed breast tumors shown as maximum intensity projections (MIPs): (**a**) Mouse 1; (**b**) Mouse 2. The images were acquired at 20 h after injection of [^{177}Lu]Lu-DOTA-folate (5 MBq; 0.5 nmol). Mice were fed with folate-free rodent chow; Tumor volume measurements collected in the time course of ~20 days before and 20 days after SPECT/CT imaging: (**c**) Mouse 1; (**d**) Mouse 2.

appeared at the similar location as the subcutaneously inoculated tumors. The images demonstrated homogenous distribution of activity in the tumor tissue which can be ascribed to our observation that the spontaneous tumors were well-vascularized.

The tumor uptake in mice injected with 5 MBq [^{177}Lu]Lu-DOTA-folate (0.5 nmol) (Mouse 1–3) was higher than the uptake in the kidneys, and consequently, the observed tumor-to-kidney ratio of accumulated activity was >1 (Fig. 6.2a/b; Fig. 6.3a/b). Injection of 25 MBq [^{177}Lu]Lu-DOTA-folate (1 nmol), as in the case of Mouse 4, resulted in visually lower tumor-to-kidney ratios than in Mouse 1–3 (Fig. 6.4 a/d/g). This discrepancy could be caused by a difference in the quantity of injected [^{177}Lu]Lu-DOTA-folate which was higher in the case of Mouse 4 (1 nmol vs. 0.5 nmol) even though it was previously demonstrated by Müller et al. that injection of molar amounts of folate in the range of 0.5 nmol to 1.0 nmol did not affect the tissue distribution significantly (Supplementary Material of [87]). Another hypothesis to explain the lower tumor-to-kidney ratio of Mouse 1–3 is related to the alteration of FR expression in the kidneys as a result of folate-deficient chow. It was reported by several groups that folate-free diet in mice decreased the FR-expression levels in normal tissues, notably in the kidneys [206-208]. If this held true in this study, it would explain the reduced kidney uptake of [^{177}Lu]Lu-DOTA-folate in mice fed with folate-free diet (Mouse 1–3).

6.3.3.   Injection of [^{177}Lu]Lu-DOTA-Folate Caused Shrinkage of Spontaneous Tumors Over Time

As demonstrated by the tumor growth curves of the respective mice, the administration of 5 MBq [^{177}Lu]Lu-DOTA-folate, which was the lowest acceptable activity to perform SPECT imaging, reduced the tumor burden in the case of Mouse 1 (Fig. 6.2c, tumor #1) and Mouse 2 (Fig. 6.2d). The volume of the second tumor of Mouse 1 (Fig. 6.2c; tumor #2) and the tumor volume of Mouse 3 (Fig. 6.3c) did, however, not change significantly within the following two weeks upon the injection of the same amount of activity. The observed tumor inhibition at 5 MBq was not expected, since the same amount of radiofolate had no therapeutic effect on the growth of NF9006 tumors of syngeneic model and it remained, thus, unclear whether the tumor shrinkage could be ascribed to the absorbed radiation dose or the radiation-induced stimulation of immune response as previously described [103,179,194]. The therapeutic effect of the radiofolate observed in Mouse 1 and Mouse 2 was probably achieved due to the smaller initial tumor volume (~200 mm^3) (Fig. 6.2c, tumor #1; Fig. 6.2d) as compared to the tumor volume of Mouse 3 and the second tumor of Mouse 1 (~400 mm^3) (Fig. 6.3c; Fig. 6.2c, tumor #2).

Mouse 4 was injected with 25 MBq [^{177}Lu]Lu-DOTA-folate to obtain more decent SPECT images but, in principle, this would be a therapeutic quantity of activity. Not surprisingly, it resulted in shrinkage of the tumor over the next 3–7 days after the first injection, however, eventually the tumor size increased again afterwards (Fig. 6.4j). Also in this case, the tumor was probably already too large at the time of radiofolate administration to achieve a durable therapeutic effect. The reduction of tumor volume was

less pronounced after the second and the third injection, which might have been related to the decreased tumor uptake as visualized on SPECT images after the second and the third injection (Fig. 6.4a–i).

In future therapy studies with spontaneous model, the therapeutic effect of [^{177}Lu]Lu-DOTA-folate should be evaluated in a systematic way to investigate the tumor response to variable quantities of [^{177}Lu]Lu-DOTA-folate. Importantly, the question on whether the therapeutic effect is reproducible in several mice and maintained over several weeks should be addressed.
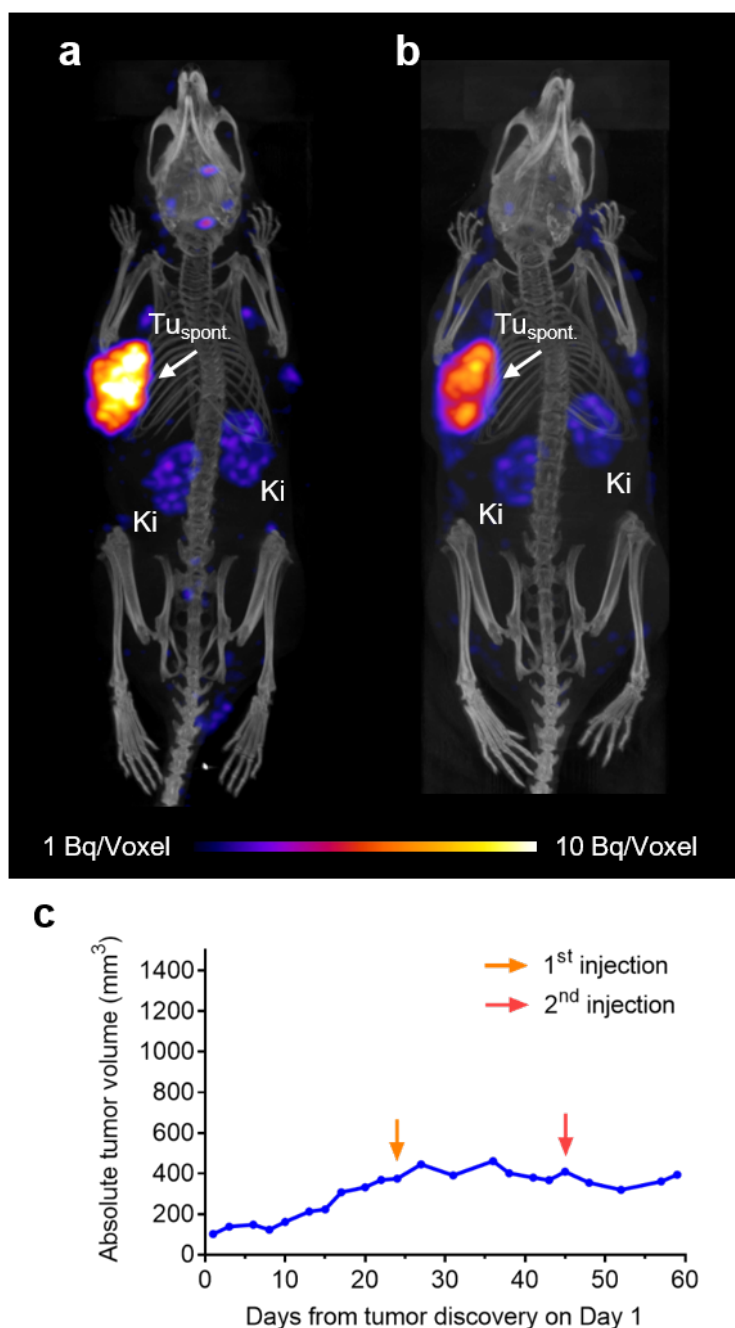
Fig. 6.3 SPECT/CT images of Mouse 3 with spontaneously developed breast tumor shown as maximum intensity projections (MIPs): (**a**) the first scan; (**b**) the second scan. The images were acquired at 20 h after injection of [^{177}Lu]Lu-DOTA-folate (5 MBq; 0.5 nmol). Mice were fed with folate-free rodent chow; (**c**) Tumor volume measurements collected in the time course of ~20 days before and 20 days after SPECT/CT imaging.
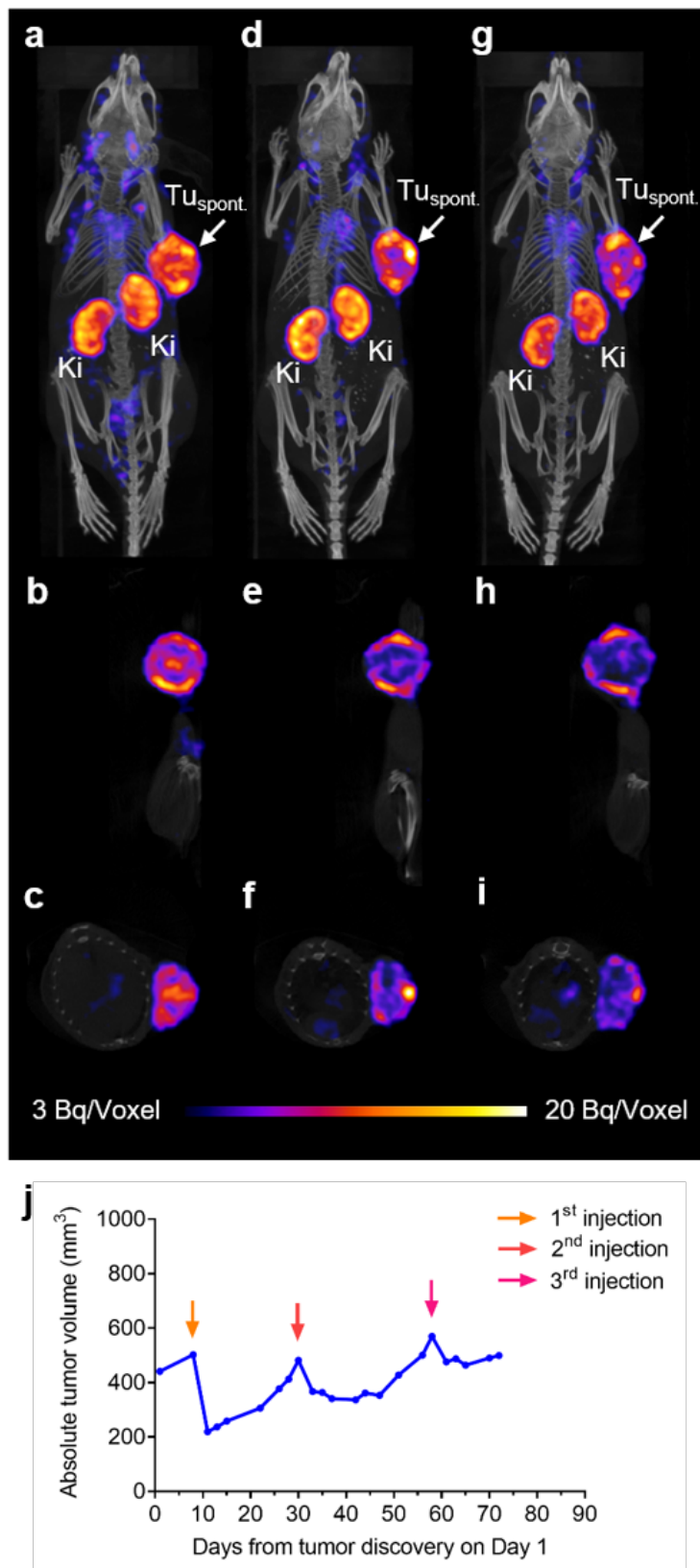
Fig. 6.4 SPECT/CT images of a mouse with a spontaneously developed tumor (Mouse 4) and the follow-up images acquired in a distance of several weeks, shown as maximum intensity projections (MIPs): (**a–c**) the first scan; (**d–f**) the second scan; (**g–i**) the third scan. (**a/d/g**) MIPs in coronal section; (**b/e/f**) MIPs in sagittal section; (**c/f/i**) MIPs in axial section; The images were acquired at 20 h after injection of [^{177}Lu]Lu-DOTA-folate (25 MBq; 1 nmol). Mouse 4 was fed with standard rodent chow; (**j**) Tumor volume measurements collected in the time course of ~90 days, before and after SPECT/CT imaging.

6.3.4. Follow-up Injections of [^{177}Lu]Lu-DOTA-Folate Showed Reduced Tumor Uptake

The follow-up SPECT/CT images of Mouse 3 (Fig. 6.3) and Mouse 4 (Fig. 6.4) were acquired ~20 days after the first scan, upon an additional injection of 5 MBq and 25 MBq [^{177}Lu]Lu-DOTA-folate, respectively. The imaging experiments revealed that the uptake of activity in tumor tissue decreased at the second time of injection in the case of both mice (Fig. 6.3a/b; Fig. 6.4 a/d/g). In an attempt to better understand this phenomenon, the sub-tumoral distribution of activity was investigated. As demonstrated on the sagittal (Fig. 6.4b/e/h) and axial sections (Fig. 6.4c/f/i) of the tumor of Mouse 4, the uptake of [^{177}Lu]Lu-DOTA-folate in the center of the tumor was lower than it was the case at the first scan. This may be a result of progressing necrosis of tumor tissue or radiation damage to tumor vasculature, which would consequently lead to insufficient blood supply in the central area of the tumor. The observation that tumor necrosis can compromise the radioligand uptake was demonstrated previously in PET imaging studies using a CXCR4 receptor-targeting [^{18}F]MCFB in a MDA-MB-231 tumor xenograft model [209,210].

6.3.5. The Tissue Uptake of [^{177}Lu]Lu-DOTA-Folate Might Be Influenced by the Diet

Similarities between the Distribution Profile in Spontaneous vs. Syngeneic Model. The uptake of [^{177}Lu]Lu-DOTA-folate in spontaneously developed tumors was $9.7 \pm 1.3\%$ IA/g at 20 h p.i. and, hence, comparable with the uptake in NF9006 tumors which was $12 \pm 1\%$ IA/g at 24 h p.i. (Fig. 6.5). These findings were in line with in vitro autoradiography data that indicated a similar FR expression level on tumor sections of both models. As expected in mice of the same strain, the accumulation in FR-positive salivary glands was also similar in both models ($p<0.05$), although with a trend of slightly increased uptake in the syngeneic model. The uptake of the radiofolate in the liver was almost equal for both models (Fig. 6.5). Despite the significantly enhanced retention in the blood of transgenic mice, the activity in the background organs, such as bones, muscles and stomach, was in the same range as for the syngeneic mice (Fig. 6.5).

Differences between the Distribution Profile in Spontaneous vs. Syngeneic Model. The kidney uptake in transgenic mice was $24 \pm 3\%$ IA/g which was a significantly higher value as compared to the renal accumulation in the syngeneic tumor mouse model ($18 \pm 3\%$ IA/g; $p<0.05$) (Fig. 6.5). The lower uptake in the kidneys of NF9006 tumor-bearing mice could be potentially the result of the folate-deficient diet. Commonly, mice that are used for the evaluation of folate-based pharmaceuticals are fed with a folate-free chow to lower the endogenous folate concentration in mouse plasma to the similar level as in human [208]. It was reported by several groups that the consequence of already a 2- to 5-week long folate-free diet is a natural loss of FRs in the kidneys and other normal tissues [206-208]. The transgenic mice used in biodistribution study were fed with standard rodent chow, and therefore, the FR expression in the kidneys of these mice was possibly higher than in the syngeneic tumor mouse model.

This in turn could be the reason for a more pronounced renal accumulation of $[^{177}Lu]Lu$-DOTA-folate in transgenic mice.

A significant difference between the models was observed with regard to the blood activity which was ~5-fold higher in transgenic mice ($9.7 \pm 1.0\%$ IA/g; 20 h p.i.) as compared to the syngeneic mouse model ($1.7 \pm 0.3\%$ IA/g; 24 h p.i.) after injection of $[^{177}Lu]Lu$-DOTA-folate (Fig. 6.5). The reason for this observation remains unclear. Based on the biodistribution data obtained with the NF9006 syngeneic model [194] and also the KB xenograft model (unpublished data), such a high activity level in the blood would only be expected within the first hours after injection. One hypothesis could be that the increased blood activity level in transgenic mice was caused by circulation of a complex of the radiofolate with the FR that was released from the kidneys. In this case, the "shedding" of renal FRs could be related to the advanced age of transgenic mice (10 months) as it was previously observed by Leamon et al. with other mouse strain [208]. It is, however, questionable whether it could contribute to an almost 5-fold increased retention of radiofolate, since the age-related FR "shedding" was reported to be a slow process taking place over several months. Moreover, according to the literature, the circulating FR-radiofolate complexes would accumulate in the liver [208,211], however, the liver uptake was almost the same for both models.

With regard to other organs, accumulation of $[^{177}Lu]Lu$-DOTA-folate observed in the lungs of transgenic mice reached $5.6 \pm 0.2\%$ IA/g (Fig. 6.5). This value was significantly higher than the corresponding uptake in the lungs of NF9006 tumor-bearing FVB background mice ($2.6 \pm 0.4\%$ IA/g; $p<0.05$) (Fig. 6.5). A possible reason for increased values in transgenic mice could be unspecific accumulation caused by the enhanced retention of the radioconjugate in the blood. A similar trend was also observed in the spleen, however, the difference was not significant ($p>0.05$) (Fig. 6.5).
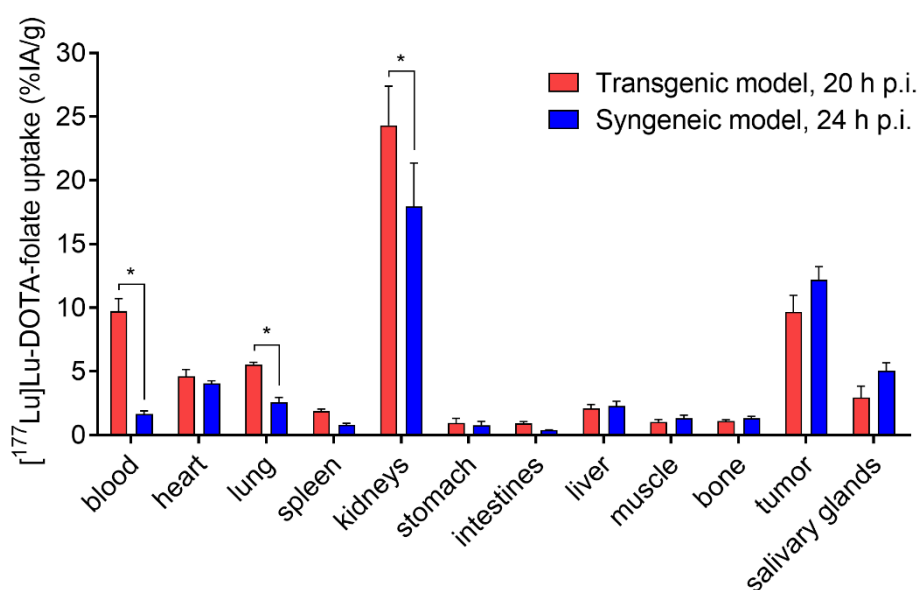
Fig. 6.5 Comparison of $[^{177}Lu]Lu$-DOTA-folate tissue distribution profile in FVB/N-Tg(MMTV-neu)-202Mul/J mice (transgenic model) and NF9006 tumor-bearing FVB/NCrl mice (syngeneic model).

In the scope of this study, it was revealed that the tissue uptake of [^{177}Lu]Lu-DOTA-folate in the MMTV-neu model was comparable to NF9006 syngeneic model with a few exceptions. The main observation that remained unclear was high blood retention of radiofolate in MMTV-neu model. This discrepancy could be problematic in safety evaluation and assessment of potential side effects of a treatment as it is known that enhanced retention of activity in the blood can lead to bone marrow toxicity. Future investigations could focus on testing whether this results was related to mice diet or age.

6.4.   Conclusion

In this study, it was demonstrated that spontaneously developed mammary gland tumors in FVB/N-Tg(MMTVneu)-202Mul/J mice are FR-positive and can be visualized using [^{177}Lu]Lu-DOTA-folate. The herein presented results give a basis to employ the MMTV-neu transgenic mice as clinically more representative model for investigation of FR-targeted (radionuclide) therapies. Notably, due to the fully functional immune system, this transgenic model could also be used for the investigation of combination treatments with immune checkpoint inhibitors or other immune-stimulatory agents. Potential limitations of using this model refer to the slow and unsynchronized tumor development, which certainly make a therapy study design challenging. Our study has demonstrated, however, that nuclear imaging techniques using FR-targeted radioconjugates could serve as valuable tools to monitor mice before and during therapy.

VII. Conclusions & Outlook

The FR-selectivity studies using 5-MTHF-based ^{18}F-labeled aza-folates [77] revealed unambiguously that 6*R*-[^{18}F]Aza-5-MTHF, corresponding to the physiological form of 5-MTHF, allows for discrimination between the FRα and the FRβ. This result is of great relevance in view of future clinical translation of a FRα-selective PET tracer that could facilitate precise and accurate selection of FRα-positive cancer patients potentially eligible for FR-targeted therapies. In vivo studies performed in the artificial mouse model with FRα/FRβ-positive xenografts gave a clear picture of the radiotracer's selectivity, however, additional experiments with an animal model combining both the FRα-positive tumor and the FRβ-positive activated macrophages in inflammation will be necessary. Selection of a suitable inflammation model will be essential for these studies, since engagement of activated macrophages in the inflammation is a prerequisite. Models of arthritis [61], ulcerative colitis [134] or bleomycin-induced lung inflammation [62], would fulfill this requirement as demonstrated in previously reported studies. In particular for the combination of inflammation and tumors in one individual mouse, an inflammation model which is easy to induce, fast and manifests with only mild symptoms, would be more favorable. One option may be to use a mouse model of contact hypersensitivity-induced ear skin inflammation which is mimicking the development of psoriasis [212].

Comparison of the novel albumin-binding radioconjugates, which were based on diastereomerically pure 6*S*-5-MTHF and 6*R*-5-MTHF, has demonstrated ~4-fold improved tumor-to-kidney ratio of accumulated activity for the 6*R*-isomer. Unexpectedly, the pharmacokinetic data of 6*S*- and 6*R*-RedFol-1 conjugates are exactly opposite to the observations reported by Boss et al. for corresponding 6*R*- and 6*S*-isomers of ^{18}F-labeled aza-5-MTHF of the integrated approach [77] as well as for the γ-click-[^{18}F]fluoroethyl-conjugates of the pendant approach [156]. The reason behind is yet unknown and further investigations would be necessary to understand the different behavior of these three pairs of 5-MTHF derivatives. Since almost no difference in KB tumor uptake was observed between the 6*S*- and 6*R*-isomers of the respective pairs, and the main difference lies in the renal uptake, the potential reason might be caused by a different binding of the radioconjugates to the human FR present on KB xenografts and the murine FR expressed in the mouse kidneys. This hypothesis could be verified by using a syngeneic tumor mouse model, and in addition, by in silico studies involving molecular docking into the crystal structure of the human and the murine FRα which could give an indication whether the folate derivatives are recognized differently.

The question on whether the high tumor-to-kidney ratio of the 6*R*-isomer or the potential (not yet confirmed) FRα selectivity of the 6*S*-isomer would be the criterion for clinical translation remains a question to be addressed in future. Therefore, of importance will be in vitro selectivity studies using FRα- and FRβ-expressing cells to confirm identical stereochemistry of the corresponding 6*R*/6*S*-pair of ^{18}F-labeled aza-5-MTHF.

The employment of 5-MTHF-based folates for FR-targeting, led to even 3–4-fold higher tumor uptake as compared to the lead folic acid-based radioconjugate, [^{177}Lu]Lu-OxFol-1. This result corresponded to the data obtained in the study of Boss et al. with 6R- and 6S-isomers of ^{18}F-labeled aza-5-MTHF. The reason for the higher uptake of 5-MTHF derivatives was, however, not elaborated in the scope of this thesis, therefore, further studies aiming at elucidation of the underlying mechanism are important. The starting hypothesis for these studies could be the potentially more efficient release of 5-MTHF from the FR upon internalization into the cell. This could be supported by the significantly lower affinity of 5-MTHF to the FR as compared to folic acid, which in combination with a low pH in the endosome leads to the easier dissociation of the radiotracer from the receptor.

Importantly, in the case of albumin-binding radioconjugates, an increased tumor uptake is a primary consequence of enhanced blood retention. It was, however, unexpected that the exchange of the targeting molecule, and even more, the minimal structural difference between 5-MTHF and folic acid, would increase the blood retention 3–5-fold, since all three radioconjugates were endowed with the same albumin-binding entity. This result is unfavorable owing to the possible bone marrow toxicity at high activity levels. Should the high blood retention be true also in patients, the concept of using 5-MTHF radioconjugates has to be further optimized. Since lack of albumin-binding properties of ^{18}F-labeled aza-5-MTHFs did not compromise their high tumor uptake [77], it was hypothesized that the albumin binder might be unnecessary to achieve high tumor-to-kidney ratios when using 5-MTHF-based DOTA-conjugates. The in vivo studies with a new couple of 6S- and 6R-5-MTHF DOTA-conjugates without the 4-(p-iodophenyl)butyric acid entity should verify whether or not our assumption is correct. Moreover, further development could focus on the employment of weaker albumin binders, such as the 4-(p-tolyl)butyric acid or ibuprofen as recently used for the preparation of PSMA radioligands [213]. Another possibility could be testing entities that bind to other plasma proteins such as transthyretin, which is less abundant in the plasma compared to albumin [159].

We have demonstrated that folate radioconjugates can efficiently deliver a radiation stimulus to the tumor in order to enhance the tumor response to an immune checkpoint inhibitor, namely the CTLA-4 antibody. Our results indicate that despite the accumulation in the kidneys, folate radioconjugates could potentially be used for the purpose of increasing the tumor immunogenicity, since already low amounts of injected activity yielded significantly better therapy results as compared to the monotherapy with the immune checkpoint antibody. This phenomenon could apply to many more radiopharmaceuticals, and therefore, open a new perspective for cancer treatments. So far, our study was focused on observing the phenomenon rather than on the underlying mechanism, therefore, it would be essential to investigate the changes in tumor microenvironment upon the treatment. Based on the studies reported by other groups, this should include comparative immune cell profiling of untreated mice and those treated with the combination of radioconjugate and immunotherapy. The investigation should include FACS analysis of subsets of different immune cells, analysis of immunogenic cell death markers as well as apoptosis, necrosis and proliferation markers. Importantly, investigation of changes in tumor infiltrating cells

would allow for adapting the application regimen. Additional in vivo studies such as depletion of specific subsets of immune cells before and during the combination treatment could be another way to prove the key players of the underlying mechanism. In order to check whether the survivor mice developed the antitumor memory, a rechallenge experiment with a new tumor cell inoculum could be performed at the end of a therapy study.

With regard to optimization of the combination treatment, one possibility would be to use higher or lower quantities of activity to investigate whether the therapeutic effect can be even more potentiated or sustained, while keeping the regimen safe for the kidneys that are the most exposed to radiation. It is noteworthy that increasing the amount of activity might have a double-edged effect because higher radiation dose might efficiently eliminate the immune cells that are circulating with the blood, and hence, the effect of immunotherapy will be modest or even compromised. Such conclusion was drawn by Rouanet et al. who investigated this concept in melanoma mice treated with a fast-clearing melanin-based radioligand. This group observed a longer survival as compared to Choi et al. who used a radiolabeled peptidomimetic targeting an integrin that was expressed not only on melanoma cells, but also on immune cells [103].

Folate-based targeted radionuclide therapy could be also tested in combination with other immunotherapies to check whether the effect is specific to the CTLA-4 antibody or generally applicable. Another consideration for the future could be investigation of the concept in a different tumor model, e.g. a metastatic model or even more clinically relevant models such as transgenic mice or PDX in mice with humanized immune system. The PDX model revealed to be effective in paralleling the human outcomes, however, adaptation of "humanized" mouse models in preclinical studies is costly and often limited [105]. Hence, a transgenic mouse model, which provides the most complete representation of tumor development, might be the best suited for the purpose of this study [105]. With a suitable metastatic model in hands, a head-to-head comparison to external beam radiation could be performed, in order to investigate whether in the case of metastatic disease single-cell targeting by systemic radiation is more advantageous as compared to external beam radiation and the abscopal effect, which is in fact a sporadic event in the clinical practice.

With regard to clinically relevant tumor mouse models, it was demonstrated in this thesis that spontaneous mammary gland tumors of FVB/N-Tg(MMTVneu)202Mul/J transgenic mice express the FRs, and can be imaged using the folic acid radioconjugate. The main unexpected finding of this study, was almost 5-fold increased blood retention of the radiofolate in MMTV-neu mice as compared to the NF9006 syngeneic mouse model. High activity levels in the blood could be problematic for investigation of FR-targeted radionuclide therapy in MMTV-neu model because it can lead to the bone marrow toxicity. As a consequence, the evaluation of safety and assessment of potential side effects of the treatment could be overestimated in this model. In future it would be necessary to test whether the observed discrepancy in blood activity was related to the difference in age or diet of both models. Furthermore, the design of such therapy study would be challenging primarily because of

unsynchronized development of the tumors, and hence, individual treatment schedule of mice. Nevertheless, the MMTV-neu spontaneous mice could be employed in future for investigation of FR-targeted radionuclide therapy in combination with other treatments, e.g. immunotherapy that requires fully functional immune system in a mouse.

In the attempt to increase the tumor-to-kidneys ratio of albumin-binding folate radioconjugates, it was demonstrated that the application of PMX prior to and after the injection of the radiofolate improved the distribution profile of the albumin-binding folate radioconjugate ([^{177}Lu]Lu-cm13) substantially. The fast renal clearance of PMX does, however, not allow an efficient blockade of the kidney uptake of long-circulating [^{177}Lu]Lu-cm13 over time, therefore, an additional injection at the later time point was necessary to maintain the effect. Such a complex application protocol would limit the applicability of PMX blockade in a clinical setting. Moreover, repeated injection of PMX would mean a high dosed antifolate, which could only be justified if it would provide a synergistic therapeutic effect as previously shown by Reber et al. [83].

The herein presented results demonstrate significant advancements with regard to a theragnostic application of radiofolates, hence, bringing them to a new level of clinical prospects (Fig. 7.1). The accomplished developments would allow for precise PET diagnosis and monitoring of FR-positive cancer patients. FR-targeted radionuclide therapy, which could be performed in a safe regiment using optimized radiopharmaceuticals that provide improved pharmacokinetic profiles, could be applied as an additional modality or an adjuvant treatment for e.g. immune checkpoint inhibitors and, hence, change the perspectives of patients with FR-positive cancer.
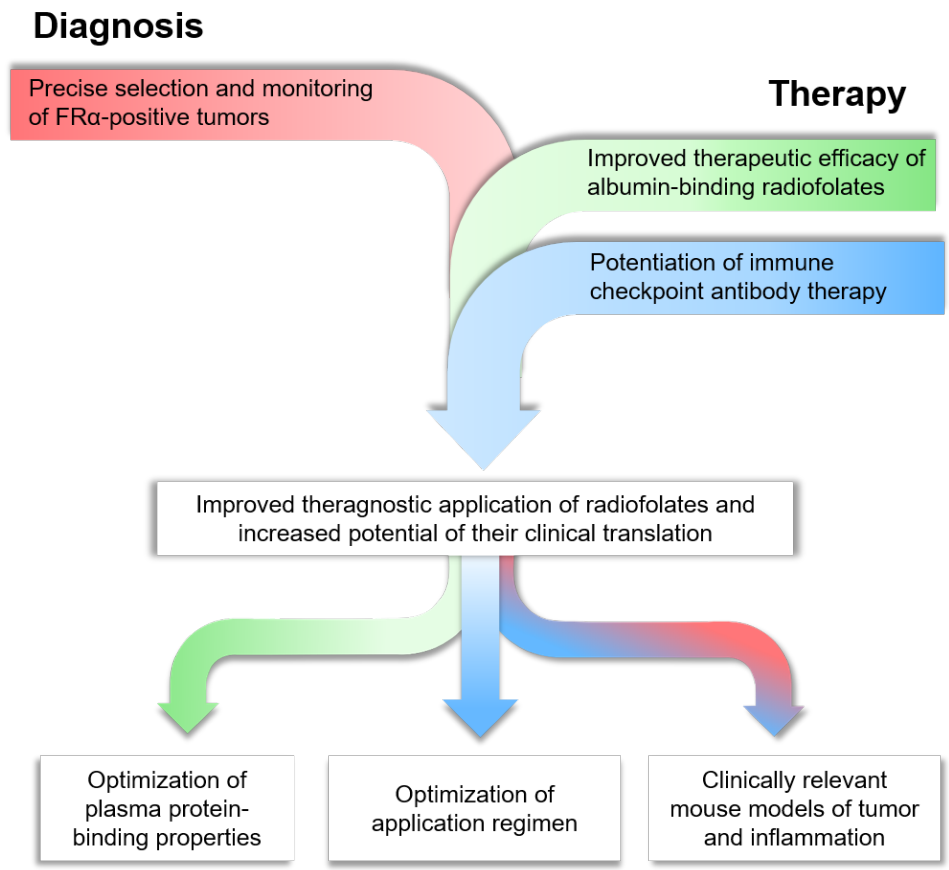
Fig. 7.1 Overview of the main conclusions and future considerations following from the herein presented thesis.

References

1. Peltek, O.O.; Muslimov, A.R.; Zyuzin, M.V.; Timin, A.S. Current outlook on radionuclide delivery systems: from design consideration to translation into clinics. *J Nanobiotechnology* **2019**, *17*, 90, doi:10.1186/s12951-019-0524-9.

2. Müller, C. Folate based radiopharmaceuticals for imaging and therapy of cancer and inflammation. *Current pharmaceutical design* **2012**, *18*, 1058-1083.

3. Saha, G.B. *Fundamentals of Nuclear Pharmacy*, 7 ed.; Springer International Publishing: 2018; 10.1007/978-3-319-57580-3pp. XVII, 428.

4. Kassis, A.I. Radiotargeting agents for cancer therapy. *Expert opinion on drug delivery* **2005**, *2*, 981-991, doi:10.1517/17425247.2.6.981.

5. Dash, A.; Knapp, F.F.; Pillai, M.R. Targeted radionuclide therapy - an overview. *Current radiopharmaceuticals* **2013**, *6*, 152-180, doi:10.2174/18744710113066660023.

6. Oyen, W.J.; Bodei, L.; Giammarile, F.; Maecke, H.R.; Tennvall, J.; Luster, M.; Brans, B. Targeted therapy in nuclear medicine - current status and future prospects. *Annals of oncology : official journal of the European Society for Medical Oncology / ESMO* **2007**, *18*, 1782-1792, doi:10.1093/annonc/mdm111.

7. Lacoeuille, F.; Arlicot, N.; Faivre-Chauvet, A. Targeted alpha and beta radiotherapy: An overview of radiopharmaceutical and clinical aspects. *Médecine Nucléaire* **2018**, *42*, 32-44, doi:https://doi.org/10.1016/j.mednuc.2017.12.002.

8. NuDat 2.8. In *https://www.nndc.bnl.gov/nudat2/*.

9. Breeman, W.A.; de Jong, M.; Kwekkeboom, D.J.; Valkema, R.; Bakker, W.H.; Kooij, P.P.; Visser, T.J.; Krenning, E.P. Somatostatin receptor-mediated imaging and therapy: basic science, current knowledge, limitations and future perspectives. *European journal of nuclear medicine* **2001**, *28*, 1421-1429, doi:10.1007/s002590100502.

10. Kwekkeboom, D.J.; Kam, B.L.; van Essen, M.; Teunissen, J.J.; van Eijck, C.H.; Valkema, R.; de Jong, M.; de Herder, W.W.; Krenning, E.P. Somatostatin-receptor-based imaging and therapy of gastroenteropancreatic neuroendocrine tumors. *Endocrine-related cancer* **2010**, *17*, R53-73, doi:10.1677/ERC-09-0078.

11. Kratochwil, C.; Stefanova, M.; Mavriopoulou, E.; Holland-Letz, T.; Dimitrakopoulou-Strauss, A.; Afshar-Oromieh, A.; Mier, W.; Haberkorn, U.; Giesel, F.L. SUV of ^{68}Ga-DOTATOC-PET/CT predicts response probability of PRRT in neuroendocrine tumors. *Molecular imaging and biology : MIB : the official publication of the Academy of Molecular Imaging* **2015**, *17*, 313-318, doi:10.1007/s11307-014-0795-3.

12. Valkema, R.; Pauwels, S.; Kvols, L.K.; Barone, R.; Jamar, F.; Bakker, W.H.; Kwekkeboom, D.J.; Bouterfa, H.; Krenning, E.P. Survival and response after peptide receptor radionuclide therapy with [^{90}Y-DOTA0,Tyr3]octreotide in patients with advanced gastroenteropancreatic neuroendocrine tumors. *Seminars in nuclear medicine* **2006**, *36*, 147-156, doi:10.1053/j.semnuclmed.2006.01.001.

13. Kwekkeboom, D.J.; de Herder, W.W.; Kam, B.L.; van Eijck, C.H.; van Essen, M.; Kooij, P.P.; Feelders, R.A.; van Aken, M.O.; Krenning, E.P. Treatment with the radiolabeled somatostatin analog [^{177}Lu-DOTA 0,Tyr3]octreotate: toxicity, efficacy, and survival. *Journal of clinical*

oncology : official journal of the American Society of Clinical Oncology **2008**, *26*, 2124-2130, doi:10.1200/JCO.2007.15.2553.

14. Kong, G.; Hicks, R.J. Peptide receptor radiotherapy: Current approaches and future directions. *Curr Treat Options Oncol* **2019**, *20*, 77, doi:10.1007/s11864-019-0677-7.

15. Velikyan, I. (Radio)theranostic patient management in oncology exemplified by neuroendocrine neoplasms, prostate cancer, and breast cancer. *Pharmaceuticals (Basel)* **2020**, *13*, doi:10.3390/ph13030039.

16. Chang, S.S. Overview of prostate-specific membrane antigen. *Rev Urol* **2004**, *6 Suppl 10*, S13-18.

17. Afshar-Oromieh, A.; Babich, J.W.; Kratochwil, C.; Giesel, F.L.; Eisenhut, M.; Kopka, K.; Haberkorn, U. The rise of PSMA ligands for diagnosis and therapy of prostate cancer. *Journal of nuclear medicine : official publication, Society of Nuclear Medicine* **2016**, *57*, 79S-89S, doi:10.2967/jnumed.115.170720.

18. Kratochwil, C.; Giesel, F.L.; Stefanova, M.; Benešová, M.; Bronzel, M.; Afshar-Oromieh, A.; Mier, W.; Eder, M.; Kopka, K.; Haberkorn, U. PSMA-Targeted radionuclide therapy of metastatic castration-resistant prostate cancer with ^{177}Lu-labeled PSMA-617. *Journal of nuclear medicine : official publication, Society of Nuclear Medicine* **2016**, *57*, 1170-1176, doi:10.2967/jnumed.115.171397.

19. Barber, T.W.; Singh, A.; Kulkarni, H.R.; Niepsch, K.; Billah, B.; Baum, R.P. Clinical outcomes of ^{177}Lu-PSMA radioligand therapy in earlier and later phases of metastatic castration-resistant prostate cancer grouped by previous taxane chemotherapy. *Journal of nuclear medicine : official publication, Society of Nuclear Medicine* **2019**, *60*, 955-962, doi:10.2967/jnumed.118.216820.

20. Emmett, L.; Crumbaker, M.; Ho, B.; Willowson, K.; Eu, P.; Ratnayake, L.; Epstein, R.; Blanksby, A.; Horvath, L.; Guminski, A., et al. Results of a prospective phase 2 pilot trial of ^{177}Lu-PSMA-617 therapy for metastatic castration-resistant prostate cancer including imaging predictors of treatment response and patterns of progression. *Clin Genitourin Cancer* **2019**, *17*, 15-22, doi:10.1016/j.clgc.2018.09.014.

21. Weineisen, M.; Schottelius, M.; Simecek, J.; Baum, R.P.; Yildiz, A.; Beykan, S.; Kulkarni, H.R.; Lassmann, M.; Klette, I.; Eiber, M., et al. [68]Ga- and ^{177}Lu-labeled PSMA I&T: Optimization of a PSMA-targeted theranostic concept and first proof-of-concept human studies. *Journal of nuclear medicine : official publication, Society of Nuclear Medicine* **2015**, *56*, 1169-1176, doi:10.2967/jnumed.115.158550.

22. Baum, R.P.; Kulkarni, H.R.; Schuchardt, C.; Singh, A.; Wirtz, M.; Wiessalla, S.; Schottelius, M.; Mueller, D.; Klette, I.; Wester, H.J. ^{177}Lu-Labeled prostate-specific membrane antigen radioligand therapy of metastatic castration-resistant prostate cancer: safety and efficacy. *Journal of nuclear medicine : official publication, Society of Nuclear Medicine* **2016**, *57*, 1006-1013, doi:10.2967/jnumed.115.168443.

23. Windisch, P.; Zwahlen, D.R.; Koerber, S.A.; Giesel, F.L.; Debus, J.; Haberkorn, U.; Adeberg, S. Clinical results of fibroblast activation protein (FAP) specific PET and implications for radiotherapy planning: Systematic review. *Cancers (Basel)* **2020**, *12*, doi:10.3390/cancers12092629.

24. Scaranti, M.; Cojocaru, E.; Banerjee, S.; Banerji, U. Exploiting the folate receptor alpha in oncology. *Nature reviews. Clinical oncology* **2020**, *17*, 349-359, doi:10.1038/s41571-020-0339-5.

25. Zheng, Y.; Cantley, L.C. Toward a better understanding of folate metabolism in health and disease. *The Journal of experimental medicine* **2019**, *216*, 253-266, doi:10.1084/jem.20181965.

26. Liu, J.J.; Ward, R.L. Folate and one-carbon metabolism and its impact on aberrant DNA methylation in cancer. *Adv Genet* **2010**, *71*, 79-121, doi:10.1016/B978-0-12-380864-6.00004-3.

27. Matherly, L.H.; Hou, Z. Structure and function of the reduced folate carrier a paradigm of a major facilitator superfamily mammalian nutrient transporter. *Vitam Horm* **2008**, *79*, 145-184, doi:10.1016/S0083-6729(08)00405-6.

28. Zhao, R.; Goldman, I.D. The proton-coupled folate transporter: physiological and pharmacological roles. *Curr Opin Pharmacol* **2013**, *13*, 875-880, doi:10.1016/j.coph.2013.09.011.

29. Zhao, R.; Min, S.H.; Wang, Y.; Campanella, E.; Low, P.S.; Goldman, I.D. A role for the proton-coupled folate transporter (PCFT-SLC46A1) in folate receptor-mediated endocytosis. *The Journal of biological chemistry* **2009**, *284*, 4267-4274, doi:10.1074/jbc.M807665200.

30. Zhao, R.; Matherly, L.H.; Goldman, I.D. Membrane transporters and folate homeostasis: intestinal absorption and transport into systemic compartments and tissues. *Expert Rev Mol Med* **2009**, *11*, e4, doi:10.1017/S1462399409000969.

31. Kelemen, L.E. The role of folate receptor alpha in cancer development, progression and treatment: cause, consequence or innocent bystander? *International journal of cancer. Journal international du cancer* **2006**, *119*, 243-250, doi:10.1002/ijc.21712.

32. Ledermann, J.A.; Canevari, S.; Thigpen, T. Targeting the folate receptor: diagnostic and therapeutic approaches to personalize cancer treatments. *Annals of oncology : official journal of the European Society for Medical Oncology / ESMO* **2015**, *26*, 2034-2043, doi:10.1093/annonc/mdv250.

33. Low, P.S.; Antony, A.C. Folate receptor-targeted drugs for cancer and inflammatory diseases. *Advanced drug delivery reviews* **2004**, *56*, 1055-1058, doi:10.1016/j.addr.2004.02.003.

34. Visentin, M.; Zhao, R.; Goldman, I.D. The antifolates. *Hematol Oncol Clin North Am* **2012**, *26*, 629-648, ix, doi:10.1016/j.hoc.2012.02.002.

35. Chattopadhyay, S.; Moran, R.G.; Goldman, I.D. Pemetrexed: biochemical and cellular pharmacology, mechanisms, and clinical applications. *Molecular cancer therapeutics* **2007**, *6*, 404-417, doi:10.1158/1535-7163.MCT-06-0343.

36. Siwowska, K.; Müller, C. Preclinical development of small-molecular-weight folate-based radioconjugates: a pharmacological perspective. *Q J Nucl Med Mol Imaging* **2015**, *59*, 269-286.

37. Jackman, A.L.; Theti, D.S.; Gibbs, D.D. Antifolates targeted specifically to the folate receptor. *Advanced drug delivery reviews* **2004**, *56*, 1111-1125, doi:10.1016/j.addr.2004.01.003.

38. Gibbs, D.D.; Theti, D.S.; Wood, N.; Green, M.; Raynaud, F.; Valenti, M.; Forster, M.D.; Mitchell, F.; Bavetsias, V.; Henderson, E., et al. BGC 945, a novel tumor-selective thymidylate synthase inhibitor targeted to alpha-folate receptor-overexpressing tumors. *Cancer research* **2005**, *65*, 11721-11728, doi:10.1158/0008-5472.CAN-05-2034.

39.   Low, P.S.; Henne, W.A.; Doorneweerd, D.D. Discovery and development of folic-acid-based receptor targeting for imaging and therapy of cancer and inflammatory diseases. *Accounts of chemical research* **2008**, *41*, 120-129, doi:10.1021/ar7000815.

40.   Armstrong, D.K.; White, A.J.; Weil, S.C.; Phillips, M.; Coleman, R.L. Farletuzumab (a monoclonal antibody against folate receptor alpha) in relapsed platinum-sensitive ovarian cancer. *Gynecologic oncology* **2013**, *129*, 452-458, doi:10.1016/j.ygyno.2013.03.002.

41.   Vergote, I.; Armstrong, D.; Scambia, G.; Teneriello, M.; Sehouli, J.; Schweizer, C.; Weil, S.C.; Bamias, A.; Fujiwara, K.; Ochiai, K., et al. A randomized, double-blind, placebo-controlled, phase III study to assess efficacy and safety of weekly farletuzumab in combination with carboplatin and taxane in patients with ovarian cancer in first platinum-sensitive relapse. *Journal of clinical oncology : official journal of the American Society of Clinical Oncology* **2016**, *34*, 2271-2278, doi:10.1200/JCO.2015.63.2596.

42.   Sato, S.; Itamochi, H. Profile of farletuzumab and its potential in the treatment of solid tumors. *OncoTargets and therapy* **2016**, *9*, 1181-1188, doi:10.2147/OTT.S98242.

43.   Gould, H.J.; Mackay, G.A.; Karagiannis, S.N.; O'Toole, C.M.; Marsh, P.J.; Daniel, B.E.; Coney, L.R.; Zurawski, V.R., Jr.; Joseph, M.; Capron, M., et al. Comparison of IgE and IgG antibody-dependent cytotoxicity in vitro and in a SCID mouse xenograft model of ovarian carcinoma. *European journal of immunology* **1999**, *29*, 3527-3537, doi:10.1002/(SICI)1521-4141(199911)29:11<3527::AID-IMMU3527>3.0.CO;2-5.

44.   Karagiannis, S.N.; Wang, Q.; East, N.; Burke, F.; Riffard, S.; Bracher, M.G.; Thompson, R.G.; Durham, S.R.; Schwartz, L.B.; Balkwill, F.R., et al. Activity of human monocytes in IgE antibody-dependent surveillance and killing of ovarian tumor cells. *European journal of immunology* **2003**, *33*, 1030-1040, doi:10.1002/eji.200323185.

45.   Moore, K.N.; Martin, L.P.; O'Malley, D.M.; Matulonis, U.A.; Konner, J.A.; Perez, R.P.; Bauer, T.M.; Ruiz-Soto, R.; Birrer, M.J. Safety and activity of mirvetuximab soravtansine (IMGN853), a folate receptor alpha-targeting antibody-drug conjugate, in platinum-resistant ovarian, fallopian tube, or primary peritoneal cancer: A phase I expansion study. *Journal of clinical oncology : official journal of the American Society of Clinical Oncology* **2017**, *35*, 1112-1118, doi:10.1200/JCO.2016.69.9538.

46.   Moore, K.N.; Vergote, I.; Oaknin, A.; Colombo, N.; Banerjee, S.; Oza, A.; Pautier, P.; Malek, K.; Birrer, M.J. FORWARD I: A phase III study of mirvetuximab soravtansine versus chemotherapy in platinum-resistant ovarian cancer. *Future Oncol* **2018**, *14*, 1669-1678, doi:10.2217/fon-2017-0646.

47.   Müller, C.; Schibli, R. Prospects in folate receptor-targeted radionuclide therapy. *Frontiers in oncology* **2013**, *3*, 249, doi:10.3389/fonc.2013.00249.

48.   Lu, Y.; Low, P.S. Folate targeting of haptens to cancer cell surfaces mediates immunotherapy of syngeneic murine tumors. *Cancer Immunol Immunother* **2002**, *51*, 153-162, doi:10.1007/s00262-002-0266-6.

49.   Fernandez, M.; Javaid, F.; Chudasama, V. Advances in targeting the folate receptor in the treatment/imaging of cancers. *Chem Sci* **2018**, *9*, 790-810, doi:10.1039/c7sc04004k.

50.   Reddy, J.A.; Dorton, R.; Westrick, E.; Dawson, A.; Smith, T.; Xu, L.C.; Vetzel, M.; Kleindl, P.; Vlahov, I.R.; Leamon, C.P. Preclinical evaluation of EC145, a folate-vinca alkaloid conjugate. *Cancer research* **2007**, *67*, 4434-4442, doi:10.1158/0008-5472.CAN-07-0033.

51.   Lorusso, P.M.; Edelman, M.J.; Bever, S.L.; Forman, K.M.; Pilat, M.; Quinn, M.F.; Li, J.; Heath, E.I.; Malburg, L.M.; Klein, P.J., et al. Phase I study of folate conjugate EC145 (Vintafolide) in patients with refractory solid tumors. *Journal of clinical oncology : official journal of the American Society of Clinical Oncology* **2012**, *30*, 4011-4016, doi:10.1200/JCO.2011.41.4946.

52.   Hanna, N.; Juhász, E.; Cainap, C.; Gladkov, O.; Ramlau, R.; Juan-Vidal, O.; Lal, R.; Symanowski, J.; Perez, W.; Nguyen, B., et al. LBA40_PR - Target: a randomized, phase Ii trial comparing vintafolide versus vintafolide plus docetaxel, versus docetaxel alone in second-line treatment of folate-receptor-positive non-small cell lung cancer (NSCLC) patients. *Annals of Oncology* **2014**, *25*, v1, doi:https://doi.org/10.1093/annonc/mdu438.48.

53.   Reddy, J.A.; Dorton, R.; Bloomfield, A.; Nelson, M.; Dircksen, C.; Vetzel, M.; Kleindl, P.; Santhapuram, H.; Vlahov, I.R.; Leamon, C.P. Pre-clinical evaluation of EC1456, a folate-tubulysin anti-cancer therapeutic. *Scientific reports* **2018**, *8*, 8943, doi:10.1038/s41598-018-27320-5.

54.   van Dam, G.M.; Themelis, G.; Crane, L.M.; Harlaar, N.J.; Pleijhuis, R.G.; Kelder, W.; Sarantopoulos, A.; de Jong, J.S.; Arts, H.J.; van der Zee, A.G., et al. Intraoperative tumor-specific fluorescence imaging in ovarian cancer by folate receptor-alpha targeting: first in-human results. *Nature medicine* **2011**, *17*, 1315-1319, doi:10.1038/nm.2472.

55.   Müller, C. Folate-based radiotracers for PET imaging - update and perspectives. *Molecules* **2013**, *18*, 5005-5031, doi:10.3390/molecules18055005.

56.   Müller, C.; Schibli, R. Folic acid conjugates for nuclear imaging of folate receptor-positive cancer. *Journal of nuclear medicine : official publication, Society of Nuclear Medicine* **2011**, *52*, 1-4, doi:10.2967/jnumed.110.076018.

57.   Yi, Y.S. Folate receptor-targeted diagnostics and therapeutics for inflammatory diseases. *Immune Netw* **2016**, *16*, 337-343, doi:10.4110/in.2016.16.6.337.

58.   Siegel, B.A.; Dehdashti, F.; Mutch, D.G.; Podoloff, D.A.; Wendt, R.; Sutton, G.P.; Burt, R.W.; Ellis, P.R.; Mathias, C.J.; Green, M.A., et al. Evaluation of ^{111}In-DTPA-folate as a receptor-targeted diagnostic agent for ovarian cancer: initial clinical results. *Journal of nuclear medicine : official publication, Society of Nuclear Medicine* **2003**, *44*, 700-707.

59.   Leamon, C.P.; Parker, M.A.; Vlahov, I.R.; Xu, L.C.; Reddy, J.A.; Vetzel, M.; Douglas, N. Synthesis and biological evaluation of EC20: a new folate-derived, (99mTc)-based radiopharmaceutical. *Bioconjugate chemistry* **2002**, *13*, 1200-1210.

60.   Paulos, C.M.; Turk, M.J.; Breur, G.J.; Low, P.S. Folate receptor-mediated targeting of therapeutic and imaging agents to activated macrophages in rheumatoid arthritis. *Advanced drug delivery reviews* **2004**, *56*, 1205-1217, doi:10.1016/j.addr.2004.01.012.

61.   Xia, W.; Hilgenbrink, A.R.; Matteson, E.L.; Lockwood, M.B.; Cheng, J.X.; Low, P.S. A functional folate receptor is induced during macrophage activation and can be used to target drugs to activated macrophages. *Blood* **2009**, *113*, 438-446, doi:10.1182/blood-2008-04-150789.

62.   Schniering, J.; Benešová, M.; Brunner, M.; Haller, S.; Cohrs, S.; Frauenfelder, T.; Vrugt, B.; Feghali-Bostwick, C.; Schibli, R.; Distler, O., et al. ^{18}F-AzaFol for detection of folate receptor-beta positive macrophages in experimental interstitial lung disease - a proof-of-concept study. *Front Immunol* **2019**, *10*, 2724, doi:10.3389/fimmu.2019.02724.

63. Müller, C.; Vlahov, I.R.; Santhapuram, H.K.; Leamon, C.P.; Schibli, R. Tumor targeting using ^{67}Ga-DOTA-Bz-folate - investigations of methods to improve the tissue distribution of radiofolates. *Nuclear medicine and biology* **2011**, *38*, 715-723, doi:10.1016/j.nucmedbio.2010.12.013.

64. Mindt, T.L.; Müller, C.; Stuker, F.; Salazar, J.F.; Hohn, A.; Mueggler, T.; Rudin, M.; Schibli, R. A "click chemistry" approach to the efficient synthesis of multiple imaging probes derived from a single precursor. *Bioconjugate chemistry* **2009**, *20*, 1940-1949, doi:10.1021/bc900276b.

65. Fani, M.; Wang, X.; Nicolas, G.; Medina, C.; Raynal, I.; Port, M.; Maecke, H.R. Development of new folate-based PET radiotracers: preclinical evaluation of ^{68}Ga-DOTA-folate conjugates. *European journal of nuclear medicine and molecular imaging* **2011**, *38*, 108-119, doi:10.1007/s00259-010-1597-8.

66. Fani, M.; Tamma, M.L.; Nicolas, G.P.; Lasri, E.; Medina, C.; Raynal, I.; Port, M.; Weber, W.A.; Maecke, H.R. In vivo imaging of folate receptor positive tumor xenografts using novel ^{68}Ga-NODAGA-folate conjugates. *Molecular pharmaceutics* **2012**, *9*, 1136-1145, doi:10.1021/mp200418f.

67. Müller, C.; Bunka, M.; Reber, J.; Fischer, C.; Zhernosekov, K.; Türler, A.; Schibli, R. Promises of cyclotron-produced [44]Sc as a diagnostic match for trivalent β⁻-emitters: in vitro and in vivo study of a [44]Sc-DOTA-folate conjugate. *Journal of nuclear medicine : official publication, Society of Nuclear Medicine* **2013**, *54*, 2168-2174, doi:10.2967/jnumed.113.123810.

68. Müller, C.; Zhernosekov, K.; Köster, U.; Johnston, K.; Dorrer, H.; Hohn, A.; van der Walt, N.T.; Türler, A.; Schibli, R. A unique matched quadruplet of terbium radioisotopes for PET and SPECT and for α- and β-radionuclide therapy: an in vivo proof-of-concept study with a new receptor-targeted folate derivative. *Journal of nuclear medicine : official publication, Society of Nuclear Medicine* **2012**, *53*, 1951-1959, doi:10.2967/jnumed.112.107540.

69. Radford, L.L.; Fernandez, S.; Beacham, R.; El Sayed, R.; Farkas, R.; Benešová, M.; Müller, C.; Lapi, S.E. New [55]Co-labeled albumin-binding folate derivatives as potential PET agents for folate receptor imaging. *Pharmaceuticals (Basel)* **2019**, *12*, doi:10.3390/ph12040166.

70. Farkas, R.; Siwowska, K.; Ametamey, S.M.; Schibli, R.; van der Meulen, N.P.; Müller, C. [64]Cu- and ^{68}Ga-based PET imaging of folate receptor-positive tumors: development and evaluation of an albumin-binding NODAGA-folate. *Molecular pharmaceutics* **2016**, *13*, 1979-1987, doi:10.1021/acs.molpharmaceut.6b00143.

71. Boss, S.D.; Ametamey, S.M. Development of folate receptor-targeted PET radiopharmaceuticals for tumor imaging - a bench-to-bedside journey. *Cancers (Basel)* **2020**, *12*, doi:10.3390/cancers12061508.

72. Bettio, A.; Honer, M.; Müller, C.; Bruhlmeier, M.; Müller, U.; Schibli, R.; Groehn, V.; Schubiger, A.P.; Ametamey, S.M. Synthesis and preclinical evaluation of a folic acid derivative labeled with ^{18}F for PET imaging of folate receptor-positive tumors. *Journal of nuclear medicine : official publication, Society of Nuclear Medicine* **2006**, *47*, 1153-1160.

73. Fischer, C.R.; Müller, C.; Reber, J.; Müller, A.; Krämer, S.D.; Ametamey, S.M.; Schibli, R. [^{18}F]fluoro-deoxy-glucose folate: a novel PET radiotracer with improved in vivo properties for folate receptor targeting. *Bioconjugate chemistry* **2012**, *23*, 805-813, doi:10.1021/bc200660z.

74. Ross, T.L.; Honer, M.; Müller, C.; Groehn, V.; Schibli, R.; Ametamey, S.M. A new ^{18}F-labeled folic acid derivative with improved properties for the PET imaging of folate receptor-positive

tumors. *Journal of nuclear medicine : official publication, Society of Nuclear Medicine* **2010**, *51*, 1756-1762, doi:10.2967/jnumed.110.079756.

75.   Betzel, T.; Müller, C.; Groehn, V.; Müller, A.; Reber, J.; Fischer, C.R.; Kramer, S.D.; Schibli, R.; Ametamey, S.M. Radiosynthesis and preclinical evaluation of 3'-aza-2'-[18F]fluorofolic acid: a novel PET radiotracer for folate receptor targeting. *Bioconjugate chemistry* **2013**, *24*, 205-214, doi:10.1021/bc300483a.

76.   Gnesin, S.; Müller, J.; Burger, I.A.; Meisel, A.; Siano, M.; Fruh, M.; Choschzick, M.; Müller, C.; Schibli, R.; Ametamey, S.M., et al. Radiation dosimetry of 18F-AzaFol: A first in-human use of a folate receptor PET tracer. *EJNMMI research* **2020**, *10*, 32, doi:10.1186/s13550-020-00624-2.

77.   Boss, S.D.; Müller, C.; Siwowska, K.; Schmid, R.M.; Groehn, V.; Schibli, R.; Ametamey, S.M. Diastereomerically pure 6R- and 6S-3'-aza-2'-18F-fluoro-5-methyltetrahydrofolates show unprecedentedly high uptake in folate receptor-positive KB tumors. *Journal of nuclear medicine : official publication, Society of Nuclear Medicine* **2019**, *60*, 135-141, doi:10.2967/jnumed.118.213314.

78.   Gent, Y.Y.; Weijers, K.; Molthoff, C.F.; Windhorst, A.D.; Huisman, M.C.; Smith, D.E.; Kularatne, S.A.; Jansen, G.; Low, P.S.; Lammertsma, A.A., et al. Evaluation of the novel folate receptor ligand [18F]fluoro-PEG-folate for macrophage targeting in a rat model of arthritis. *Arthritis Res Ther* **2013**, *15*, R37, doi:10.1186/ar4191.

79.   Haller, S.; Reber, J.; Brandt, S.; Bernhardt, P.; Groehn, V.; Schibli, R.; Müller, C. Folate receptor-targeted radionuclide therapy: preclinical investigation of anti-tumor effects and potential radionephropathy. *Nuclear medicine and biology* **2015**, *42*, 770-779, doi:10.1016/j.nucmedbio.2015.06.006.

80.   Müller, C.; Schibli, R.; Krenning, E.P.; de Jong, M. Pemetrexed improves tumor selectivity of 111In-DTPA-folate in mice with folate receptor-positive ovarian cancer. *Journal of nuclear medicine : official publication, Society of Nuclear Medicine* **2008**, *49*, 623-629, doi:10.2967/jnumed.107.047704.

81.   Müller, C.; Reddy, J.A.; Leamon, C.P.; Schibli, R. Effects of the antifolates pemetrexed and CB3717 on the tissue distribution of 99mTc-EC20 in xenografted and syngeneic tumor-bearing mice. *Molecular pharmaceutics* **2010**, *7*, 597-604, doi:10.1021/mp900296k.

82.   Müller, C.; Mindt, T.L.; de Jong, M.; Schibli, R. Evaluation of a novel radiofolate in tumour-bearing mice: promising prospects for folate-based radionuclide therapy. *European journal of nuclear medicine and molecular imaging* **2009**, *36*, 938-946, doi:10.1007/s00259-008-1058-9.

83.   Reber, J.; Haller, S.; Leamon, C.P.; Müller, C. 177Lu-EC0800 combined with the antifolate pemetrexed: preclinical pilot study of folate receptor targeted radionuclide tumor therapy. *Molecular cancer therapeutics* **2013**, *12*, 2436-2445, doi:10.1158/1535-7163.MCT-13-0422-T.

84.   Müller, C.; Schibli, R.; Forrer, F.; Krenning, E.P.; de Jong, M. Dose-dependent effects of (anti)folate preinjection on 99mTc-radiofolate uptake in tumors and kidneys. *Nuclear medicine and biology* **2007**, *34*, 603-608, doi:10.1016/j.nucmedbio.2007.06.001.

85.   Müller, C.; Bruhlmeier, M.; Schubiger, P.A.; Schibli, R. Effects of antifolate drugs on the cellular uptake of radiofolates in vitro and in vivo. *Journal of nuclear medicine : official publication, Society of Nuclear Medicine* **2006**, *47*, 2057-2064.

86.   Zhao, R.; Qiu, A.; Tsai, E.; Jansen, M.; Akabas, M.H.; Goldman, I.D. The proton-coupled folate transporter: impact on pemetrexed transport and on antifolates activities compared with the reduced folate carrier. *Molecular pharmacology* **2008**, *74*, 854-862, doi:10.1124/mol.108.045443.

87.   Müller, C.; Struthers, H.; Winiger, C.; Zhernosekov, K.; Schibli, R. DOTA conjugate with an albumin-binding entity enables the first folic acid-targeted ^{177}Lu-radionuclide tumor therapy in mice. *Journal of nuclear medicine : official publication, Society of Nuclear Medicine* **2013**, *54*, 124-131, doi:10.2967/jnumed.112.107235.

88.   Dumelin, C.E.; Trussel, S.; Buller, F.; Trachsel, E.; Bootz, F.; Zhang, Y.; Mannocci, L.; Beck, S.C.; Drumea-Mirancea, M.; Seeliger, M.W., et al. A portable albumin binder from a DNA-encoded chemical library. *Angew Chem Int Ed Engl* **2008**, *47*, 3196-3201, doi:10.1002/anie.200704936.

89.   Dennis, M.S.; Jin, H.; Dugger, D.; Yang, R.; McFarland, L.; Ogasawara, A.; Williams, S.; Cole, M.J.; Ross, S.; Schwall, R. Imaging tumors with an albumin-binding Fab, a novel tumor-targeting agent. *Cancer research* **2007**, *67*, 254-261, doi:10.1158/0008-5472.CAN-06-2531.

90.   Siwowska, K.; Haller, S.; Bortoli, F.; Benešová, M.; Groehn, V.; Bernhardt, P.; Schibli, R.; Müller, C. Preclinical comparison of albumin-binding radiofolates: impact of linker entities on the in vitro and in vivo properties. *Molecular pharmaceutics* **2017**, *14*, 523-532, doi:10.1021/acs.molpharmaceut.6b01010.

91.   Topalian, S.L.; Drake, C.G.; Pardoll, D.M. Immune checkpoint blockade: a common denominator approach to cancer therapy. *Cancer Cell* **2015**, *27*, 450-461, doi:10.1016/j.ccell.2015.03.001.

92.   Sharma, P.; Allison, J.P. The future of immune checkpoint therapy. *Science* **2015**, *348*, 56-61, doi:10.1126/science.aaa8172.

93.   Gotwals, P.; Cameron, S.; Cipolletta, D.; Cremasco, V.; Crystal, A.; Hewes, B.; Mueller, B.; Quaratino, S.; Sabatos-Peyton, C.; Petruzzelli, L., et al. Prospects for combining targeted and conventional cancer therapy with immunotherapy. *Nature reviews. Cancer* **2017**, *17*, 286-301, doi:10.1038/nrc.2017.17.

94.   Singh, S.; Hassan, D.; Aldawsari, H.M.; Molugulu, N.; Shukla, R.; Kesharwani, P. Immune checkpoint inhibitors: a promising anticancer therapy. *Drug discovery today* **2020**, *25*, 223-229, doi:10.1016/j.drudis.2019.11.003.

95.   Zappasodi, R.; Merghoub, T.; Wolchok, J.D. Emerging concepts for immune checkpoint blockade-based combination therapies. *Cancer Cell* **2018**, *33*, 581-598, doi:10.1016/j.ccell.2018.03.005.

96.   Melero, I.; Berman, D.M.; Aznar, M.A.; Korman, A.J.; Perez Gracia, J.L.; Haanen, J. Evolving synergistic combinations of targeted immunotherapies to combat cancer. *Nature reviews. Cancer* **2015**, *15*, 457-472, doi:10.1038/nrc3973.

97.   Joshi, S.; Durden, D.L. Combinatorial approach to improve cancer immunotherapy: rational drug design strategy to simultaneously hit multiple targets to kill tumor cells and to activate the immune system. *J Oncol* **2019**, *2019*, 5245034, doi:10.1155/2019/5245034.

98.   Demaria, S.; Coleman, C.N.; Formenti, S.C. Radiotherapy: changing the game in immunotherapy. *Trends Cancer* **2016**, *2*, 286-294, doi:10.1016/j.trecan.2016.05.002.

99. Hernandez, R.; Walker, K.L.; Grudzinski, J.J.; Aluicio-Sarduy, E.; Patel, R.; Zahm, C.D.; Pinchuk, A.N.; Massey, C.F.; Bitton, A.N.; Brown, R.J., et al. ^{90}Y-NM600 targeted radionuclide therapy induces immunologic memory in syngeneic models of T-cell non-Hodgkin's lymphoma. *Commun Biol* **2019**, *2*, 79, doi:10.1038/s42003-019-0327-4.

100. Hernandez, R.; Grudzinski, J.J.; Aluicio-Sarduy, E.; Massey, C.F.; Pinchuk, A.N.; Bitton, A.N.; Patel, R.; Zhang, R.; Kumar, A.V.; Iyer, G., et al. ^{177}Lu-NM600 targeted radionuclide therapy extends survival in syngeneic murine models of triple-negative breast cancer. *Journal of nuclear medicine : official publication, Society of Nuclear Medicine* **2019**, 10.2967/jnumed.119.236265, doi:10.2967/jnumed.119.236265.

101. Choi, J.; Beaino, W.; Fecek, R.J.; Fabian, K.P.L.; Laymon, C.M.; Kurland, B.F.; Storkus, W.J.; Anderson, C.J. Combined VLA-4-targeted radionuclide therapy and immunotherapy in a mouse model of melanoma. *Journal of nuclear medicine : official publication, Society of Nuclear Medicine* **2018**, *59*, 1843-1849, doi:10.2967/jnumed.118.209510.

102. Wu, Y.; Pfeifer, A.K.; Myschetzky, R.; Garbyal, R.S.; Rasmussen, P.; Knigge, U.; Bzorek, M.; Kristensen, M.H.; Kjaer, A. Induction of anti-tumor immune responses by peptide receptor radionuclide therapy with ^{177}Lu-DOTATATE in a mrine model of a human neuroendocrine tumor. *Diagnostics (Basel)* **2013**, *3*, 344-355, doi:10.3390/diagnostics3040344.

103. Rouanet, J.; Benboubker, V.; Akil, H.; Hennino, A.; Auzeloux, P.; Besse, S.; Pereira, B.; Delorme, S.; Mansard, S.; D'Incan, M., et al. Immune checkpoint inhibitors reverse tolerogenic mechanisms induced by melanoma targeted radionuclide therapy. *Cancer Immunol Immunother* **2020**, 10.1007/s00262-020-02606-8, doi:10.1007/s00262-020-02606-8.

104. Ruggeri, B.A.; Camp, F.; Miknyoczki, S. Animal models of disease: pre-clinical animal models of cancer and their applications and utility in drug discovery. *Biochemical pharmacology* **2014**, *87*, 150-161, doi:10.1016/j.bcp.2013.06.020.

105. Day, C.P.; Merlino, G.; Van Dyke, T. Preclinical mouse cancer models: a maze of opportunities and challenges. *Cell* **2015**, *163*, 39-53, doi:10.1016/j.cell.2015.08.068.

106. Sanmamed, M.F.; Chester, C.; Melero, I.; Kohrt, H. Defining the optimal murine models to investigate immune checkpoint blockers and their combination with other immunotherapies. *Annals of oncology : official journal of the European Society for Medical Oncology / ESMO* **2016**, *27*, 1190-1198, doi:10.1093/annonc/mdw041.

107. Bhatnagar, A.; Wang, Y.; Mease, R.C.; Gabrielson, M.; Sysa, P.; Minn, I.; Green, G.; Simmons, B.; Gabrielson, K.; Sarkar, S., et al. AEG-1 promoter-mediated imaging of prostate cancer. *Cancer research* **2014**, *74*, 5772-5781, doi:10.1158/0008-5472.CAN-14-0018.

108. Tafreshi, N.K.; Doligalski, M.L.; Tichacek, C.J.; Pandya, D.N.; Budzevich, M.M.; El-Haddad, G.; Khushalani, N.I.; Moros, E.G.; McLaughlin, M.L.; Wadas, T.J., et al. Development of targeted alpha particle therapy for solid tumors. *Molecules* **2019**, *24*, doi:10.3390/molecules24234314.

109. Shaw, T.J.; Senterman, M.K.; Dawson, K.; Crane, C.A.; Vanderhyden, B.C. Characterization of intraperitoneal, orthotopic, and metastatic xenograft models of human ovarian cancer. *Mol Ther* **2004**, *10*, 1032-1042, doi:10.1016/j.ymthe.2004.08.013.

110. Gomez-Cuadrado, L.; Tracey, N.; Ma, R.; Qian, B.; Brunton, V.G. Mouse models of metastasis: progress and prospects. *Dis Model Mech* **2017**, *10*, 1061-1074, doi:10.1242/dmm.030403.

111. Aryee, K.E.; Shultz, L.D.; Brehm, M.A. Immunodeficient mouse model for human hematopoietic stem cell engraftment and immune system development. *Methods Mol Biol* **2014**, *1185*, 267-278, doi:10.1007/978-1-4939-1133-2_18.

112. Siwowska, K.; Schmid, R.M.; Cohrs, S.; Schibli, R.; Müller, C. Folate receptor-positive gynecological cancer cells: in vitro and in vivo characterization. *Pharmaceuticals (Basel)* **2017**, *10*, doi:10.3390/ph10030072.

113. Yu, D.; Wolf, J.K.; Scanlon, M.; Price, J.E.; Hung, M.C. Enhanced c-erbB-2/neu expression in human ovarian cancer cells correlates with more severe malignancy that can be suppressed by E1A. *Cancer research* **1993**, *53*, 891-898.

114. Ocak, M.; Gillman, A.G.; Bresee, J.; Zhang, L.; Vlad, A.M.; Müller, C.; Schibli, R.; Edwards, W.B.; Anderson, C.J.; Gach, H.M. Folate receptor-targeted multimodality imaging of ovarian cancer in a novel syngeneic mouse model. *Molecular pharmaceutics* **2015**, *12*, 542-553, doi:10.1021/mp500628g.

115. Reddy, J.A.; Dorton, R.; Bloomfield, A.; Nelson, M.; Vetzel, M.; Guan, J.; Leamon, C.P. Rational combination therapy of vintafolide (EC145) with commonly used chemotherapeutic drugs. *Clinical cancer research : an official journal of the American Association for Cancer Research* **2014**, *20*, 2104-2114, doi:10.1158/1078-0432.CCR-13-2423.

116. Guo, W.; Hinkle, G.H.; Lee, R.J. ^{99m}Tc-HYNIC-folate: a novel receptor-based targeted radiopharmaceutical for tumor imaging. *Journal of nuclear medicine : official publication, Society of Nuclear Medicine* **1999**, *40*, 1563-1569.

117. Reddy, J.A.; Nelson, M.; Dircksen, C.; Vetzel, M.; Johnson, T.; Cross, V.; Westrick, E.; Qi, L.; Hahn, S.; Santhapuram, H.K., et al. Pre-clinical studies of EC2629, a highly potent folate - receptor-targeted DNA crosslinking agent. *Scientific reports* **2020**, *10*, 12772, doi:10.1038/s41598-020-69682-9.

118. Uyar, D.; Schilder, R.J.; Naumann, R.W.; Braiteh, F.S.; Hamilton, E.; Diab, S.; Moroney, J.; Penson, R.T.; Smith, J.; Abrahams, C., et al. Abstract C095: Antitumor activity of STRO-002, a novel anti-folate receptor-α (FRα) antibody drug conjugate (ADC), in patient-derived xenograft (PDX) models and preliminary phase I dose escalation safety outcomes in patients with ovarian carcinoma (OC). *Molecular cancer therapeutics* **2019**, *18*, C095-C095, doi:10.1158/1535-7163.Targ-19-c095.

119. Paulos, C.M.; Reddy, J.A.; Leamon, C.P.; Turk, M.J.; Low, P.S. Ligand binding and kinetics of folate receptor recycling in vivo: impact on receptor-mediated drug delivery. *Molecular pharmacology* **2004**, *66*, 1406-1414, doi:10.1124/mol.104.003723.

120. Müller, C.; Schubiger, P.A.; Schibli, R. In vitro and in vivo targeting of different folate receptor-positive cancer cell lines with a novel ^{99m}Tc-radiofolate tracer. *European journal of nuclear medicine and molecular imaging* **2006**, *33*, 1162-1170, doi:10.1007/s00259-006-0118-2.

121. Parker, N.; Turk, M.J.; Westrick, E.; Lewis, J.D.; Low, P.S.; Leamon, C.P. Folate receptor expression in carcinomas and normal tissues determined by a quantitative radioligand binding assay. *Analytical biochemistry* **2005**, *338*, 284-293, doi:10.1016/j.ab.2004.12.026.

122. Low, P.S.; Kularatne, S.A. Folate-targeted therapeutic and imaging agents for cancer. *Current opinion in chemical biology* **2009**, *13*, 256-262, doi:10.1016/j.cbpa.2009.03.022.

123. Assaraf, Y.G.; Leamon, C.P.; Reddy, J.A. The folate receptor as a rational therapeutic target for personalized cancer treatment. *Drug Resist Update* **2014**, *17*, 89-95, doi:10.1016/j.drup.2014.10.002.

124. Zhang, Z.; Wang, J.; Tacha, D.E.; Li, P.; Bremer, R.E.; Chen, H.; Wei, B.; Xiao, X.; Da, J.; Skinner, K., et al. Folate receptor alpha associated with triple-negative breast cancer and poor prognosis. *Arch Pathol Lab Med* **2014**, *138*, 890-895, doi:10.5858/arpa.2013-0309-OA.

125. Norton, N.; Youssef, B.; Hillman, D.W.; Nassar, A.; Geiger, X.J.; Necela, B.M.; Liu, H.; Ruddy, K.J.; Polley, M.C.; Ingle, J.N., et al. Folate receptor alpha expression associates with improved disease-free survival in triple negative breast cancer patients. *NPJ Breast Cancer* **2020**, *6*, 4, doi:10.1038/s41523-020-0147-1.

126. Pribble, P.; Edelman, M.J. EC145: a novel targeted agent for adenocarcinoma of the lung. *Expert opinion on investigational drugs* **2012**, *21*, 755-761, doi:10.1517/13543784.2012.671294.

127. Teng, L.; Xie, J.; Teng, L.; Lee, R.J. Clinical translation of folate receptor-targeted therapeutics. *Expert opinion on drug delivery* **2012**, *9*, 901-908, doi:10.1517/17425247.2012.694863.

128. Xu, L.; Bai, Q.; Zhang, X.; Yang, H. Folate-mediated chemotherapy and diagnostics: An updated review and outlook. *J Control Release* **2017**, *252*, 73-82, doi:10.1016/j.jconrel.2017.02.023.

129. Farran, B.; Pavitra, E.; Kasa, P.; Peela, S.; Rama Raju, G.S.; Nagaraju, G.P. Folate-targeted immunotherapies: Passive and active strategies for cancer. *Cytokine Growth Factor Rev* **2019**, *45*, 45-52, doi:10.1016/j.cytogfr.2019.02.001.

130. Fisher, R.E.; Siegel, B.A.; Edell, S.L.; Oyesiku, N.M.; Morgenstern, D.E.; Messmann, R.A.; Amato, R.J. Exploratory study of ^{99m}Tc-EC20 imaging for identifying patients with folate receptor-positive solid tumors. *Journal of nuclear medicine : official publication, Society of Nuclear Medicine* **2008**, *49*, 899-906, doi:10.2967/jnumed.107.049478.

131. Antony, A.C. Folate receptors. *Annual review of nutrition* **1996**, *16*, 501-521, doi:10.1146/annurev.nu.16.070196.002441.

132. Wang, X.; Shen, F.; Freisheim, J.H.; Gentry, L.E.; Ratnam, M. Differential stereospecificities and affinities of folate receptor isoforms for folate compounds and antifolates. *Biochemical pharmacology* **1992**, *44*, 1898-1901, doi:10.1016/0006-2952(92)90089-2.

133. Maziarz, K.M.; Monaco, H.L.; Shen, F.; Ratnam, M. Complete mapping of divergent amino acids responsible for differential ligand binding of folate receptors alpha and beta. *The Journal of biological chemistry* **1999**, *274*, 11086-11091, doi:10.1074/jbc.274.16.11086.

134. Vaitilingam, B.; Chelvam, V.; Kularatne, S.A.; Poh, S.; Ayala-Lopez, W.; Low, P.S. A folate receptor-alpha-specific ligand that targets cancer tissue and not sites of inflammation. *Journal of nuclear medicine : official publication, Society of Nuclear Medicine* **2012**, *53*, 1127-1134, doi:10.2967/jnumed.111.099390.

135. Almuhaideb, A.; Papathanasiou, N.; Bomanji, J. ^{18}F-FDG PET/CT imaging in oncology. *Ann Saudi Med* **2011**, *31*, 3-13, doi:10.4103/0256-4947.75771.

136. Verweij, N.J.F.; Yaqub, M.; Bruijnen, S.T.G.; Pieplenbosch, S.; Ter Wee, M.M.; Jansen, G.; Chen, Q.; Low, P.S.; Windhorst, A.D.; Lammertsma, A.A., et al. First in man study of [^{18}F]fluoro-PEG-folate PET: a novel macrophage imaging technique to visualize rheumatoid arthritis. *Scientific reports* **2020**, *10*, 1047, doi:10.1038/s41598-020-57841-x.

137. Deng, Y.; Wang, Y.; Cherian, C.; Hou, Z.; Buck, S.A.; Matherly, L.H.; Gangjee, A. Synthesis and discovery of high affinity folate receptor-specific glycinamide ribonucleotide formyltransferase inhibitors with antitumor activity. *Journal of medicinal chemistry* **2008**, *51*, 5052-5063, doi:10.1021/jm8003366.

138. Müller, C.; Forrer, F.; Schibli, R.; Krenning, E.P.; de Jong, M. SPECT study of folate receptor-positive malignant and normal tissues in mice using a novel ^{99m}Tc-radiofolate. *Journal of nuclear medicine : official publication, Society of Nuclear Medicine* **2008**, *49*, 310-317, doi:10.2967/jnumed.107.045856.

139. Gu, Z.; Taschereau, R.; Vu, N.T.; Prout, D.L.; Silverman, R.W.; Lee, J.T.; Chatziioannou, A.F. Performance evaluation of G8, a high-sensitivity benchtop preclinical PET/CT tomograph. *Journal of nuclear medicine : official publication, Society of Nuclear Medicine* **2019**, *60*, 142-149, doi:10.2967/jnumed.118.208827.

140. Luyckx, M.; Votino, R.; Squifflet, J.L.; Baurain, J.F. Profile of vintafolide (EC145) and its use in the treatment of platinum-resistant ovarian cancer. *Int J Womens Health* **2014**, *6*, 351-358, doi:10.2147/IJWH.S39696.

141. Kamen, B.A.; Smith, A.K. A review of folate receptor alpha cycling and 5-methyltetrahydrofolate accumulation with an emphasis on cell models in vitro. *Advanced drug delivery reviews* **2004**, *56*, 1085-1097, doi:10.1016/j.addr.2004.01.002.

142. Leamon, C.P.; Reddy, J.A. Folate-targeted chemotherapy. *Advanced drug delivery reviews* **2004**, *56*, 1127-1141, doi:10.1016/j.addr.2004.01.008.

143. Chen, Q.; Meng, X.; McQuade, P.; Rubins, D.; Lin, S.A.; Zeng, Z.; Haley, H.; Miller, P.; Gonzalez Trotter, D.; Low, P.S. Folate-PEG-NOTA-Al^{18}F: a new folate based radiotracer for PET imaging of folate receptor-positive tumors. *Molecular pharmaceutics* **2017**, *14*, 4353-4361, doi:10.1021/acs.molpharmaceut.7b00415.

144. Curtin, N.J.; Hughes, A.N. Pemetrexed disodium, a novel antifolate with multiple targets. *Lancet Oncol* **2001**, *2*, 298-306.

145. Reber, J.; Struthers, H.; Betzel, T.; Hohn, A.; Schibli, R.; Müller, C. Radioiodinated folic acid conjugates: evaluation of a valuable concept to improve tumor-to-background contrast. *Molecular pharmaceutics* **2012**, *9*, 1213-1221, doi:10.1021/mp200511t.

146. Bischof, M.; Weber, K.J.; Blatter, J.; Wannenmacher, M.; Latz, D. Interaction of pemetrexed disodium (ALIMTA, multitargeted antifolate) and irradiation in vitro. *International journal of radiation oncology, biology, physics* **2002**, *52*, 1381-1388.

147. Bischof, M.; Huber, P.; Stoffregen, C.; Wannenmacher, M.; Weber, K.J. Radiosensitization by pemetrexed of human colon carcinoma cells in different cell cycle phases. *International journal of radiation oncology, biology, physics* **2003**, *57*, 289-292.

148. Oleinick, N.L.; Biswas, T.; Patel, R.; Tao, M.; Patel, R.; Weeks, L.; Sharma, N.; Dowlati, A.; Gerson, S.L.; Fu, P., et al. Radiosensitization of non-small-cell lung cancer cells and xenografts by the interactive effects of pemetrexed and methoxyamine. *Radiother Oncol* **2016**, *121*, 335-341, doi:10.1016/j.radonc.2016.10.007.

149. Gudkov, S.V.; Shilyagina, N.Y.; Vodeneev, V.A.; Zvyagin, A.V. Targeted radionuclide therapy of human tumors. *International journal of molecular sciences* **2015**, *17*, doi:10.3390/ijms17010033.

150. Nitipir, C.; Niculae, D.; Orlov, C.; Barbu, M.A.; Popescu, B.; Popa, A.M.; Pantea, A.M.S.; Stanciu, A.E.; Galateanu, B.; Ginghina, O., et al. Update on radionuclide therapy in oncology. *Oncol Lett* **2017**, *14*, 7011-7015, doi:10.3892/ol.2017.7141.

151. Strosberg, J.; El-Haddad, G.; Wolin, E.; Hendifar, A.; Yao, J.; Chasen, B.; Mittra, E.; Kunz, P.L.; Kulke, M.H.; Jacene, H., et al. Phase 3 trial of ^{177}Lu-DOTATATE for midgut neuroendocrine tumors. *The New England journal of medicine* **2017**, *376*, 125-135, doi:10.1056/NEJMoa1607427.

152. ^{177}Lu-DOTATATE approved by FDA. *Cancer Discov* **2018**, *8*, OF2, doi:10.1158/2159-8290.CD-NB2018-021.

153. Rahbar, K.; Ahmadzadehfar, H.; Kratochwil, C.; Haberkorn, U.; Schafers, M.; Essler, M.; Baum, R.P.; Kulkarni, H.R.; Schmidt, M.; Drzezga, A., et al. German multicenter study investigating ^{177}Lu-PSMA-617 radioligand therapy in advanced prostate cancer patients. *Journal of nuclear medicine : official publication, Society of Nuclear Medicine* **2017**, *58*, 85-90, doi:10.2967/jnumed.116.183194.

154. Sartor, A.O.; Morris, M.J.; Messman, R.; Krause, B.J. VISION: An international, prospective, open-label, multicenter, randomized phase III study of ^{177}Lu-PSMA-617 in the treatment of patients with progressive PSMA-positive metastatic castration-resistant prostate cancer (mCRPC). *Journal of Clinical Oncology* **2020**, *38*, TPS259-TPS259, doi:10.1200/JCO.2020.38.6_suppl.TPS259.

155. Sega, E.I.; Low, P.S. Tumor detection using folate receptor-targeted imaging agents. *Cancer metastasis reviews* **2008**, *27*, 655-664, doi:10.1007/s10555-008-9155-6.

156. Boss, S.D.; Müller, C.; Siwowska, K.; Buchel, J.I.; Schmid, R.M.; Groehn, V.; Schibli, R.; Ametamey, S.M. Reduced ^{18}F-folate conjugates as a new class of PET tracers for folate receptor imaging. *Bioconjugate chemistry* **2018**, *29*, 1119-1130, doi:10.1021/acs.bioconjchem.7b00775.

157. Müller, C.; Bunka, M.; Haller, S.; Köster, U.; Groehn, V.; Bernhardt, P.; van der Meulen, N.; Türler, A.; Schibli, R. Promising prospects for [44]Sc-/[47]Sc-based theragnostics: application of [47]Sc for radionuclide tumor therapy in mice. *Journal of nuclear medicine : official publication, Society of Nuclear Medicine* **2014**, *55*, 1658-1664, doi:10.2967/jnumed.114.141614.

158. Umbricht, C.A.; Benešová, M.; Schibli, R.; Müller, C. Preclinical development of novel PSMA-targeting radioligands: modulation of albumin-binding properties to improve prostate cancer therapy. *Molecular pharmaceutics* **2018**, *15*, 2297-2306, doi:10.1021/acs.molpharmaceut.8b00152.

159. Müller, C.; Farkas, R.; Borgna, F.; Schmid, R.M.; Benesova, M.; Schibli, R. Synthesis, radiolabeling, and characterization of plasma protein-binding ligands: Potential tools for modulation of the pharmacokinetic properties of (radio)pharmaceuticals. *Bioconjugate chemistry* **2017**, *28*, 2372-2383, doi:10.1021/acs.bioconjchem.7b00378.

160. Siwowska, K.; Guzik, P.; Domnanich, K.A.; Monné Rodríguez, J.M.; Bernhardt, P.; Ponsard, B.; Hasler, R.; Borgna, F.; Schibli, R.; Köster, U., et al. Therapeutic potential of [47]Sc in comparison to ^{177}Lu and [90]Y: preclinical investigations. *Pharmaceutics* **2019**, *11*, doi:10.3390/pharmaceutics11080424.

161. Haller, S.; Pellegrini, G.; Vermeulen, C.; van der Meulen, N.P.; Köster, U.; Bernhardt, P.; Schibli, R.; Müller, C. Contribution of Auger/conversion electrons to renal side effects after radionuclide therapy: preclinical comparison of [161]Tb-folate and ^{177}Lu-folate. *EJNMMI research* **2016**, *6*, 13, doi:10.1186/s13550-016-0171-1.

162.	Guzik, P.; Benešová, M.; Ratz, M.; Monné Rodríguez, J.M.; Deberle, L.M.; Schibli, R.; Müller, C. Preclinical evaluation of 5-methyltetrahydrofolate-based radioconjugates - new perspectives for folate receptor-targeted radionuclide therapy. *European journal of nuclear medicine and molecular imaging* **2020**, 10.1007/s00259-020-04980-y, doi:10.1007/s00259-020-04980-y.

163.	Sellers, R.S.; Morton, D.; Michael, B.; Roome, N.; Johnson, J.K.; Yano, B.L.; Perry, R.; Schafer, K. Society of toxicologic pathology position paper: organ weight recommendations for toxicology studies. *Toxicol Pathol* **2007**, *35*, 751-755, doi:10.1080/01926230701595300.

164.	Michael, B.; Yano, B.; Sellers, R.S.; Perry, R.; Morton, D.; Roome, N.; Johnson, J.K.; Schafer, K.; Pitsch, S. Evaluation of organ weights for rodent and non-rodent toxicity studies: A review of regulatory guidelines and a survey of current practices. *Toxicol Pathol* **2007**, *35*, 742-750, doi:10.1080/01926230701595292.

165.	Leach, D.R.; Krummel, M.F.; Allison, J.P. Enhancement of antitumor immunity by CTLA-4 blockade. *Science* **1996**, *271*, 1734-1736, doi:10.1126/science.271.5256.1734.

166.	Pardoll, D.M. The blockade of immune checkpoints in cancer immunotherapy. *Nature reviews. Cancer* **2012**, *12*, 252-264, doi:10.1038/nrc3239.

167.	Mahoney, K.M.; Rennert, P.D.; Freeman, G.J. Combination cancer immunotherapy and new immunomodulatory targets. *Nat Rev Drug Discov* **2015**, *14*, 561-584, doi:10.1038/nrd4591.

168.	Lechner, M.G.; Karimi, S.S.; Barry-Holson, K.; Angell, T.E.; Murphy, K.A.; Church, C.H.; Ohlfest, J.R.; Hu, P.; Epstein, A.L. Immunogenicity of murine solid tumor models as a defining feature of in vivo behavior and response to immunotherapy. *J Immunother* **2013**, *36*, 477-489, doi:10.1097/01.cji.0000436722.46675.4a.

169.	Hu, Z.I.; Ho, A.Y.; McArthur, H.L. Combined radiation therapy and immune checkpoint blockade therapy for breast cancer. *International journal of radiation oncology, biology, physics* **2017**, *99*, 153-164, doi:10.1016/j.ijrobp.2017.05.029.

170.	Sevenich, L. Turning "cold" Into "hot" tumors-opportunities and challenges for radio-immunotherapy against primary and metastatic brain cancers. *Frontiers in oncology* **2019**, *9*, 163, doi:10.3389/fonc.2019.00163.

171.	Hu, Z.I.; McArthur, H.L.; Ho, A.Y. The abscopal effect of radiation therapy: What is it and how can we use it in breast cancer? *Curr Breast Cancer Rep* **2017**, *9*, 45-51, doi:10.1007/s12609-017-0234-y.

172.	Siegel, R.L.; Miller, K.D.; Jemal, A. Cancer statistics, 2019. *CA Cancer J Clin* **2019**, *69*, 7-34, doi:10.3322/caac.21551.

173.	Early Breast Cancer Trialists' Collaborative, G. Effects of chemotherapy and hormonal therapy for early breast cancer on recurrence and 15-year survival: an overview of the randomised trials. *Lancet* **2005**, *365*, 1687-1717, doi:10.1016/S0140-6736(05)66544-0.

174.	Weigelt, B.; Peterse, J.L.; van 't Veer, L.J. Breast cancer metastasis: markers and models. *Nature reviews. Cancer* **2005**, *5*, 591-602, doi:10.1038/nrc1670.

175.	Denkert, C. The immunogenicity of breast cancer - molecular subtypes matter. *Annals of oncology : official journal of the European Society for Medical Oncology / ESMO* **2014**, *25*, 1453-1455, doi:10.1093/annonc/mdu235.

176.	Demaria, S.; Kawashima, N.; Yang, A.M.; Devitt, M.L.; Babb, J.S.; Allison, J.P.; Formenti, S.C. Immune-mediated inhibition of metastases after treatment with local radiation and CTLA-

4 blockade in a mouse model of breast cancer. *Clinical cancer research : an official journal of the American Association for Cancer Research* **2005**, *11*, 728-734.

177. Demaria, S.; Pilones, K.A.; Vanpouille-Box, C.; Golden, E.B.; Formenti, S.C. The optimal partnership of radiation and immunotherapy: from preclinical studies to clinical translation. *Radiation research* **2014**, *182*, 170-181, doi:10.1667/RR13500.1.

178. Yilmaz, M.T.; Elmali, A.; Yazici, G. Abscopal effect, from myth to reality: from radiation oncologists' perspective. *Cureus* **2019**, *11*, e3860, doi:10.7759/cureus.3860.

179. Chen, H.; Zhao, L.; Fu, K.; Lin, Q.; Wen, X.; Jacobson, O.; Sun, L.; Wu, H.; Zhang, X.; Guo, Z., et al. Integrin αvβ3-targeted radionuclide therapy combined with immune checkpoint blockade immunotherapy synergistically enhances anti-tumor efficacy. *Theranostics* **2019**, *9*, 7948-7960, doi:10.7150/thno.39203.

180. Yordanova, A.; Eppard, E.; Kürpig, S.; Bundschuh, R.A.; Schönberger, S.; Gonzalez-Carmona, M.; Feldmann, G.; Ahmadzadehfar, H.; Essler, M. Theranostics in nuclear medicine practice. *OncoTargets and therapy* **2017**, *10*, 4821-4828, doi:10.2147/OTT.S140671.

181. O'Shannessy, D.J.; Somers, E.B.; Maltzman, J.; Smale, R.; Fu, Y.S. Folate receptor alpha (FRA) expression in breast cancer: identification of a new molecular subtype and association with triple negative disease. *Springerplus* **2012**, *1*, 22, doi:10.1186/2193-1801-1-22.

182. Necela, B.M.; Crozier, J.A.; Andorfer, C.A.; Lewis-Tuffin, L.; Kachergus, J.M.; Geiger, X.J.; Kalari, K.R.; Serie, D.J.; Sun, Z.; Moreno-Aspitia, A., et al. Folate receptor-alpha (FOLR1) expression and function in triple negative tumors. *PloS one* **2015**, *10*, e0122209, doi:10.1371/journal.pone.0122209.

183. Aboulhagag, N.A.E.; Torky, R.F.; Fadel, S.A. Folate receptor alpha is associated with poor clinicopathological perspectives in breast carcinoma. *Pathophysiology* **2018**, *25*, 71-76, doi:10.1016/j.pathophys.2018.01.002.

184. Oehler-Janne, C.; Jochum, W.; Riesterer, O.; Broggini-Tenzer, A.; Caravatti, G.; Vuong, V.; Pruschy, M. Hypoxia modulation and radiosensitization by the novel dual EGFR and VEGFR inhibitor AEE788 in spontaneous and related allograft tumor models. *Molecular cancer therapeutics* **2007**, *6*, 2496-2504, doi:10.1158/1535-7163.MCT-07-0253.

185. Riesterer, O.; Oehler-Janne, C.; Jochum, W.; Broggini-Tenzer, A.; Vuong, V.; Pruschy, M. Ionizing radiation and inhibition of angiogenesis in a spontaneous mammary carcinoma and in a syngenic heterotopic allograft tumor model: a comparative study. *Radiat Oncol* **2011**, *6*, 66, doi:10.1186/1748-717X-6-66.

186. Morrison, B.W.; Leder, P. neu and ras initiate murine mammary tumors that share genetic markers generally absent in c-myc and int-2-initiated tumors. *Oncogene* **1994**, *9*, 3417-3426.

187. Cefai, D.; Schwaninger, R.; Balli, M.; Brunner, T.; Gimmi, C.D. Functional characterization of Fas ligand on tumor cells escaping active specific immunotherapy. *Cell Death Differ* **2001**, *8*, 687-695, doi:10.1038/sj.cdd.4400862.

188. Schmid, M.C.; Bisoffi, M.; Wetterwald, A.; Gautschi, E.; Thalmann, G.N.; Mitola, S.; Bussolino, F.; Cecchini, M.G. Insulin-like growth factor binding protein-3 is overexpressed in endothelial cells of mouse breast tumor vessels. *International journal of cancer. Journal international du cancer* **2003**, *103*, 577-586, doi:10.1002/ijc.10874.

189. Riesterer, O.; Honer, M.; Jochum, W.; Oehler, C.; Ametamey, S.; Pruschy, M. Ionizing radiation antagonizes tumor hypoxia induced by antiangiogenic treatment. *Clinical cancer research : an official journal of the American Association for Cancer Research* **2006**, *12*, 3518-3524, doi:10.1158/1078-0432.CCR-05-2816.

190. Guy, C.T.; Webster, M.A.; Schaller, M.; Parsons, T.J.; Cardiff, R.D.; Muller, W.J. Expression of the neu protooncogene in the mammary epithelium of transgenic mice induces metastatic disease. *Proceedings of the National Academy of Sciences of the United States of America* **1992**, *89*, 10578-10582, doi:10.1073/pnas.89.22.10578.

191. Müller, W.J.; Arteaga, C.L.; Muthuswamy, S.K.; Siegel, P.M.; Webster, M.A.; Cardiff, R.D.; Meise, K.S.; Li, F.; Halter, S.A.; Coffey, R.J. Synergistic interaction of the Neu proto-oncogene product and transforming growth factor alpha in the mammary epithelium of transgenic mice. *Molecular and cellular biology* **1996**, *16*, 5726-5736, doi:10.1128/mcb.16.10.5726.

192. Reddy, J.A.; Xu, L.C.; Parker, N.; Vetzel, M.; Leamon, C.P. Preclinical evaluation of ^{99m}Tc-EC20 for imaging folate receptor-positive tumors. *Journal of nuclear medicine : official publication, Society of Nuclear Medicine* **2004**, *45*, 857-866.

193. Salvat, F. PENELOPE2014: A code system for Monte-Carlo simulation of electron and photon transport. *OECD/NEA Data Bank: NEA/NSC/DOC* **2015**, *3*.

194. Guzik, P.; Siwowska, K.; Fang, H.Y.; Cohrs, S.; Bernhardt, P.; Schibli, R.; Müller, C. Promising potential of ^{177}Lu-DOTA-folate to enhance tumor response to immunotherapy - a preclinical study using a syngeneic breast cancer model. *European journal of nuclear medicine and molecular imaging* **2020**, 10.1007/s00259-020-05054-9, doi:10.1007/s00259-020-05054-9.

195. Nesseler, J.P.; Lee, M.H.; Nguyen, C.; Kalbasi, A.; Sayre, J.W.; Romero, T.; Nickers, P.; McBride, W.H.; Schaue, D. Tumor size matters-understanding concomitant tumor immunity in the context of hypofractionated radiotherapy with immunotherapy. *Cancers (Basel)* **2020**, *12*, doi:10.3390/cancers12030714.

196. Zhang, S.C.; Hu, Z.Q.; Long, J.H.; Zhu, G.M.; Wang, Y.; Jia, Y.; Zhou, J.; Ouyang, Y.; Zeng, Z. Clinical implications of tumor-infiltrating immune cells in breast cancer. *J Cancer* **2019**, *10*, 6175-6184, doi:10.7150/jca.35901.

197. Yu, J.W.; Bhattacharya, S.; Yanamandra, N.; Kilian, D.; Shi, H.; Yadavilli, S.; Katlinskaya, Y.; Kaczynski, H.; Conner, M.; Benson, W., et al. Tumor-immune profiling of murine syngeneic tumor models as a framework to guide mechanistic studies and predict therapy response in distinct tumor microenvironments. *PloS one* **2018**, *13*, e0206223, doi:10.1371/journal.pone.0206223.

198. Wen, F.T.; Thisted, R.A.; Rowley, D.A.; Schreiber, H. A systematic analysis of experimental immunotherapies on tumors differing in size and duration of growth. *Oncoimmunology* **2012**, *1*, 172-178, doi:10.4161/onci.1.2.18311.

199. Dhandapani, M.; Goldman, A. Preclinical Cancer Models and Biomarkers for Drug Development: New Technologies and Emerging Tools. *J Mol Biomark Diagn* **2017**, *8*, doi:10.4172/2155-9929.1000356.

200. Frese, K.K.; Tuveson, D.A. Maximizing mouse cancer models. *Nature reviews. Cancer* **2007**, *7*, 645-658, doi:10.1038/nrc2192.

201. Gutmann, D.H.; Hunter-Schaedle, K.; Shannon, K.M. Harnessing preclinical mouse models to inform human clinical cancer trials. *The Journal of clinical investigation* **2006**, *116*, 847-852, doi:10.1172/JCI28271.

202. Patel, N.R.; Piroyan, A.; Ganta, S.; Morse, A.B.; Candiloro, K.M.; Solon, A.L.; Nack, A.H.; Galati, C.A.; Bora, C.; Maglaty, M.A., et al. In Vitro and In Vivo evaluation of a novel folate-targeted theranostic nanoemulsion of docetaxel for imaging and improved anticancer activity against ovarian cancers. *Cancer biology & therapy* **2018**, *19*, 554-564, doi:10.1080/15384047.2017.1395118.

203. Patrick, T.A.; Kranz, D.M.; van Dyke, T.A.; Roy, E.J. Folate receptors as potential therapeutic targets in choroid plexus tumors of SV40 transgenic mice. *Journal of neuro-oncology* **1997**, *32*, 111-123, doi:10.1023/a:1005713115147.

204. Gawlick, U.; Kranz, D.M.; Schepkin, V.D.; Roy, E.J. A conjugate of a tumor-targeting ligand and a T cell costimulatory antibody to treat brain tumors. *Bioconjugate chemistry* **2004**, *15*, 1137-1145, doi:10.1021/bc049911e.

205. Muller, W.J.; Arteaga, C.L.; Muthuswamy, S.K.; Siegel, P.M.; Webster, M.A.; Cardiff, R.D.; Meise, K.S.; Li, F.; Halter, S.A.; Coffey, R.J. Synergistic interaction of the Neu proto-oncogene product and transforming growth factor alpha in the mammary epithelium of transgenic mice. *Molecular and cellular biology* **1996**, *16*, 5726-5736, doi:10.1128/mcb.16.10.5726.

206. da Costa, M.; Rothenberg, S.P.; Sadasivan, E.; Regec, A.; Qian, L. Folate deficiency reduces the GPI-anchored folate-binding protein in rat renal tubules. *Am J Physiol Cell Physiol* **2000**, *278*, C812-821, doi:10.1152/ajpcell.2000.278.4.C812.

207. Gates, S.B.; Mendelsohn, L.G.; Shackelford, K.A.; Habeck, L.L.; Kursar, J.D.; Gossett, L.S.; Worzalla, J.F.; Shih, C.; Grindey, G.B. Characterization of folate receptor from normal and neoplastic murine tissue: influence of dietary folate on folate receptor expression. *Clinical cancer research : an official journal of the American Association for Cancer Research* **1996**, *2*, 1135-1141.

208. Leamon, C.P.; Reddy, J.A.; Dorton, R.; Bloomfield, A.; Emsweller, K.; Parker, N.; Westrick, E. Impact of high and low folate diets on tissue folate receptor levels and antitumor responses toward folate-drug conjugates. *The Journal of pharmacology and experimental therapeutics* **2008**, *327*, 918-925, doi:10.1124/jpet.108.143206.

209. Brickute, D.; Braga, M.; Kaliszczak, M.A.; Barnes, C.; Lau, D.; Carroll, L.; Stevens, E.; Trousil, S.; Alam, I.S.; Nguyen, Q.D., et al. Development and Evaluation of an (18)F-Radiolabeled Monocyclam Derivative for Imaging CXCR4 Expression. *Molecular pharmaceutics* **2019**, *16*, 2106-2117, doi:10.1021/acs.molpharmaceut.9b00069.

210. Nofiele, J.T.; Cheng, H.L. Establishment of a lung metastatic breast tumor xenograft model in nude rats. *PloS one* **2014**, *9*, e97950, doi:10.1371/journal.pone.0097950.

211. Rubinoff, M.; Abramson, R.; Schreiber, C.; Waxman, S. Effect of a folate-binding protein on the plasma transport and tissue distribution of folic acid. *Acta Haematol* **1981**, *65*, 145-152, doi:10.1159/000207170.

212. Hemmerle, T.; Zgraggen, S.; Matasci, M.; Halin, C.; Detmar, M.; Neri, D. Antibody-mediated delivery of interleukin-4 to the neo-vasculature reduces chronic skin inflammation. *J Dermatol Sci* **2014**, *76*, 96-103, doi:10.1016/j.jdermsci.2014.07.012.

213. Deberle, L.M.; Benesova, M.; Umbricht, C.A.; Borgna, F.; Buchler, M.; Zhernosekov, K.; Schibli, R.; Muller, C. Development of a new class of PSMA radioligands comprising ibuprofen as an albumin-binding entity. *Theranostics* **2020**, *10*, 1678-1693, doi:10.7150/thno.40482.